Corrosion Behaviour of Alumix 123 P/M Alloy and AA2014-T6 in 3.5wt% NaCl

by

William David Judge

Submitted in partial fulfillment of the requirements
for the degree of Master of Applied Science

at

Dalhousie University
Halifax, Nova Scotia
August 2015

This thesis is dedicated to my grandfather, Larry Judge, for his love and support throughout my life

TABLE OF CONTENTS

LIST OF TABLES

LIST OF FIGURES

ABSTRACT

The corrosion behaviour of the commercial aluminum powder metallurgy (P/M) alloy 'Alumix 123' and a compositionally similar wrought alloy, AA2014-T6, has been studied in naturally aerated 3.5wt% NaCl electrolyte by a variety of electrochemical methods and the subsequent corrosion morphology characterized by scanning electron microscopy (SEM) and energy dispersive X-ray spectroscopy (EDS). The P/M material was sintered in an industrial setting and was studied in the 'as-sintered' condition or after a standard sizing operation, denoted by the T1 and T2 temper, respectively. The electrochemical methods employed included open circuit potential (OCP), cathodic potentiodynamic polarization, cyclic potentiodynamic polarization, and potentiostatic polarization.

The OCP of Alumix 123-T1 stabilized at potentials near the onset of hydrogen evolution, where corrosion was partially under anodic control and proceeded via cathodic hydrogen evolution. This is postulated to be due to a reduction in cathode area or depassivation induced by propagating crevice corrosion within residual porosity. In this state, most of the anodic current on Alumix 123-T1 was generated from creviced areas within residual porosity which eventually repassivated when the concentration of anodic reaction products exceeded the solubility limit and precipitation occurred.

The OCP of Alumix 123-T2 stabilized at the pitting potential, where corrosion was predominantely under cathodic control and proceeded via cathodic oxygen reduction. The sizing operation of Alumix 123-T2 reduced the amount of residual porosity through plastic deformation and sealed surface porosity with sizing fluid so that crevice corrosion did not initiate.

In Alumix 123-(T1, T2), pitting was not always associated with copper- and iron-rich intermetallics. This behaviour was attributed to the refractory layer formed on the P/M materials as a result of the sintering process, which retained integrity over these intermetallics. Above the pitting potential of Alumix 123-(T1, T2), crystallographic pitting was scarcely observed and the majority of attack was intergranular in nature.

The OCP of AA2014-T6 stabilized at the pitting potential where corrosion was predominantly under cathodic control and proceeded via cathodic oxygen reduction. In AA2014-T6 pitting was associated with copper- and iron-rich intermetallics. SEM observations of AA2014-T6 suggested that copper is redeposited on copper- and iron-rich intermetallics and that cathodic trenching around iron-rich intermetallics may have liberated copper from the matrix in a non-Faradaic process. Above the pitting potential of AA2014-T6, there was extensive attack by crystallographic pitting and intergranular corrosion.

LIST OF ABBREVIATIONS AND SYMBOLS USED

a.u.	Arbitrary units
ads	Adsorped
avg	Average
AESEC	Atomic emission spectroelectrochemistry
AMS	Aerospace Material Specification
ASTM	American Society for Testing and Materials
CR	Corrosion rate
d	Particle diameter
D_{10}	Particle diameter at 10% of the cumulative particle size distribution
D_{50}	Particle diameter at 50% of the cumulative particle size distribution
D_{90}	Particle diameter at 90% of the cumulative particle size distribution
DC	Direct-chill (casting)
E_{corr}	Corrosion potential
E_{pit}	Pitting potential
E_{repass}	Repassivation potential
EBS	Ethylene bisstearamide
EDS	Energy dispersive X-ray spectroscopy
EW	Equivalent weight
GP	Guinier-Preston (zone)
hr	Hour
i_{corr}	Corrosion current density
i_{pass}	Passive current density
ICP-OES	Inductively coupled plasma optical emission spectroscopy
IGC	Intergranular corrosion
ISO	International Organization for Standardization
LPS	Liquid phase sintering
m	Mass
M	Molarity
MEC	Minerals Engineering Centre, Dalhousie University

MPIF	Metal Powder Industries Federation
NDE	Negative difference effect
NIST	National Institute of Standards and Technology
NSERC	National Sciences and Engineering Council of Canada
OCP	Open circuit potential
P/M	Powder metallurgy
PAR	Princeton Applied Research
PDF	Powder diffraction file
ppm	Parts per million
sat'd	Saturated
SCC	Stress corrosion cracking
SCE	Saturated calomel electrode; E = +0.241V_{SHE}
SEM	Scanning electron microscope
SHE	Standard hydrogen electrode; E ≡ 0V
SSSS	Super saturated solid solution
t	Time
T	Temperature
wt%	Weight percent
XPS	X-ray photoelectron spectroscopy
XRD	X-ray diffraction
yr	Year
β_c	Cathodic Tafel slope
θ	Diffraction angle
λ	Wavelength
ρ	Density

ACKNOWLEDGEMENTS

I am sincerely grateful to my supervisors, Dr. Georges Kipouros and Dr. Paul Bishop, for their continued support and excellent leadership throughout the course of this work, without this the culmination of this work would not be possible. I am also grateful for the financial support provided by the National Sciences and Engineering Research Council of Canada (NSERC) and AUTO21 Network of Centers of Excellence, and the industrial cooperation from ECKA Granules and GKN Sinter Metals. I would like to thank Dr. George Jarjoura and Dr. Abdulwahab Ibrahim for helpful discussions and assistance with electrochemical instrumentation, and Dr. Kevin Plucknett for thorough review of this work.

I would also like to thank a number of people at Dalhousie University for their help: Allison Fulford and Hilary Lynd of Sexton Library, Marlyn McCann and Joe Wickens of Document Delivery, Dean Grijm of the machine shop, Patricia Scallion of the Institute for Research in Materials, Dan Chevalier and Gerald Fraser of the Minerals Engineering Centre, Md. Aminul Islam of the Advanced Tribology Lab, Matt Harding and Randy Cooke of the Particulate Material Research Group, and the rest of the students, faculty, and staff of the Materials Engineering Program and Department of Process Engineering and Applied Science.

CHAPTER 1 INTRODUCTION

Conventional 'press-and-sinter' powder metallurgy (P/M) aluminum alloys are fabricated to near net shape and serve as a low-cost alternative to conventional die cast and machined aluminum parts [1]. Aluminum P/M has found application where the high strength, low weight, natural corrosion resistance, and good conductivity of aluminum can be combined with the cost-effective mass production technology of P/M manufacturing [1-3].

There is expected to be increased demand for aluminum P/M dependent upon current research and development efforts with China and India identified as potential markets [1]. Most research and development has been focused on improving established material properties such as modulus, high temperature strength, wear resistance, and fatigue [1]; however in other areas, such as corrosion resistance, even basic material properties including corrosion rate have not been specified and made available to design engineers.

In this work, the corrosion behaviour of the commercial aluminum P/M alloy 'Alumix 123' has been evaluated as part of a continuing effort from our laboratory to assess the corrosion behaviour of commercial aluminum P/M alloys with an emphasis on electrochemistry [4]. Prior corrosion evaluations have been confined to salt spray tests which only assign a letter-rating of 'A' through 'E' based on specimen appearance [5-7]. Electrochemical studies aim to identify fundamental corrosion mechanisms and provide quantitative thermodynamic and kinetic information which can be used to predict material performance and design systems of corrosion prevention and inhibition. The corrosion behaviour of a compositionally similar wrought alloy, AA2014-T6, has been studied simultaneously to provide a comparison to the P/M material.

CHAPTER 2 BACKGROUND

2.1 ALUMINUM-COPPER ALLOY SYSTEMS

2.1.1 Wrought Alloys

Several different types of wrought aluminum-copper alloys exist which can be broadly categorized according to Table 2.1. Some relationships among some commonly used aluminum-copper alloys are shown in Figure 2.1. These alloys comprise 2*xxx* series in the Aluminum Association alloy designation system [8]. The second digit in 2*xxx* indicates the alloy modification; '0' being the original alloy and other values (1, 2, 3, *etc.*) indicating modifications of the original alloy [9]. The third and fourth digits in 2*xxx* serve to identify each unique alloy [9].

The development of aluminum-copper alloys began in 1906 after the accidental discovery of natural aging of 'duralumin,' whose composition corresponds to present day alloy 2017 [10]. The industrial use of duralumin was limited by its poor fabricability [10]. In 1926, alloy 2025 containing no magnesium and a controlled amount of silicon was developed for improved forgability [10].

Alloy 2014 was then developed in 1928 in an attempt to combine the magnesium addition of alloy 2017 with the silicon addition of alloy 2025 [10]. The result was an alloy with improved forgability that also responded very well to artificial aging [10]. Alloy 2014 is used primarily as a general purpose high strength forging alloy but extruded and rolled product are sometimes used as well [10].

Table 2.1 – General composition limits for wrought aluminum-copper alloys [11].

	5% Cu wrought	Durals	Al-Cu-Ni alloys[a]
Cu	4-6	3.0-5	2-5
Fe	to 0.7	to 0.7	to 1.5
Si	to 2	to 1.0	to 1.5
Mg	< 0.1	0.4-1.7	0.1-2
Mn	to 1.5	0.5-1.5	to 0.5
Ni	to 1.0	< 0.2	0.5-2.5
Zn	< 0.5	< 0.2	< 0.2
Sn	< 0.1	< 0.05	< 0.05
Pb	to 1	< 0.05	< 0.05
Bi	to 1	< 0.05	< 0.05
Cd	to 2	< 0.05	< 0.05
Li	to 2	< 0.05	< 0.05
Ti	to 0.1	to 0.1	to 0.1
V	to 0.2	< 0.05	< 0.05
W	< 0.05	< 0.05	< 0.05
Ag	to 1	< 0.05	< 0.05
Zr	to 0.5	to 0.2	< 0.05
Sb	< 0.05	< 0.05	< 0.05
Cr	to 0.2	to 0.2	to 0.2

[a]These alloys can be subdivided in two groups: the Y alloy type, whose basic composition is 4% Cu, 2% Ni, 1.5% Mg; and the Hyduminiums, which usually have lower copper contents and in which iron replaces some of the nickel.

The strength of alloy 2014 is primarily based off precipitation hardening. The presence of magnesium and silicon together enhance aging [11]. The iron content is kept as low as practically possible [11] as iron forms intermetallics which embrittle the alloy and simultaneously reduce the amount of copper for artificial aging [11]. The embrittling effect of iron is reduced by the presence of manganese – whose intermetallics are not embrittling and absorb some iron [11].

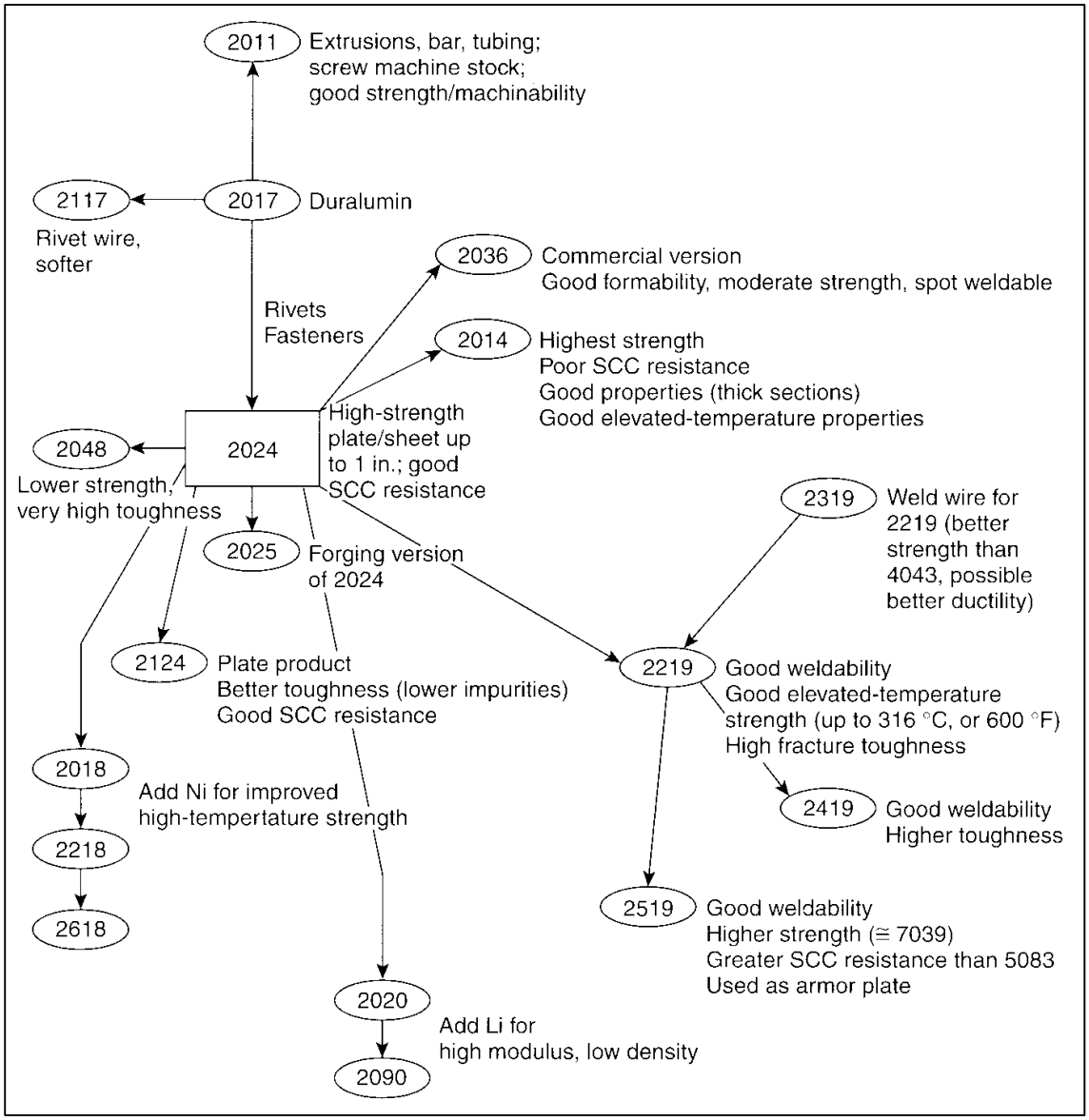

Figure 2.1 – Relationships among commonly used aluminum-copper alloys [12].

2.1.2 Powder Metallurgy Alloys

Conventional 'press-and-sinter' aluminum P/M alloys were developed as a low-cost alternative for small and complex conventional die cast and machined parts [13]. Some commercial P/M alloys based off the aluminum-copper alloy system that have been developed, but not necessarily remain in production, are shown in Table 2.2.

Aluminum P/M was commercialized in the 1960s by Alcoa [14-16] and has been in large scale commercial production [2,3,7,17-26] in the applications outlined in Table 2.3. Perhaps the most defining moment for aluminum P/M came in the early 1990s when General Motors began manufacturing the camshaft bearing caps in the cylinder head assembly of their Northstar engines from 201AB aluminum P/M alloy [27]. In one line of Chrysler cars, 20 aluminum P/M cam caps are used per engine and offer 35% cost savings over die cast and machined caps [28].

Table 2.2 – Compositions of some commercial 'press-and-sinter' aluminum-copper P/M alloys (wt%) [1,3,17]. Balance Al.

Manufacturer	Alloy	Cu	Mg	Si	Mn	Sn
ALCAN	22	2.0	1.0	0.3	–	–
ALCAN	24	4.4	0.5	0.9	0.4	–
ALCOA	201AB	4.4	0.5	0.8	–	–
ALCOA	202AB	4.0	–	–	–	–
AMPAL	2712	3.8	1.0	0.75	–	–
AMPAL	2712A	4.4	0.5	0.6	–	–
AMPAL	2905	3.0	1.2	0.25	–	0.6
ECKA	13	4.5	0.5	–	–	–
ECKA	123	4.5	0.5	0.7	–	–
SINTERAL	–	2.0	0.6	–	–	–
(various)	–	3.4	0.6	0.5	–	–

Table 2.3 – Applications of aluminum P/M [3].

Property	Description	Examples
Light weight and low noise	Light weight of aluminum P/M parts reduces power requirements and lowers vibrations and noise levels in machines with unbalanced motion	Ratchets, gears, cams, levers, *ect.* for appliances, portable power tools, copiers, computers, *ect.*
Corrosion resistance	Natural corrosion resistance of aluminum enables one to use aluminum P/M for mildy corrosive environments	Pumps, outdoor equipment, meters, gauges, fluid control devices
Conductivity	High thermal and electrical conductivity of aluminum and non-magnetic characteristics are especially useful in electronics	Audio-visual equipment, cassette recorders, electronic devices including computers, telephones, TV, *ect.*
Special finishes	A variety of attractive colorful and decorative finishes are possible on aluminum parts.	Office equipment, hot water pots, typewriters, faucet and other kitchen appliances, *ect.*

2.1.3 Temper Designations

The temper designation system for aluminum alloys is used to indicate the thermomechanical treatment and sequence history of an aluminum alloy product [9]. The basic temper designation system, shown in Table 2.4, is applicable to all product forms.

The as-fabricated temper (-F) is used for shaped products with no special control over the amount of strain hardening or thermal treatment during processing and usually indicates a semi-finished product which will be further processed to a finished form or temper [9]. The annealed temper (-O) is used for products that are thermally treated to the lowest strength and highest ductility condition to increase workability [9]. The strain hardened temper (-H) is used for products that are strengthened by varying amounts of plastic deformation and, in some cases, supplementary thermal treatment [9]. Wrought aluminum-copper alloys are rarely strain hardened [11]. The solution heat treated temper (-W) is an unstable temper used for heat treated and quenched products, and indicates a semi-finished product that will be subsequently worked or age hardened [9]. The heat treated (-T) temper is for products thermally treated, with or without supplementary strain hardening, to produce stable tempers [9]. Subsequent digits in the T1 to T10 tempers indicate variations in the processing of heat treated products that can signify: residual stress relief, modifications in quenching, heat treatment by user, additional cold work between quenching and aging, additional cold work following aging, special corrosion resistance, or special/premium properties [9].

The natural differences in P/M manufacturing have resulted in slight modifications to the traditional definitions shown in Table 2.5. At present, there are no standardized definitions for P/M tempers.

Table 2.4 – Basic temper designations for wrought aluminum alloys [9].

Letter	Description	Digit(s)	Description
-F	As fabricated		
-O	Annealed		
-W	Solution heat treated		
-H	Strain hardened	-H1	No thermal treatment
		-H2	Partially annealed
		-H3	Stabilized
		-H4	Lacquered or painted
-T	Heat treated	-T1	Cooled from hot working, naturally aged
		-T2	Cooled from hot working, cold worked, naturally aged
		-T3	Solution heat treated, cold worked, naturally aged
		-T4	Solution heat treated, naturally aged
		-T5	Cooled from hot working, artificially aged
		-T6	Solution heat treated, artificially aged
		-T7	Solution heat treated, overaged/stabilized
		-T8	Solution heat treated, cold worked, artificially aged
		-T9	Solution heat treated, artificially aged, cold worked
		-T10	Cooled from hot working, cold worked, artificially aged

Table 2.5 – Some temper designations used for P/M aluminum alloys [5,7].

Letter	Description	Digit(s)	Description
-O	Annealed[a]		
-T	Heat treated	-T1	Cooled from sintering temperature to 260°C in nitrogen (at uncontrolled rate), air cooled to room temperature
		-T2	As sintered, repressed
		-T4	Solution heat treated in air, cold water quenched, naturally aged
		-T41	Repressed, heat treated to T4
		-T6	Solution heat treated in air, cold water quenched, artificially aged
		-T61	Repressed, heat treated to T6
		-T8	Solution heat treated in air, repressed, artificially aged

[a]Annealed 1 hour, furnace cooled at max rate of $10°C \cdot hr^{-1}$ to 260°C or lower

2.2 PROCESSING AND STRUCTURE OF ALUMINUM-COPPER ALLOYS

2.2.1 Wrought Alloys

2.2.1.1 Ingot Casting

Melting, remelting, or holding of primary aluminum typically takes place in a reverberatory furnace which operates continuously [29]. Alloy additions are added directly to the melt [29]. Elements with low melting points are introduced as pure metals and elements with high melting points are introduced as master alloys to help with dissolution [29]. If dissolution remains problematic, master alloys can also be added directly to the electrolytic cell where there is higher turbulence and temperatures [29]. Once a satisfactory composition is achieved the melt is treated to reduce hydrogen, alkalis, and non-metallic inclusions [30]. The melt is then degassed and fluxed with Ar-Cl_2 gas mixtures and finally passed through ceramic foam filters to remove insoluble constituents [30].

Virtually all aluminum alloy ingots are cast by the direct-chill (DC) process [30], shown in Figure 2.2. Extrusion ingot is cast in cylindrical form and sheet ingot in rectangular form [30], Figure 2.3. The ingots are not cast under equilibrium conditions, so the structure is dependent upon the casting variables as well as chemical composition [11,30-32]. Important structural characteristics of the ingot include: grain size and shape, cell size and dendrite arm spacing, macro- and micro-segregation, and primary constituents [30]. Grain size is controlled by grain refining additions whereas cell size, segregation, and primary constituents are affected by composition and solidification rate [30,32].

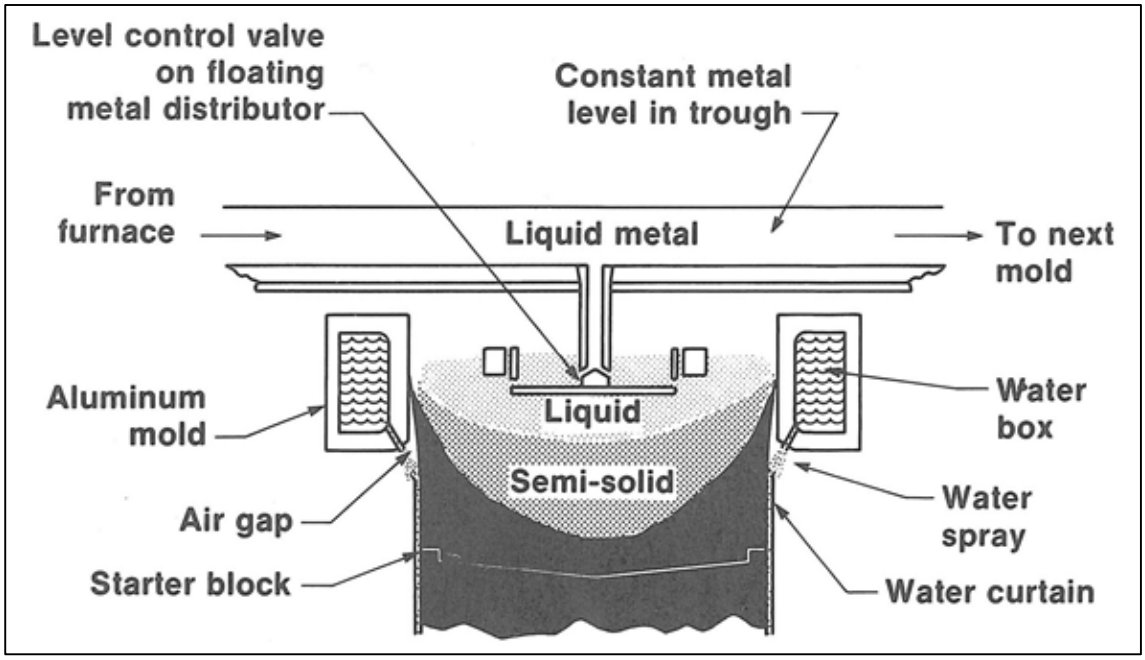

Figure 2.2 – Schematic of the vertical DC casting process [30].

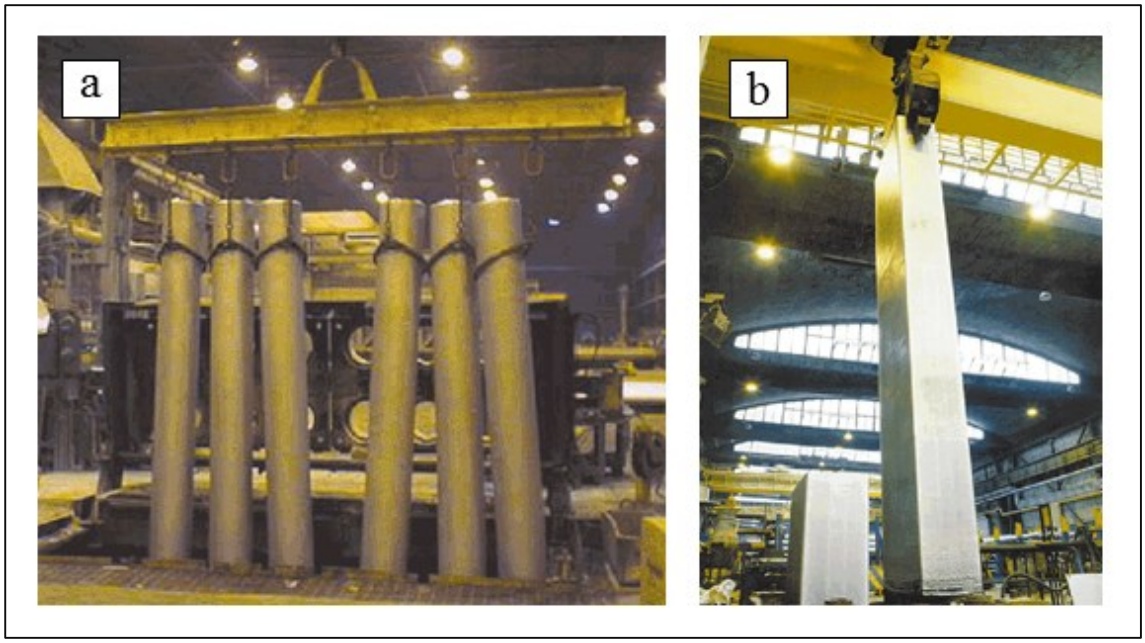

Figure 2.3 – Typical DC cast aluminum: (a) extrusion logs; (b) sheet ingot [33].

2.2.1.2 Forming

The as-cast ingot structure has numerous characteristics that are unattractive for subsequent operations, including macro- and micro-segregation, low melting point eutectics, brittle intermetallic phases, supersaturated solid solutions of finely dispersed precipitates, and skin enriched with up to 30wt% copper containing primary iron-, manganese-, or nickel-bearing crystals [11,30,31,34]. It is standard practice to scalp the ingot to remove the skin and then homogenize it to help remedy the rest of the unattractive characteristics [11].

Homogenization temperature is determined by alloy composition; generally the temperature of the lowest melting point eutectic should not be exceeded [11,34]. Magnesium-free alloys can be homogenized at 525-540°C while alloys containing magnesium must be homogenized below 525°C [11]. Homogenization time depends on diffusivity considerations; large ingots can require up to 24 hours [11]. Excessive homogenization time or temperature will lead to recrystallization and grain growth [11]. Ingots for hot working are cooled slowly from the homogenization to the working temperature in order to precipitate and spheroidize soluble constituents [11]. Hot working temperatures range from 375-525°C [11].

Generally at least 60-70% deformation is required to produce the desired properties in wrought products [11]. The properties of wrought products are commonly anisotropic; the reference directions are shown in Figure 2.4. Light reductions result in only slight directionality and coarse grains while heavy reductions lead to extreme elongation of grains in the working direction [11].

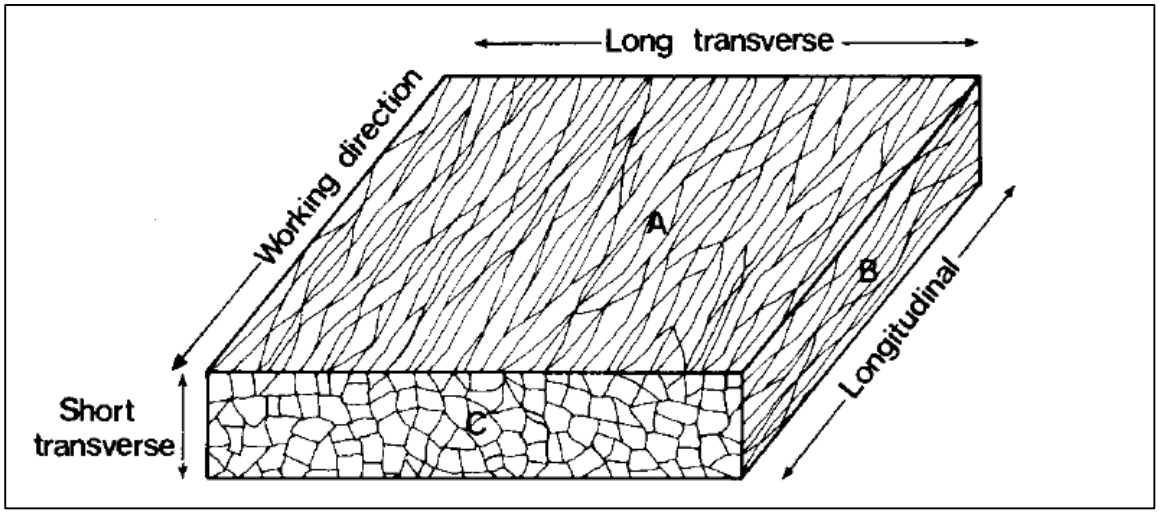

Figure 2.4 – Directions in wrought materials [11].

Formability is highest in the annealed condition and lower in the naturally or artificially aged condition [11]. Alloys containing magnesium are significantly more prone to cracking [11]. Iron, silicon, nickel, manganese, titanium, and chromium have little effect on formability [11]. In magnesium-containing alloys, bismuth, lead, and tin form brittle intermetallics that reduce formability [11]. Dissolved hydrogen reduces formability and can lead to blistering and cracking [11].

Copper lowers the recrystallization temperature and slows the recrystallization rate, especially if present in solution or as fine precipitates [11]. Iron, silicon, magnesium, and nickel do not affect the recrystallization temperature but can refine grain size [11]. Chromium, manganese, and vanadium only raise the recrystallization when in solid solution [11].

2.2.1.3 Precipitation Hardening

Materials are precipitation hardened only after some form of solution heat treatment and accelerated cooling [11]. To optimize this process the solution heat treatment temperature must be below the solidus and must be held for sufficient time to diffuse all soluble elements and distribute them evenly [11] – specifics are dependent upon alloy composition and product form [11,35]. Most wrought products are quenched in to a cold water bath with a maximum permissible quench delay of 5-15 seconds [35].

Five distinct structures have been identified in the precipitation hardening process of aluminum-copper alloys [11]: the supersaturated solid solution (SSSS), Guinier-Preston (GP) 1 zones, GP2 zones (θ" phase), θ' phase, and θ phase ($CuAl_2$). As aging progresses these structures typically appear consecutively in the order: SSSS → GP1 → GP2 (θ") → θ' → θ [11].

GP1 zones are one or two atomic layers of pure copper in the (100) planes of the matrix surrounded by planes of almost entirely aluminum atoms [11]. They are coherent with the matrix and distort (shrink) the lattice up to 10-15 planes away from the copper layers [11]. These zones grow up to a size of 30-70×10^{-10}m at 300°K or 100-150×10^{-10}m at 350-400°K [11]. As GP1 zones grow, hardness is increased and ductility decreases [11].

GP2 zones have a tetragonal lattice with five interchanging sheets of aluminum and copper (3 sheets aluminum, 2 sheets copper) in the (100) planes [11]. GP2 zones are coherent with the matrix and can grow to 100-1000×10^{-10}m in diameter and 10-40× 10^{-10}m thick [11]. As GP2 zones grow, hardness increases as dislocation motion is

inhibited by the increased lattice strain [11]. When the stress fields from different GP2 zones reach each other peak hardness is reached and θ' phase begins to appear [11].

The θ' phase has a tetragonal lattice and is considered a separate phase from the matrix [11]. Each θ' particle is surrounded by a ring of dislocations so that no lattice strains are present in the matrix [11].

θ' particles occur at defects, slip planes, and grain boundaries and grow up to 100-6000$\times10^{-10}$m in diameter and 100-150$\times10^{-10}$m thick depending on aging time and temperature [11]. When the matrix softens and recrystallizes to form the ring of dislocations surrounding θ' particles, new advancing dislocations are able to bypass θ' particles due to the lack of lattice strain in the matrix [11]. Maximum strength occurs with a mixture of GP2 zones and θ' precipitates [11].

The equilibrium θ phase ($CuAl_2$) forms after prolonged aging time or temperature [11]. It has a tetragonal lattice and is incoherent with the matrix [11]. It can nucleate from θ' particles or directly from the matrix, which results in different crystallographic orientation relationships between θ and the matrix [11].

2.2.1.4 Characteristics of Secondary Phases

Secondary phases can be classified as either soluble or insoluble [11]. The soluble phases are comprised of: copper, lithium, magnesium, silicon, or zinc [11]. The insoluble phases contain at least one element with limited solid solubility such as iron, manganese, or nickel [11]. A summary of phases likely to occur in aluminum-copper alloys is shown in Table 2.6.

The soluble phases formed depend on the amount of soluble elements available and their ratio [11]. With high Mg:Cu and Mg:Si ratios, the $CuMg_4Al_6$ phase is favoured [11]. At lower Mg:Cu and Mg:Si ratios, the $CuMgAl_2$ phase is formed [11]. If the ratio Mg:Si is low then $Cu_2Mg_8Si_6Al_5$ is formed, typically in conjunction with $CuAl_2$ [11]. Some copper can be confined to iron-, manganese-, or nickel-bearing compounds, Table 2.6, including $(CuFe)Al_6$, Cu_2FeAl_7, $(CuFeMn)Al_6$, $Cu_2Mn_3Al_{20}$, and Cu_4NiAl_7 [11]. When >1wt% silicon is present, however, iron and manganese can preferentially combine with silicon as $FeSiAl_5$ over Cu_2FeAl_7 and $(CuFeMn)_3Si_2Al_{15}$ over $(CuFeMn)Al_6$ and $Cu_2Mn_3Al_{20}$ [11], Table 2.6.

Magnesium is usually combined with silicon or copper, except in alloys containing bismuth, lead, or tin where Mg_2Pb, Mg_2Bi_3, or Mg_2Sn are formed [11]. In commercial alloys magnesium never combines with iron or manganese [11]. When silicon-containing insoluble phases are formed, silicon will first appear as Mg_2Si and then recombine with iron or manganese [11]. When nickel is present with manganese or iron it will combine with them as the Mn_3NiAl_{16} or $FeNiAl_9$ at the expense of their other compounds: $(CuNi)_2Al_3$, Cu_4NiAl_7, $Cu_2Mn_3Al_{20}$, and $(FeMn)Al_6$ [11].

Table 2.6 – Phases formed in aluminum-copper alloys [11].

Cu	Cu < 2% in solid soln.	Cu > 2% $CuAl_2$	Fe ≫ Si Cu_2FeAl_7 or $(CuFe)Al_6$	Mg > 1/2 Si $CuMgAl_2$ or $CuMg_4Al_6$	Mn ≫ Fe $Cu_2Mn_3Al_{20}$ or $(CuFeMn)Al_6$	Mg < Si $Cu_2Mg_8Si_6Al_5$ $(CuFeMn)_3Si_2Al_{15}$	Ni > 0.1% Cu_4NiAl_7 or $(CuNi)_2Al_3$ or $Cu_2(FeNi)Al_7$ or $(CuFeNi)Al_6$
Fe	Si > 2 Mg Fe_2SiAl_8 or $FeSiAl_5$	Fe ≫ Si Cu_2FeAl_7 or $(CuFe)Al_6$ or $FeAl_3$		Mn > 0.1% $(CuFeMn)Al_6$ or $(CuFeMn)_3Si_2Al_{15}$	Ni > 0.1% $FeNiAl_9$ or $(CuFeNi)Al_6$ or $(CuFeNi)_2Al_3$ or $Cu_2(FeNi)Al_7$		
Si	Si > Fe $FeSiAl_5$	Si < Fe, Mg > Si Mg_2Si	*Mg* ≈ Si $Cu_2Mg_8Si_6Al_5$	Mn > 0.1% $(CuFeMn)_3Si_2Al_{15}$	Si ≫ Mg + Fe Si		
Mg	Mg < 0.2% in solid soln.	Si > 0.6 Mg < 1 Mg Mg_2Si	Si ≈ Mg $Cu_2Mg_8Si_6Al_5$	Si ≪ 0.6 Mg $CuMgAl_2$	Cu < Mg $CuMg_4Al_6$		
Mn	Mn < 0.2% in solid soln.	Fe > Si $(FeMn)Al_6$	Fe < Si $(CuFeMn)_3Si_2Al_{15}$	Fe. Si ≪ Mn $Cu_2Mn_3Al_{20}$	Ni > 0.1% Mn_3NiAl_{16}		
Zn	Zn < 2% in solid soln.	Zn > 2% $Cu_5Zn_2Al_3$					
Ni	Cu ≫ Fe Cu_4NiAl_7	Cu < 2 Fe, Fe ≫ Si $FeNiAl_9$ or $(CuFeNi)Al_6$ or $(CuFeNi)_2Al_3$ or $Cu_2(FeNi)Al_7$		Mn > 0.1% Mn_3NiAl_{16}			
Pb	Mg, Bi < 0.1% Pb	Bi < 0.1 Pb, Mg > 1.7 Si Mg_2Pb		Bi > 0.1 Pb $BiPb_3$			
Bi	Pb > 0.2 Bi $BiPb_3$	Pb < 0.2 Bi, Mg > 1.7 Si Bi_2Mg_3					
Sn	Mg < 1.7 Si Sn	Mg ≫ 1.7 Si Mg_2Sn					
Cd	Cd (?)						
Ti	$TiAl_3$						
Ag	Ag < 0.3% in solid soln.	Ag > 0.3% Ag_2Al	Mg ≫ 1.7 Si $(AgCuAl)_{49}Mg_{32}$ or AgMg (?)				

2.2.2 Powder Metallurgy Alloys

2.2.2.1 Raw Materials

Virtually all P/M grade aluminum powder is produced by air atomization [1,3,36]. Air atomized aluminum powder is preferred due to its superior shape, size, and flow characteristics [14,15,37-42]. The shape of air atomized aluminum powder is irregular or tear-drop, Figure 2.5 [43-45]. Particle size and distribution are controlled by process variables [36,39,46,47] and through the application of post-atomization size classification techniques. Air atomized aluminum is normally sieved in to different grades by manufacturers [1] – the P/M grade powder having an average particle size of 40-100μm [3,39,48,49]. Typical commercial composition limits are ~0.15wt%Fe (max), ~0.10wt%Si (max), and 0.30wt%O (max) [3,14,15,23,42,44,47]. The oxide is mostly present as a thin protective layer on the surface of the powder particles [23,41,47,50] and is thought to be at least partially amorphous [1]. The oxide layer contains 'oxide islands' throughout the surface which are a result of the oxygen content of the atomizing gas [44]. Powder particles solidify with a dendritic cell pattern, Figure 2.5, with iron and silicon-enriched cell boundaries [50,51].

Aluminum pre-mixes can be prepared from: (i) purely elemental mixes, (ii) partially elemental mix and partly pre-alloyed powder, or (iii) completely pre-alloyed powder [3]. Many investigators have found elemental copper powder superior to pre-alloyed or composite powder [14,15,39,52-54] and this reflects in the use of elemental copper in commercial pre-mixes [7,14,15,42,49,55]. Finer copper powders ($d<45\mu m$) are superior over coarser powders with respect to sintered tensile strength [40,56], sintered pore size [56,57] and surface finish after sintering [57]. Such powders also promote the formation of liquid earlier during sintering [57,58].

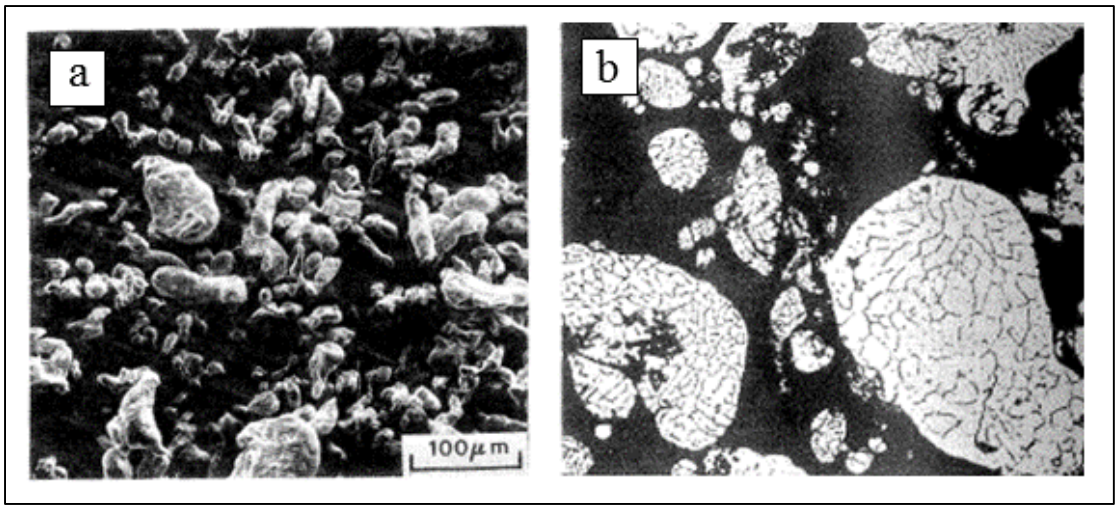

Figure 2.5 – Atomized 1202 Grade aluminum powder: (a) SEM micrograph; (b) cross sectional microstructure [51].

Copper powder for aluminum P/M can be produced by electrolytic deposition from aqueous solution which is normally an integrated operation in copper smelters and refineries [59,60]. Copper is deposited as a high purity dendritic deposit with powder size and distribution controlled by the conditions of deposition [59,60].

Traditionally, elemental magnesium powder has been produced by mechanical means [43,61,62] which yields material unsuitable for powder metallurgy applications [39]. A satisfactory powder can be produced by mechanically pulverizing a brittle master alloy [39,43,63,64]; Al-50wt% Mg is suitable [39,63,64] but anywhere between 20-70wt% Mg can be easily pulverized [65].

Commercial pre-mixes have contained silicon as a pre-alloy [49,55] or elemental [7,42,49,51] powder addition. Elemental silicon powder can be produced by milling [66,67] while master alloy powders can be produced by atomization [43,57] or mechanical pulverization [61]. The presence of silicon as a pulverized master alloy can result in superior precipitation hardening [68].

Commercial aluminum P/M alloys typically contain 1.2 or 1.5wt% admixed internal lubricant [1,3] with a low ash and moisture content to maintain the low dew point during sintering [3,7,14,15,19]. Zinc stearate lubricants have been used in the past, however these partially dissociate to zinc oxide which interferes with sintering [3,66,69]. Organic fatty acids or waxes are more suitable [14,15,19,42]. The prevailing lubricant is ethylene bisstearamide (EBS) [1,3].

Raw materials are normally blended in an inert atmosphere at the plant of the powder manufacturer [3,36,42]. Powder pre-mixes are subject to several quality control checks, such as particle size distribution, apparent density, tap density, and flowability [2,36]. A flowchart detailing the manufacturing of an aluminum pre-mix is shown in Figure 2.6. Oxidation during storage or transport is normally not an issue [2].

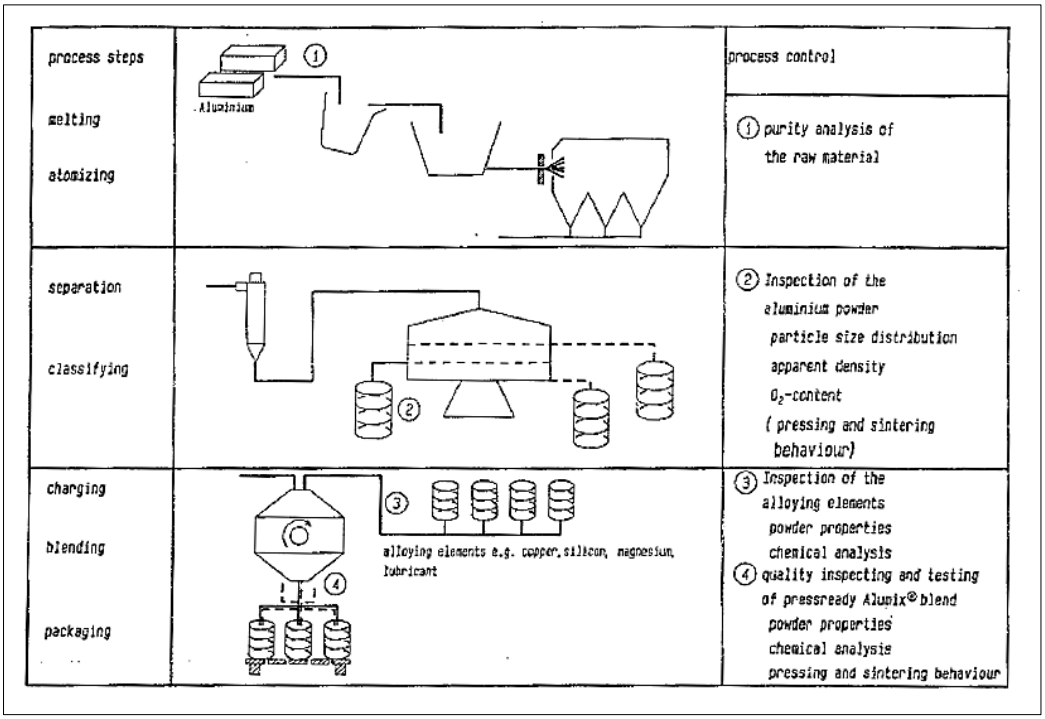

Figure 2.6 – Flowchart of the production process for ECKA ALUMIX blends and process control measures [36].

2.2.2.2 Compaction

Aluminum P/M alloys are compacted with standard mechanical or hydraulic presses in closed steel dies [14,15,19,20,23], although tungsten carbide tools are recommended for high-volume production runs [3,19,23]. This can be done on existing tooling designed for ferrous or cuprous P/M materials [2,5-7,14,15,42]. In fact, the excellent compressibility of aluminum powder allows for larger cross sectional parts to be pressed on the same equipment [2,3,5,7,14,15,42].

Internal or die wall lubrication is an absolute necessity for compaction [3,7,14,15,42]. Without lubricant, aluminum powder has severe seizing and galling characteristics against steel dies [14,15,18,39,68]. Lubricant also promotes a homogenous density distribution [55], however there is always some density variation due to friction on the die wall and die face [70], Figure 2.7. Increasing lubricant content decreases ejection force but also decreases green strength by inhibiting the cold welding of particles [55]. Lubricant also helps prevent dusting during transfer of the powder pre-mix to the hopper [3].

Successful compaction requires information on flow rate, apparent density, and compressibility of powder blends [49]. Compressibility of aluminum powder is sensitive to impurities, particularly iron, silicon, and oxygen [39]. Compressibility decreases with increasing copper content, probably due to the mechanical properties of the metal [66,71]. Copper particles can assist in compaction and ejection by dislodging aluminum particles that have adhered to the die wall [68]. Silicon slightly lowers compressibility but reduces ejection pressure and improves green surface finish [66].

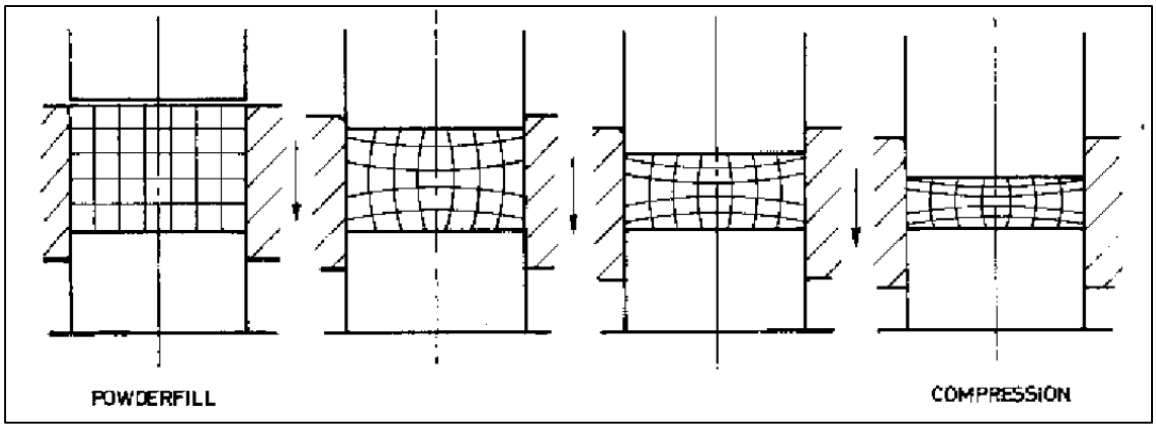

Figure 2.7 – Density variation during the pressing of a cylindrical compact in a floating die [70].

Pressing to 85-95% green density is desirable [42,71,72] as higher compaction pressures cause pressure cracks [54], increase distortion during sintering [73], and result in blowholes and poor densification [40,71]. At higher green densities, close particle contacts and large contact areas interfere with liquid phase sintering [74]. The good compressibility of aluminum powder yields compacts with high green strength [23] but this is also partially a result of the nodular and irregular shape of the air atomized aluminum powder which allows for good interlocking [7,14,15]. Handling parts after pressing is not normally a problem due to the high green strength of aluminum P/M alloys [3].

2.2.2.3 Sintering

Nitrogen is the preferred atmosphere for industrial sintering of aluminum P/M alloys [1-3,14,15,42,75]. Nitrogen offers the best sintered properties [1,3,14,15,42,50,75,76], is economical in bulk quantities, and requires no special handling, gas re-generation, or adsorbent drying [1,3,7,75,76]. The dew point of the nitrogen atmosphere should be controlled to below –40°C (equivalent to ~120ppm moisture) [1-3,7,14,15,42,75], although the optimum dew point varies somewhat between different alloys [1] . At higher moisture contents sintered properties decrease sharply [14,15,19] and the lubricant can oxidize during de-lubrication [55]. Standard grade nitrogen normally has a dew point of –60°C, but moisture and oxygen are picked up on the way to the sinter zone [3].

Most commercial aluminum P/M alloys are sintered between 590-620°C for 15-30 minutes [1-3,7,14,15,42,75,76]. Industrially, sintering typically takes place in a muffle-type furnace with a wire mesh belt conveyor [3,7,14,15,42,75,77], Figure 2.8, that has a thermal profile similar to the one shown in Figure 2.9. These furnaces operate with three different zones. Namely those for de-lubrication, sintering, and cooling [3].

The lubricant is removed as a vapour phase during the de-lubrication stage which typically takes place at 345-425°C for 15-20 minutes [1,3,23,75,76]. The upper limit is controlled by the onset of diffusional reactions between components of the powder pre-mix [55]. A directed nitrogen curtain flows counter to the belt movement so that lubricant vapor and other volatiles are prevented from entering the sinter zone [3,23,75].

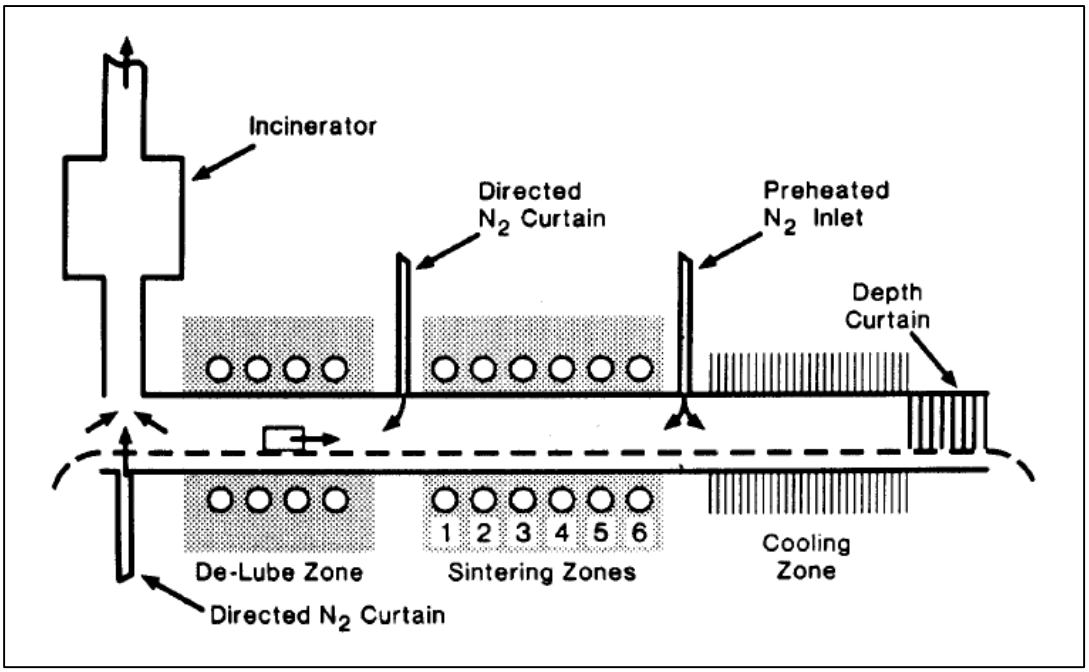

Figure 2.8 – Continuous muffle type furnace for sintering aluminum [3].

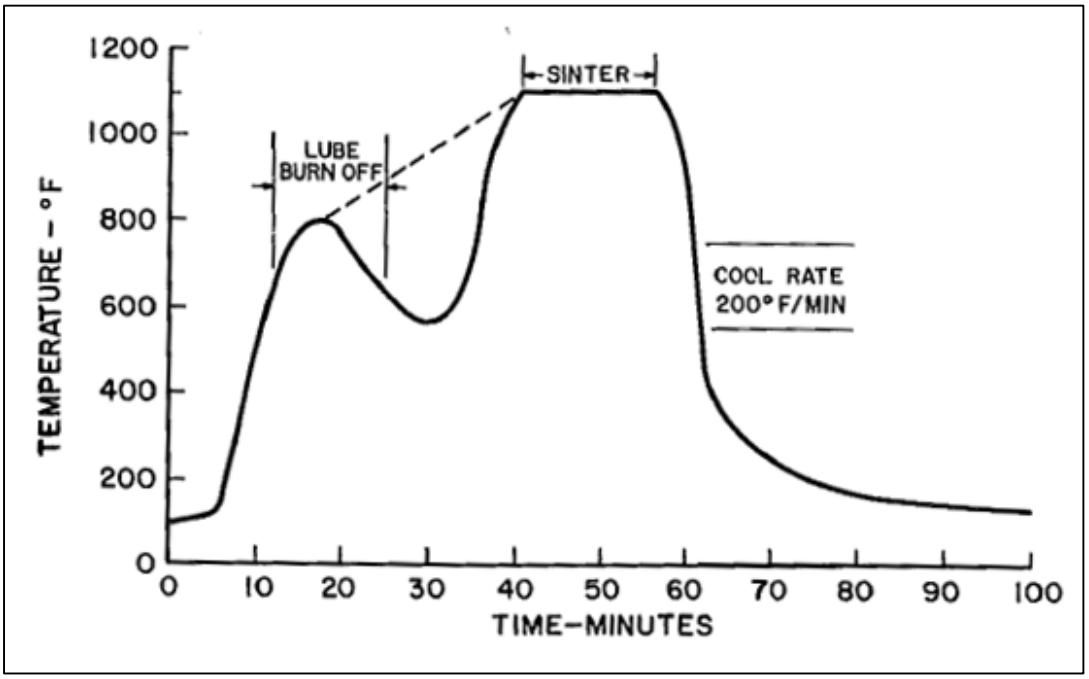

Figure 2.9 – Heating cycle for a continuously sintered aluminum P/M part [75]. The dashed line indicates the new heating cycle for the furnace after a design modification.

Precise temperature and dew point control are necessary for the sinter zone [1,3,14,15,42,75]. Sintering temperature should be controlled to ±5°C [1,2,7,20,23,42] and temperature across the belt width should not vary more than ±2.8°C [1,3,27,75]. The dew point and thermal profile of the sintering zone is normally checked weekly, while complete furnace profiles are checked on a monthly basis [3]. At the exit of the sinter zone is a gas inlet where diverted curtains of pre-heated nitrogen are introduced to maintain a lubricant- and moisture-free atmosphere in the sinter zone and to prevent back-diffusion of cold nitrogen from the cool zone [3,75]. The gas flow is pre-heated to the sinter temperature to prevent the cooling of smaller parts [1,3].

The parts exit the sinter zone in to a water-jacketed section [75] and experience cooling rates of about 5-30°C per minute [73]. The protective atmosphere should be maintained in the cooling zone until parts cool to at least 427°C or less [23]. Afterwards parts can be cooled to room temperature in air [23]. At the exit of the cool zone, a depth curtain made of fibrous glass wool, 30-60cm long helps keep a dry atmosphere in the furnace [3].

These furnaces can typically sinter about 1000 to 2500 parts per hour depending on part shape and size [1]. A 6 inch wide mesh belt furnace sinters about 40lb per hour [75] while using an 18 inch belt can increase production rates up to 250lb per hour [2]. Belt speeds can be 2-10 inches per minute because of the good thermal conductivity of aluminum and short sinter times [23].

2.2.2.4 Structure Formation

During heating, prior to liquid phase sintering (LPS), there are several transformations that occur on the surface of aluminum particles: absorbed water is dehydrated, $Al(OH)_3$ is decomposed to γ-Al_2O_3, and amorphous Al_2O_3 is crystallized to γ-Al_2O_3 [1,3]. The density and volume change associated with crystallization [1] and the thermal expansion of underlying aluminum metal [3,78,79] is thought to crack the oxide layer and expose bare aluminum.

The LPS of aluminum-copper based alloys occurs mostly under non-equilibrium conditions but can still be interpreted via the equilibrium aluminum-copper phase diagram [73], Figure 2.10. LPS takes place in at least two stages [80], Figure 2.11. The first stage, which is characterized by volume growth [40,48,55,57,58,66,69,74,80-84], commences above 548°C where contact melting of aluminum and copper particles occurs [52,53,55,57,58,72,83-88]. All metallic copper and surrounding aluminum particles are rapidly consumed, leaving behind 'melt-off' pores at the sites of original copper particles [40,58,78,79,84-87]. The appearance of the eutectic melt occurs locally and does not induce any volume changes [80,84]. The liquid phase rapidly spreads over the surface of aluminum particles, possibly between metallic aluminum and its oxide layer in some places [3,23,51-53,55,57,58,89], and copper from the melt begins diffusing in to the aluminum particles resulting in compact growth [3,58,80-84]. The compact growth stage lasts a matter of minutes and occurs before the compact has reached the isothermal sintering temperature [80]. The magnitude of growth surpasses the amount which can be attributed to the diffusion of copper from the melt [80]. The additional growth is probably due to 'negative rearrangement' caused by non-uniform diffusion over the surface of particles [48,80,84].

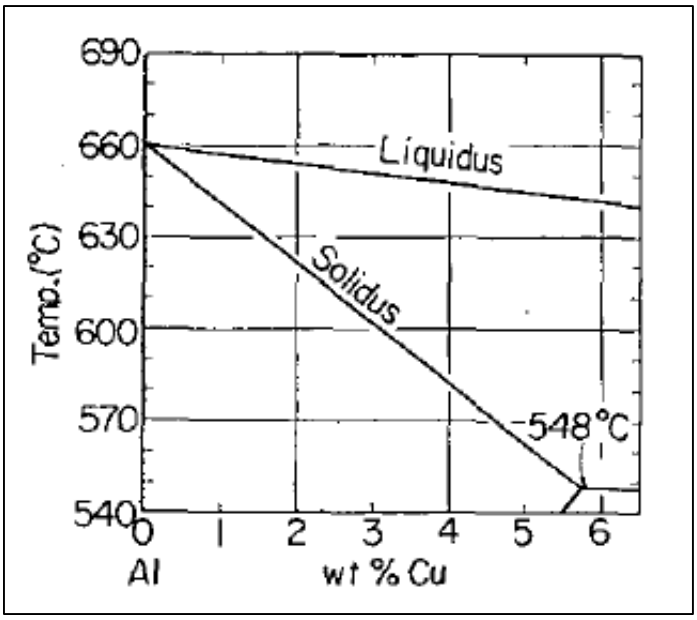

Figure 2.10 – Equilibrium phase diagram of the aluminum-copper system near the aluminum-rich solidus [86].

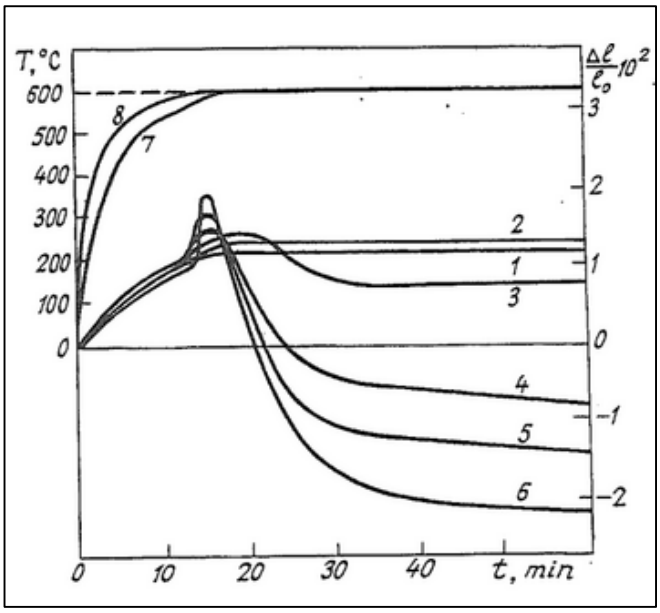

Figure 2.11 – Effect of copper content on deformation of Al-Cu powder compacts during sintering at 600°C under vacuum [80,84]. The copper concentration 1: 1wt%; 2: 2wt%; 3: 3wt%; 4: 4wt%; 5: 5wt%; 6: 6wt%. 7 – the compact temperature; 8 – the temperature in the dilatometer tube.

The second stage of sintering, which is characterized by volume shrinkage [40,48,55,58,66,69,74,80-84,86], occurs only if, for a given alloy composition, the isothermal sintering temperature lies above the solidus and below the liquidus on the aluminum-copper phase diagram [72,80,82,84,86], Figure 2.10. As the temperature of the compact rises, the decreasing solid solubility of copper, Figure 2.10, results in the formation and decomposition of a super saturated solid solution to a liquid phase along grain and subgrain boundaries within aluminum particles [48,58,80-82,84]. Volume shrinkage is brought about primarily by rearrangement of the fragmented aluminum particles from capillary forces [66,80,83,84]. The contribution of solution-reprecipitation to densification is probably small [80-83]. The majority of shrinkage occurs before the compact has reached its isothermal sintering temperature, which makes it unlikely that the composition of the liquid or solid is close enough to equilibrium for the solution-reprecipitation mechanism to occur [80-83].

Once the isothermal sintering temperature is reached, the melt becomes saturated and the solid and liquid phase can be considered to be in chemical equilibrium which allows for grain growth by the solution-reprecipitation process [82,85,87], Figure 2.12. During this stage a polyhedral structure is formed and the microstructure coarsens with longer isothermal holding times [40,82,85,87].

Additions of magnesium enhance LPS [1] and magnesium also plays a role in reducing the aluminum oxide layer [1,90], probably via formation of the spinel phase ($MgAl_2O_4$) [1,90]. Magnesium is also thought to act as a local oxygen getter [1]. In magnesium-containing alloys, the expansion event occurs earlier and the magnitude of densification increases [55,91]. The addition of magnesium as an elemental or Al-35wt%Mg eutectic master alloy leads to the fastest densification, but these alloys coarsen

rapidly when sintered above 595°C [92,93]. Excessive sintering times can lead to evaporation of magnesium near the surface [76,93].

Small amounts (<1wt%) of silicon also enhance LPS [1,91]. However, these alloys are more sensitive to sintering conditions due to the tendency of silicon to oxidize [68]. Larger amounts of elemental silicon (2.5 or 5.5wt%) cause excess liquid during sintering, slow the diffusion of copper and result in undissolved silicon along the grain boundaries, even after long sinter times [66].

Sintering may also be significantly influenced by the presence of trace elements [91,94,95] and impurities [96]. This is usually a result of influencing the amount of liquid phase present [95] or affecting surface tension and wettability [91,94].

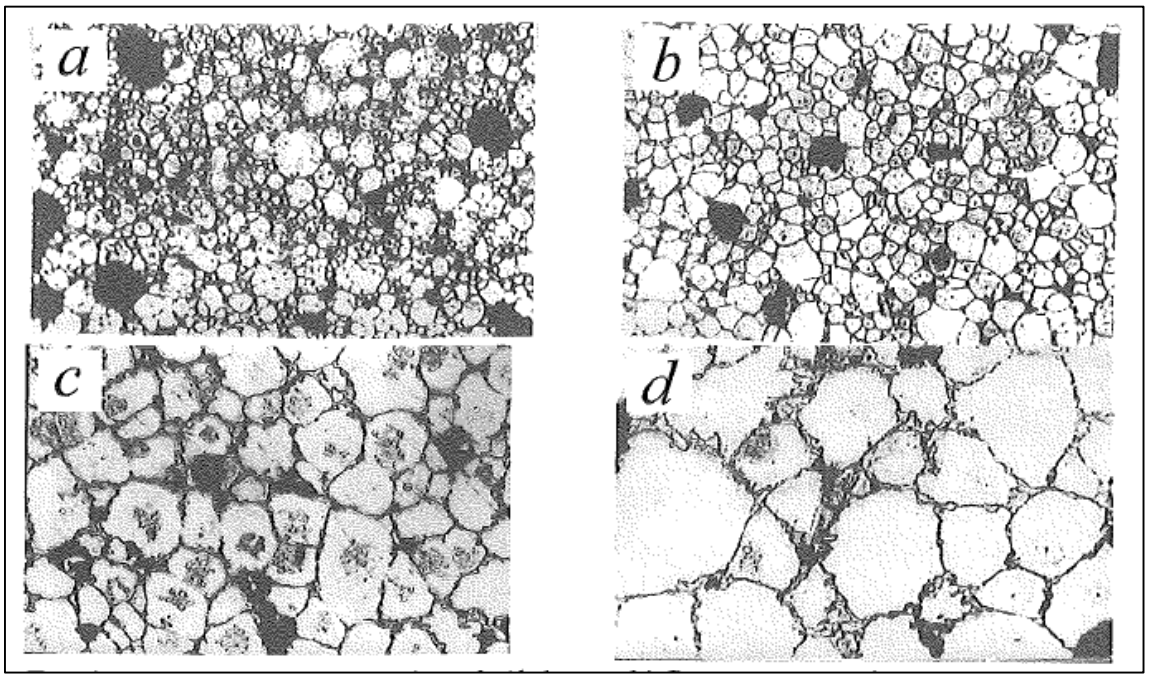

Figure 2.12 – Structure formation of Al-6Cu sintered at 620°C under vacuum [80,82]: (a) during growth stage; (b) during shrinkage stage; (c) after shrinkage; (d) after isothermal hold. Etched, ×140 magnification.

The sintering atmosphere plays an important role in densification [1,97], Figure 2.13. During the densification stage under nitrogen, the first rapid contraction is followed by a second contraction with lower shrinkage rate and then a third rapid contraction [1]. The second contraction event is related to the formation of individual nanoscale aluminum nitride (AlN) crystals inside pores [1] which assist in densification by locally consuming nitrogen and establishing a pressure differential. The third rapid shrinkage event is due to pore filling by a persistent liquid whose meniscus forces are destabilized by the pressure differential created by the formation of aluminum nitride [1].

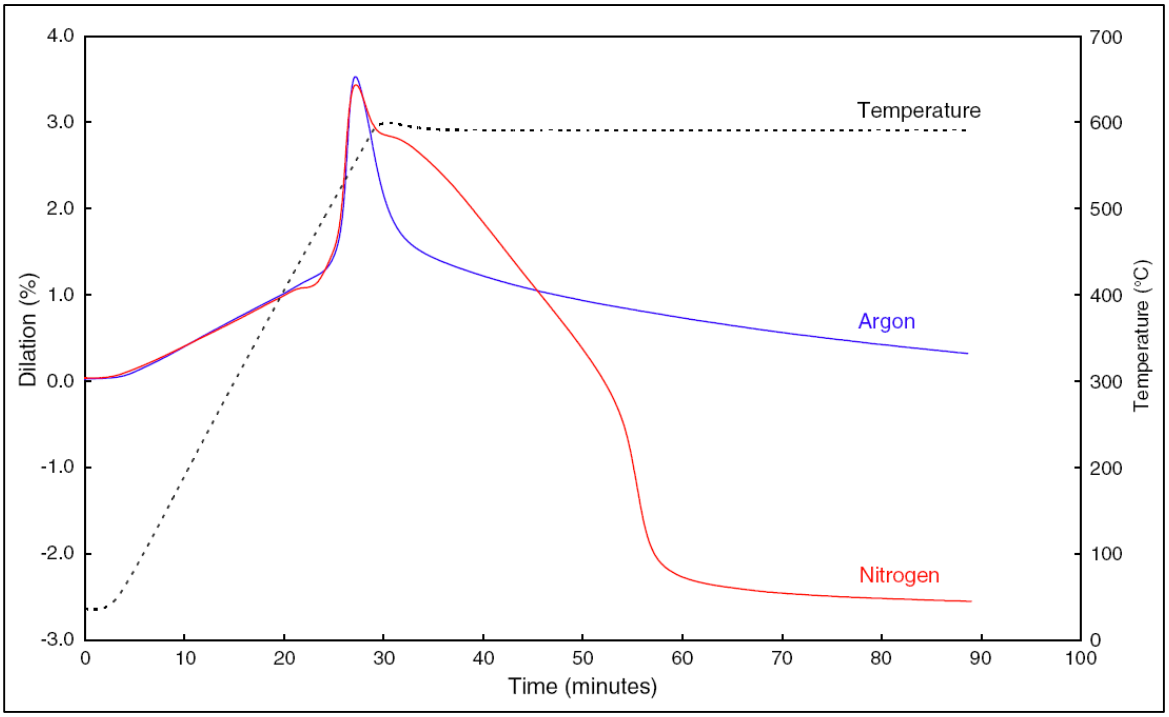

Figure 2.13 – Dilatometer curve of Al-3.8Cu-1Mg-0.7Si under argon and nitrogen [91]. The expansion and initial shrinkage is similar under both atmospheres, but the total shrinkage is substantially greater under nitrogen.

2.2.2.5 Secondary Operations

Aluminum P/M alloys are highly responsive to a number of post-sintering operations. For instance, they have excellent formability in the as sintered condition permitting sizing for close dimensional control, coining for a detailed surface, or repressing for increased strength [2,3,14,15,23,26,42,50,75], Figure 2.14.

P/M alloys also respond to precipitation hardening, in a similar manner to wrought alloys, by natural or artificial aging [2,3,5-7,14,15,23,26,39,42,67,75,76,98-100]. They are solutionized in air or controlled atmosphere at 504-538°C for 30 minutes and then cold-water quenched [23,26,27,67].

P/M alloys are then naturally aged at room temperature for a minimum of four days [27] or artificially aged at 165-200°C [67,85]. In general, they precipitation harden faster than their wrought counterparts [43,67]. During aging precipitates are homogenously distributed in the matrix, however upon over-aging θ precipitates exist preferentially at grain boundaries and pore surfaces [67]. The magnitude of hardening is primarily influenced by the copper content in solution and porosity, but grain size can also have an effect [67]. The presence of magnesium improves response to heat treatment [93].

Sintered P/M bodies are also excellent preforms for forgings [7,42,101] with scrap loss reduced by 80% compared to conventional forgings [7]. Hot working collapses residual porosity and breaks up microstructural constituents (*i.e.* oxides) so as to increase interparticle bonding and density [51,101]. Cold forming should be done in the as sintered condition or within 24 hours of quenching [23]. Some parts are formed after solutionizing when they are the most ductile [27].

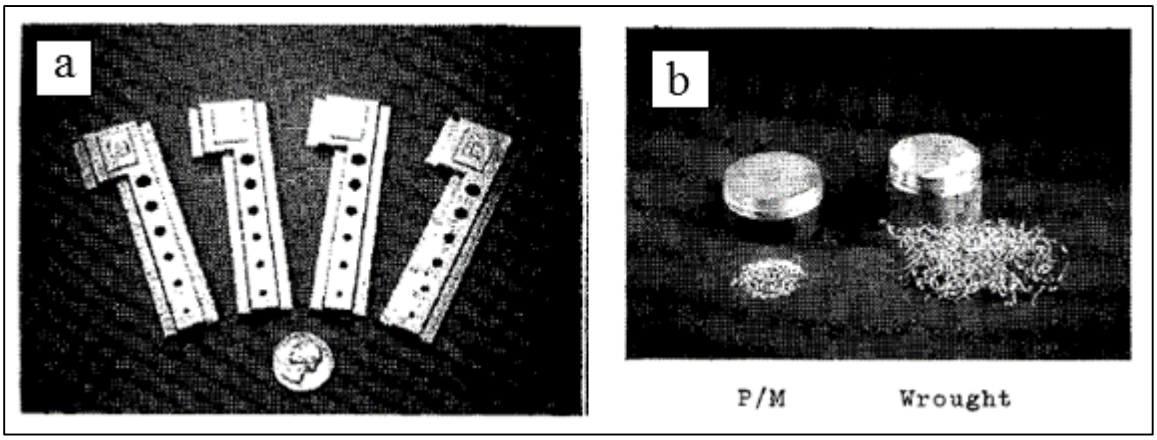

Figure 2.14 – Secondary operations on aluminum P/M parts [2]: (a) coining for a detailed surface; (b) machining with better chip characteristics than wrought counterparts.

The machinablility of P/M parts is excellent and actually superior to wrought parts with respect to chip breaking characteristics [2,3,5-7,14,15,20,23,26], Figure 2.14. If possible, parts should be machined after heat treatment for superior chip breaking characteristics [2,26]. Sintered carbide tooling is preferred since the sharp cutting edge prevents smearing [26].

Most finishing operations can be applied to P/M alloys including: chemical cleaning, mechanical finishing, anodizing, coloring, electroplating, and painting [2,3,7,14,15,20,42]. Press fitting is a practical and economical method of joining parts, but joining by adhesive bonding or threaded fasteners is possible [26]. Prior to joining, parts should be solution treated for maximum ductility [26].

2.3 CORROSION BEHAVIOUR OF ALUMINUM–COPPER ALLOYS IN NEAR-NEUTRAL, CHLORIDE-CONTAINING ELECTROLYTES

2.3.1 Electrode Processes

2.3.1.1 Cathodic Processes

The electrochemical corrosion of metals involves cathodic, anodic, and electronic and ionic conduction processes with the total rate of corrosion being determined by the process with the rate limiting kinetics [102-108]. The resistance associated with the cathodic reaction usually has the greatest influence on corrosion rate [102-108].

The cathodic process in the corrosion of aluminum and aluminum alloys in near-neutral electrolytes and under atmospheric conditions proceeds along two paths [102-113]: depolarization with hydrogen evolution and depolarization with oxygen ionization, which act in parallel and independent of each other.

The cathodic process of oxygen reduction consists of several stages [102-108]: (i) passage of oxygen from the atmosphere into the electrolyte, (ii) transmission of oxygen by convection through the main body of solution, (iii) transmission of oxygen through the static layer of electrolyte adjacent to the cathode, (iv) reduction of oxygen at the cathode to hydroxide ions, and (v) diffusion of hydroxide ions away from the cathode. The passage of oxygen into solution, its convection to the cathode, and the diffusion of hydroxide away from the cathode generally do not influence the rate of the cathodic process [102-108]. Oxygen diffusion to the cathode and oxygen ionization at the cathode are the primary high resistance processes that limit the rate of the cathodic process (*i.e.* concentration and chemical polarization, respectively) [102-108].

Oxygen reduction at the cathode proceeds along two parallel paths, direct reduction of oxygen to hydroxide ion [102-108,114,115]:

(1) $O_2 + 4e^- + 2H_2O = 4OH^-$

and reduction of oxygen to hydrogen peroxide, with the further partial reduction of hydrogen peroxide [102-108,114,115]:

(2) $O_2 + 2e^- + 2H_2O = H_2O_2 + 2OH^-$

(3) $H_2O_2 + 2e^- = 2OH^-$

The cathodic process of hydrogen evolution also consists of several stages [108]: (i) transport of water molecules to the cathode, (ii) ionization of water molecules, (iii) removal of hydroxide ion, (iv) recombination (chemical desorption) of hydrogen atoms or electrochemical desorption of hydrogen atoms, (v) diffusion of hydrogen atoms or formation and detachment of hydrogen bubbles. It can be considered to consist of the following stages [108]:

(4) $H_2O + e^- = H_{ads} + OH^-$

(5) $H_{ads} + H_{ads} = H_2$

(6) $H_{ads} + H_2O + e^- = H_2 + OH^-$

Hydrogen evolution is electrochemically independent from oxygen reduction but has an indirect influence on the process [108]. Evolving hydrogen bubbles agitate the electrolyte and decrease the diffusion layer which can increase the diffusion limited oxygen current by up to 50% [108]. Of the two cathodic processes, oxygen reduction has lower resistance and is the predominant cathodic process, but there is still some hydrogen evolution that occurs at open circuit conditions [102-107].

Aluminum is strongly polarized to potentials of hydrogen evolution [102-108,110,116,117], as are the aluminum-copper alloys, Figure 2.15. Aluminum is an inefficient cathode for oxygen reduction [102-108], not because of poor catalytic activity, but because of its negative electrode potential and the instability of the oxide film in alkaline conditions [102-108]. Under cathodic polarization, alkali formed at the cathode significantly affects the local pH [108,116-123] and, in the vicinity of the cathode, dissolves the oxide film which shifts the electrode potential more negative due to exposure of bare aluminum [102-108,117,119,120,122,124].

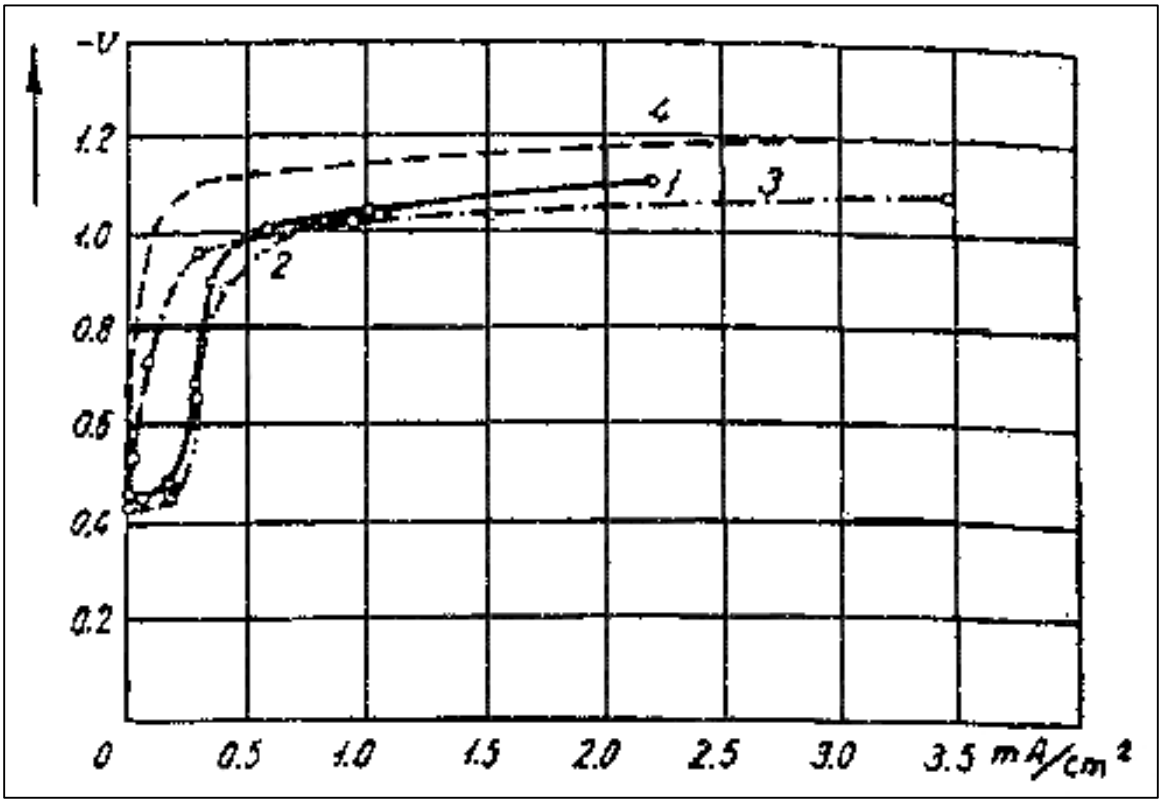

Figure 2.15 – Cathodic polarization curves for duralumin (*i.e.* AA2017-T4) in 0.5M NaCl [102-107]. 1: direct course with agitated electrolyte; 2: reverse course with agitated electrolyte; 3: with static electrolyte; 4: technical unalloyed aluminum in agitated electrolyte. Abscissa is in V_{NHE}.

At potentials around $-1.0V_{SCE}$ or more negative, hydrogen evolution becomes significant [102-107]. Aluminum is also a poor cathode for hydrogen evolution [102-107,123,125]. However, at potentials around $-1.5V_{SCE}$ or more negative, the efficiency of hydrogen evolution increases [110,111,117,119-121,123,124,126], Figure 2.15, due to total hydration of the oxide layer which renders it ionically conductive [110,125,127]. As the hydrated part of the duplex film penetrates toward the metal, hydrogen evolution may take place directly on aluminum metal [125,127]. A stable oxide film cannot be maintained [111,119-121,123,124] and aluminum dissolution occurs partly by a chemical process [125,127]. At potentials around $-1.7V_{SCE}$ or more negative, the formation of aluminum hydride as an intermediate monolayer at the metal/oxide interface or in the oxide before hydrogen evolution becomes possible [125,127].

2.3.1.2 Anodic Processes

In near-neutral solutions the oxide film on aluminum is stable and aluminum ions can only enter solution by migrating through the oxide film [128]. The 3 valence electrons of aluminum are in different orbitals ($3s^2 3p^1$) so it is probable that oxidation proceeds in a two-step process at the metal/oxide interface [111]:

(7) $Al = Al^+ + e^-$

(8) $Al^+ = Al^{3+} + 2e^-$

Reaction (8) is probably the rate limiting step [111]. The formation of sub-valent ions is also responsible for the so-called 'negative difference effect[1]' (NDE) [108,129] and the fact that the dissolution of aluminum has a Faradaic efficiency above 1 [108,131,132], *i.e.* aluminum dissolves with an effective valence of 2.4-2.6 [118,130,131]. So long as Reaction (8) is the rate limiting step, a certain amount of Al^+ ions are expected to react with water and release hydrogen at the oxide/solution interface [111,133]. The flux of Al^+ ions, and therefore the amount of hydrogen evolved, is proportional to anodic polarization which is in accordance with observations [111].

The anodic dissolution of aluminum is highly irreversible – its potential is well below the stability of H_2O [129,132] and the Al^{3+} ion has a large hydration energy [129]. This also means the anodic process is not susceptible to concentration polarization [134]. Even if the concentration of Al^{3+} exceeds the solubility product of the hydroxide, precipitation occurs away from the electrode surface and does not influence the processes occurring on the electrode surface.

[1]The difference between hydrogen evolution at open circuit and on anodic polarization is referred to as the 'difference effect' in the Russian literature [108,129]. Aluminum is unusual in that this difference is negative – *i.e.* hydrogen evolution increases linearly with increasing anodic current [111,130]. This behaviour is referred to as the 'negative difference effect' and is only seen in near-neutral solutions [129].

The active dissolution of aluminum is thermodynamically possible at all potentials noble to its standard electrode potential $-1.90V_{SCE}$ [111]. This potential represents elemental aluminum with no impurities, an oxide layer possessing no electronic conductivity or water permeability, in pure water with a pH of 7 [111]. Considerable active dissolution occurs above a characteristic breakdown potential, *i.e.* the 'pitting potential' [111]. Above the pitting potential, there are large increases in current associated with localized attack or pitting [111,120,122,133,135-138]. Above this potential, the oxide loses its stability and anywhere on the electrode surface is subject to attack [139,140]. The interface is shown schematically in Figure 2.16. There may be an induction period before pitting begins [111,121,141].

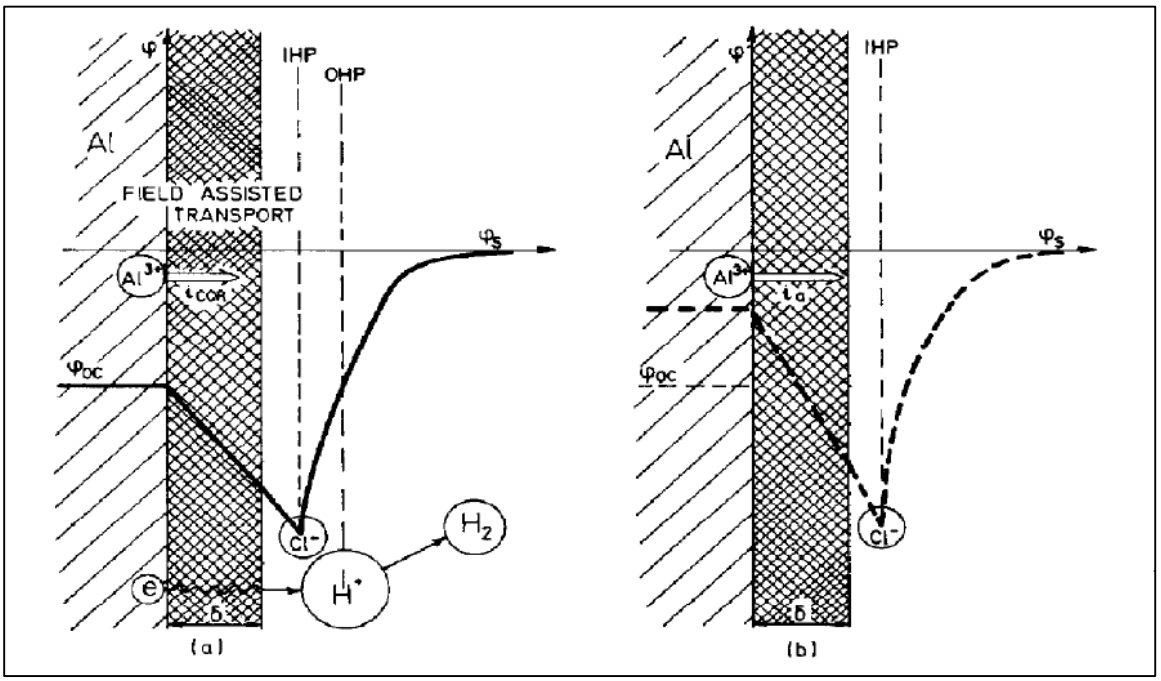

Figure 2.16 – Schematic representation of Al-solution interface in chloride solutions [133]: (a) at the open circuit potential; (b) during the anodic polarization.

The anodic dissolution of aluminum is strongly affected by the chloride ion [108,112,117,122,133,136,137,142-144]. The pitting potential is not affected by pH in the range 4-11 [111,122,145] but becomes more negative with increasing chloride concentration [111,121,122,136,137,142,144,146]. The activating effect of chloride may be related to the absorption of chloride ions [129,142,147] or the formation of complexes [111,121,130,147] such as: $Al(OH)_2Cl$, $Al(OH)Cl_2$, $AlCl_3$, $Al(OH)Cl^+$, and $AlCl_2^+$, all of which are highly soluble [111]. The adsorption of chloride affects the electric field in the double layer, Figure 2.16, in a way that accelerates the transport of aluminum ions through the oxide layer [111]. Furthermore if chlorine becomes incorporated into the oxide film this would increase the number of charge carriers [111].

On increasing anodic polarization to high current densities, dissolution goes through an ohmic-limited region and then a mass transport limited region [130]; in the latter, dissolution is limited by convective diffusion. Aluminum is unable to form a salt film in solution of less than 80% saturation due to the vigorous hydrogen evolution [130]. When anodic polarization is decreased from high values the dissolution potential deviates to more negative values [111,138] and upon cessation a new open circuit potential is established at more negative values [135,146]. This potential is also referred to as the 'repassivation potential' and is thought to be the result of an increase in anodic area on the electrode surface [135,146]. The repassivation potential is not as strictly reproducible as the pitting potential and is somewhat dependent upon the amount on anodic current passed [135]. The deactivation process occurs quickly (*ca.* 1ms) [111] and may be related to desorption of chlorine [147].

2.3.2 Electrochemical Characteristics of Intermetallic Phases

Traditionally the intermetallics in aluminum alloys have been classified according to nobility concepts [144]. This is not an accurate representation of the corrosion of aluminum alloys since it does not take into account kinetic information. A more complete classification has been proposed to be [144]: (i) noble particles with high electrochemical activity, (ii) noble particles with low electrochemical activity, (iii) active particles with high self-dissolution rates, and (iv) active particles with low self-dissolution rates. Some corrosion potentials for intermetallic phases are shown in Figure 2.17. In general, the most efficient cathodes are constituents containing iron or copper [102-108,148,149]. Oxygen reduction and hydrogen evolution kinetics are enhanced on these intermetallics [148-150]. The cathodic efficiency of iron-containing intermetallics is attributed to the stability of iron in alkaline solutions [144]. Intermetallics containing significant zinc, magnesium, or silicon typically do not show a passive region [144].

The Mg_2Si compound actively dissolves unless at high pH (12.5) [151]. It has a very negative potential (*ca.* $-1.5V_{SCE}$) and may be subject to selective dissolution of silicon [151].

The corrosion of the $CuMgAl_2$ phase is characterized by selective dissolution of aluminum and magnesium [137,148,151-157], leaving a copper rich residue. Copper and cuprous oxide (Cu_2O) have been identified in the remnants of corroded $CuMgAl_2$ by electron [152] and X-ray [158] diffraction. The de-alloying occurs on both cathodic [156] and anodic [137,152-155] polarization. Its mechanism is not completely understood. The oxide layer on $CuMgAl_2$ is not very protective and once broken down magnesium selectively dissolves [159]. It is thought that the dissolution of magnesium prevents repassivation and results in the simultaneous dissolution of aluminum [159].

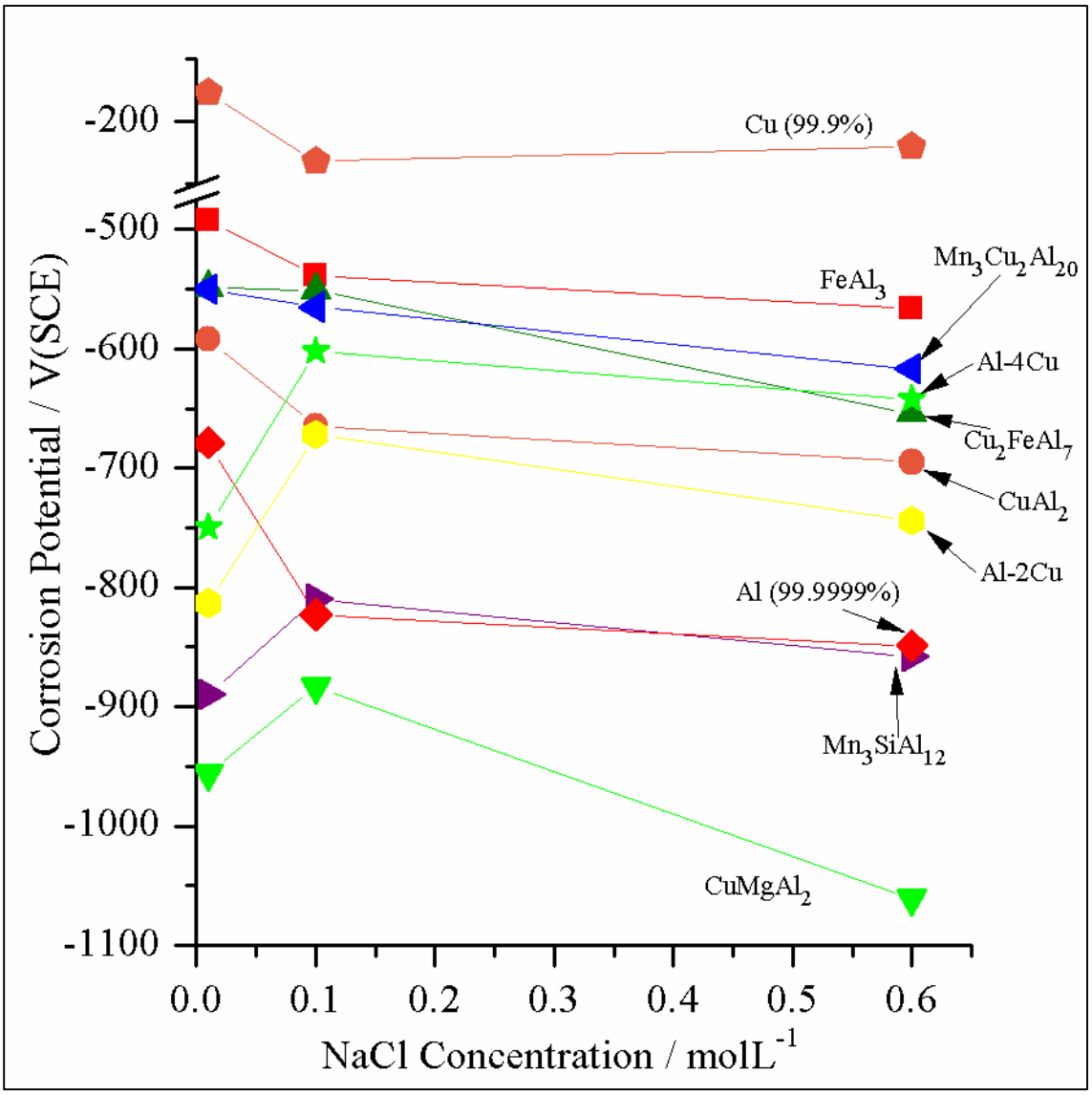

Figure 2.17 – Corrosion potentials for intermetallic compounds common in aluminum alloys as a function of sodium chloride concentration in pH=6 solution. Data from [144].

After de-alloying, the copper-rich remnant reorganizes into a crystalline nanoporous structure or 'sponge' with very high surface area [155,159] and enhanced oxygen reduction kinetics [148,155,156]. Any cathodic hydroxide produced further destabilizes

aluminum but has no effect on copper [155,159]. There is evidence for non-Faradaic liberation of de-alloyed copper clusters by convective forces [156]. It is considered to be a borderline case as to whether $CuMgAl_2$ de-alloys to a mechanically stable structure [159].

The $CuAl_2$ intermetallic behaves similarly to $CuMgAl_2$ in that it is subject to selective de-alloying of aluminum [123,160]. De-alloying may proceed by selective dissolution of only aluminum or the dissolution of aluminum and copper and then redeposition of copper [160]. *In situ* atomic emission spectroelectrochemistry (AESEC) suggests that $CuAl_2$ is not susceptible to the same mechanism of non-Faradaic liberation of de-alloyed copper clusters as $CuMgAl_2$ [123]. $CuAl_2$ has a high cathodic Tafel slope which indicates an oxide film is present and stable on cathodic polarization [123]. This is consistent with observations that the cathodic behaviour of $CuAl_2$ is not affected by increases in pH [151]. XPS studies of $CuAl_2$ indicate that metallic copper may be present in the oxide film or enriched at the oxide/metal interface [150].

The iron-containing intermetallics $FeAl_3$, Al_7Cu_2Fe, $Al_{20}Cu_2(MnFe)_3$, and $(FeMn)_3Si_2Al_{15}$ are not significantly affected by increases in pH [137,144,148,151,161], probably due to the stability of iron in alkaline solutions [144,151]. The Al_7Cu_2Fe phase supports remarkably high cathodic currents ($>100\mu Acm^{-2}$) and becomes a more efficient cathode at higher pH [144]. The $FeAl_3$, $Al_{20}Cu_2(MnFe)_3$, and $(FeMn)_3Si_2Al_{15}$ intermetallics are subject to de-alloying of aluminum [137,161].

2.3.3 Localized Corrosion

2.3.3.1 Passive Film Breakdown

The thickness of the natural air-formed oxide layer on aluminum is usually between 150-250Å but varies depending upon environmental conditions [108]. It contains absorbed water vapour and a small amount of carbon dioxide [162]. It has a duplex structure with an inner barrier layer consisting of mostly amorphous Al_2O_3 and a porous outer layer that is partially hydrated [113,162,163]. The oxide film is virtually insoluble between pH 4-8 [111,132,162].

Pitting is the result of several processes [142]: adsorption of chloride on the oxide surface, penetration of chloride ions through the oxide film, and localized dissolution of aluminum at the metal oxide interface, Figure 2.18. In solution, the outer layer of the natural air-formed oxide film is covered with a layer of hydroxyl groups whose charge is determined by its Lewis acid-base properties [142]. The isoelectric point of the natural air-formed oxide on aluminum is at pH of 9 or 9.5 [111,142], which means in neutral solutions the electrode surface acquires a positive charge, Reaction 1 in Figure 2.18, and is susceptible to adsorption of chloride ions, Reaction 2 in Figure 2.18 [142]. Adsorption is primarily the result of coulombic forces and induction of the adsorbent by the approaching chloride ion [142]. There is considerable evidence supporting the adsorption of chloride [111,121,122,133,142,147,164].

The chloride ion may penetrate the oxide film via oxygen vacancies [111,121,142], ‘water channels’ [142], localized film dissolution or thinning [111,142], or an ion exchange mechanism caused by complexing affinity [111]. Partial penetration through local flaws or cracks in the film is also possible [142]; cracking may be a result of stresses induced by adsorbed chloride [111].

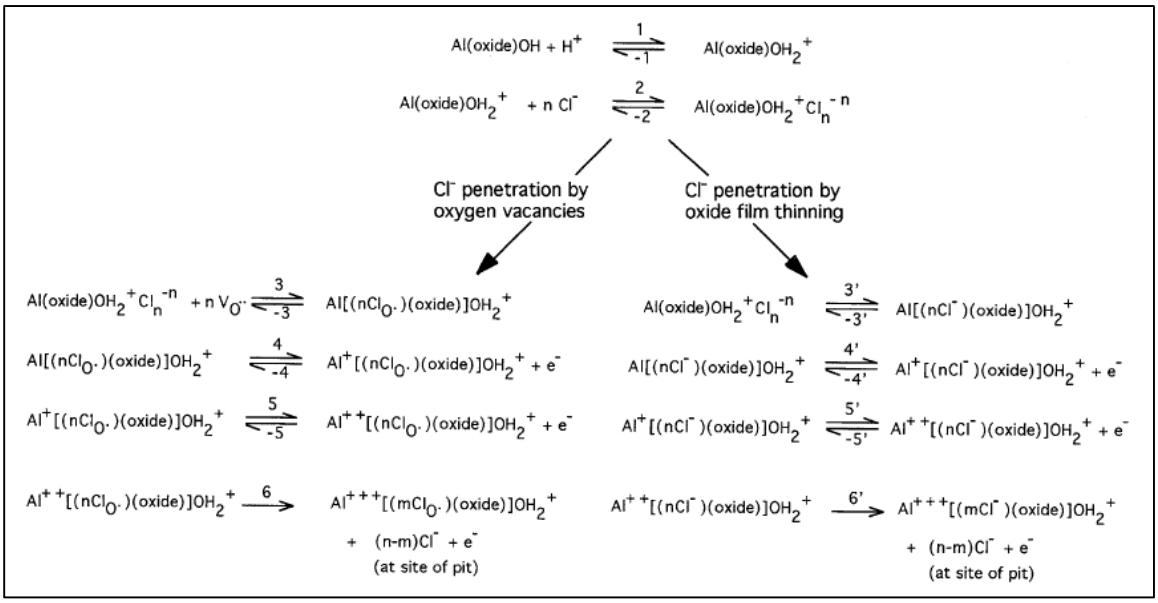

Figure 2.18 – Electrode kinetic scheme for pit initiation on pure aluminum in chloride solutions [142]. In Al(oxide)OH: 'Al' represents the atoms immediately below the oxide layer and 'OH' represents the outer layer of surface hydroxyl groups. $V_O^{\bullet\bullet}$ represents an oxygen vacancy in the oxide film. $Cl_O^{\bullet}$ represents a chloride ion occupying an oxygen lattice site.

After penetration, dissolution of aluminum occurs at the metal/oxide interface in a series of one-electron transfer reactions, Reactions 3-6, Figure 2.18 [142]. The water necessary for dissolution may exist in the oxide film itself or can penetrate through pores, cracks, or structural defects at impurities or surface heterogeneities [142]. Pits are associated with blisters underneath the oxide layer which form, grow, and eventually rupture due to hydrogen pressure [142].

Pits also form on cathodic polarization as a result of local alkalinity [119,120], especially in the presence of oxygen [110]. Cathodic pits are about 10-20μm in diameter, with pit diameter increasing in proportion to polarization [120].

2.3.3.2 Localized Corrosion Involving Intermetallic Phases

Intermetallic phases are associated with a distinct localized attack morphology known as 'trenching' where circumferential pitting appears mainly in the matrix phase as a ring of attack around the periphery of particles [151]. Cathodic trenching is trenching caused by alkaline attack from hydroxide ions produced by cathodic reactions occurring on the intermetallic [148,149]. The trenches can grow large enough that the cathodic phase becomes dislodged from the electrode and the area repassivates [120,124].

Anodic trenching is caused by galvanic coupling of the matrix and intermetallic [149]. The matrix surrounding soluble copper-containing intermetallics is depleted of copper and as a result has a more negative pitting potential [149,152]. This mechanism is supported by the observation that trench characteristics are influenced by chloride ion concentration – which has no effect on oxygen reduction kinetics, but influences pitting potential [149].

$CuMgAl_2$ is initially anodic to the matrix [144,148,154]. It is subject to de-alloying of aluminum and magnesium, preferentially from edges first [137,152-155], and its copper-rich remnants eventually become cathodic to the matrix [137,148,155,156,159,165,166]. The porous de-alloyed structure is subject to non-Faradaic liberation of copper [166], Figure 2.19. Copper containing clusters (10-100nm in diameter), which are mechanically removed by convection of the electrolyte, are held in the corrosion product gel and transported by convection [159,165]. The copper clusters are electrically isolated from the electrode and attain their own natural corrosion potential which allows for their oxidation [159,165]. The copper ions can then be redeposited on the matrix causing secondary pitting [159,165] or redeposited on other cathodic particles [148,155].

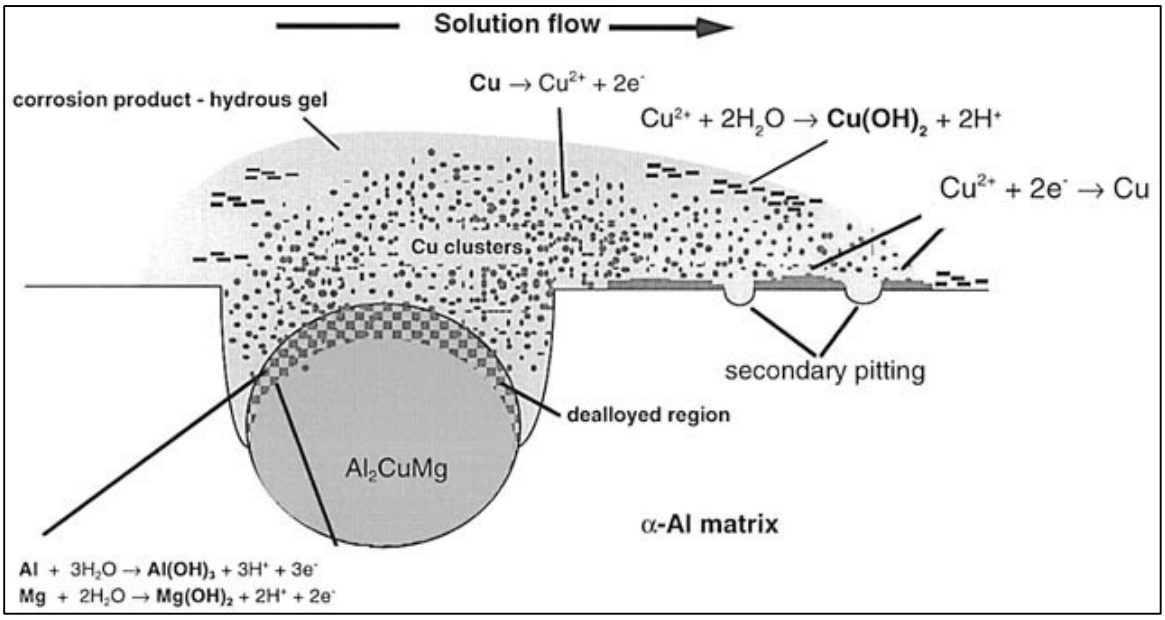

Figure 2.19 – Schematic illustration of a mechanism for redistribution of copper by dissolution of large $CuMgAl_2$ and $CuAl_2$ intermetallic particles in aluminum alloys [166].

Trenching is also observed around $CuAl_2$ [148,152], possibly the result of $CuAl_2$ locally polarizing the surrounding matrix above its pitting potential [148]. Aluminum is de-alloyed in a similar manner to $CuMgAl_2$, Figure 2.19 [159,165], however *in situ* AESEC seems to suggest that it is not susceptible to the non-Faradaic liberation of de-alloyed copper clusters [123].

Trenching is also observed around $Al_{20}Cu_2(MnFe)_3$ [149,152,153] but less than the copper-rich soluble intermetallics [149] and only after other active particles are consumed [137,153]. $Al_{20}Cu_2(MnFe)_3$ is expected to be cathodic to the matrix [148,153,155] and can be a site for the deposition of dissolved copper in solution [155].

2.3.4 Effect of Major Alloying Elements

In general, increasing the copper content reduces corrosion resistance [108,113,167-172]. The amount of copper in solid solution primarily controls the electrode potential [11] but the presence of $CuAl_2$ also has some influence [173]. The corrosion and pitting potential become more noble with increasing amounts of copper [139,172,174,175]. The pitting dissolution rate decreases with copper in solid solution [175] and pit interiors become enriched with copper [174]. Copper in solid solution enhances oxygen reduction currents on the matrix [144]. Copper has a low hydrogen overvoltage and significantly increases the amount of cathodic hydrogen evolution [102-108,117,123]. Pure aluminum corrodes with only oxygen reduction, but annealed duralumin (*i.e.* AA2017) corrodes with equal amounts of oxygen reduction and hydrogen evolution at open circuit conditions in 0.5M NaCl [108]. When copper is present as $CuAl_2$ it increases the amount of hydrogen evolution without affecting oxygen reduction [108]. The ratio of hydrogen evolution to oxygen reduction remains constant even under different conditions of aeration.

Copper-containing intermetallics act as efficient cathodes [102-108,148,149] and also affect the continuity of the oxide film [102-108]. The morphology of the copper-containing intermetallics determines the magnitude of their effect on corrosion rate. A larger amount of electrolyte is involved in diffusion to the edges of cathodic inclusions, so the limiting diffusion current for oxygen reduction is related to not only the cathode area but also the cathode perimeter [102-108,176]. This so-called 'edge effect' can have a large effect depending on the size and distribution of precipitates [102-108,176]. Any copper is also a potential source for dissolution and cathodic redeposition of metallic copper which accelerates corrosion [163,164,168,177].

Moderate additions (0.5wt%) of magnesium improve corrosion resistance [113,167,170]. Higher amounts of magnesium decrease corrosion resistance [170]. It is postulated that magnesium ions may affect the cathodic process if incorporated into the oxide film [164]. Silicon has a beneficial effect in the range 0.5-0.8wt% [170,178]. If free silicon is present it is detrimental [167,168].

Manganese (<0.6wt%) improves corrosion resistance [167,169,170], especially in the presence of 0.5-0.6wt% silicon [170]. Compounds of manganese can absorb some iron which helps prevent the formation of more harmful iron-rich intermetallics [113,167,168,178]. Manganese does not counteract the negative effects of nickel or cobalt [167]. Large amounts of manganese (>1.5wt%) form ternary compounds with aluminum and copper that decrease corrosion resistance [169,170].

2.3.5 Effect of Minor Alloying Elements and Impurities

In general, the presence of impurities has a detrimental effect on corrosion resistance [129,167,168,178,179], however their microsegregation (*e.g.* to grain boundaries or the surface film) is more important than the impurity content [111,167,168]. Impurities may affect the electrode potential and corrosion rate [111,135,145] but generally do not change the pitting potential [111,136,145] or affect dissolution rate at current densities above 0.01mAcm^{-2} [111]. Impurities usually affect the cathodic process [180,181] and typically increase the amount of hydrogen evolution [111,120]. The most common impurities in aluminum-copper alloys are iron, nickel, tin, lead, zinc, and antimony [178].

Iron is the most common impurity and is detrimental to corrosion resistance in contents from 0.2-1.5wt% [113,170,171,178]. Its compounds act as efficient cathodes [102-108,148,149], affect the continuity of the oxide film [102-108,162] and enhance aluminum dissolution [182]. It forms a compound with aluminum and copper, Cu_2FeAl_7, which supports cathodic currents orders of magnitude larger than other intermetallics [151]. Nickel behaves similarly to iron and is harmful to corrosion resistance [113,171,178].

Tin (0.2-0.7wt%) has a negative effect on corrosion resistance [113,178,183]. Lead (0.3-0.7wt%) and antimony (0.1-0.6wt%) are not detrimental to corrosion resistance [113,169,178,183].

Zinc (<1wt%) is usually present in solid solution and has no detrimental effect on corrosion or stress corrosion [178,183-185]. It may have a slight effect on the pitting potential and cathodic current [186,187] or increase the potential difference between the matrix and $CuAl_2$ [169].

Titanium (0.2wt%) is usually added as a grain refiner and has no effect on corrosion resistance [171,183] but has a beneficial effect on resistance to SCC [113,178,188-192]. It may slightly shift the corrosion or pitting potential [191,193] and also the potential difference between the matrix and $CuAl_2$ [193]. The use of niobium instead of titanium as a grain refiner has no adverse effect on corrosion resistance [171]. Chromium (0.2wt%) improves resistance to corrosion and SCC [113,178,183] but its effect is less than is seen in other aluminum alloys (*e.g.* Al-Zn alloys) [178].

2.3.6 Effect of Thermomechanical Treatment and Sequence History

Metal working and heat treatment procedures bring about changes in structure that can have a dramatic effect on corrosion behaviour, particularly: resistance to intergranular corrosion (IGC), stress corrosion cracking (SCC), and exfoliation corrosion [113,171,178,193,194].

If the quench rate after solution heat treatment is too slow or there is delay between removal from the furnace and quenching, there is excessive precipitation at grain boundaries which lowers resistance to IGC, SCC, and exfoliation [35,113,157,194]. There are residual stresses from quenching which are compressive near the surface and actually enhance resistance to SCC [113,194]. However, subsequent machining operations frequently leave the tensile area exposed which lowers resistance to SCC [194]. Stretching after quenching helps relieve stresses and improves resistance to SCC [113,194,195]. During artificial aging, resistance to IGC and SCC drastically decreases with short aging times and then increases as full aging is approached [113,194,195]. The changes in IGC and SCC resistance are the result of the potential difference between the grain bodies and the copper-depleted area near the grain boundaries [113,174,194-197], Figure 2.20. The copper-depleted region is anodic to the grain interiors and to the grain boundary precipitates [113,174,194-197]. The best resistance to IGC and SCC occurs when precipitation occurs evenly throughout the matrix [113,194].

Working changes grain structure to the extent that IGC, SCC, and exfoliation resistance are affected [194]. Long, thin, 'pancake-like' grains are the most susceptible to exfoliation [113,194]. The resistance to SCC is best in the longitudinal direction and worst in the short transverse direction [113,194,195].

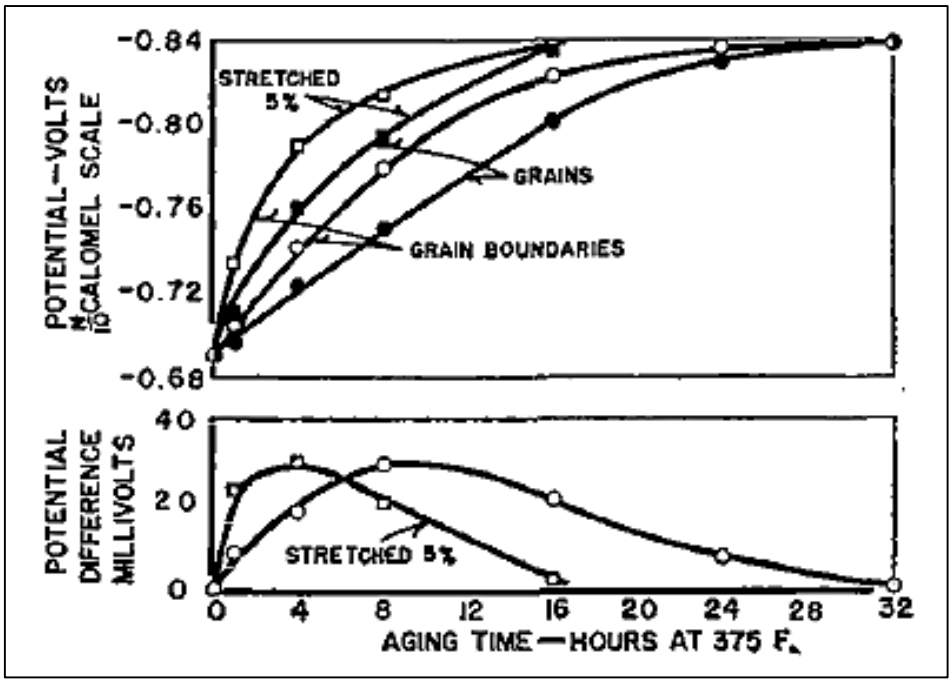

Figure 2.20 – The potentials of the grains and grain boundaries of an Al-4wt%Cu alloy which was heat-treated at 930°F (500°C), quenched in cold water, and aged at 375°F (190°C) [195]. Solution of 53gL^{-1} NaCl + 3gL^{-1} H_2O_2.

Sheet product is thin enough that it is fully recrystallized during heat treatments and is very resistant to SCC in all directions [113,194]. Plate products are not fully recrystallized during heat treatments and cannot be quenched as rapidly as thin sheet and are more susceptible to SCC than sheet [113,194]. The center of the plate contains elongated grains which are susceptible to SCC, especially in the short transverse direction [113,194].

Rod and bar product has similar SCC resistance to plate product [113]. It has superior SCC resistance in the longitudinal direction and poor SCC resistance in the transverse direction [113,194]. Extrusions have a SCC resistance similar to rolled products [194]. The recrystallized outer surface band on extrusions is not susceptible to exfoliation [113,194].

The corrosion behaviour of forgings depends upon metal flow patterns [113,194]. Their SCC resistance is similar to extrusions and rolled products [194] but typically have lower resistance in the longitudinal direction as a result of non-uniform metal flow [113]. Forgings may also be more susceptible because their residual stresses from quenching cannot be relieved by stretching or pressing [113].

CHAPTER 3 EXPERIMENTAL

3.1 POWDER METALLURGY PROCESSING

3.1.1 Compaction

Green compact 'pucks' were made by compacting 2.5g of powder pre-mix in a 15mm diameter, tungsten carbide, floating die assembly manufactured by Quala-Die, Inc. (St. Marys, Pennsylvania, U.S.A.), Figure 3.1. Compacting pressure was applied using a SATEC Series 5594-200HVL load frame (1MN capacity) manufactured by Instron Industrial Products (Grove City, Pennsylvania, U.S.A.). The desired compaction pressure was approached in a step-wise manner with a loading rate of $2kNs^{-1}$. Samples sintered industrially were all compacted at 300MPa. Samples sintered in the laboratory were compacted at: 100, 200, 300, 400, 500, or 600MPa.

Figure 3.1 – Floating die assembly for powder compaction.

3.1.2 Sintering

A portion of samples were sintered amongst industrial production at GKN Sinter Metals (Conover, North Carolina, U.S.A.). This plant regularly sinters Alumix 123 parts in high volume. The samples were sintered under a nitrogen atmosphere in a continuous wire mesh belt conveyor furnace employing standard operating conditions for industrially sintering Alumix 123. The pucks were placed on a shallow tray which was then placed on the wire mesh belt conveyor of the furnace. The pucks were oriented on the tray so that the flat circular face of the puck that was in contact with the lower punch during powder compaction was adjacent to the tray.

Samples sintered in the laboratory were done so in a Lindberg/Blue M 3-zone horizontal tube furnace with a stainless steel retort, Figure 3.2, manufactured by Thermo Electron Corporation (Asheville, North Carolina, U.S.A.). During the entire sinter cycle the temperature in the immediate vicinity of the compacts was measured with a thermocouple connected to a digital thermometer with a sensitivity of 0.1°C. Prior to sintering the furnace was evacuated (<7Pa) and purged with nitrogen twice. The sinter cycle consisted of a 30 minute de-lubrication stage at 400°C followed by a 20 minute sinter at 595°C. The entire sinter cycle took place under an atmosphere of flowing (20L per minute) ALPHAGAZ 1 nitrogen (>99.999% pure; H_2O: <3ppm; O_2: <2ppm) sold by Air Liquide America Specialty Gases LLC (Houston, Texas, U.S.A.). After the sinter cycle was completed, samples were gas quenched in a water cooled jacket and remained under flowing nitrogen until their temperature reached 100°C, upon which they were removed from the furnace and air cooled to room temperature.

Figure 3.2 – Horizontal tube furnace for sintering.

3.1.3 Sizing

Samples were sized using the same load frame used for powder compaction but in a larger (30mm diameter) die assembly in order to accommodate the expansion of the samples as a result of sintering. The die assembly used for sizing was of the same type and manufacture as used for powder compaction, except containing the larger diameter die. Prior to sizing samples, the peripheries of their flat circular faces were carefully deburred – the samples were held at an inclination and the edges abraded using motion and force applied by hand against a piece of stationary SiC paper.

Sizing fluid was obtained from GKN Sinter Metals (Conover, North Carolina, U.S.A.) and as per industry norm was diluted with 3 parts water to 1 part sizing fluid in order to emulate industry as much as possible. As per industry recommendations, immediately prior to sizing, samples were thoroughly coated by full submersion in to a

container of sizing fluid. During sizing, the pucks were oriented so that the flat circular face of the puck that was in contact with the lower punch during powder compaction was in contact with the lower punch during sizing. Only industrially sintered samples were sized. The sizing pressure was approached in a step-wise manner with a loading rate of $2kNs^{-1}$. Sizing pressures were 100, 200, 300, 310, 390, 400, 460, 500, or 600MPa. Samples that were corrosion tested were all sized at 310MPa which corresponds to a reduction in height of 5%.

3.1.4 Processing Response

The change in diameter, height, and mass of samples upon sintering and the change in height of samples upon sizing were measured. Diameter was measured using calipers with a sensitivity of 0.01mm, height was measured using a micrometer with a sensitivity of 0.001mm, and mass was measured using a scale with a sensitivity of 0.0001g.

Green and sintered density was measured in accordance with Metal Powder Industries Federation (MPIF) Standard 42. Specimens were weighed in air and in deionized water containing a small amount of wetting agent. Specimens were suspended in the deionized water by 0.12mm diameter copper wire using the 'twisted wire arrangement.' The temperature of the deionized water was measured by a digital thermometer with a sensitivity of 0.1°C and its density calculated with correction for the presence of dissolved air according to recent equations [198] which are recommended by the National Institute of Standards and Technology (NIST). The presence of solid lubricant in the powder pre-mix effectively sealed the exterior of the green compacts

during compaction so that no oil impregnation was necessary. Green density was calculated using the following equation:

(9) $$\rho_{green} = \frac{m_{air}\,\rho_{H_2O}}{m_{air} - m_{H_2O}}$$

Prior to weighing the porous sintered samples in deionized water, they were sealed by vacuum oil impregnation at room temperature. The specimens were submersed in hydraulic oil of ISO viscosity grade 46 and the pressure over the sample was reduced to <7kPa and held for 30 minutes. Afterwards the pressure was increased to ambient atmospheric pressure and the specimens were kept immersed for 30 minutes. Sintered density was calculated using the following equation:

(10) $$\rho_{sintered} = \frac{m_{air(no\ oil)}\,\rho_{H_2O}}{m_{air(oil)} - m_{H_2O(oil)}}$$

The theoretical density of Alumix 123 was calculated from its nominal composition as 2.777gcm^{-3} according to the equations from the Aluminum Association (Arlington, Virginia, U.S.A.).

3.2 ELECTROCHEMICAL TESTING

3.2.1 Sample Preparation

Wrought AA2014-T6 test specimens were prepared from 3.25 inch (83mm) diameter extruded rod so that the transverse plane was in contact with the electrolyte during electrochemical testing. The rod was sectioned with a band saw along the transverse plane into 4mm thick slices and a hole-saw drilled in to the longitudinal plane of the slices was used to extract 0.625 inch (15.9mm) diameter test specimens.

Wrought AA2014-T6 test specimens and laboratory sintered Alumix 123-T1 samples were polished using standard metallographic techniques immediately prior to electrochemical testing. Samples were abraded on successively finer grits of wet SiC paper (240, 320, 400, and 600 grit), then polished using successively finer oil-based diamond suspensions (9, 6, 3, and 1μm) on manufacturer recommended polishing clothes, cleaned ultrasonically in acetone and then in deionized water, and finally thoroughly rinsed with deionized water and dried using a hand drier. The SiC paper, diamond suspensions, and polishing clothes were from BUEHLER (Lake Bluff, Illinois, U.S.A.).

Industrially sintered Alumix 123-T1 samples were tested 'as-sintered' with no polishing but the peripheries of their flat circular faces had to be deburred so that a sufficient seal and electrical contact could be maintained during testing. The samples were held at an inclination and the edges abraded using motion and force applied by hand against a piece of stationary SiC paper. The surface of the flat circular face which was exposed to the electrolyte during testing was not disturbed by the deburring operation. During testing the sample was oriented so that the flat circular face, which was in contact with the upper punch during powder compaction, was exposed to the electrolyte.

Industrially sintered and sized Alumix 123-T2 samples were tested 'as-sized' with no polishing. These samples were previously deburred prior to the sizing operation. These samples retained some sizing fluid in their pores and on their surface which was present during testing. During electrochemical testing, the sample was oriented so that the flat circular face which was in contact with the upper punch during sizing was exposed to the electrolyte.

3.2.2 Electrolyte Preparation

All electrochemical testing was conducted in a naturally aerated 3.5wt% NaCl electrolyte. The solution was prepared immediately prior to electrochemical testing using analytical-grade NaCl (>99.0% assay) obtained from Fisher Scientific (Fair Lawn, New Jersey, U.S.A.) and ultrapure 'Type 1' deionized water (>18MΩ·cm) obtained from a Direct-Q® 5UV-R water purification system, Figure 3.3, manufactured by EMD Millipore Corporation (Billerica, Massachusetts, U.S.A.).

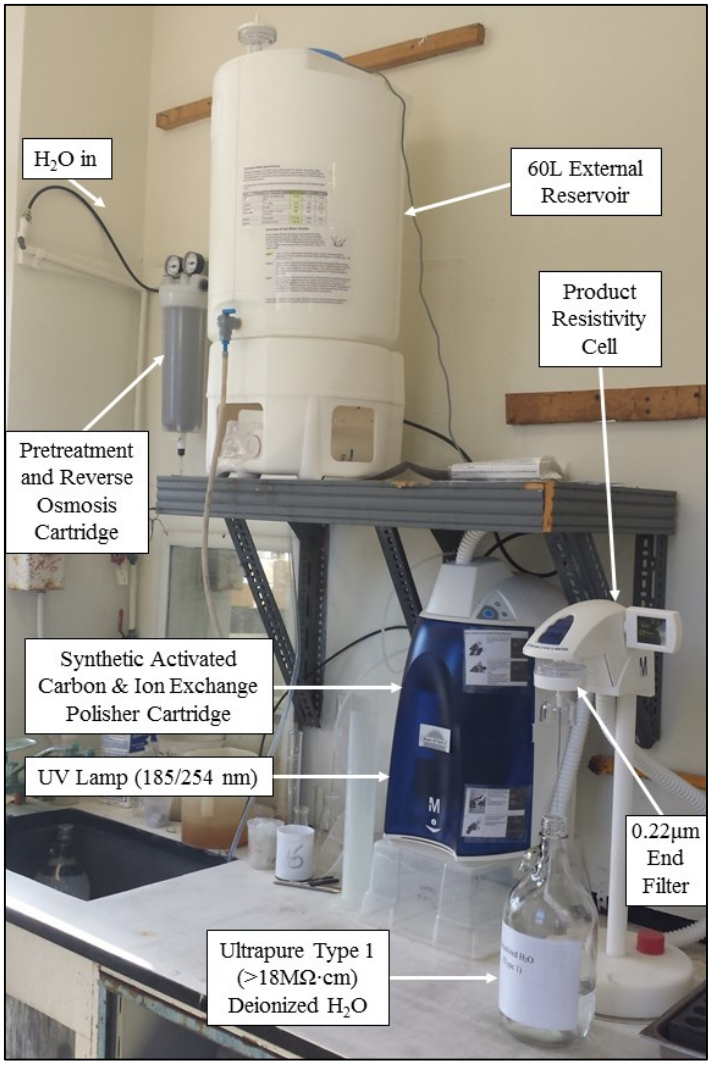

Figure 3.3 – Water purification system for electrolyte preparation.

3.2.3 Electrochemical Cell & Potentiostat

Standard electrochemical instrumentation consisting of a three electrode bulb cell connected to a Model 273A Potentiostat/Galvanostat manufactured by EG&G Princeton Applied Research (Princeton, New Jersey, U.S.A.), which incorporated a grounded electrometer, was used for electrochemical measurements, Figure 3.4. The potentiostat was connected to a desktop computer and controlled via CorrWare® software sold by Scribner Associates, Inc. (Southern Pines, North Carolina, U.S.A.). The potentiostat was calibrated by the use of a laboratory-made 'dummy cell.'

The standard three electrode 1L glass bulb cell contained a working electrode assembly that exposed a nominal area of exactly $1cm^2$ of the test specimen to the electrolyte, two high purity fully dense 0.25 inch (6.35mm) diameter graphite counter electrodes, and a saturated calomel reference electrode (SCE) (KCl(sat'd) | Hg_2Cl_2(s) | Hg(l) | Pt), Figure 3.4.

Apart from the reference electrode, the entire electrochemical cell was comprised from the Model K0047 Corrosion Cell System and Model K0105 Flat Specimen Holder manufactured by Princeton Applied Research (Oak Ridge, Tennessee, U.S.A.). The working electrode sample holder was composed of 303 stainless steel encapsulated in a rigid fluorocarbon 'Tefzel-280' and the area around the test specimen was sealed with a 'DuPont Kalrez' fluorocarbon elastomer washer, Figure 3.5. The sample holder is suspended in the electrolyte by a 303 stainless steel rod which screws into the top of the sample holder. The rod is isolated from the electrolyte by a glass tube which is sealed to the working electrode body with a DuPont Kalrez O-ring and kept in place by a thumb nut and Teflon washer, Figure 3.5.

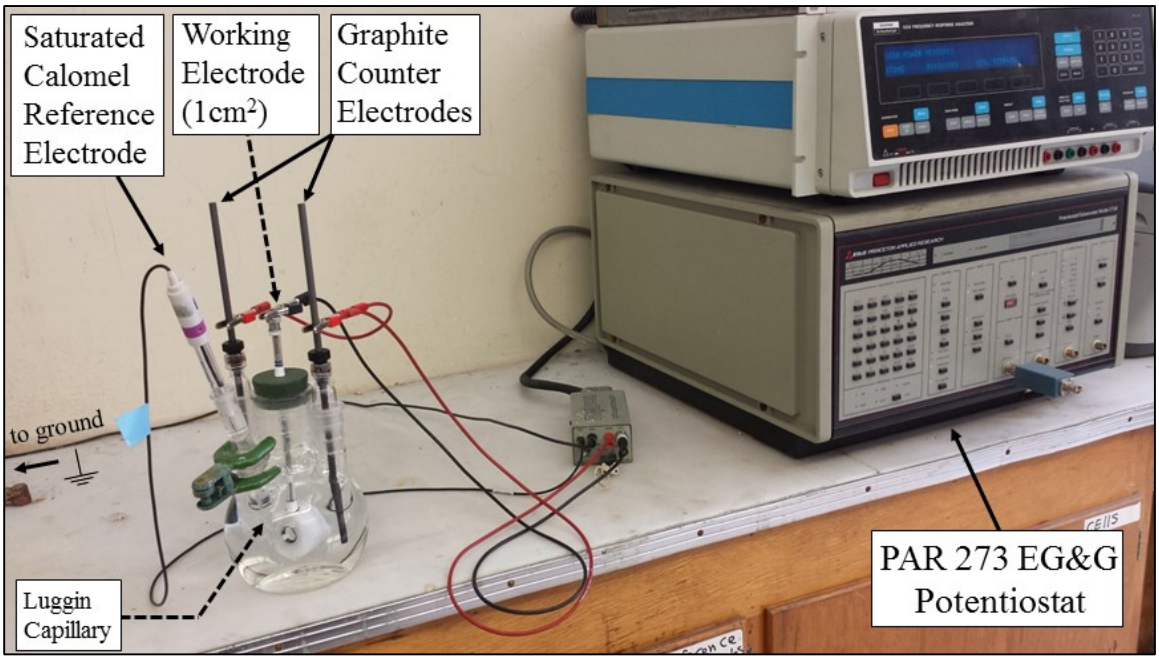

Figure 3.4 – Electrochemical cell and potentiostat used for electrochemical measurement.

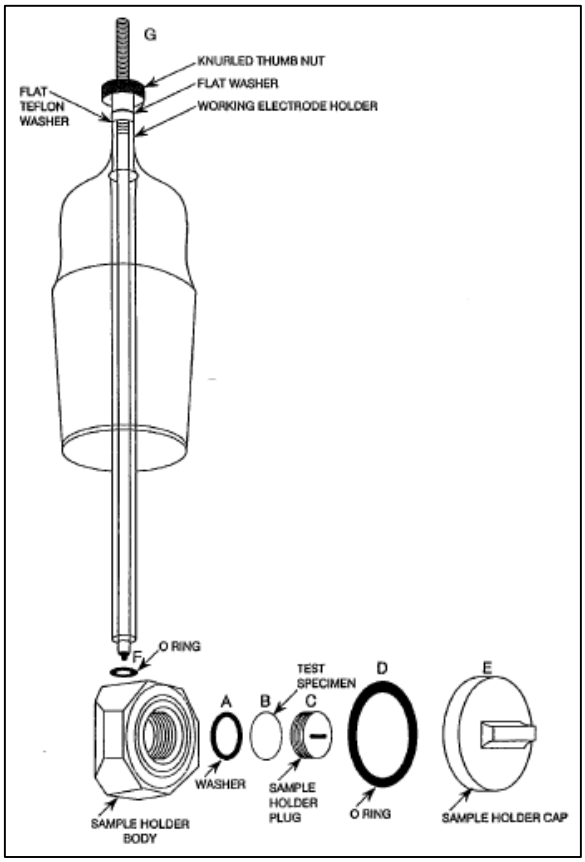

Figure 3.5 – Schematic of the working electrode (from *Princeton Applied Research*)

The reference electrode was a glass body Accumet® SCE with a porous ceramic junction manufactured by Fisher Scientific (Fair Lawn, New Jersey, U.S.A.), and was brought in close proximity to the working electrode via a Luggin capillary which was filled with 3.5wt% NaCl electrolyte and equipped with an ultra low-leakage 'Vycor' frit. The reference electrode was regularly checked against a laboratory standard.

Electrochemical tests were conducted in approximately 900mL of 3.5wt% NaCl electrolyte under naturally aerated conditions at ambient temperature (22±3°C). During testing approximately 23cm^2 of nominal counter electrode surface area was in contact with the electrolyte. All current densities are based off the nominal area of test specimen exposed to the electrolyte (1cm^2).

3.2.4 Open Circuit Potential

The potential of the working electrode under open circuit conditions was monitored versus time for a period of 1 hour for the wrought samples and 2 hours for the P/M samples. The P/M samples were monitored for a longer period of time because they were highly non-planar and took longer to equilibrate with the electrolyte. The potential at the conclusion of the test is referred to as the 'open circuit potential' (OCP). Prior to all subsequent applied-potential electrochemical testing, the open circuit potential was monitored and allowed to stabilize for the times indicated above.

3.2.5 Potentiodynamic Polarization

3.2.5.1 Cathodic Polarization

During cathodic polarization the potential of the working electrode was varied continuously at a rate of $0.1667 mV s^{-1}$ ($0.6 V hr^{-1}$) from the open circuit potential (OCP) to $-2.000 V_{SCE}$.

3.2.5.2 Cyclic Polarization

During cyclic polarization the potential of the working electrode was varied continuously at a rate of $0.1667 mV s^{-1}$ ($0.6 V hr^{-1}$) from a potential more negative than the OCP to a predefined anodic current density or potential and then the direction of the scan was reversed to the cathodic direction until a predefined potential was reached. The characteristic test potentials and current densities varied between different samples and are outlined below. The polarization curves were analysed using the CorrView™ software sold by Scribner Associates, Inc. (Southern Pines, North Carolina, U.S.A.). The corrosion current (i_{corr}) and corrosion potential (E_{corr}) of all samples were found by Tafel extrapolation; however the method of extrapolation had to be modified for different samples as outlined below. For all samples the repassivation potential (E_{repass}) was defined as the potential where the anodic current density reaches a value of 1μA on the reverse scan.

For wrought AA2014-T6 samples the potential of the working electrode was varied from $-0.875 V_{SCE}$ until an anodic current density of $0.01 A cm^{-2}$ was reached and then the direction of the scan was reversed to the cathodic direction until a potential of –

1.000V_{SCE}. The corrosion current was found by the intersection of manually-fitted anodic and cathodic Tafel curves.

For industrially sintered Alumix 123-T1 samples the potential of the working electrode was varied continuously from –1.250V_{SCE} until an anodic current density of 0.01Acm^{-2} was reached and then the direction of the scan was reversed to the cathodic direction until a potential of –1.000V_{SCE}. The anodic branch of the polarization curve of these samples displayed non-Tafelian dependence and could not be accurately extrapolated by the conventional means. The corrosion current was found by the intersection of the manually-fitted cathodic Tafel curve with the corrosion potential. The passive current (i_{pass}) was taken as the current density immediately prior to breakdown at the pitting potential.

For industrially sintered and sized Alumix 123-T2 samples the potential of the working electrode was varied continuously from –0.875V_{SCE} until an anodic current density of 0.01Acm^{-2} was reached and then the direction of the scan was reversed to the cathodic direction until a potential of –1.000V_{SCE}. The corrosion current was found by the intersection of manually-fitted anodic and cathodic Tafel curves.

For laboratory sintered Alumix 123-T1 samples the potential of the working electrode was varied continuously from –1.250V_{SCE} until a potential of –0.400V_{SCE} and then the direction of the scan was reversed to the cathodic direction until a potential of –1.000V_{SCE}. The anodic branch of the polarization curve of these samples displayed non-Tafelian dependence and could not be accurately extrapolated by the conventional means. The corrosion current was found by the intersection of the manually-fitted cathodic Tafel curve with the corrosion potential. The passive current (i_{pass}) was taken as the current density immediately prior to breakdown at the pitting potential.

Corrosion rate was calculated from corrosion current in accordance with ASTM G102. Equivalent weight (EW) was calculated based off nominal composition and as per norm only alloy components present in amounts over 1wt% were included, meaning for both AA2014-T6 and Alumix 123 calculations were made for an alloy containing 95.5wt% Al and 4.5wt% Cu. The valence of aluminum and copper were taken to be 3 and 2 respectively and the equivalent weight (EW) of the alloys calculated to be 9.29 gram equivalents. Corrosion rate (CR) in $mmyr^{-1}$ was calculated by:

(11) $$CR = 3.27 \times 10^{-3} \frac{i_{corr}}{\rho} EW$$

where corrosion current (i_{corr}) is in μAcm^{-2} and density (ρ) is in gcm^{-3}. The density of AA2014-T6 was taken as $2.80 gcm^{-3}$ as per the Aluminum Association. The sintered density of Alumix 123 was used for corrosion rate calculations.

3.2.6 Potentiostatic Polarization

During all potentiostatic polarization experiments current transients were recorded as a function of time and at rate of 1 point per second. All sample types were subject to the same potentiostatic tests. Potentiostatic polarization experiments were conducted at: $-1.100 V_{SCE}$, $-0.750 V_{SCE}$, and $-0.700 V_{SCE}$ for 6 hours and at $-1.500 V_{SCE}$ and $-0.500 V_{SCE}$ for 3 hours. These potentials were identified as points of interest from potentiodynamic polarization experiments.

3.3 MATERIALS CHARACTERIZATION

3.3.1 Chemical Analysis

Chemical analysis by inductively coupled plasma optical emission spectroscopy (ICP-OES) was performed by the Minerals Engineering Centre (MEC) at Dalhousie University using a Vista-Pro CCD Simultaneous ICP-OES, Figure 3.6, manufactured by Varian, Inc. (Palo Alto, California, U.S.A.). All samples were analyzed using standard operating procedures and alongside appropriate quality control samples certified by the National Bureau of Standards (Washington, D.C., U.S.A.). Chemical analysis of Alumix 123 was performed on a sintered compact.

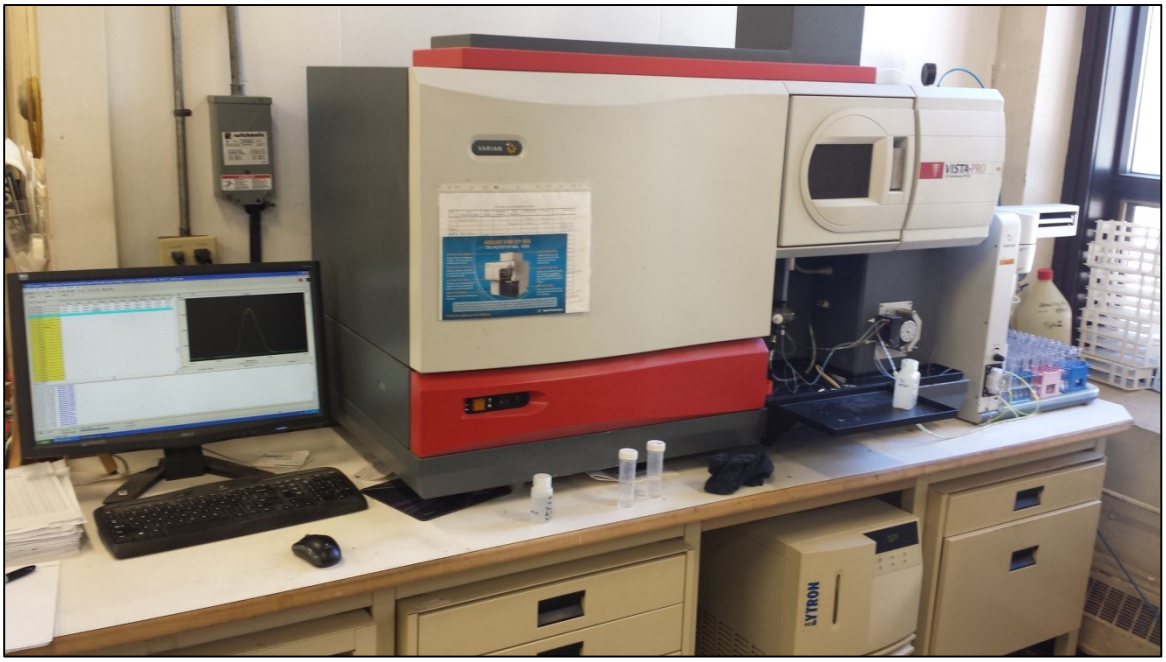

Figure 3.6 – Inductively coupled plasma emission spectrometer for chemical analyses.

3.3.2 Particle Size Analysis

Particle size measurements were performed by the MEC at Dalhousie University using a Mastersizer 3000 laser diffraction particle size analyzer, Figure 3.7, manufactured by Malvern Instruments (Malvern, Worcestershire, United Kingdom). Particle size was analyzed using standard operating procedures. Methanol was used as a dispersant.

Figure 3.7 – Laser diffraction particle size analyzer.

3.3.3 Optical Microscopy

Optical micrographs were captured in monochrome using a BX51 light microscope and DP71 digital camera, Figure 3.8, both manufactured by Olympus (Shinjuku-ku, Tokyo, Japan), and Image-Pro 6.3 software sold by Media Cybernetics (Bethesda, Maryland, U.S.A.). Alumix 123 pre-mix was mounted in epoxy resin by mixing 2 parts pre-mix with 3 parts epoxy resin, as per literature recommendations [51], and then polished using standard metallographic techniques. To view the microstructure

of air atomized aluminum particles, the mounted pre-mix was etched using Keller's reagent. All other samples were etched in a solution of 2g NaOH, 5g NaF, and 93mL deionized H_2O.

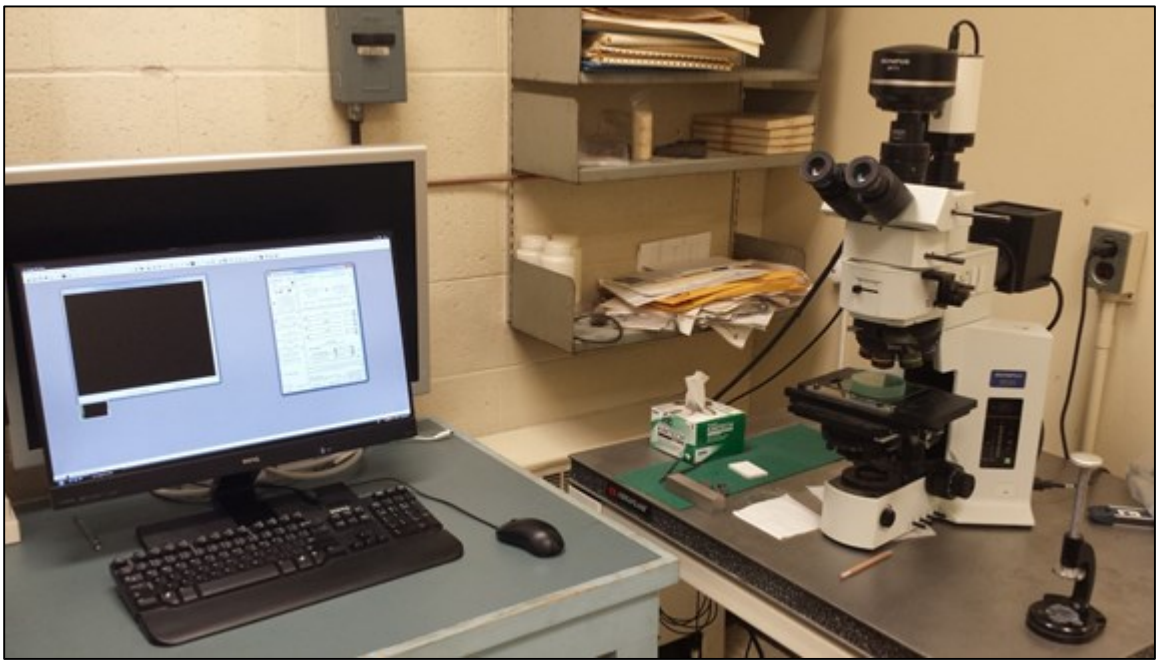

Figure 3.8 – Optical microscope and digital capture system.

3.3.4 Scanning Electron Microscopy

Electron micrographs were captured using a Model S-4700 cold field emission scanning electron microscope (SEM), Figure 3.9, manufactured by Hitachi High-Technologies Corporation (Minato-ku, Tokyo, Japan). The SEM contains an integrated INCA X-Max^N 80mm silicon drift detector (SDD) manufactured by Oxford Instruments (Abingdon, Oxfordshire, United Kingdom) that is used for energy dispersive X-ray spectroscopy (EDS). For imaging, the SEM was operated with a 10kV accelerating

voltage and 20μA emission current. For EDS, the SEM was operating with a 20kV accelerating voltage and 10μA emission current. The working distance was always kept close to 12mm. In order to analyse Alumix 123 powder pre-mix it was secured to a pin stub mount with silver chloride paste. Prior to analysis in the SEM, sized P/M samples were treated in a Soxhlet apparatus for 8 hours with petroleum ether to remove sizing fluid.

To analyse cross sections some samples were mounted by vacuum impregnation with a low viscosity self-curing resin, sectioned, and polished. Before mounting, the sized P/M samples were treated in a Soxhlet apparatus for 8 hours with petroleum ether to remove sizing fluid. Prior to examination in the SEM, mounted samples were carbon coated using a DV-502A high vacuum evaporator platform manufactured by Denton Vacuum (Moorestown, New Jersey, U.S.A.).

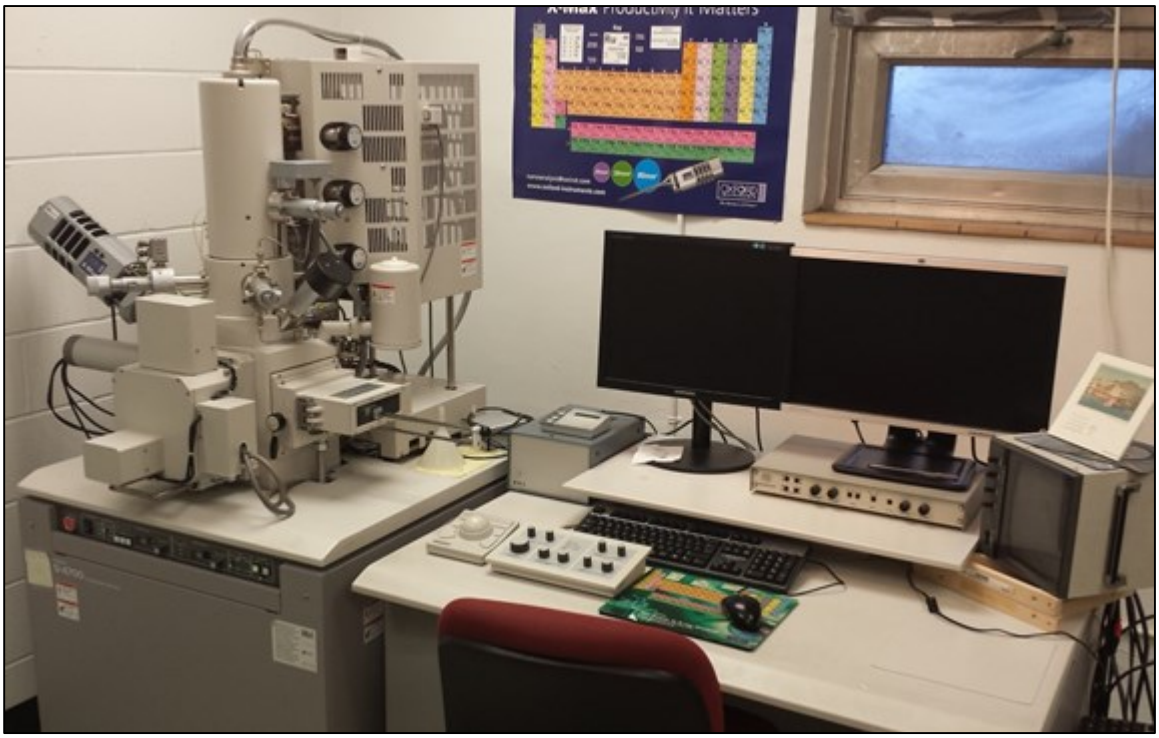

Figure 3.9 – Scanning electron microscope with integrated energy dispersive X-ray spectroscopy system.

3.3.5 X-Ray Diffraction

X-ray diffraction (XRD) patterns were collected using $CuK_{\alpha 1}$ radiation (λ=1.54Å) in a D8 ADVANCE X-ray diffractometer, Figure 3.10, manufactured by Bruker (Madison, Wisconsin, U.S.A.) operating with a tube voltage of 40kV and a tube current of 40mA.

Figure 3.10 – X-ray diffractometer.

CHAPTER 4 MATERIALS

Alumix 123 was obtained from ECKA Granules Germany GmbH (Fürth, Bavaria, Germany) as a 'press ready' pre-mix containing 1.5wt% admixed 'Licowax C' solid lubricant and blended by the manufacturer. The product was analysed by the manufacturer and certified to quality control standards for particle size distribution, apparent density, flowability, and chemical composition.

Wrought AA2014-T6 was obtained as a 3.25 inch (83mm) diameter extruded rod from the Tennalum Division of Kaiser Aluminum (Jackson, Tennessee, U.S.A.) and conformed to ASTM B211 and AMS-QQ-A-225/4 standards.

CHAPTER 5 CHARACTERIZATION OF RAW MATERIALS

5.1 ALUMIX 123

The analysed chemical composition of Alumix 123 is shown in Table 5.1, particle size distribution in Figure 5.1, and polished cross section in Figure 5.2. The small increase in particle size frequency between 10 and 30μm may be due to the admixed solid lubricant or alloy additions which are typically added in fine particle size to promote a homogenous distribution.

The pre-mix is comprised of elemental and master alloy powders, Figure 5.3 through Figure 5.6, whose approximate composition is shown in Table 5.2. The elemental aluminum powder has a nodular and irregular shape which is characteristic of air atomization [1,3,36] and contains some silicon and iron as impurities, Table 5.2. The cross sectional microstructure, Figure 5.4, has a dendritic cell pattern which is typical of air atomized aluminum.

Table 5.1 – Chemical analysis of Alumix 123 by ICP-OES (wt%). Balance Al.

Composition	Cu	Mg	Si	Fe	Mn	Others (each)	Others (total)
Nominal[a]	4.30-4.70	0.40-0.60	0.50-0.80	–	–	–	–
Analysed	4.57	0.52	0.80	0.11	<0.01	–[b]	0.21

[a]Plus 1.40-1.60wt% lubricant

[b]Ca: 0.03; Ga: 0.01; K: <0.01; Na: 0.02; Ni: 0.01; P: 0.03; Pb: 0.01; S: 0.02; Sn: 0.02; V: 0.01; Zn: 0.05

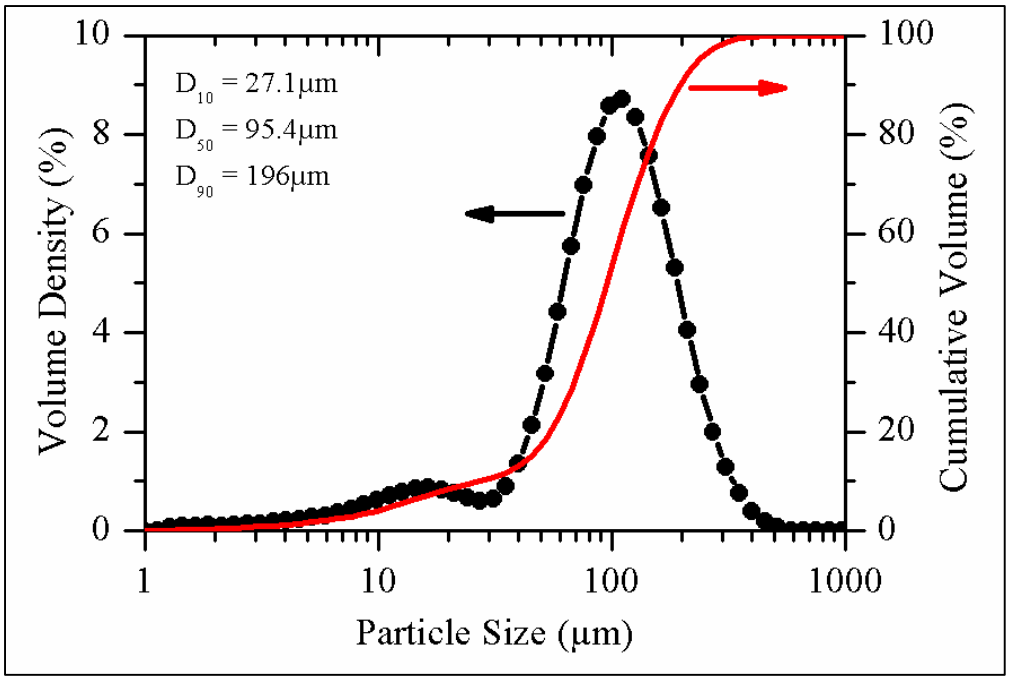

Figure 5.1 – Particle size distribution of Alumix 123.

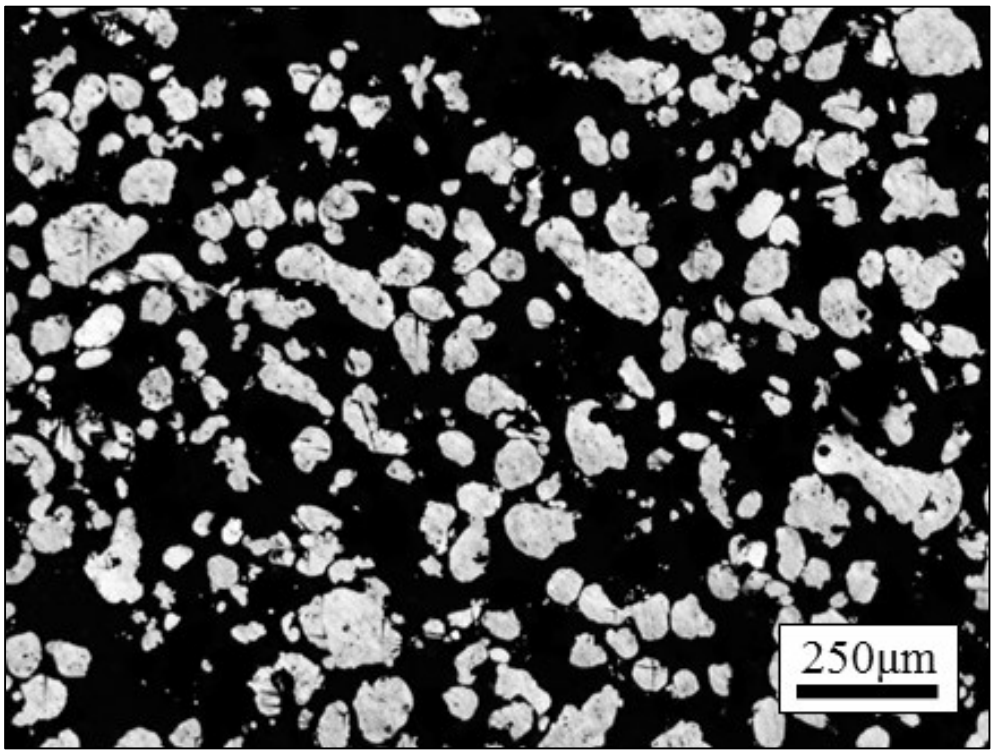

Figure 5.2 – Optical micrograph of polished cross section of Alumix 123 pre-mix mounted in epoxy resin (unetched).

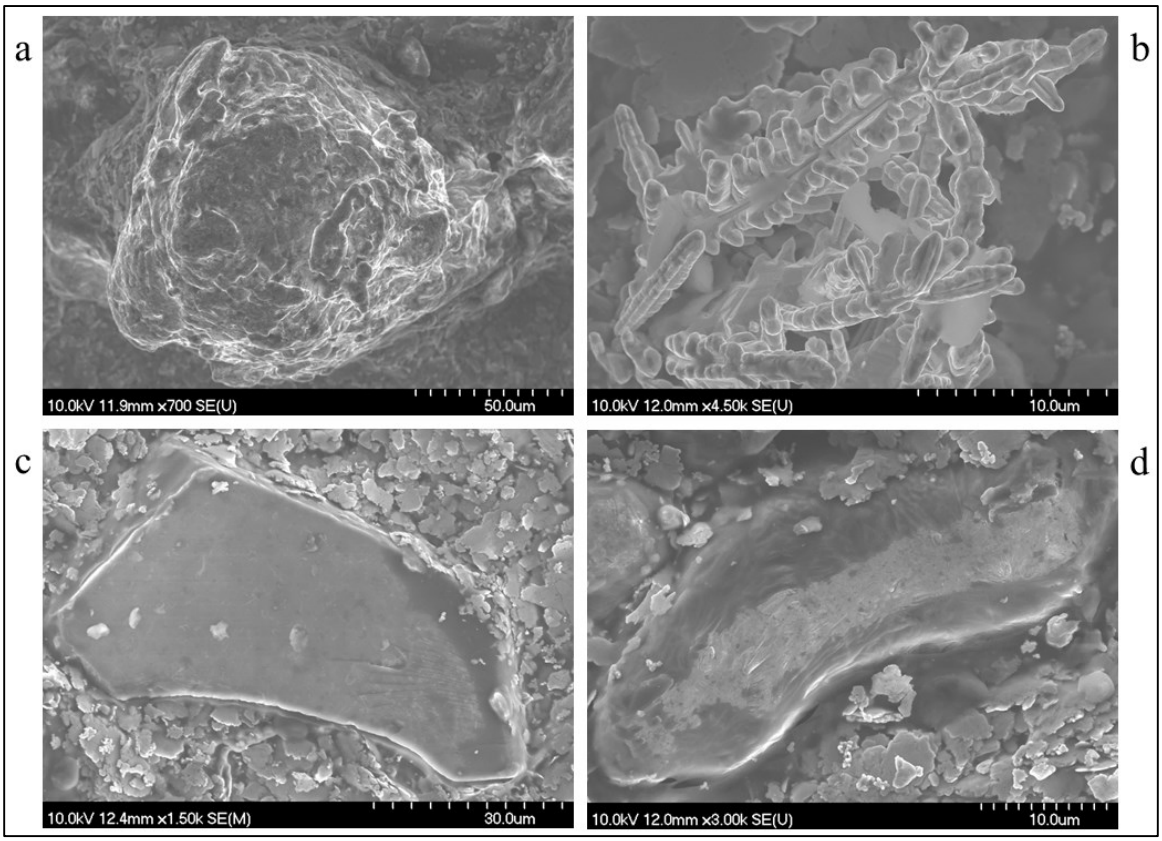

Figure 5.3 – SEM micrographs of different particles in Alumix 123: (a) elemental aluminum; (b) elemental copper; (c) magnesium-containing master alloy; (d) silicon-containing master alloy. The powders were mounted on silver chloride paste.

Table 5.2 – Summary of EDS point analyses of different particles in Alumix 123 (wt%).

Particle Type	EDS Point Analysis (wt%)[a]					
	Al	Cu	Mg	Si	Other	*No.* of points
Al	99.8±0.3	–	–	0.1±0.3	0.1±0.1 Fe	9
Cu	–	100.0±0.0	–	–	–	2
Mg-containing	50.2±2.6	–	49.7±2.7	0.1±0.2	0.0±0.1Zn	12
Si-containing	90.1±3.2	–	–	9.9±3.1	0.0±0.1 Fe	16

[a]Values are given as mean ± standard deviation

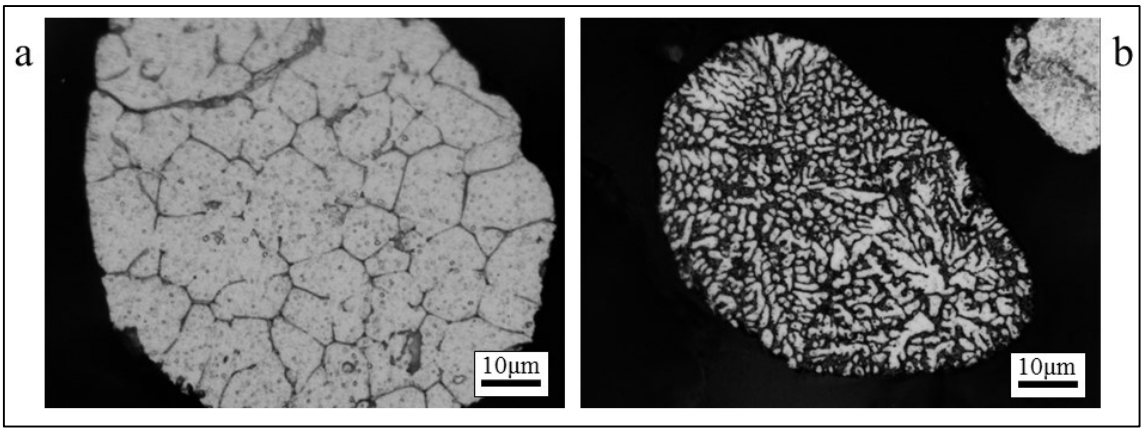

Figure 5.4 – Optical micrograph of cross sectional microstructure of different particles of Alumix 123 mounted in epoxy resin (etched): (a) elemental aluminum; (b) silicon-containing master alloy.

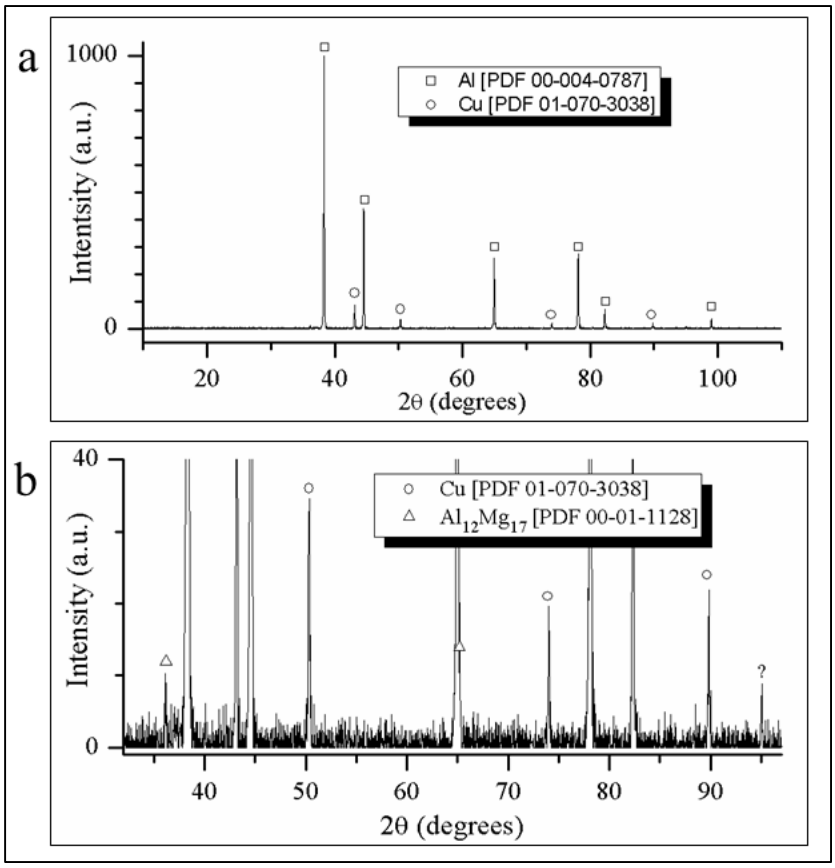

Figure 5.5 – XRD pattern of Alumix 123 powder pre-mix: (a) full pattern; (b) close up of smaller peaks.

The elemental copper powder has a high purity, Table 5.2, and dendritic shape, Figure 5.3, characteristic of electrolytic deposition from aqueous solution. The XRD pattern for the powder pre-mix, Figure 5.5, contains peaks corresponding to elemental copper. Other investigators [55,199-201] have also found Alumix 123 to contain elemental copper powder.

The magnesium-containing particles have a jagged and angular particle shape, Figure 5.3, and in some areas 'saw tooth' pattern marks are apparent, Figure 5.6. These features are indicative of a mechanical powder production process. The high magnesium content of the master alloy, Table 5.2, would make it easy to pulverize. Based on the composition in Table 5.2, the $Al_{12}Mg_{17}$ intermetallic is expected to be the only phase present [11] and in the XRD pattern for the pre-mix, Figure 5.5, there is a small peak which could correspond to this phase. Other investigators [55,200,201] have found Alumix 123 to contain magnesium as a master alloy powder – some of which also found a composition of Al-50wt%Mg by EDS analyses [200,201] and suggested the angular morphology to be the result of mechanical grinding [200].

The silicon-containing particles are rounded and have an ellipsoid or cylindrical particle shape, Figure 5.3, with a rough, irregular surface, Figure 5.6. These features may be the result of an atomization process – although the silicon-containing particles are much more elongated and smoother than the elemental aluminum powder which is also believed to be air atomized. The silicon-content of the master alloy, Table 5.2, would presumably increase fluidity and could have modified particle shape and solidification during atomization. The cross sectional microstructure of the silicon-containing particles, Figure 5.4, is consistent with rapid cooling, which would be experienced during atomization. Other investigators [55,200,201] have found Alumix 123 to contain silicon

as a master alloy powder. One investigation [200] suggested the master alloy powder was produced by atomization. Independent EDS analyses found the composition of the master alloy to be Al-12.5wt%Si [200] and Al-12wt%Si [201] – well within the standard error in Table 5.2.

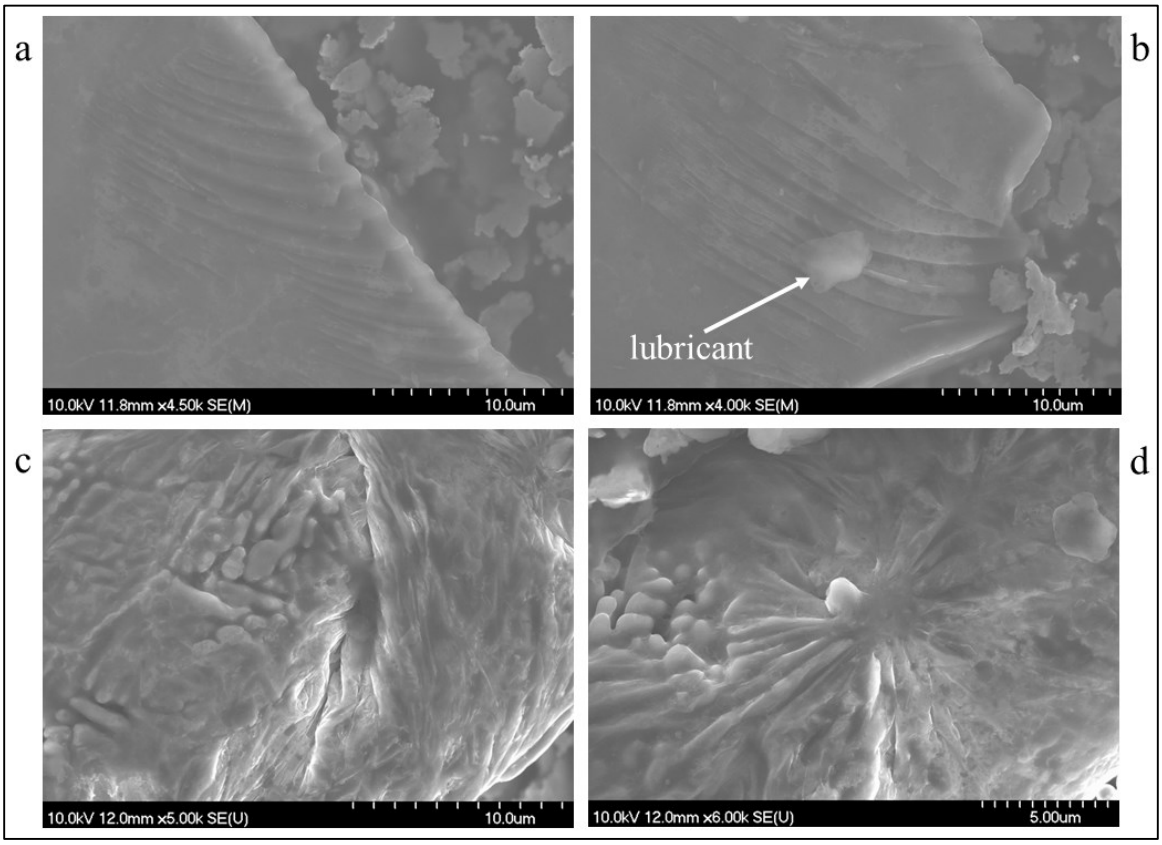

Figure 5.6 – SEM micrographs of surface characteristics of different particles in Alumix 123: (a), (b) magnesium-containing master alloy; (c), (d) silicon-containing master alloy. The powders were mounted on silver chloride paste.

5.2 AA2014-T6

The analysed chemical composition of the wrought AA2014-T6 extruded rod is shown in Table 5.3. Optical and SEM micrographs are shown in Figure 5.7 and Figure 5.8, respectively. The grain structure is clearly elongated in the direction of working and there are two distinct phases which are apparent from the micrographs: one with a round globular morphology and another with Chinese script morphology. These phases are shown with higher magnification in Figure 5.9.

The round globular phase is probably θ-$CuAl_2$ which may originate from the cast ingot structure. In some areas this phase appeared aligned in the direction of extrusion which suggested it was present during extrusion and not completely dissolved during subsequent solution heat treatment. However, the solution heat treatment and artificial aging regime involved in the T6 temper probably spheroidized this constituent. θ-$CuAl_2$ or its derivative θ' should also be present along grain boundaries although these precipitates were not visible in the SEM or optical microscope. EDS point analyses of the round globular phase is close to stoichiometric θ-$CuAl_2$, Table 5.4; the discrepancy may be explained by the fact that the θ-$CuAl_2$ phase actually contains slightly less copper than given by its formula [11] and that EDS analysis may invoke electron interaction with the surrounding matrix. Electron interaction with the matrix may also explain the detection of silicon, which is expected to have a low solubility in $CuAl_2$ [11,202]. There is further evidence for the presence of θ-$CuAl_2$ in the XRD pattern of this alloy, Figure 5.10, which contains peaks corresponding to this phase.

Table 5.3 – Chemical analysis of AA2014-T6 by ICP-OES (wt%). Balance Al.

Composition	Cu	Mg	Si	Mn	Fe	Cr	Zn	Ti	Others (each)	Others (total)
Nominal[a]	3.9-5.0	0.20-0.8	0.50-1.2	0.40-1.2	0.7	0.10	0.25	0.15	0.05	0.15
Analysed	4.73	0.49	0.56	1.15	0.36	0.07	0.20	0.02	–[b]	0.12

[a]Maximum unless shown as a range

[b]Bi: 0.03; Ca: 0.01; Ga: 0.01; K: <0.01; Na: 0.01; Ni: 0.03; P: <0.01; Pb: 0.01; V: 0.01

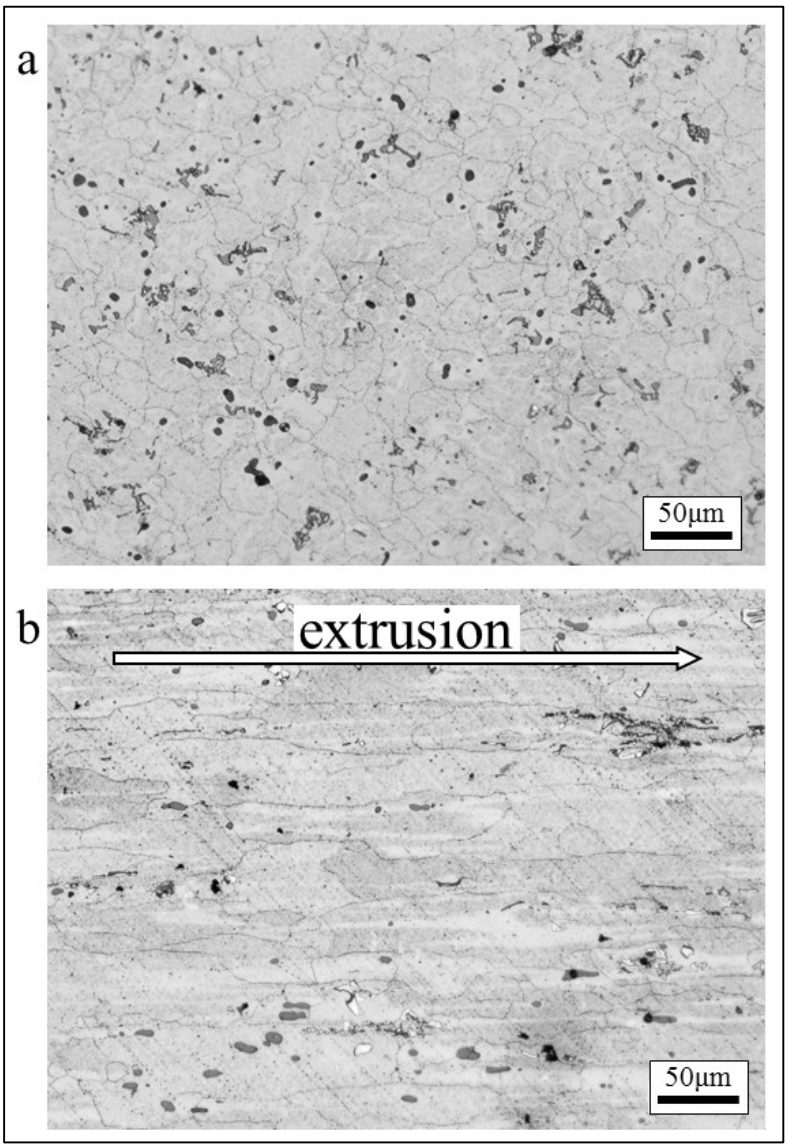

Figure 5.7 – Optical micrographs of AA2014-T6 (etched): (a) transverse plane; (b) longitudinal plane.

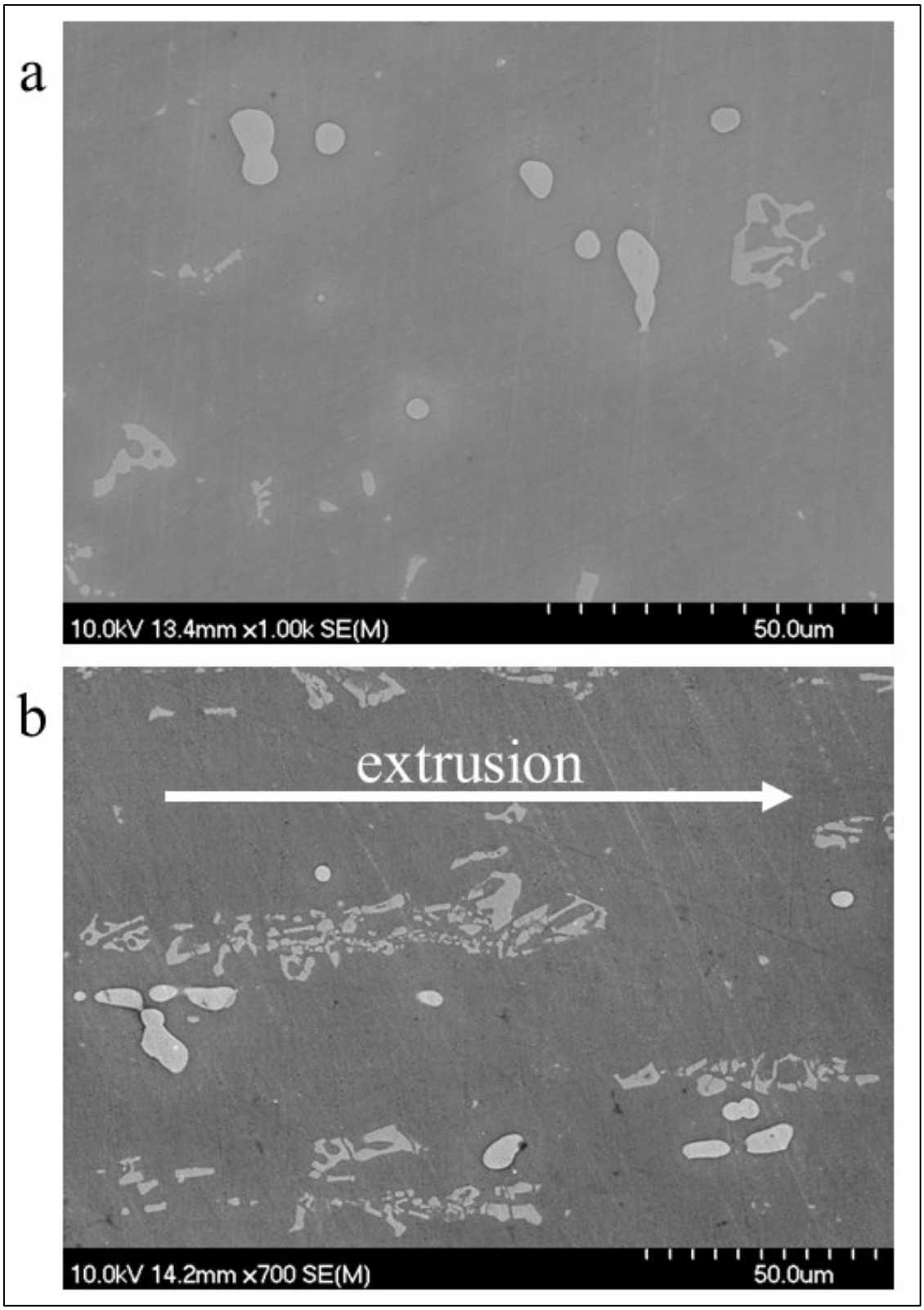

Figure 5.8 – SEM micrographs of AA2014-T6: (a) transverse plane; (b) longitudinal plane.

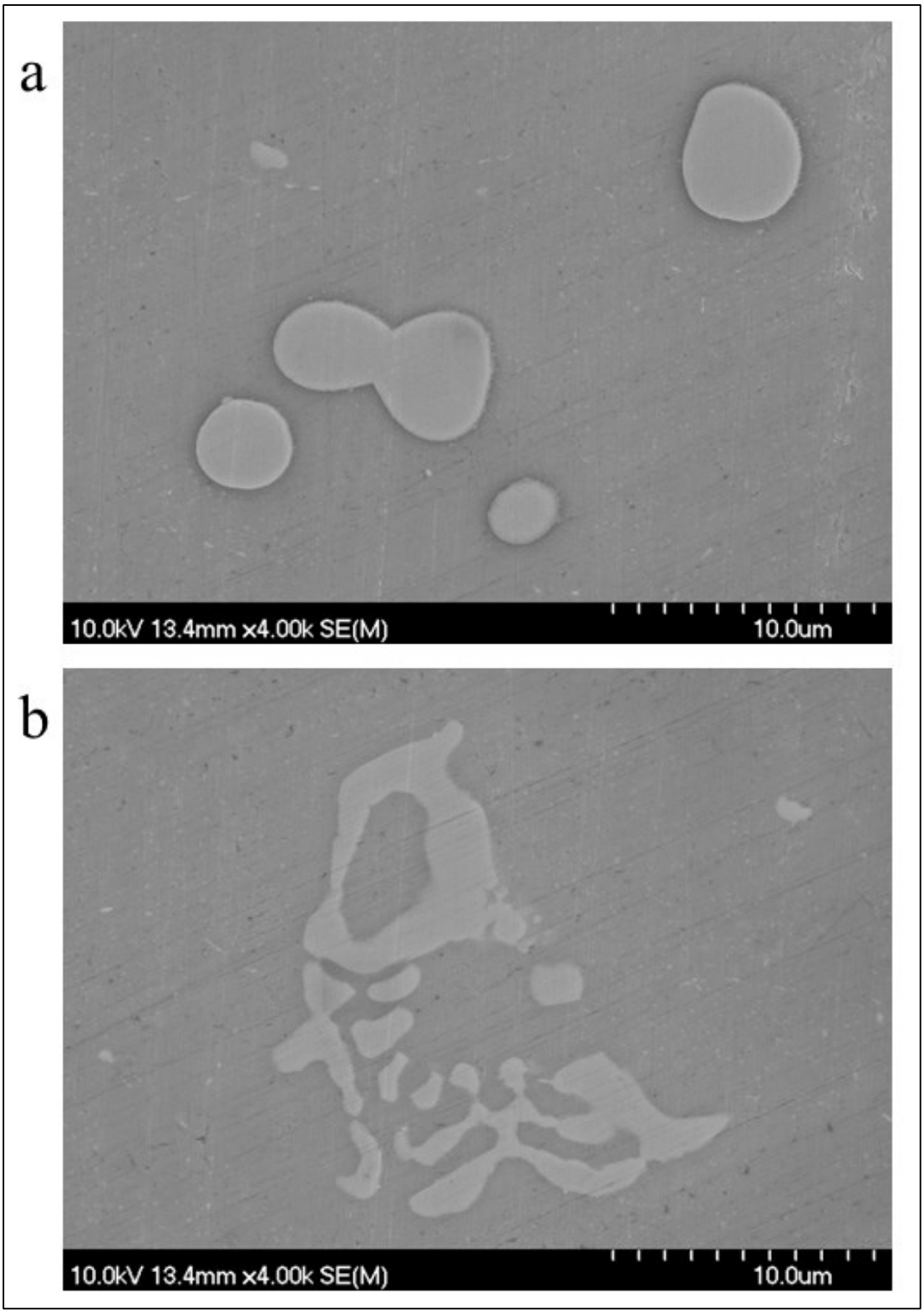

Figure 5.9 – SEM micrographs of constituents in AA2014-T6 (transverse plane): (a) round, globular constituent; (b) Chinese script constituent.

Table 5.4 – Summary of EDS point analyses of major phases in AA2014-T6 (wt%).

Phase	EDS Point Analysis (wt%)[a]							
	Al	Cu	Mg	Si	Mn	Fe	Cr	*No.* of points
Matrix	93.2±0.9	5.0±0.1	0.4±0.0	0.7±0.3	0.7±0.6	–	–	7
Round, globular[b]	48.7±2.2	51.0±2.1	–	0.3±0.1	–	–	–	9
Chinese script[c,d]	61.2±3.9	7.5±0.7	–	6.4±0.5	10.2±1.7	14.4±1.6	0.3±0.1	12

[a]Values are given as mean ± standard deviation
[b]$CuAl_2$ formula: Al: 45.9; Cu: 54.1
[c]$(CuFeMn)_3Si_2Al_{15}$ formula: Al: 62.1-64.7; Si: 8.6-9.0; (CuFeMn): 26.3-29.3
[d]$(CuMnFe)_3SiAl_{12}$ formula: Al: 59.7-62.7; Si: 5.2-5.4; (CuFeMn): 31.9-35.1

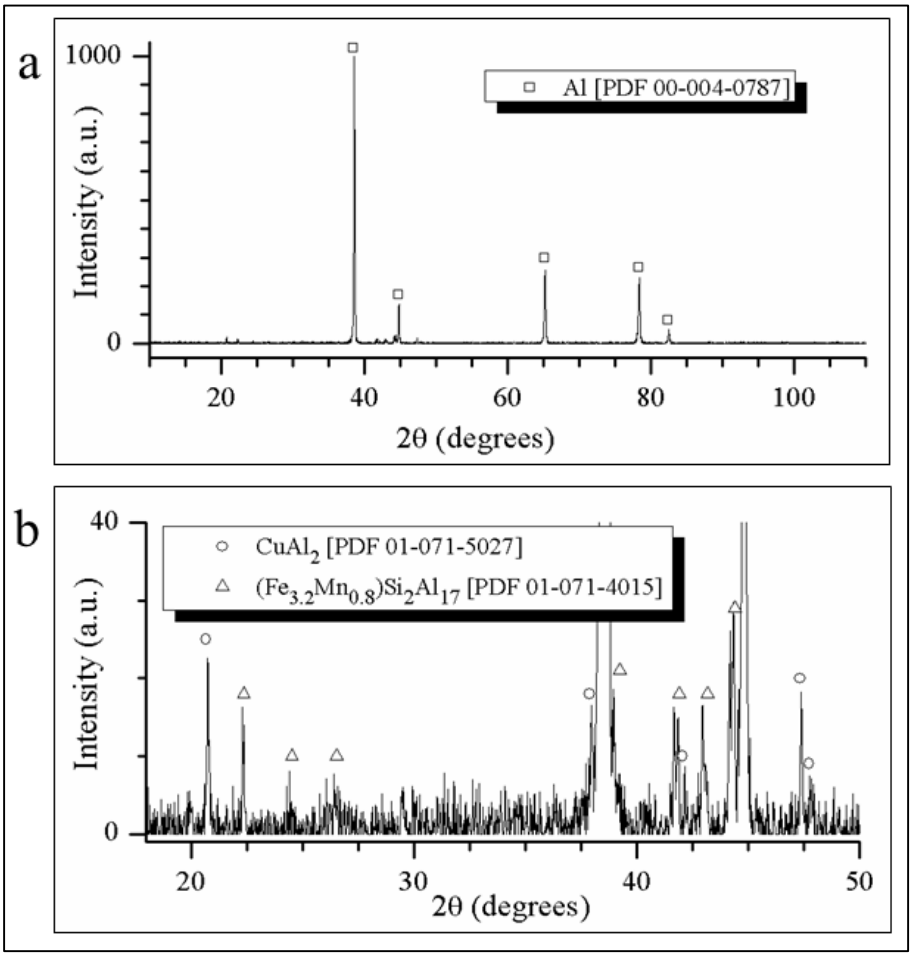

Figure 5.10 – XRD pattern of AA2014-T6 (transverse plane): (a) full pattern; (b) close-up of smaller peaks.

The Chinese script phase appears to be fragmented and aligned in the direction of working, Figure 5.8, indicating this phase was present during extrusion and its morphology was not significantly affected by subsequent heat treatment – suggesting the presence of elements which have low solubility in aluminum. This phase was found by EDS analyses, Table 5.4, to consist of aluminum, copper, iron, manganese, silicon, and a small amount of chromium. The phase relations involving these elements are complex and convoluted by the ability of intermetallics to take other elements in to solution. There are no universally agreed upon formulae and compositional information for these intermetallics, so a conclusive identification of the Chinese script phase is beyond the scope of this work. Based on the available evidence a probable candidate is the α-AlFeMnSi phase which has been described by the formula $(FeMn)_3Si_2Al_{15}$ or $(FeMn)_3SiAl_{12}$ [11,202], and is the result of some miscibility between the α-AlFeSi (Fe_2SiAl_8) and α-AlMnSi ($Mn_3Si_2Al_{15}$ or Mn_3SiAl_{12}) phases. The α-AlFeMnSi phase may contain chromium in place of iron and manganese, and may also absorb copper into solution as $(CuFeMn)_3Si_2Al_{15}$ or $(CuMnFe)_3SiAl_{12}$ [11]. These formulae are in approximate agreement with the EDS analyses of the Chinese script phase, Table 5.4. Copper may also replace silicon in α-AlFeMnSi [11] which may partly explain the discrepancy between the analysed silicon and that given by the formulae in Table 5.4.

Referring to the XRD pattern, Figure 5.10, there is a good match in the powder diffraction database for an intermetallic of the formula $(Fe_{3.2}Mn_{0.8})Si_2Al_{17}$ which has a composition closely corresponding to α-AlFeMnSi (*i.e.* $(FeMn)_3Si_2Al_{15}$ or $(FeMn)_3SiAl_{12}$), the same crystal structure as α-AlFeMnSi (cubic) [11], and a lattice parameter within the possible confines for α-AlFeMnSi given by [11]. The only inconsistency from the powder diffraction file then is the presence of copper and

chromium in the Chinese script. In their amounts detected by EDS both of these elements have been found to stabilize the cubic structure of α-AlFeMnSi [203] and presumably would not drastically alter the diffraction pattern of this intermetallic.

The matrix was found by EDS point analyses, Table 5.4, to contain a large amount copper, in fact an amount exceeding the bulk content of the alloy, Table 5.3, indicating there must be electron interaction with surrounding copper-rich constituents during analysis. In addition to θ' and θ-$CuAl_2$, there is expected to be Q-phase ($Cu_2Mg_8Si_6Al_5$) precipitates present in this alloy [11,202] which could be distributed throughout the matrix as finer precipitates and contributed to the excess copper detection. Upon close examination of Figure 5.9 there seems to be lighter-coloured areas in contrast with the matrix that are of smaller size than the round, globular θ-$CuAl_2$ and may possibly be another type of precipitate, for instance Q-phase. This would also explain the detection of silicon and magnesium in the matrix, Table 5.4, although these elements may be present as Mg_2Si as well or in the case of magnesium in solid solution with aluminum. There was also manganese detected in the matrix, Table 5.4, which may not be the result of electron interaction with the Chinese script phase as iron was not simultaneously detected. A source of manganese is potentially $Cu_2Mn_3Al_{20}$ or $(CuMn)Al_6$ dispersoids which are expected to be present in this alloy [202], however it is not clear if this would contribute manganese X-ray peaks to the extent observed. It is worth pointing out that these particular products contained manganese and silicon contents near the maximum and minimum permissible values, respectively, Table 5.3, which may have influenced the amount of manganese-containing dispersoids formed.

CHAPTER 6 P/M PROCESSING OF ALUMIX 123

The effect of compaction pressure on the green and sintered density of Alumix 123 is shown in Figure 6.1. Laboratory sintered specimens were prepared using a variety of compaction pressures in order to study the effect of this parameter on green density, sintered density, and corrosion behaviour. The highest practical green and sintered density is achieved with a compaction pressure of 300MPa, Figure 6.1; higher compaction pressures lead to no practical increase in green or sintered density and only serve to increase die wear. With this information, and recommendations from industry, all industrially sintered specimens were prepared using a compaction pressure of 300MPa. The industrially sintered material possessed a superior sintered density compared to the laboratory sintered material, Figure 6.1, which was probably due to the use of pre-heated nitrogen in the sinter zone or better control and uniformity of temperature in the industrial furnace.

Under the usual sintering conditions, the highest sintered density attainable for Alumix 123 was approximately 92% theoretical density, Figure 6.1, which is comparable to other laboratory findings [55,199,200,204] where Alumix 123 was sintered at 590-600°C for 20-30 minutes. Extending the isothermal sintering time to 60 or 120 minutes does not significantly increase densification [199,200]. The low sintered density of Alumix 123 can be interpreted in terms of the swelling of compacts as a result of sintering, Figure 6.2, which has been attributed to expansion and phase transformations in the lubricant [55] and formation of transient liquids of the Al-Mg, Al-Cu-Mg, and Al-Cu-Mg-Si systems [200] during heating to the isothermal sintering temperature.

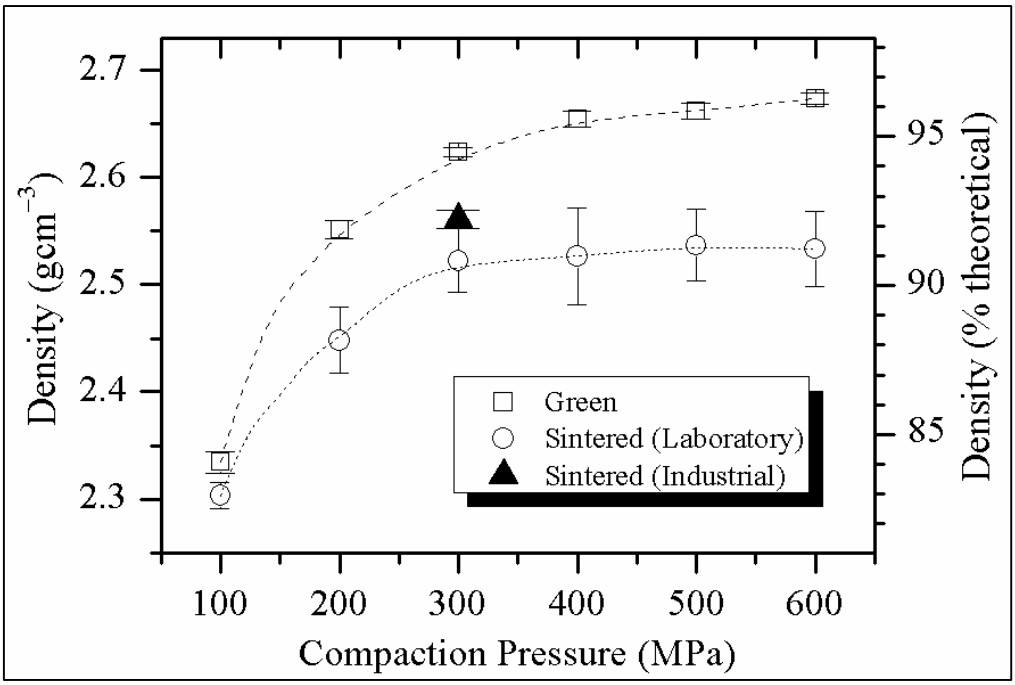

Figure 6.1 – Green and sintered density of Alumix 123 as a function of compaction pressure.

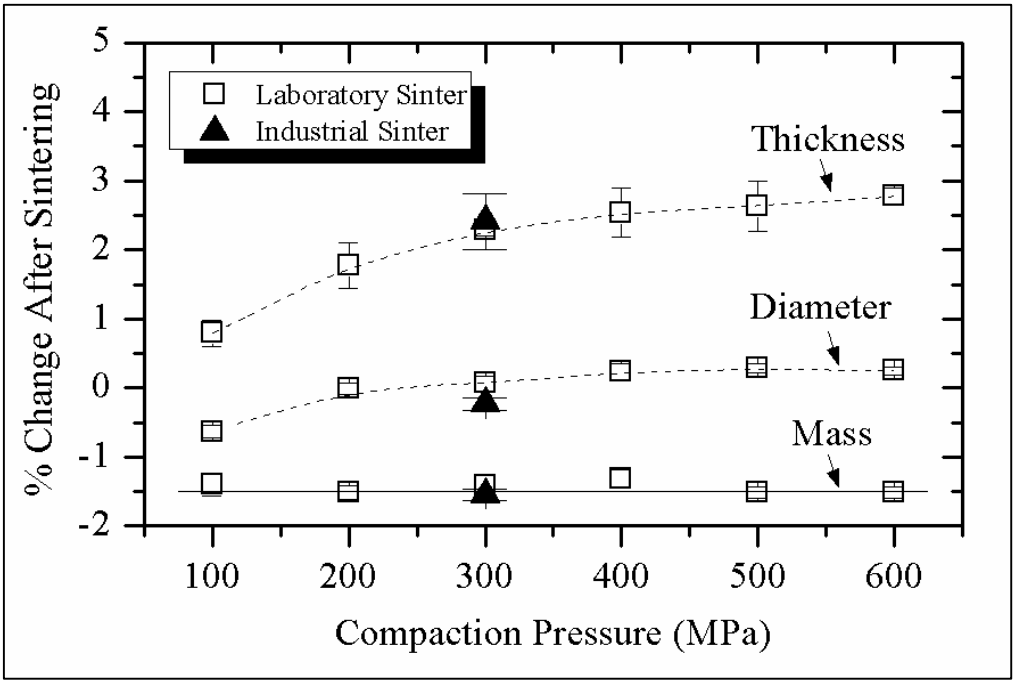

Figure 6.2 – Sintering-induced dimensional and mass changes measured for green compacts of Alumix 123 as functions of compaction pressure.

The swelling of compacts occurred principally along the axis of uniaxial pressing, Figure 6.2, which could have been related to the contact area between metallic particles and their preferential orientation along the axis perpendicular to uniaxial pressing [55]. Expansion and phase transformations of the lubricant in the gap between contacting metallic particles would then lead to the preferential expansion of compacts along the axis of uniaxial pressing [55]. In a similar manner, if the contact area between the elemental alloy or master alloy additions and the base elemental aluminum powder was larger along the axis perpendicular to uniaxial pressing, then liquid phases may have preferentially formed and spread in this direction, leading to the increased swelling of compacts along the axis of uniaxial pressing. This mechanism is supported by Al-Cu pressed wire model experiments [86] where pure copper wire was uniaxially compacted amongst pure aluminum wire while oriented along the axis perpendicular to uniaxial pressing. During sintering, the Al-Cu eutectic penetrated rapidly along the axis perpendicular to uniaxial pressing but caused a much larger swelling along the axis of uniaxial pressing [86].

The distribution of porosity in Alumix 123-T1 was highly non-uniform, Figure 6.3; there was less porosity in the center of the compacts and along the face which was adjacent to the mesh belt during sintering. This is postulated to be related to the local sintering atmosphere in the area. The oxygen partial pressure near the exterior of compacts was probably higher than in the centre of compacts due to the continuous flow of fresh nitrogen which contained oxygen and water vapour contaminants that led to oxidation and disturbed the sintering and densification mechanisms of Alumix 123 in these areas.

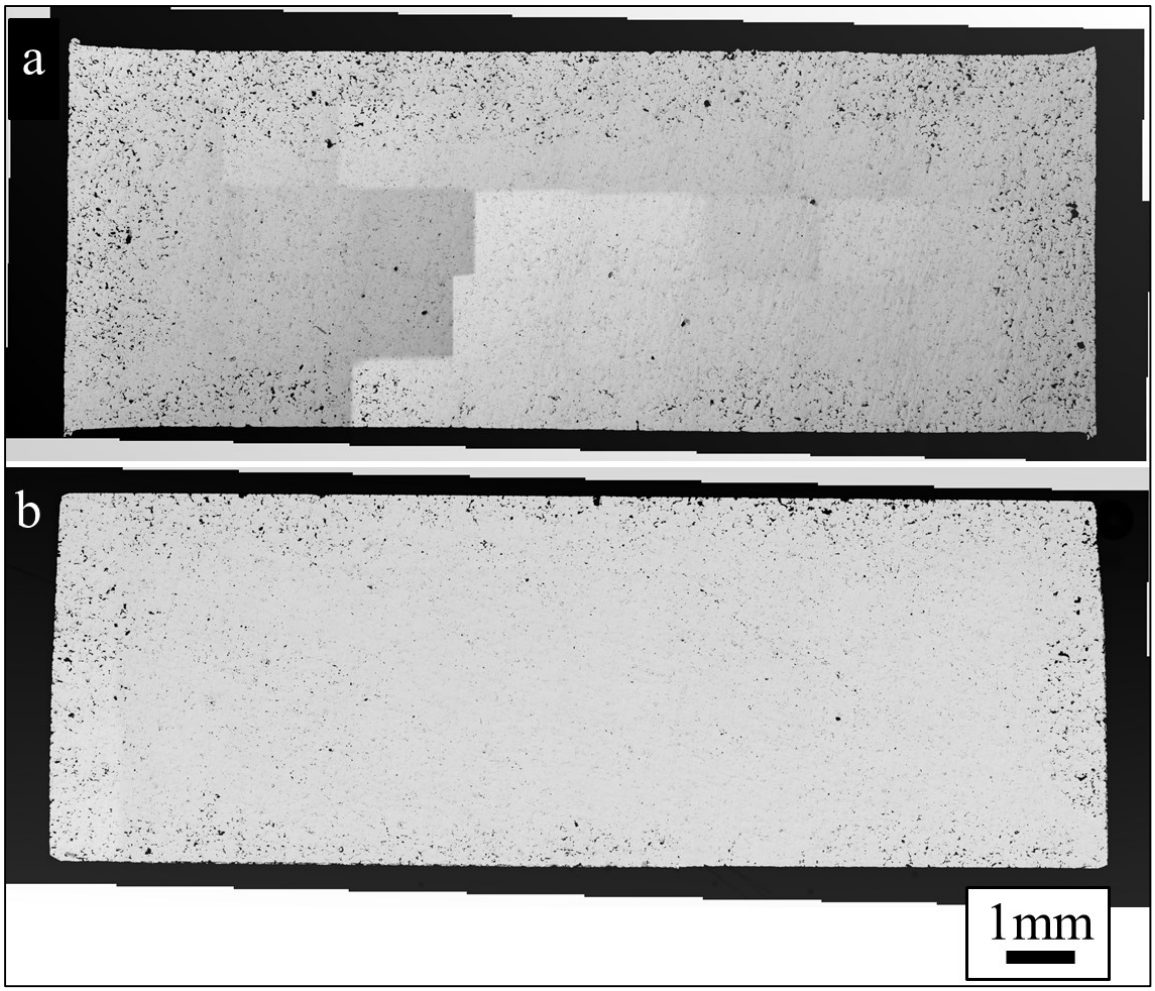

Figure 6.3 – Optical micrographs stitched together to show the distribution of porosity throughout the longitudinal plane of industrially sintered (unetched): (a) Alumix 123-T1; (b) Alumix 123-T2(5%).

As expected, the sizing operation reduced the total amount of porosity in Alumix 123-T2, Figure 6.3. The effect of sizing pressure on reduction in thickness is shown in Figure 6.4. It should be pointed out that the sizing operation here was analogous to open die forging. Due to dimensional instability as a result of sintering, specimens were sized in a larger diameter die (30mm) than used for powder compaction meaning no force was exerted on specimens in the radial direction during sizing. This explains the large amount of plastic deformation in specimens at high sizing pressures, Figure 6.4. The sizing pressures in Figure 6.4 are reported with respect to the original compact diameter (15mm).

The surface of Alumix 123-T1 and Alumix 123-T2(5%) in the 'as-sintered' and 'as-sized' condition, which was the condition of these materials in subsequent electrochemical testing, are shown in Figure 6.5. The surfaces were rough, highly non-planar, and contained areas which appeared of darker contrast in the SEM, Figure 6.5. These darker areas were found to contain significant carbon, oxygen, and sometimes nitrogen by EDS analyses and are believed to be remnants from the ethylene bisstearamide (EBS) lubricant which may have redeposited on the surface of compacts during the de-lubrication stage of sintering.

The surface of Alumix 123 compacts was found by EDS analyses to be enriched with carbon (*ca.* 6wt%), oxygen (*ca.* 8wt%), and magnesium (*ca.* 2wt%), as compared to EDS analyses of polished compacts. The carbon and oxygen concentration may have been due to the continuous flow of fresh nitrogen over the exterior of compacts during sintering. The fresh nitrogen contains a small amount of contaminants such as carbon dioxide, oxygen, and water vapour which may have reacted with the compacts and incorporated into a refractory layer.

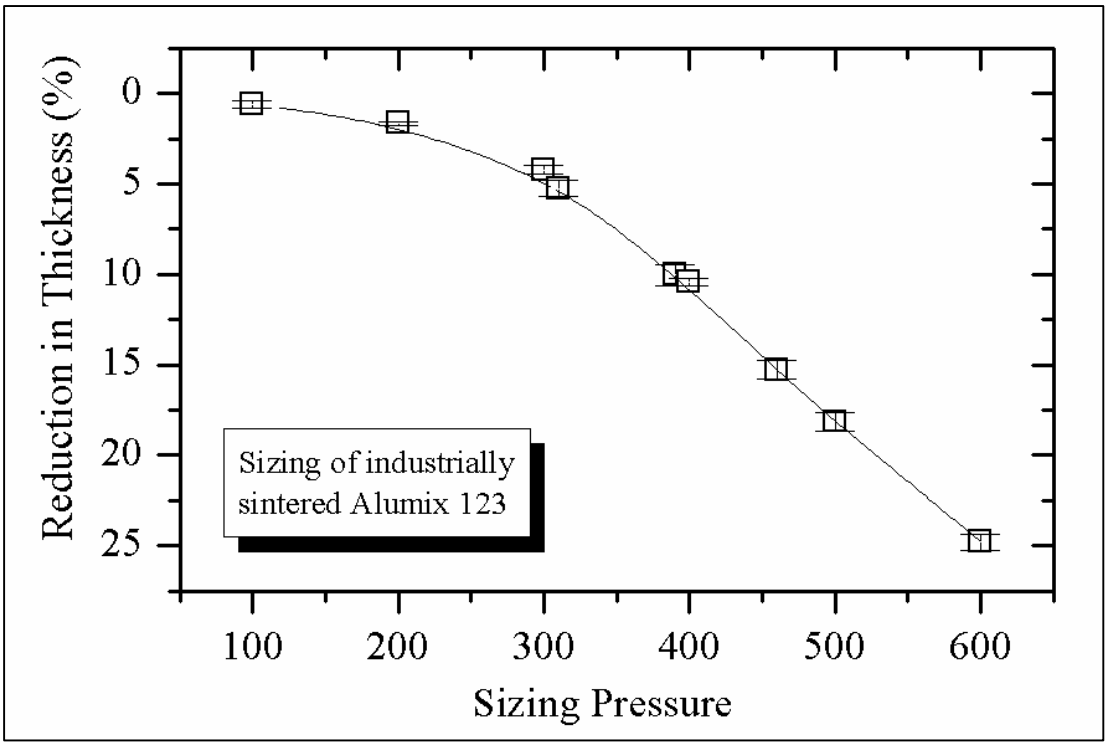

Figure 6.4 – Sizing curve for industrially sintered Alumix 123 specimens. All specimens were initially compacted at 300MPa.

The magnesium on the surface of compacts was probably in the oxidized state and its concentration could be related to its high vapour pressure or affinity for oxygen in aluminum P/M systems. The first liquid phase to form during sintering of Alumix 123 corresponds to the fusion of the magnesium-containing master alloy particles to a magnesium-rich liquid phase [200] and the evaporation and transport of magnesium in the vapour phase may have led to its eventual oxidation and deposition near the surface of compacts. Magnesium also acts as a local oxygen getter and disrupts the aluminum oxide layer via formation of Al_2MgO_4 [1] and the flow of fresh nitrogen over the exterior of compacts continually introduces more oxygen to the area and may have led to the continued migration and oxidation of magnesium on the surface of compacts.

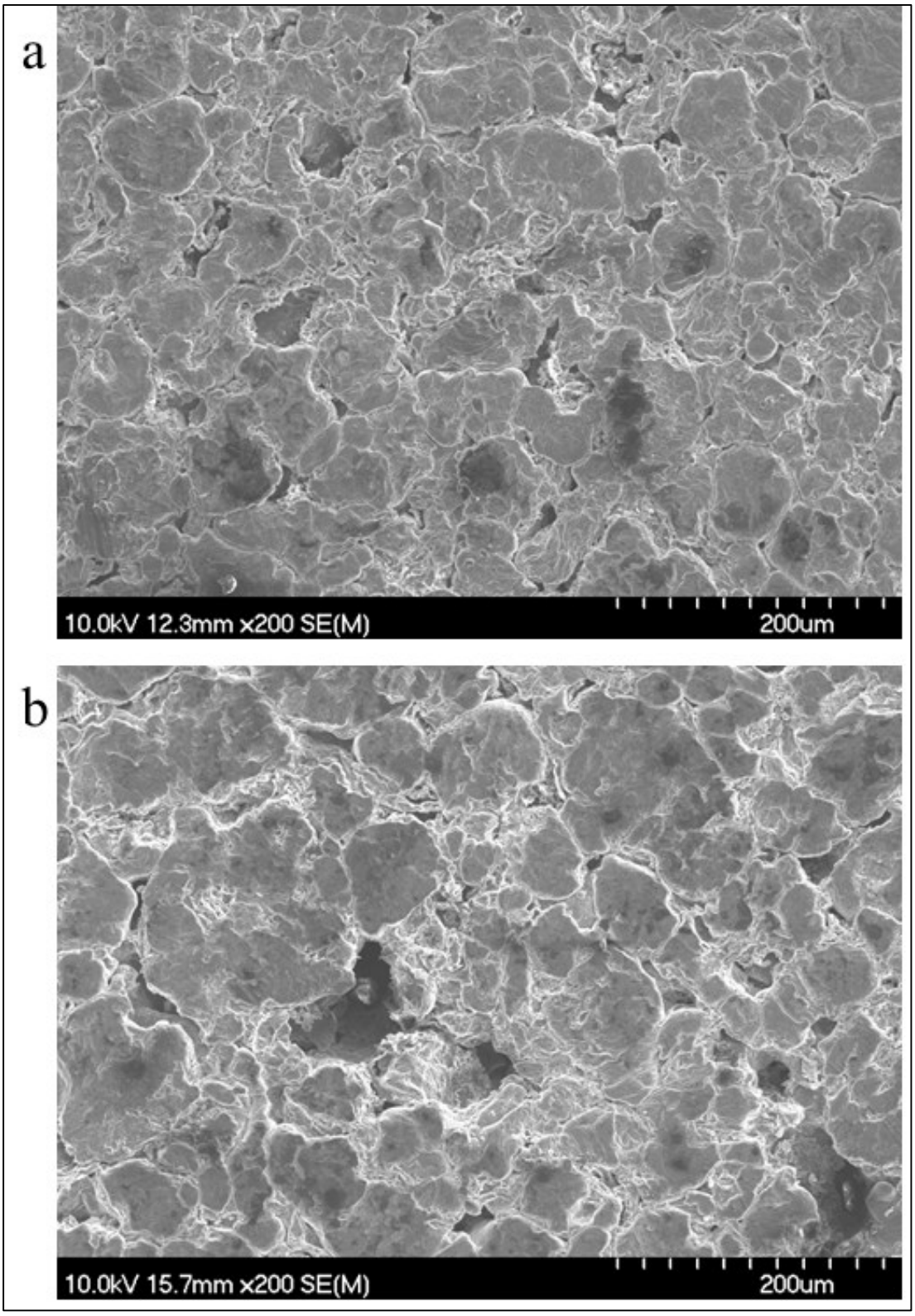

Figure 6.5 – SEM micrograph of industrially sintered: (a) Alumix 123-T1; (b) Alumix123-T2(5%) with no polishing.

Optical and SEM micrographs of polished Alumix 123-T1 compacts, Figure 6.6 and Figure 6.7, showed a polyhedral grain structure with secondary phases distributed predominantly along grain boundaries. Three types of intermetallics were identified in the microstructure of industrially sintered Alumix 123-T1, Figure 6.8. The composition of the intermetallics, Table 6.1, as well as their morphology and location in the microstructure suggest some of them may have formed as a result of solidification or decomposition of the persistent liquid phase present during sintering.

The copper-rich intergranular phase contained less copper than would be expected for $CuAl_2$ and additionally contained magnesium and silicon in amounts beyond what would be expected for $CuAl_2$ in solid state equilibrium [11]. This phase may have formed from the persistent liquid phase present at the sintering temperature and may not be in equilibrium as a result of the rapid cooling experienced at the end of the sinter cycle. There was evidence of $CuAl_2$ in the XRD pattern of Alumix 123-T1, Figure 6.9. Other investigators have also identified $CuAl_2$ in Alumix 123-T1 by XRD [200,204]. The presence of Al-Cu-Mg-Si constituents along grain boundaries has also been noted in Alcoa's 201AB alloy (analogous to Alumix 123) [3,51,75].

The iron-containing intergranular constituents were more rounded and compact than the copper-rich intergranular ones and contained predominantly aluminum, iron, silicon, and copper. Their morphology and composition somewhat matched the α-AlFeSi phase (Fe_2SiAl_8) which is typically present as a Chinese script [11]. Other ternary Al-Fe-Si and Al-Cu-Fe phases are usually present as platelets or needles [11]. Aluminum, iron, silicon, and copper do not usually form compounds together [11] and it may be that this phase solidified far from equilibrium during the rapid cooling from the sintering temperature. Iron is known to segregate to the liquid phase during sintering [85,200,204].

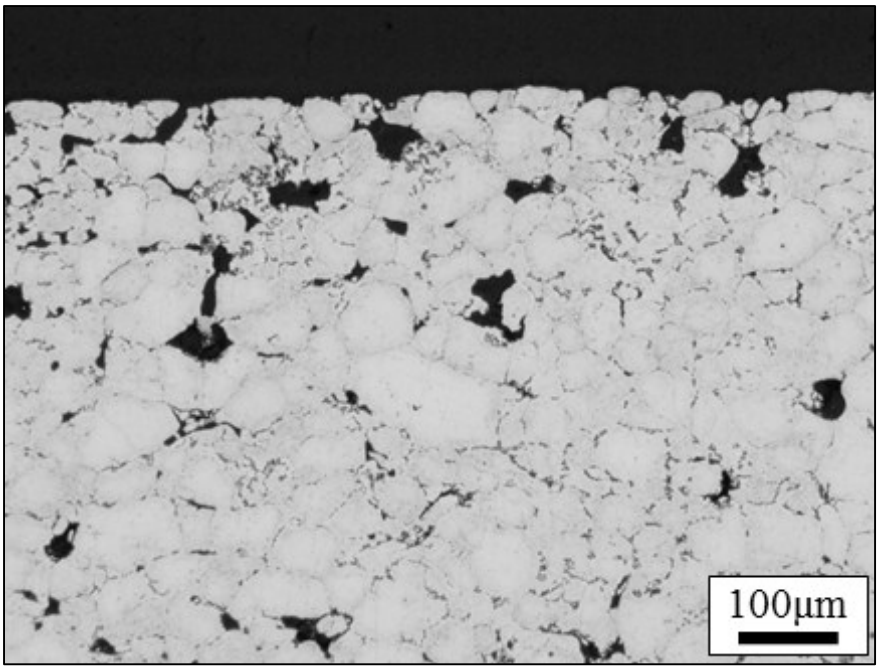

Figure 6.6 – Optical micrograph of industrially sintered Alumix 123-T1 (etched). The micrograph was taken in longitudinal plane near the edge of the sample.

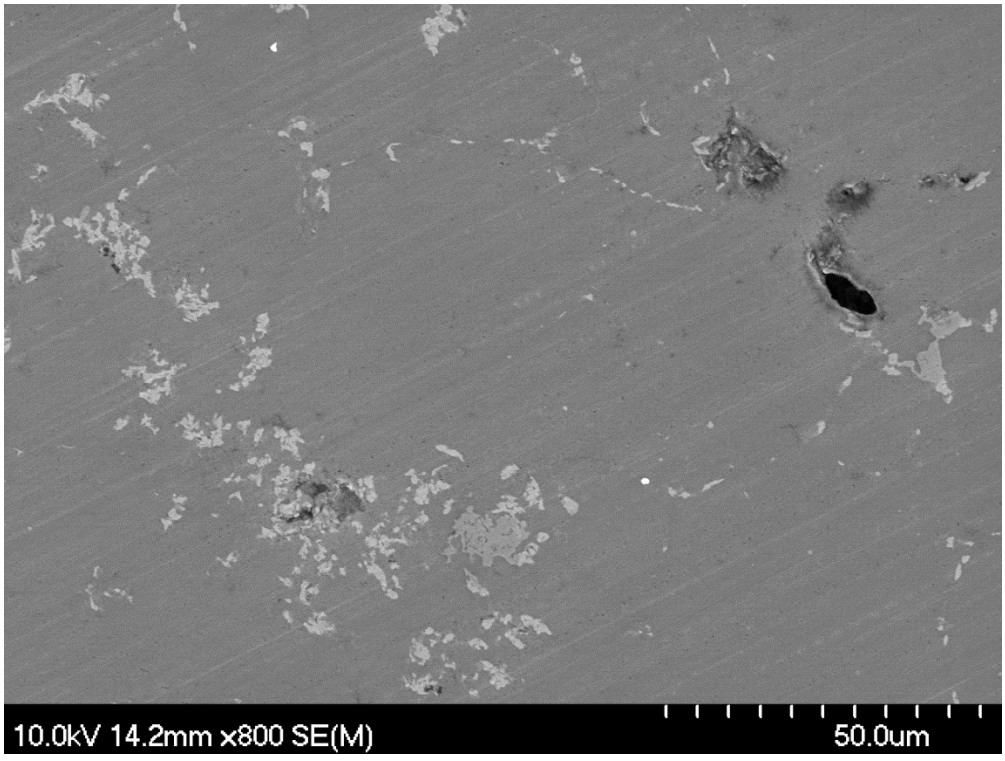

Figure 6.7 – SEM micrograph of industrially sintered Alumix 123-T1.

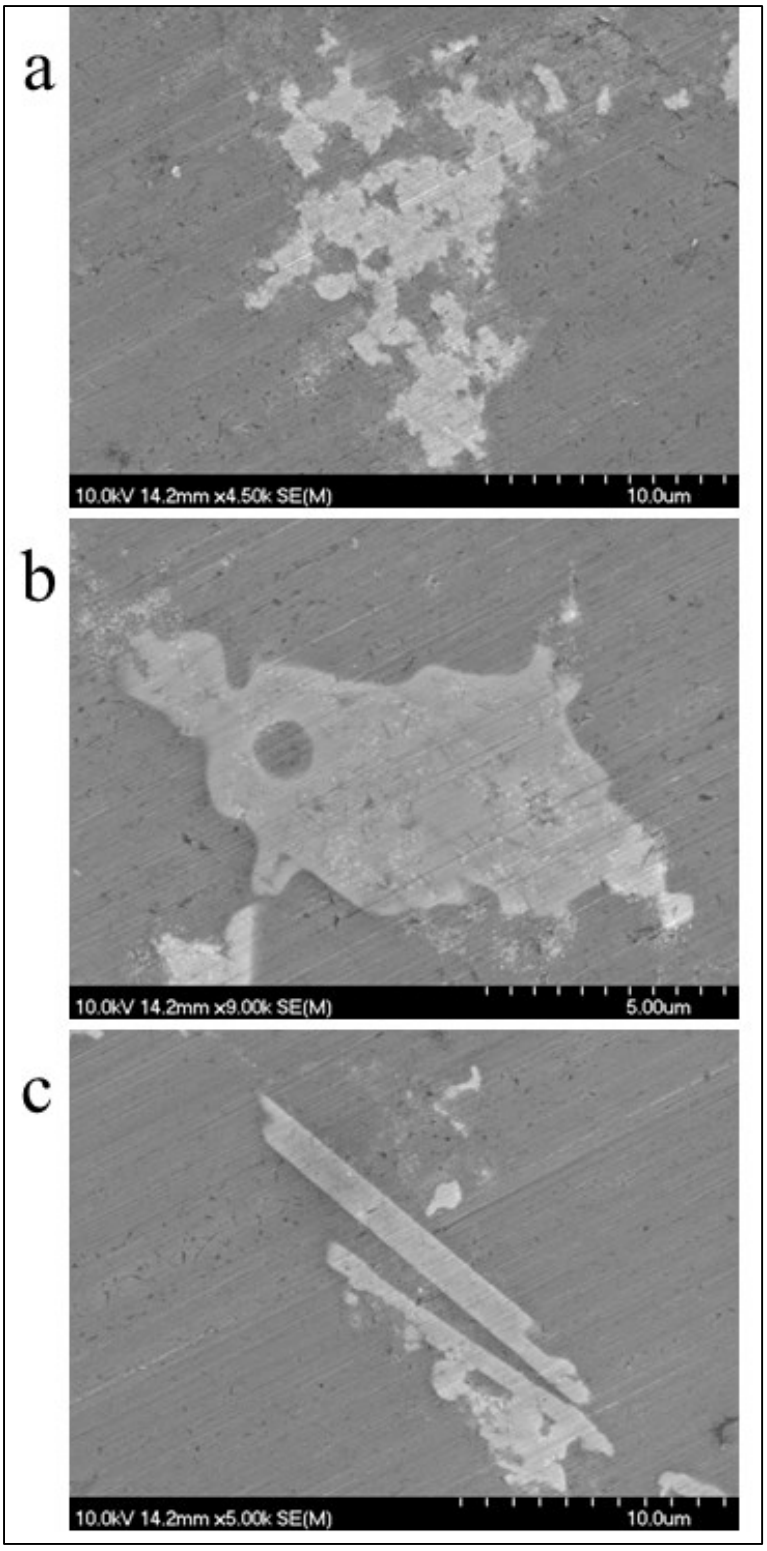

Figure 6.8 – SEM micrographs of constituents in industrially sintered Alumix 123-T1: (a) copper-rich intergranular; (b) iron-containing intergranular; (c) iron-containing needles.

Table 6.1 – Summary of EDS point analyses of major phases in industrially sintered Alumix 123-T1 (wt%).

Phase	EDS Point Analysis (wt%)[a]					
	Al	Cu	Mg	Si	Fe	*No.* of points
Matrix	94.3±0.5	4.9±0.4	0.2±0.1	0.6±0.1	–	9
Cu-rich intergranular[b]	57.0±3.9	40.1±3.9	2.0±0.5	0.9±0.5	–	23
Fe-containing intergranular[c]	49.4±2.2	13.5±0.6	1.3±0.7	6.7±0.3	29.1±2.3	14
Fe-containing needles[d]	48.2±0.7	34.6±0.5	–	0.7±0.2	16.5±0.2	3

[a]Values are given as mean ± standard deviation
[b]$CuAl_2$ formula: Al: 45.9; Cu: 54.1
[c]Fe_2SiAl_8 formula: Al: 60.6; Fe: 31.6; Si: 7.8
[d]Cu_2FeAl_7 formula: Al: 46.9; Cu: 36.9; Fe: 16.2

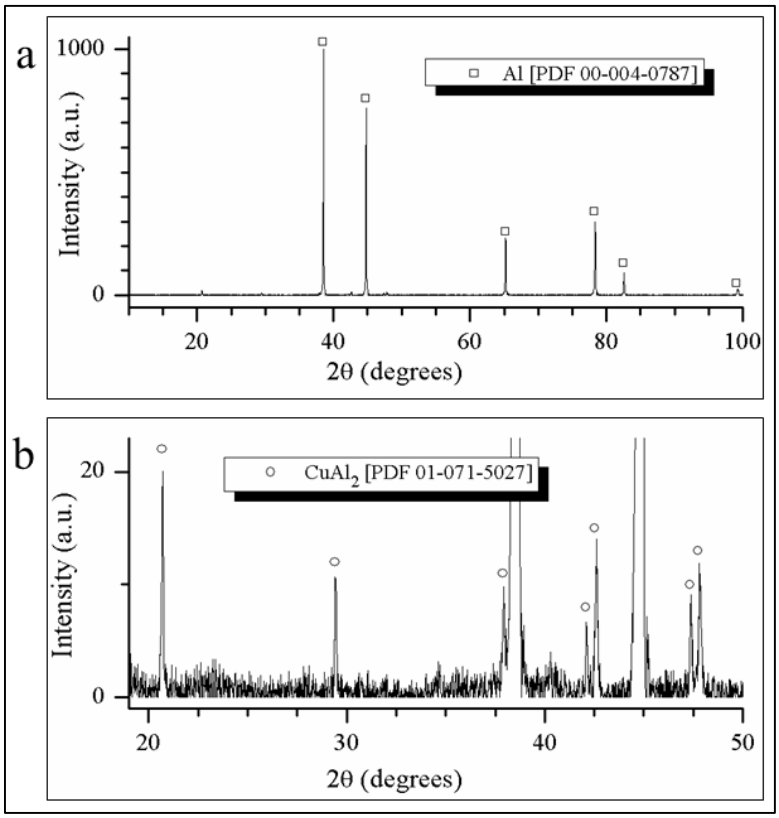

Figure 6.9 – XRD pattern of industrially sintered Alumix 123-T1 (polished): (a) full scan; (b) close up of smaller peaks.

The iron-containing needle-like constituents had a morphology and composition closely matching that of the β(FeCu) phase (Cu_2FeAl_7) [11]. This phase may have formed in areas which were isolated from magnesium and silicon during sintering or in areas of the compact that experienced slower cooling rates after sintering. These constituents were scarcely found and are not considered to be a major phase present in Alumix 123-T1. Other investigators have noticed needle-like iron-containing constituents in Alumix 123, however only after solution heat treatment [200,204].

The matrix was found by EDS point analyses to contain copper, magnesium, and silicon, Table 6.1, in amounts which could be related to their solubilities in solid aluminum at the isothermal sintering temperature. The amount of copper detected exceeds the bulk copper content of the alloy which may indicate there was electron interaction with surrounding copper-rich phases during EDS analyses.

CHAPTER 7 CORROSION BEHAVIOUR OF ALUMIX 123 P/M ALLOY AND AA2014-T6. PART I: OCP AND POTENTIODYNAMIC POLARIZATION

W.D. Judge[1], D.P. Bishop[1], and G.J. Kipouros[2,*]

[1]Materials Engineering, Process Engineering and Applied Science, Dalhousie University, 1360 Barrington Street, Room F201, Halifax, Nova Scotia, Canada, B3H 4R2

[2]Chemical Engineering, College of Engineering, University of Saskatchewan, 57 Campus Drive, Saskatoon, Saskatchewan, Canada, S7N 5A9

(*Corresponding author: georges.kipouros@usask.ca)

Status: To be submitted to *Journal of the Electrochemical Society*

The following experimental procedures, results, and discussions were completed by W.D. Judge with reviewer and editorial roles played by D.P. Bishop and G.J. Kipouros.

ABSTRACT

The corrosion behaviour of the commercial aluminum powder metallurgy (P/M) alloy 'Alumix 123' and a compositionally similar wrought alloy, AA2014-T6, has been studied in naturally aerated 3.5wt% NaCl through open circuit potential (OCP), cathodic polarization, and cyclic potentiodynamic polarization experiments, and the corrosion morphology at open circuit conditions characterized by scanning electron microscopy (SEM) and energy dispersive X-ray spectroscopy (EDS). The P/M alloy was sintered in an industrial setting and was tested in either the 'as-sintered' condition (T1 temper) or after a standard sizing operation (T2 temper). The OCP of Alumix 123-T1 stabilized at more negative values, which is believed to be a reaction to a reduction in cathode area or depassivation induced by propagating crevice corrosion within residual porosity. In this state, the corrosion of Alumix 123-T1 was partially under anodic control and proceeded with the cathodic evolution of hydrogen. The OCP of Alumix 123-T2 and AA2014-T6 stabilized at the pitting potential where corrosion was mostly under cathodic control and proceeded with the cathodic reduction of oxygen. In the P/M materials pitting was not associated with copper- or iron-rich intermetallics, this was attributed to the refractory layer formed as a result of the sintering process.

Keywords: aluminum alloy; corrosion; electrochemistry; powder metallurgy; crevice corrosion; intermetallics; Alumix 123; AA2014

7.1 INTRODUCTION

The ‘press-and-sinter’ powder metallurgy (P/M) process is a net- or near-net-shape technology which enables the mass production of small and complex parts on an economic scale superior to conventional die casting and machining operations. The process typically involves the uniaxial die compaction of a powder pre-mix in to a friable ‘green compact’ of net- or near-net-shape, which is then sintered at elevated temperature to form a metallurgically coherent body and may be subject to additional secondary operations such as heat treatment, coining, or sizing. Sizing, in which a sintered body is repressed in a die to improve dimensional tolerances, is a common secondary operation in commercial P/M due to slight dimensional changes which are induced by the sintering process.

In aluminum P/M alloys, the processing history is indicated by temper designations in a similar manner to conventional aluminum alloys, however with slight modifications to temper definitions [7]. The T1 temper, which traditionally represents wrought aluminum product which has been cooled from hot working, is used to denote P/M aluminum product which has been cooled from the sintering temperature. Likewise, the T2 temper, which traditionally represents wrought aluminum product which has been cooled from hot working and subsequently cold worked, is used to denote P/M aluminum product which has been cooled from the sintering temperature and sized.

Commercial P/M aluminum has been utilized in a variety of products including business machines, consumer appliances, portable power tools, and audio-visual equipment [1,2]; sometimes with production rates in excess of 1 million parts per month [2]. However, the most notable applications have been in the automotive industry [1,27,28,73,205]. In particular, the camshaft bearing caps for consumer automobiles

[27,73], where over 50 million have been produced since production began in 1991 [205] – in some instances resulting in 35% cost savings over traditionally produced caps [28]. In the 2000s, automotive P/M production declined due to financial and energy crises which saw North American automobile manufacturers lose market share to importers which do not utilize as many P/M parts [206]. Even in North America, P/M aluminum is produced in tonnages below that of P/M ferrous, cuprous, and nickelous alloys [206] which is arguably not representative when considering the prevalence of aluminum as a cast or wrought material. The aluminum P/M industry has great potential for growth, especially in foreign markets such as China and India, but this is dependent upon the improvements in material properties and process design generated by current research and development efforts [1]. Most efforts have focused on improving established material properties including tensile strength, wear resistance, and fatigue [1]. The corrosion resistance of P/M aluminum has received much less attention yet is an important consideration for design engineers and should not be considered analogous to the behaviour of conventional aluminum alloys. For example, in ferrous P/M alloys there are unique corrosion mechanisms operating which are absent in wrought materials of the same composition [207-209].

In this work the corrosion behaviour of the commercial P/M aluminum alloy 'Alumix 123' has been studied by electrochemical methods in naturally aerated 3.5wt% NaCl electrolyte. With the exception of recent work from this laboratory [4], prior corrosion evaluations of P/M aluminum have been restricted to salt spray tests [5-7], which only assign a letter rating of 'A' through 'E' based on specimen appearance. The aim of the electrochemical investigations is to identify fundamental corrosion mechanisms, and to provide quantitative thermodynamic and kinetic information which

can be used to predict material performance and design systems of corrosion prevention and inhibition. The corrosion behaviour of a compositionally similar wrought alloy, AA2014-T6, has been studied simultaneously to provide a comparison to the P/M material and point of reference with the open literature.

7.2 EXPERIMENTAL

7.2.1 Materials

Alumix 123 pre-mix was obtained from ECKA Granules Germany GmbH (Fürth, Bavaria, Germany). The pre-mix contained 1.5wt% admixed 'Licowax C' solid lubricant and was certified to quality control standards for particle size distribution, apparent density, flowability, and chemical composition by the manufacturer. Compositional chemical analysis of Alumix 123 by ICP-OES performed by the Minerals Engineering Centre, Dalhousie University is shown in Table 7.1. Its cumulative size distribution was also measured by laser particle size analysis, performed by the Minerals Engineering Centre, Dalhousie University, and its D_{10}, D_{50}, and D_{90} determined to be 27.1, 95.4, and 196μm, respectively. AA2014-T6 was obtained from Kaiser Aluminum (Jackson, Tennessee, U.S.A.) as a 3.25 inch diameter extruded rod certified to ASTM B211 standard. Compositional chemical analysis of AA2014 by ICP-OES, performed by the Minerals Engineering Centre, Dalhousie University, is included in Table 7.1.

Table 7.1 – Chemical analyses of Alumix 123 and AA2014 by ICP-OES (wt%).

Material	Al	Cu	Mg	Si	Mn	Fe	Others
Alumix 123[a]	Balance	4.57	0.52	0.80	<0.01	0.11	–[b]
AA2014	Balance	4.73	0.49	0.56	1.15	0.36	–[c]

[a]Analysis was performed on a sintered compact
[b]Zn: 0.05; Remaining: 0.16(total), <0.05(each)
[c]Cr: 0.07; Ti: 0.02; Zn: 0.20; Remaining: 0.12(total), <0.05(each)

7.2.2 P/M Processing

Green compacts were prepared by uniaxially compacting 2.5g of powder pre-mix at 300MPa in a 15mm diameter tungsten carbide floating die assembly using an Instron SATEC Series 5594-200HVL load frame (1MN capacity). The average green density was 2.623±0.004gcm^{-3} (94.5±0.2% theoretical) determined in accordance with Metal Powder Industries Federation (MPIF) Standard 42.

Green compacts were sintered at GKN Sinter Metals (Conover, North Carolina, U.S.A.) under a nitrogen atmosphere in a continuous wire mesh belt conveyor furnace employing standard operating procedures for industrial sintering of Alumix 123. Here, the green compacts were placed on a shallow tray which was then placed on the wire mesh belt of the furnace amongst other industrial product. The green compacts were oriented on the tray so that the flat circular face of the compact which was in contact with the lower punch during powder compaction was adjacent to the tray. The average change in height, diameter, and mass as a result of sintering was +2.41±0.40%, –0.23±0.09%, and –1.55±0.08% respectively. The average sintered density was 2.561±0.008gcm^{-3} (92.2±0.3% theoretical) determined in accordance with MPIF Standard 42. The

processing response here was typical for industrial product and consistent with other laboratory investigations [55,199,200,204].

Sintered compacts were sized with the same load frame used for powder compaction but in a larger diameter (30mm) die in order to accommodate the dimensional changes that resulted from the sintering process. Prior to sizing, sintered compacts were carefully deburred by hand against SiC paper. Sizing fluid was provided by GKN Sinter Metals (Conover, North Carolina, U.S.A.). Sintered compacts were fully submersed in sizing fluid and then sized at 310MPa which corresponded to a 5% reduction in height. During sizing, the compacts were oriented so that the flat circular face of the compact that was in contact with the lower punch during powder compaction was in contact with the lower punch during sizing.

7.2.3 Materials Preparation

Alumix 123 was tested in the 'as-sintered' or 'as-sized' states which are herein denoted by the T1 and T2 temper, respectively. Prior to testing Alumix 123-T1 compacts had to be carefully deburred by hand against SiC paper so that a satisfactory seal and electrical contact could be maintained in the electrode assembly. During testing, compacts were oriented so that the flat circular face that was in contact with the upper punch during powder compaction was in contact with the electrolyte. In the case of Alumix 123-T2, this face also corresponded to that which was in contact with the upper punch during sizing.

AA2014-T6 specimens were prepared by sectioning the extruded rod along the transverse plane in to 4mm thick slices, from which 16mm diameter specimens were extracted using a hole-saw drilled in the longitudinal direction. Hence, during testing, the

transverse plane was in contact with the electrolyte. AA2014-T6 specimens were polished using standard metallographic techniques immediately prior to testing. They were abraded on successively finer grits of wet SiC paper, polished using successively finer oil-based diamond suspensions (to 1μm), degreased ultrasonically in acetone, thoroughly rinsed in deionized water, and dried with a blow dryer.

7.2.4 Electrochemical Testing

All electrochemical tests were conducted at ambient temperature in naturally aerated 3.5wt% NaCl electrolyte which was prepared immediately prior to testing using analytical-grade NaCl (>99.0% assay) and ultrapure 'Type 1' deionized water (>18MΩ·cm). The electrochemical instrumentation consisted of a standard three electrode glass bulb cell (1L capacity) connected to a Princeton Applied Research (PAR) Model 273A EG&G Potentiostat/Galvanostat which incorporated a grounded electrometer and was connected to a desktop computer and controlled via Scribner Associates CorrWare® software. The potentiostat was calibrated by the use of a laboratory-made 'dummy cell.' The glass bulb cell contained a working electrode assembly that exposed a nominal area of $1cm^2$ of the test specimen, two high purity fully dense 6.35mm diameter graphite counter electrodes, and a saturated calomel reference electrode (SCE) brought in close proximity to the working electrode via a Luggin capillary. The reference electrode was from Fisher Scientific – the rest of the electrochemical cell was comprised of the PAR Model K0047 'Corrosion Cell System' and Model K0105 'Flat Specimen Holder.'

The open circuit potential (OCP) of the working electrode was monitored versus time for a period of 2 hours for Alumix 123-(T1, T2) and 1 hour for AA2014-T6. The P/M samples were monitored for a longer period of time because they were highly non-

planar and took longer to equilibrate with the electrolyte. The potential at the conclusion of the test was taken to be the OCP of the specimen. Prior to all potentiodynamic testing, the OCP was monitored and allowed to stabilize for the times indicated above.

During cathodic potentiodynamic polarization the potential of the working electrode was varied continuously at a rate of $0.1667 mVs^{-1}$ from the OCP to $-2.0V_{SCE}$. During cyclic potentiodynamic polarization the potential of the working electrode was varied continuously at a rate of $0.1667 mVs^{-1}$ from $-1.25V_{SCE}$ for Alumix 123-T1 or $-0.875V_{SCE}$ for Alumix 123-T2 and AA2014-T6 until an anodic current density of $0.01 Acm^{-2}$ was reached, upon which the direction of the scan was reversed until a potential of $-1.0V_{SCE}$.

The polarization diagrams were analysed using Scribner Associates CorrView™ software. The corrosion current (i_{corr}) and corrosion potential (E_{corr}) were found by Tafel extrapolation, the passive current (i_{pass}) was taken as the current density immediately prior to breakdown at the pitting potential (E_{pit}), and the repassivation potential (E_{repass}) was taken as the potential where the anodic current density reached a value of 1μA on the reverse scan. The corrosion rate was calculated from i_{corr} in accordance with ASTM G102. The equivalent weight of both alloys was calculated to be 9.29 gram equivalents. The sintered density of Alumix 123-T1 was used for P/M calculations. The density of AA2014-T6 was taken as $2.80 gcm^{-3}$ as per the Aluminum Association.

7.2.5 Materials Characterization

Micrographs were captured using a Hitachi Model S-4700 cold field emission scanning electron microscope (SEM) containing an integrated Oxford INCA X-Max^N 80mm silicon drift detector for energy dispersive X-ray spectroscopy (EDS). The SEM

was operated with a 10kV accelerating voltage and 20μA emission current for imaging whereas a 20kV accelerating voltage and 10μA emission current was implemented for EDS analyses. Immediately after corrosion testing, specimens were thoroughly rinsed with deionized water and dried with a blow dryer. Prior to analysis in the SEM, Alumix 123-T2 specimens were treated in a Soxhlet apparatus for 8 hours with petroleum ether to remove all traces of sizing fluid. To analyse cross sections, some specimens were mounted by vacuum impregnation with a self-curing epoxy resin, sectioned, polished, and carbon coated using a high vacuum evaporator platform.

X-ray diffraction (XRD) patterns were recorded in the range 10-110° (2θ) in a Bruker D8 ADVANCE diffractometer operated with $CuK_{\alpha 1}$ radiation (λ=1.54Å), a tube voltage of 40kV, and a tube current of 40mA.

7.3 RESULTS & DISCUSSION

7.3.1 Microstructure of Alumix 123-(T1, T2) and AA2014-T6

The structure of Alumix 123-T1 was characterized by a large amount of irregular-shaped interconnecting porosity and polyhedral aluminum grains (grain size *ca.* 50-100μm) with intermetallics situated along grain boundaries. The distribution of porosity in the longitudinal plane was profoundly non-uniform. There was significantly less porosity in the center of the compacts and along the edge of the compact which was adjacent to the mesh belt during sintering, meaning the surface exposed to the electrolyte during electrochemical testing contained more porosity than indicated by bulk density measurements.

In Alumix 123-T1, the aluminum grains were found by EDS analyses to contain: Al: 94.3±0.5; Cu: 4.9±0.4; Si: 0.6±0.1; and Mg: 0.2±0.1 wt%. Two predominant

intermetallics were identified by SEM and EDS: a copper-rich intergranular phase containing: Al: 57.0±3.9; Cu: 40.1±3.9; Mg: 2.0±0.5; and Si: 0.9±0.5 wt%, and an iron-rich intergranular phase containing: Al: 49.4±2.2; Fe: 29.1±2.3; Cu: 13.5±0.6; Si: 6.7±0.3; and Mg: 1.3±0.7 wt%. Both of these intermetallics were probably the result of the solidification of a liquid phase under conditions far from equilibrium. Iron, which is present as an impurity, may have segregated to the liquid phase during sintering. There were no obvious peaks in the XRD trace of Alumix 123-T1 corresponding to any iron-rich intermetallics. The copper-rich intergranular phase may be a metastable variant of θ-$CuAl_2$ – the XRD trace of Alumix 123-T1 showed several clear peaks corresponding to this phase. More detailed information on structure formation during sintering is given by [1,55,80,199,200,204].

A high surface roughness and non-planarity existed in Alumix 123-T1, Figure 7.1, probably due to the sintering process and original surface characteristics of the air-atomized aluminum present in the pre-mix. Across the surface of Alumix 123-T1 were areas which were in stark contrast to the aluminum grains, Figure 7.1, and by EDS analyses were found to largely consist of carbon, oxygen, and sometimes nitrogen. These are believed to be remnants from the ethylene bisstearamide (EBS) lubricant present in the pre-mix which may have been redeposited on the surface of compacts during the de-lubrication stage of sintering.

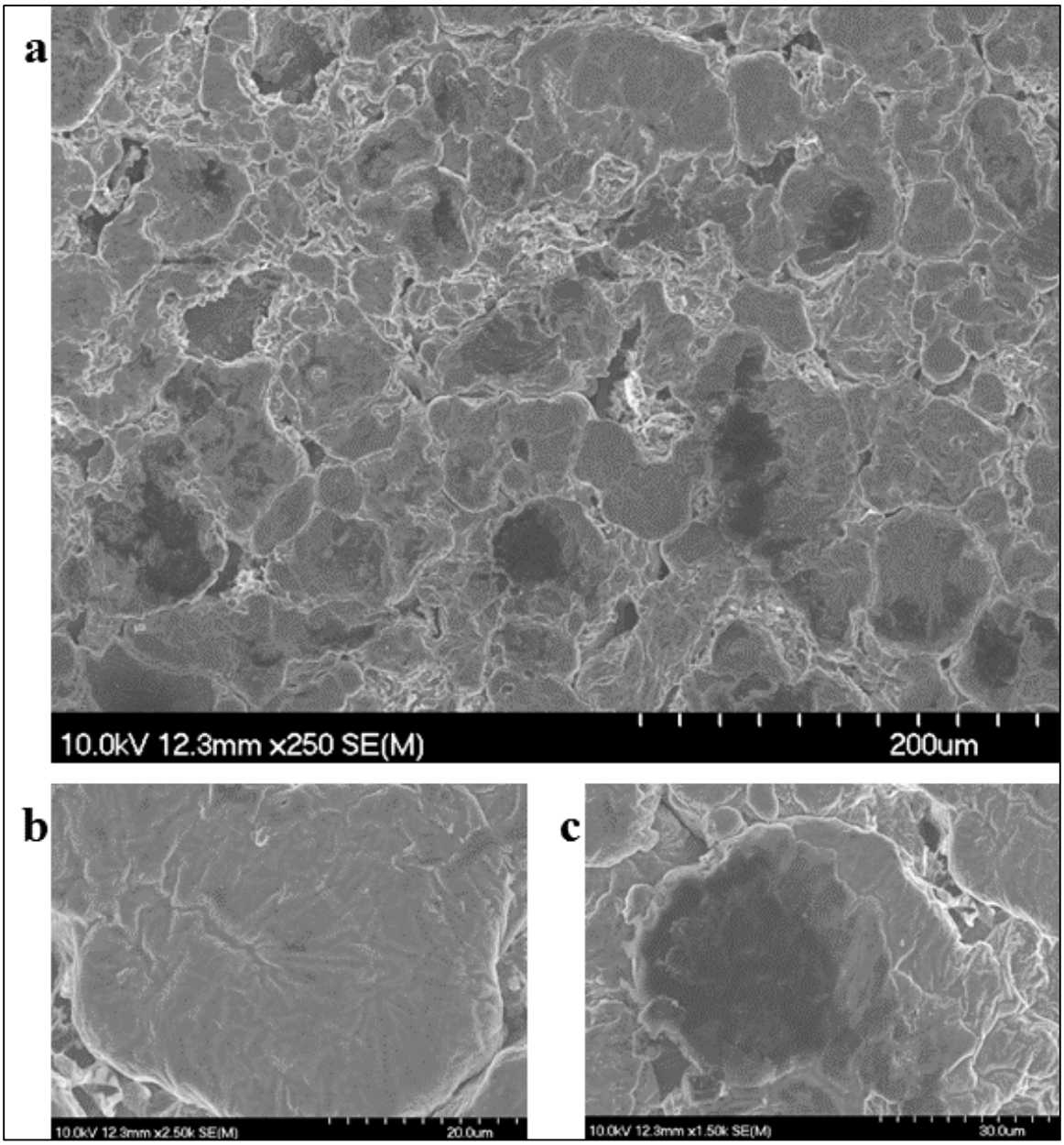

Figure 7.1 – SEM micrographs of Alumix 123-T1: a) general microstructure; b) close up of an aluminum grain; c) close up of a carbon-rich area which is believed to be a remnant from the EBS lubricant.

Compared to the interior, the surface of Alumix 123-T1 was enriched with carbon (*ca.* 6wt%), oxygen (*ca.* 8wt%), and magnesium (*ca.* 2wt%), as found by EDS analyses. EDS cannot resolve the source of these elements, whether they are contained in an oxide, hydroxide, hydrate, carbonate, *etc.* or mixture thereof, so their origin can only be speculated. Such a refractory surface layer may have gradually grown during sintering due to the continuous flow of fresh nitrogen which contained a small amount of contaminants like carbon dioxide, oxygen, and water vapour. The concentration of magnesium may be related to its role during sintering or its high vapour pressure. Magnesium is believed to enable the sintering of bare aluminum metal by reducing the aluminum oxide layer (via Al_2MgO_4 formation) and acting as a local oxygen getter [1]. Near the surface of the compacts these conditions may not be possible because the local atmosphere and oxygen partial pressure are continually restored by the flow of fresh nitrogen leading to increased amounts of oxidized magnesium. Magnesium is also a component of various transient and persistent liquid phases formed during sintering [200] and its liberation and transport in the vapour phase may have eventually led to its oxidation and deposition near the surface of the compacts.

The structure of Alumix 123-T2, Figure 7.2, was essentially the same as Alumix 123-T1, except the sizing operation, as expected, closed off a significant amount of porosity and deformed the surface layer so that it was more planar. Retained porosity on the surface was probably filled and sealed with sizing fluid as force was applied during sizing. In some areas, the surface layer appeared to have cracked as the underlying metal deformed in the transverse direction, Figure 7.2.

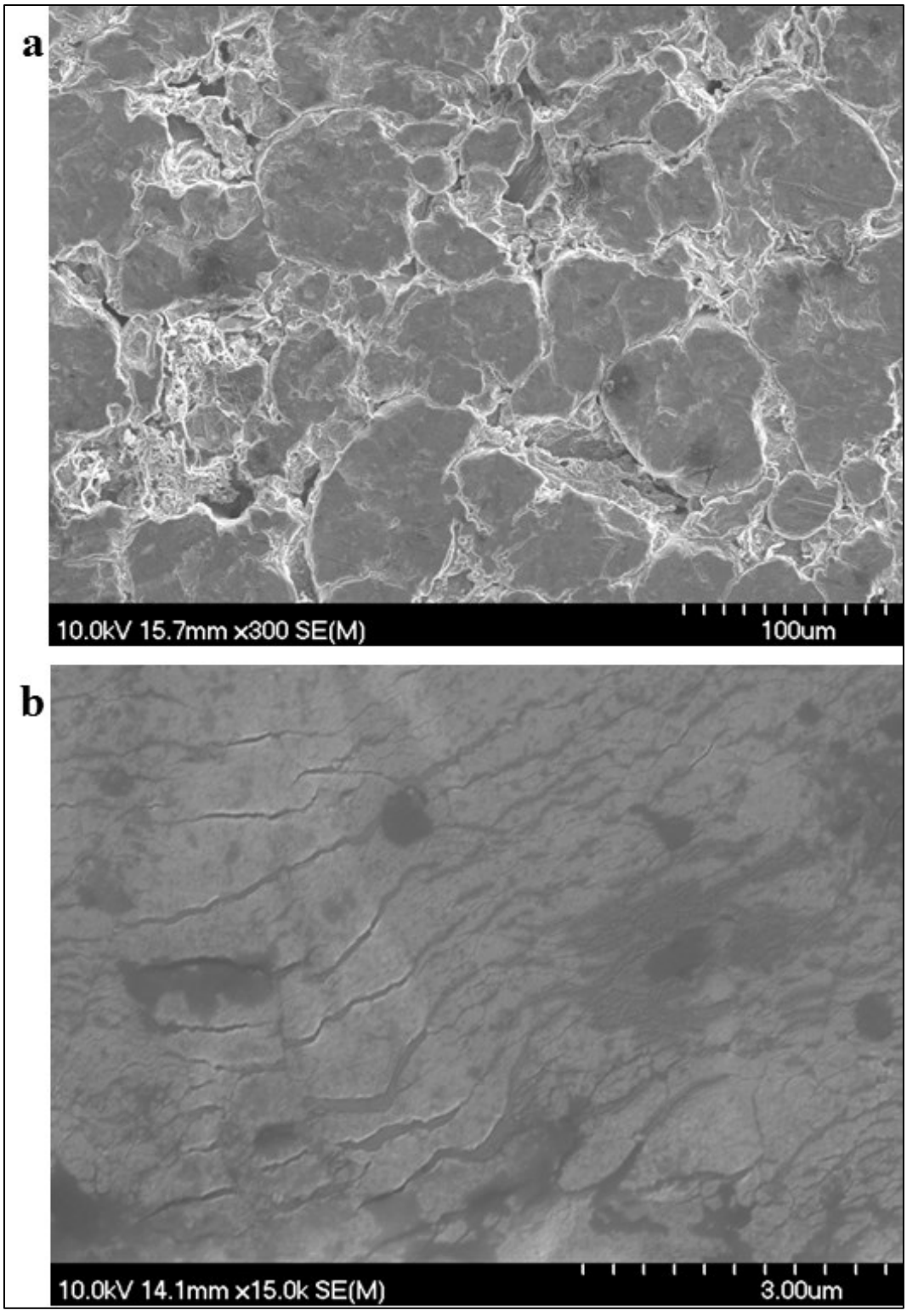

Figure 7.2 – SEM micrographs of Alumix 123-T2: a) general microstructure; b) close up an aluminum grain showing cracks in the refractory surface layer as a result of the sizing operation.

In AA2014-T6, two types of intermetallics were readily identifiable, as seen in Figure 7.3. The intermetallic with a round, globular morphology was believed to be θ-$CuAl_2$ – its morphological and compositional characteristics were a close match to those of θ-$CuAl_2$, given by [11], and there were found to be peaks which corresponded to θ-$CuAl_2$ in the XRD trace of AA2014-T6. By EDS analyses, the composition of the round, globular phase was found to be: Cu: 51.0±2.1; Al: 48.7±2.2; and Si: 0.3±0.1 wt%; again consistent with the θ phase. The intermetallic with a Chinese script morphology was believed to be α-AlFeMnSi ($(CuFeMn)_3Si_2Al_{15}$) – its morphology and composition were consistent with the descriptions of α-AlFeMnSi given by [11,203], and there were found to be peaks which corresponded to α-AlFeMnSi in the XRD trace of AA2014-T6. By EDS analyses, the composition of the Chinese script phase was found to be: Al: 61.2±3.9; Fe: 14.4±1.6; Mn: 10.2±1.7; Cu: 7.5±0.7; Si: 6.4±0.5; and Cr: 0.3±0.1 wt%. In addition to those phases previously discussed, it is conceivable that Q-phase ($Cu_2Mg_8Si_6Al_5$) precipitates and $Cu_2Mn_3Al_{20}$ or $(CuMn)Al_6$ dispersoids may have been present in the alloy [11,202]. However, neither phase was positively detected with the methods employed. In some SEM micrographs there appeared to be a distribution of micron and sub-micron areas of lighter contrast which could be some other type of precipitate, however these may also be fine θ' or θ-$CuAl_2$ precipitates which are expected to be present along grain boundaries.

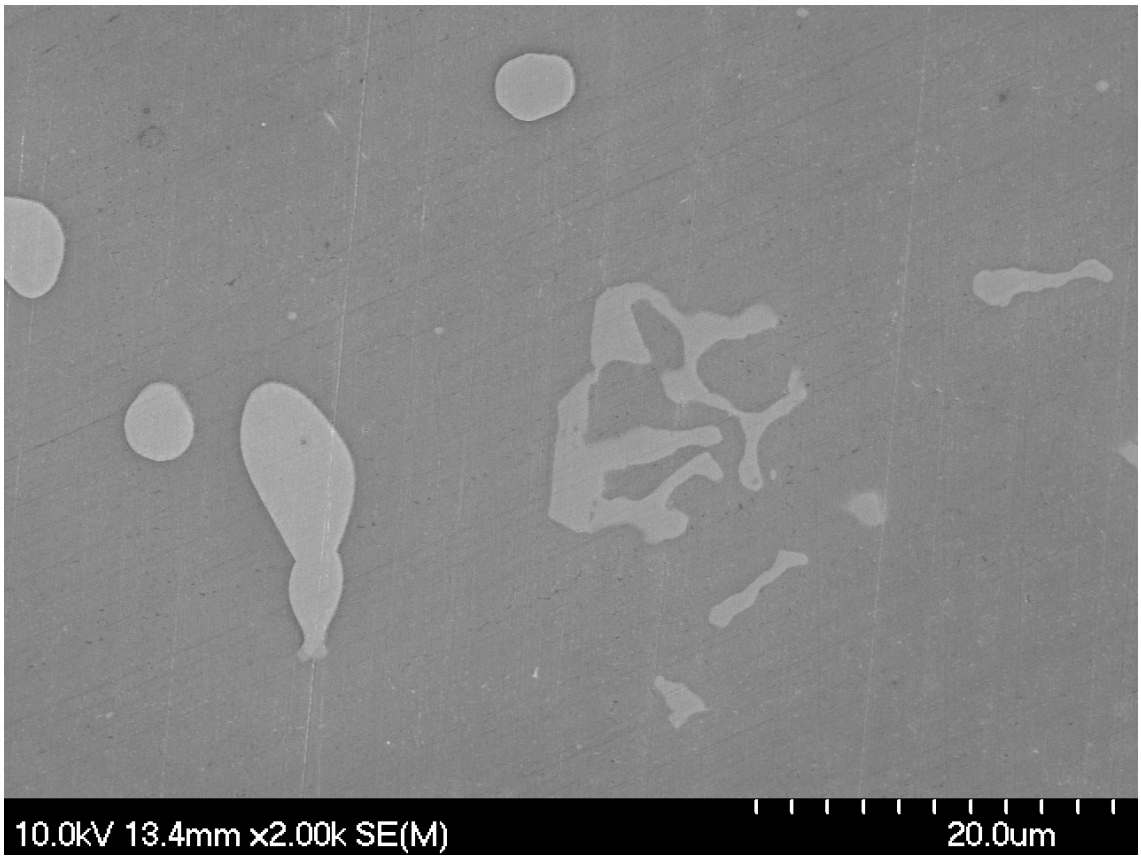

Figure 7.3 – SEM micrograph of AA2014-T6. The phase with the round, globular morphology is believed to be θ-$CuAl_2$ and the phase with the Chinese script morphology is believed to be α-AlFeMnSi.

7.3.2 Electrochemistry

Typical plots during the attainment of the OCP of Alumix 123-(T1, T2) and AA2014-T6 are presented in Figure 7.4. For the sake of comparison, the OCP of AA2014-T6 in Figure 7.4 was monitored for 2 hours instead of the usual 1 hour. No significant changes in electrode potential for Alumix 123-T2 and AA2014-T6 were observed throughout the duration of the test, which means that dynamic equilibrium was quickly established and maintained by these electrodes. The slight ennoblement of the

electrode potential of Alumix 123-T2 could be a result of the strain induced in the microstructure by the sizing operation and the small, consistent fluctuations in the OCP are probably related to surface roughness. Initially, the electrode potential of Alumix 123-T1 was similar to Alumix 123-T2 and AA2014-T6, however after a short incubation period the OCP began to shift to more negative values with the deviation eventually becoming quite substantial. The most obvious difference between these materials was the presence of a large amount of deep, interconnected porosity in Alumix 123-T1. It is hypothesized that the transience in the OCP of Alumix 123-T1 was related to the initiation and propagation of crevice corrosion in these areas.

Crevice corrosion, which has been studied extensively [210-214], initiates by a differential aeration mechanism which differentiates the electrode into macro-cells where creviced areas behave as anodes. In the case of Alumix 123-T1, the shift in electrode potential to more negative values may be a reaction to the reduced cathodic area, or the result of a breakdown of passivity in creviced areas caused by the migration of chloride ions and hydrolyses of anodic reaction products. The return of the electrode potential to slightly more noble values after the initial negative shift, Figure 7.4, could be related to a change in the composition of the creviced electrolyte due to the onset of hydrogen evolution or a gradual approach towards equilibrium dependent upon the ionic mobility and diffusivity of corrosion products and reactants to and from creviced areas.

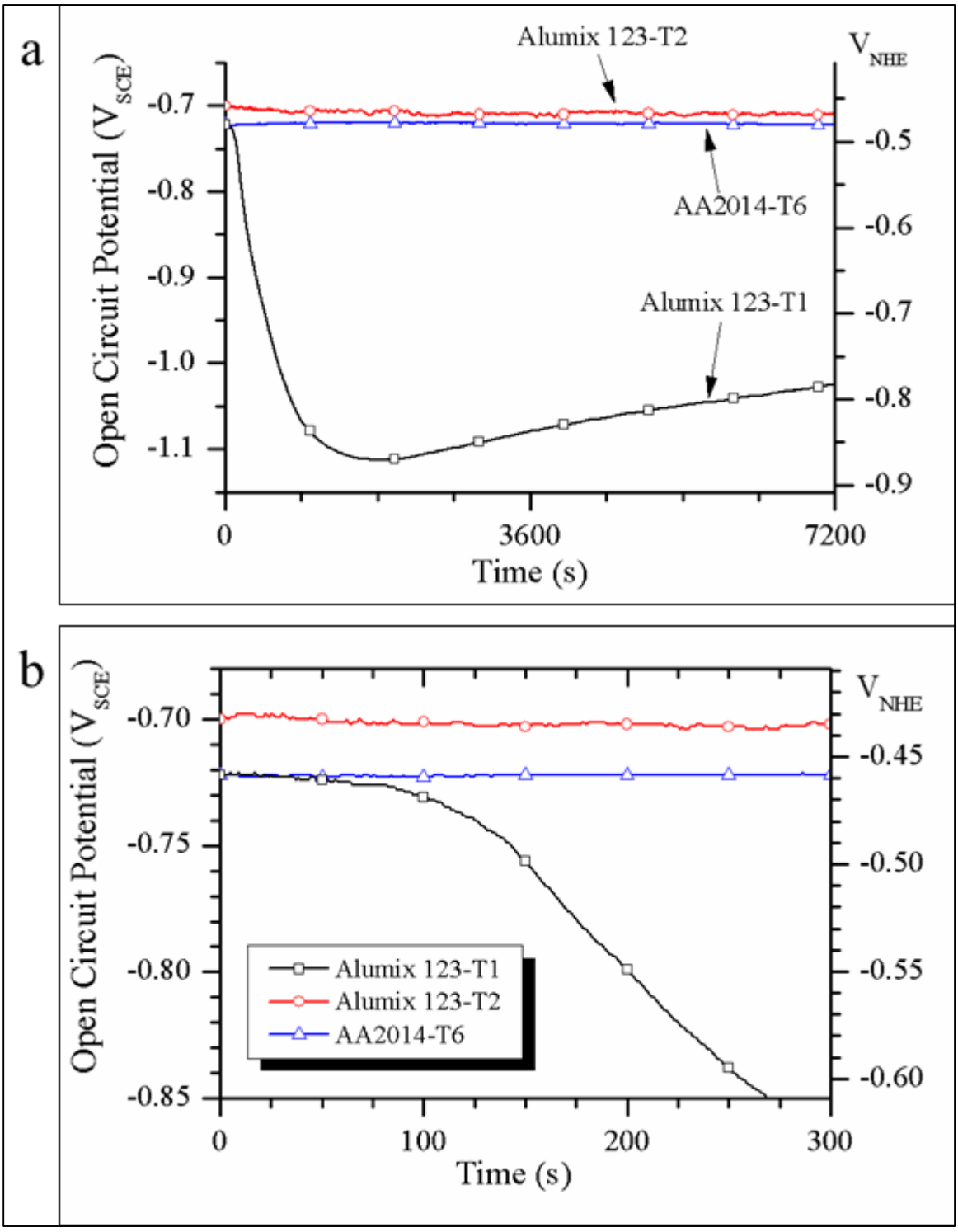

Figure 7.4 – Attainment of the open circuit potential (OCP) of Alumix 123-(T1, T2) and AA2014-T6 as a function of time: (a) full transient; (b) close up of initial transient.

To verify if the electrode potential of Alumix 123-T1 was controlled by the onset of hydrogen evolution the cathodic polarization diagrams in Figure 7.5 were constructed. All current densities presented were based off a nominal geometric area exposed to the electrolyte which for the P/M materials, especially Alumix 123-T1, was a gross underestimation. The cathodic process in the corrosion of Alumix 123-T1 at open circuit appears to be under more activation-control and this, in conjunction with its highly-negative OCP, suggests the corrosion of Alumix 123-T1 proceeded with a cathodic process involving hydrogen evolution [102-108]. Eventually, at sufficiently negative potentials, the current passed becomes substantial, and is usually attributed to the total hydration of the oxide layer which renders it ionically conductive and allows hydrogen evolution to take place directly on aluminum metal [110,125,127]. It is difficult to compare this feature in Figure 7.5 as the true current densities are not available.

The cathodic polarization of Alumix 123-T2 and AA2014-T6 appears to be under more diffusion-control near open circuit which is characteristic for a cathodic process involving the reduction of oxygen [102-108]. The limiting diffusion current for Alumix 123-T2 is about an order of magnitude larger than that of AA2014-T6, which is thought to be primarily due to the increased surface roughness and electrochemically active area of Alumix 123-T2, although the P/M materials were believed to have a unique refractory layer which may behave differently than the usual oxide layer present on aluminum.

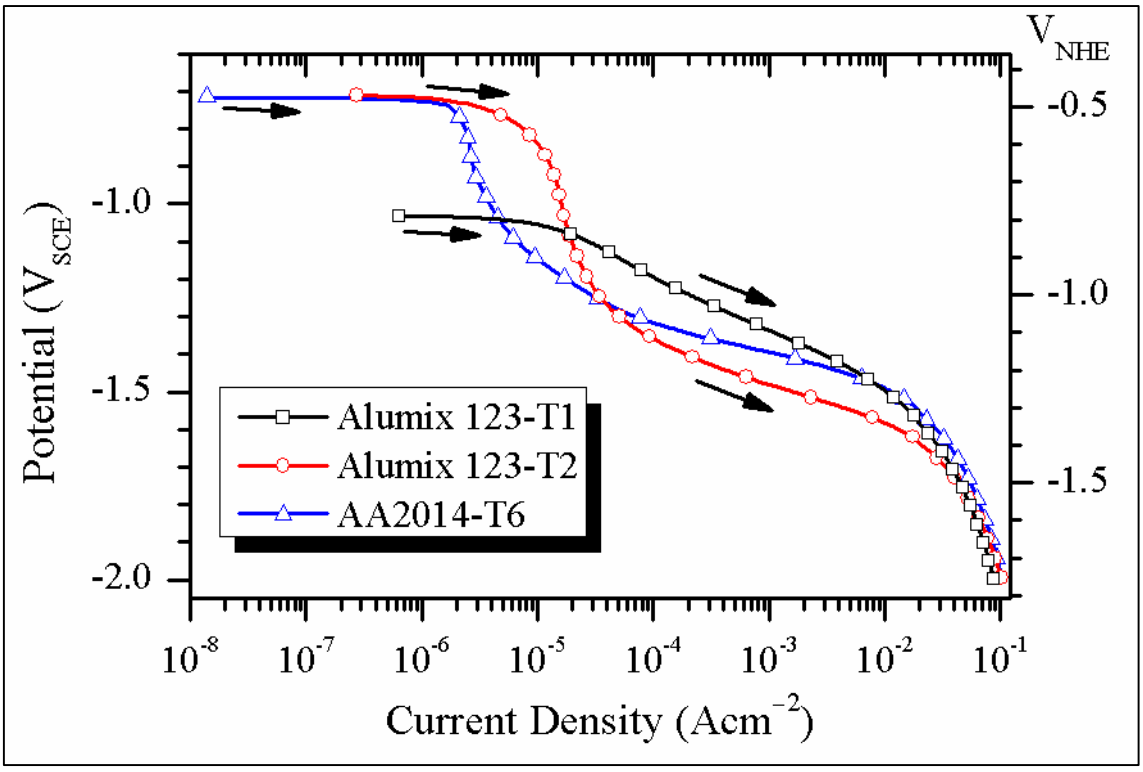

Figure 7.5 – Cathodic polarization diagrams of Alumix 123-(T1, T2) and AA2014-T6 using a scan rate of 0.1667mVs^{-1}.

It would appear that, based on the diffusion-limited nature of the cathodic process, the corrosion of Alumix 123-T2 and AA2014-T6 at open circuit should be under more cathodic control than Alumix 123-T1, and this was observed to be the case with the cyclic polarization diagrams presented in Figure 7.6. It seems that at open circuit conditions, Alumix 123-T2 and AA2014-T6 are polarized to their pitting potential and their corrosion current is predominantly limited by the amount of charge which can be consumed in cathodic reactions. On the other hand, the corrosion of Alumix 123-T1 at open circuit appears to be at least partially under anodic control.

There were two distinct regions in the anodic polarization of Alumix 123-T1: one where the current passed was essentially independent of the applied potential and one

where considerable active dissolution took place that was largely dependent on the applied potential. The behaviour in the first region was characteristic of passivity while the behaviour in the second region was characteristic of breakdown or pitting. The situation here, however, was not so explicit because in the crevice corrosion model most of the anodic current was generated in the creviced areas where passivity is questionable. It should be pointed out that the active dissolution of aluminum metal is thermodynamically possible at all potentials noble to its standard electrode potential, –1.90V_{SCE} [108], regardless of its relation to the pitting potential which represents the stability of the oxide layer.

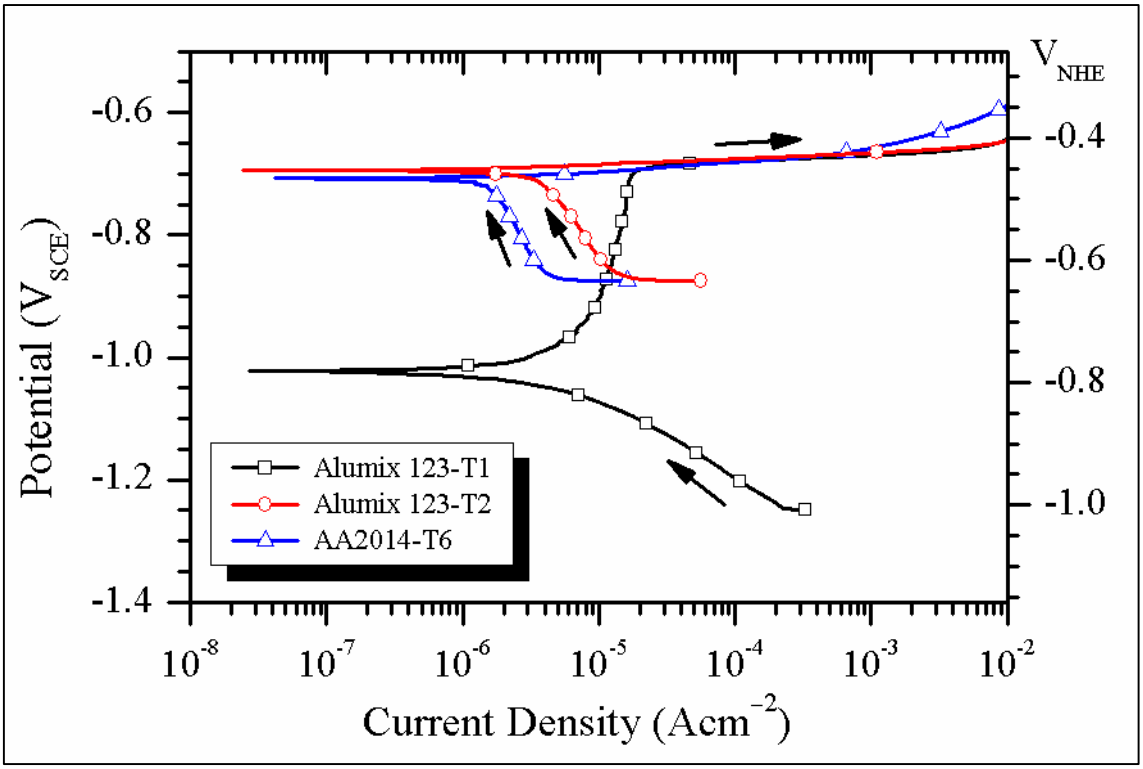

Figure 7.6 – Polarization diagrams of Alumix 123-(T1, T2) and AA2014-T6 using a scan rate of 0.1667mVs^{-1}. The reverse scans have been excluded from the figure for clarity.

A summary of the electrochemical data gathered on Alumix 123-(T1, T2) and AA2014-T6 is presented in Table 7.2. The authors would again like to remind the reader that electrochemical measurements were based off a nominal geometric area exposed to the electrolyte which for the P/M materials was an underestimation due to the presence of surface connected porosity. Despite the appearance of passivity upon polarization, the corrosion rate of Alumix 123-T1 was over four times greater than AA2014-T6. Of equal significance, was the effect of the sizing operation on the P/M material which reduced the corrosion rate by one half. While substantial, the corrosion rate of the sized P/M alloy still remained twice that of the wrought material. The data in Table 7.2 are in agreement with the literature on AA2014-T6 [215-221].

The pitting and repassivation characteristics summarized in Table 7.2 indicate that at open circuit conditions pitting is expected to initiate and propagate freely in Alumix 123-T2 and AA2014-T6, while any pitting in Alumix 123-T1 should spontaneously repassivate. For Alumix 123-T1, this was shown by the complete cyclic polarization diagram, Figure 7.7, where repassivation occurred at potentials noble to the corrosion potential. There was a disparity between the repassivation potentials of the P/M materials which may be explained by the lower true anodic current density passed on Alumix 123-T1 during cyclic polarization resulting from its higher surface area. When measured by the cyclic polarization method, the repassivation potential is known to be sensitive to the amount of anodic current passed during polarization [135].

Table 7.2 – Summary of electrochemical data of Alumix 123-(T1, T2) and AA2014-T6. Values are given as mean ± standard deviation (*no.* of experiments).

	Alumix 123-T1	Alumix 123-T2	AA2014-T6
Open Circuit Potential E_{OCP} (mV_{SCE})	−1017±20 (37)	−711±4 (33)	−717±5 (56)
Cathodic Tafel slope β_c ($mVdecade^{-1}$)	−144±15 (11)	−386±101 (13)	−509±163 (27)
Corrosion Potential E_{corr} (mV_{SCE})	−1039±17 (11)	−688±5 (13)	−701±8 (27)
Corrosion Current i_{corr} (μAcm^{-2})	7.40±1.85 (11)	3.46±0.77 (13)	1.82±0.49 (27)
Corrosion Rate CR (10^{-2} $mmyr^{-1}$)	8.77±2.19 (11)	4.09±0.92 (13)	1.97±0.54 (27)
Pitting Potential E_{pit} (mV_{SCE})	−692±5 (11)	–	–
Passive Current i_{pass} (μAcm^{-2})	13.01±5.89 (11)	–	–
Repassivation Potential E_{repass} (mV_{SCE})	−818±7 (11)	−859±6 (13)	−909±7 (27)

Also of particular interest in Table 7.2, was the shift in the corrosion potential of Alumix 123-T1 away from the OCP in the opposite direction of potentiodynamic scan. In conventional electrodes there is a shift in the corrosion potential away from the OCP in the direction of the potentiodynamic scan due to the storage of charge at the double layer [222]. This behaviour of Alumix 123-T1 could be related to chemical phenomena, like alkalization, occurring during cathodic polarization and may be further evidence that the OCP was affected by the composition of creviced electrolyte.

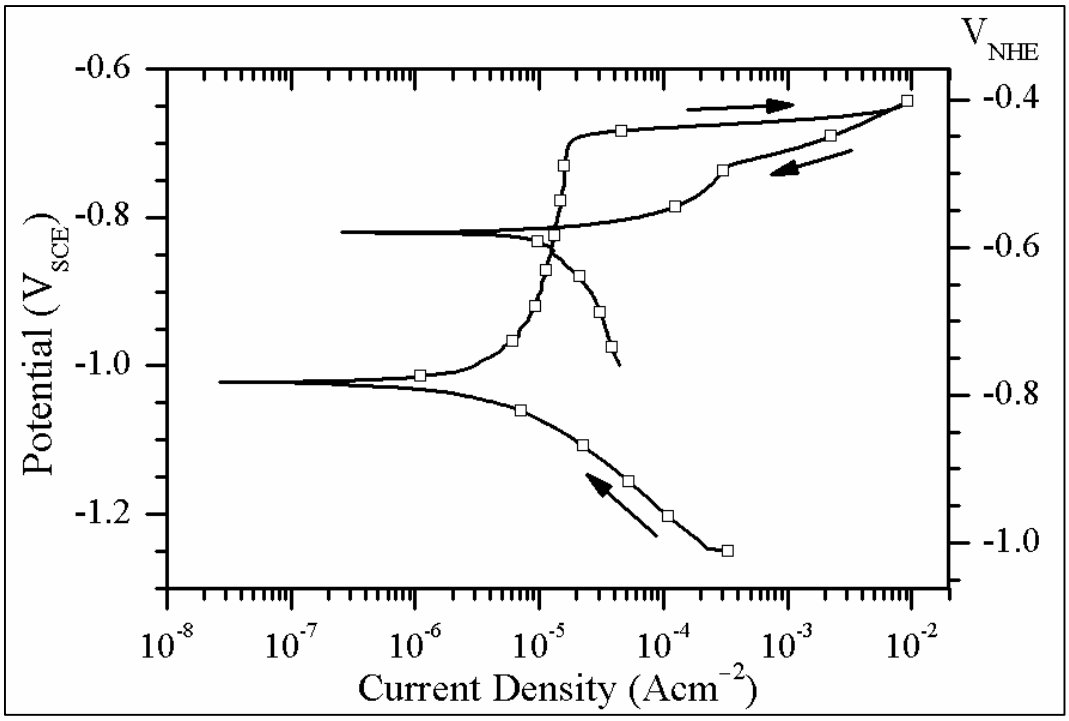

Figure 7.7 – Cyclic polarization diagram of Alumix 123-T1 using a scan rate of $0.1667 mVs^{-1}$.

7.3.3 Microstructure after Open Circuit Corrosion

The electrode face of Alumix 123-T1 after 2 hours exposure at open circuit conditions is shown in Figure 7.8. In some areas, particularly around pores, there appeared to be a fine, speckled distribution of corrosion product, Figure 7.8, which upon viewing under high magnification was revealed to be fine nano-scale nodules. The main constituent of such nodules is usually Bayerite (α-$Al(OH)_3$) [113], but this should not be assumed for Alumix 123-T1 because of the enrichment of the surface with magnesium. If these nodules were directly involved in the corrosion process, their location around some pores could be indicative of a macro-cell in the area since the half-cell reactions would be expected to occur in close proximity to one another.

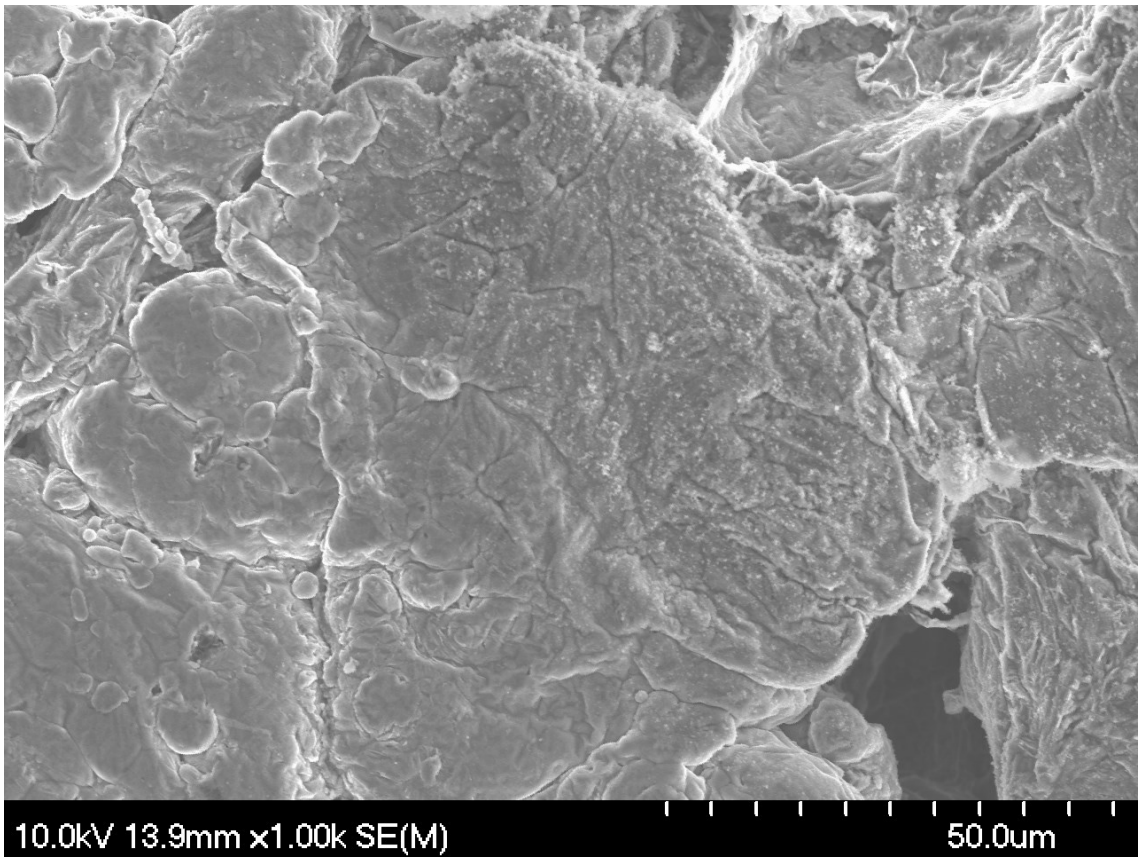

Figure 7.8 – SEM micrograph of Alumix 123-T1 after 2 hours at OCP.

Pitting was observed in Alumix 123-T1, Figure 7.9, but the pits did not seem to be associated with any copper- or iron-rich intermetallics. This probably means the refractory layer formed during sintering retained integrity over these intermetallics, unlike in traditional aluminum alloys. It remains unclear if the film breakdown was more stochastic in nature or was partial to local heterogeneities in the refractory layer, such as magnesium aggregation or lubricant residues. Electrochemical measurements indicated that any pitting in Alumix 123-T1 should spontaneously repassivate at open circuit conditions. Therefore, any pitting observed must be either 'cathodic pitting' caused by local alkalinity generated at cathodic sites or pitting which initiated in the short

incubation period before the deviation of the OCP to more negative values. Regardless of the mechanism, the location of the pits probably signified weak or thin points in the refractory layer where electrons or chloride ions preferentially migrated.

In the cross section of Alumix 123-T1, Figure 7.10, there appeared to be corrosion product accumulated within some porosity which was found by EDS analyses to consist primarily of aluminum and oxygen. If the oxidation of aluminum occurred within the vicinity of the corrosion product deposit it would suggest the anodic process has been occurring within certain areas of pores. However, there is also the possibility that occluded electrolyte remained in some areas after washing and drying of the specimen. Regardless, it is apparent the electrolyte was able to penetrate the compacts through porosity.

In the corrosion morphology of Alumix 123-T2, Figure 7.11, blistering was quite apparent and seemed to be associated with the areas around specific pores. Fine corrosion product nodules were incorporated in to the surface of some blisters, Figure 7.12. Blistering is normally a consequence of a pitting mechanism involving the penetration of chloride through the oxide layer followed by the localized dissolution of aluminum and hydrogen generation at the metal/oxide interface [142]. In the present case, there may also be partial chloride penetration through cracks introduced in the refractory layer from the sizing operation. Electrochemical measurements indicated that at open circuit conditions Alumix 123-T2 was polarized to the pitting potential so instability of the refractory layer is expected.

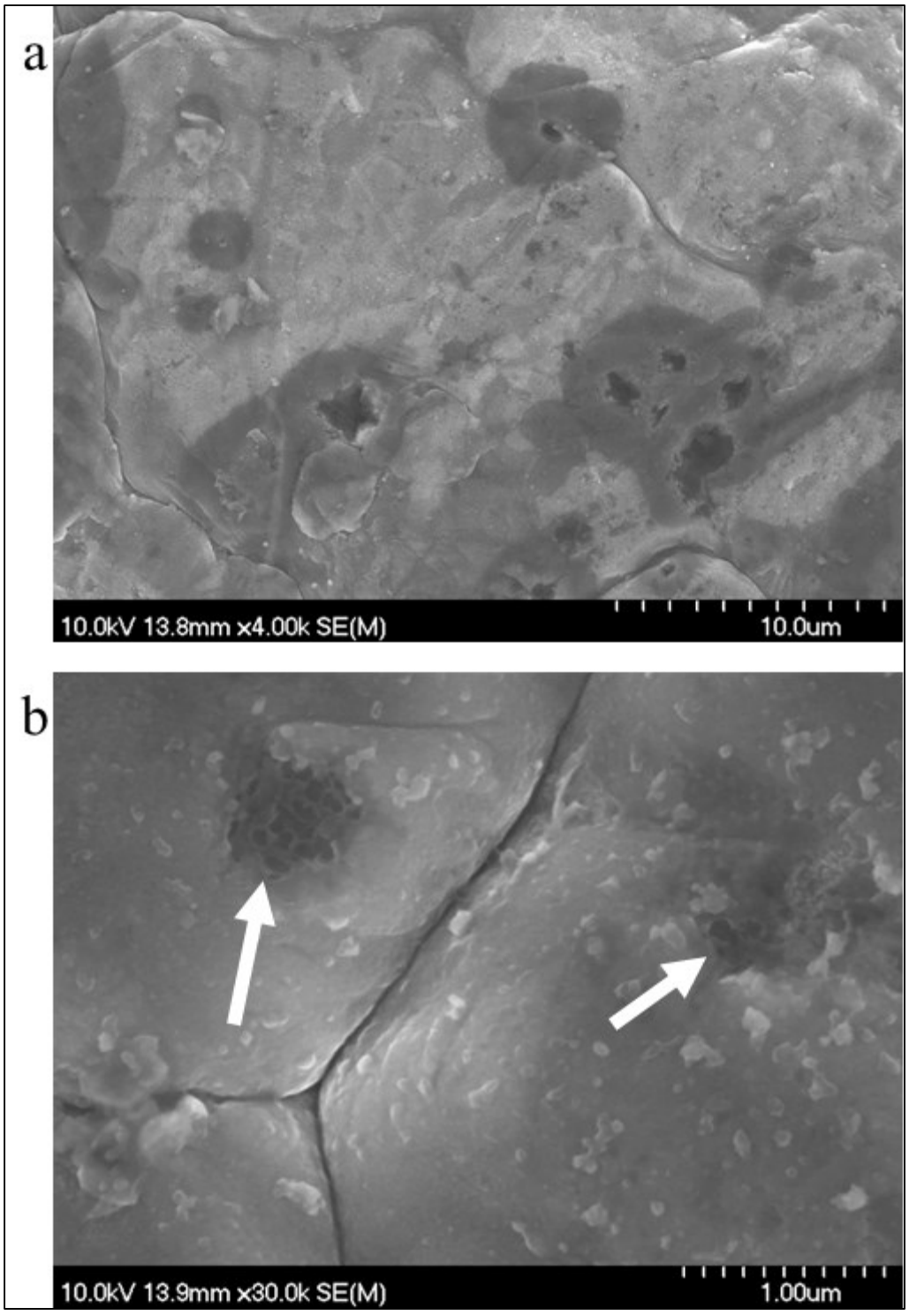

Figure 7.9 – SEM micrographs of pitting in Alumix 123-T1 after 2 hours at OCP: a) cluster of pits which are not associated with copper-rich phases in the area; b) high magnification micrograph showing interior structure of some pits (indicated by arrows).

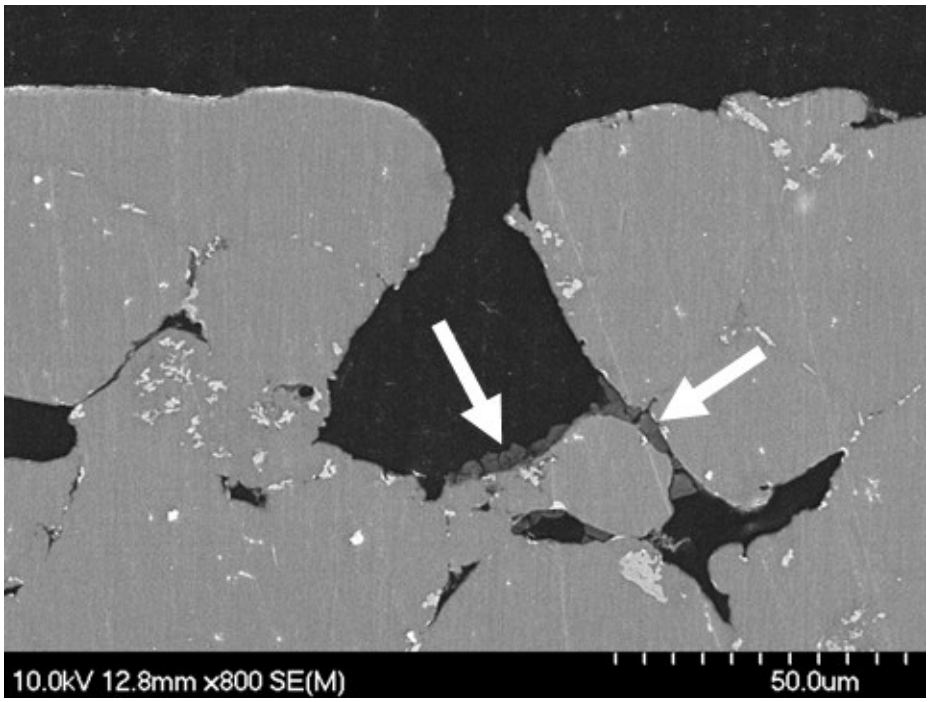

Figure 7.10 – SEM micrograph of the cross sectional microstructure of Alumix 123-T1 after 2 hours at OCP. The corrosion product indicated by the arrows was found by EDS analyses to consist primarily of aluminum and oxygen.

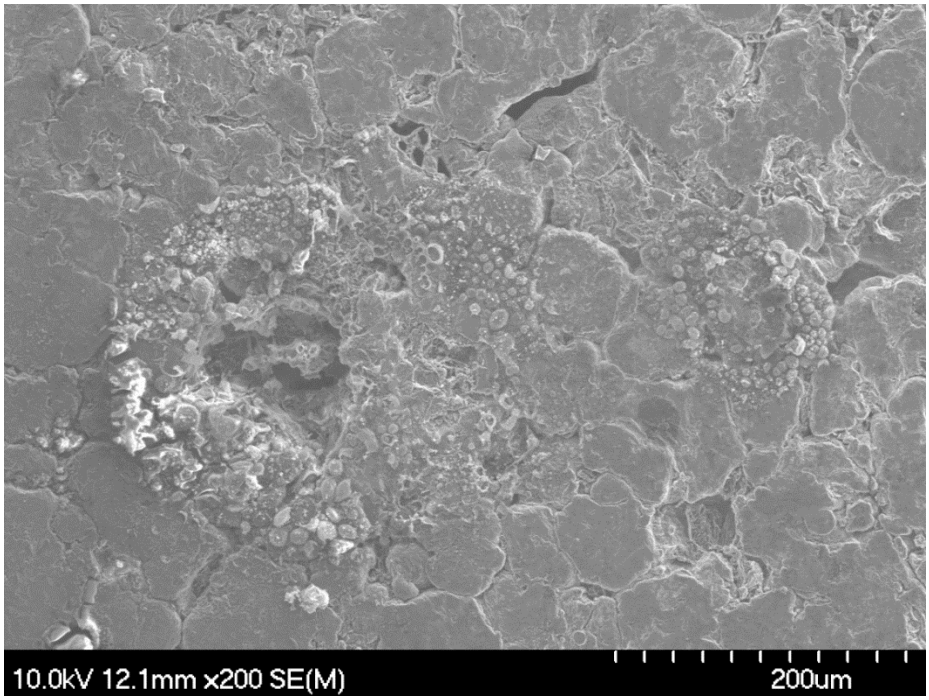

Figure 7.11 – SEM micrograph of Alumix 123-T2 after 2 hours at OCP.

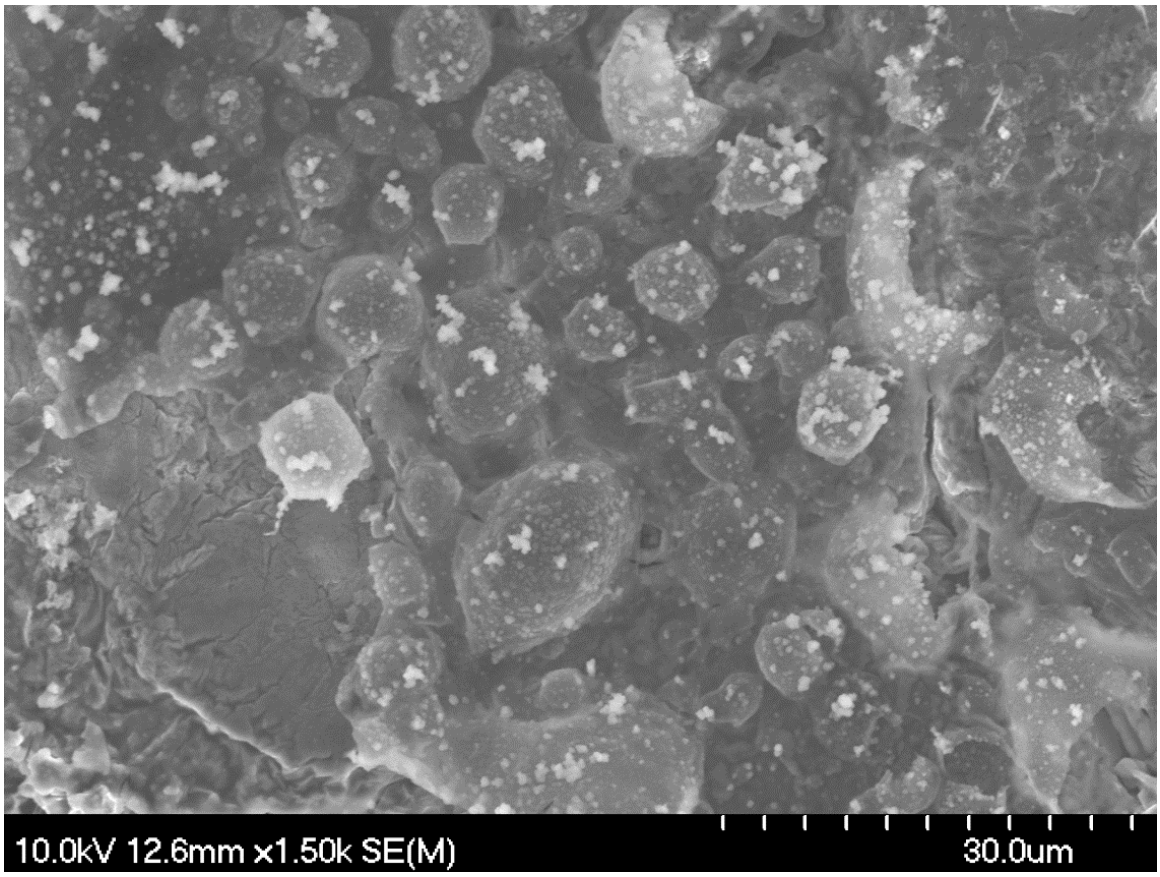

Figure 7.12 – SEM micrograph of blistering in Alumix 123-T2 after 2 hours at OCP.

The reason for the association of blistering with areas surrounding some residual porosity was not immediately clear. The residual porosity may be a preferential site for evolving gas bubbles to form which may have occluded the surrounding electrolyte and intensified film breakdown in the area. This was supported by the observation that the circumference of all blistered regions were quite circular, Figure 7.11. The presence of sizing fluid in these areas was also expected which may somehow create favourable conditions for the adsorption or penetration of chlorine.

In the corroded microstructure of AA2014-T6, Figure 7.13, pitting was observed in the matrix, adjacent to intermetallic particles, and along grain boundaries. Virtually all

pits in the matrix and along grain boundaries appeared to be associated with small intermetallic particles, Figure 7.14. It was not possible to identify these small intermetallics by the methods employed here; however, the particles along grain boundaries are believed to be θ' or θ-$CuAl_2$ while the particles in the matrix are not so discernible. The absence of an intermetallic particle in some pits, Figure 7.14, was believed to be caused by attack which was so extensive that a once-present intermetallic was dislodged from the matrix.

The attack around θ-$CuAl_2$ was believed to be due to the anodic trenching mechanism outlined by [149,152], where the pitting potential of the surrounding copper-depleted matrix is exceeded at open circuit conditions leading to its active dissolution. Evidently, the θ-$CuAl_2$ intermetallic was subjected to selective dealloying of aluminum [123,160,166,223], as it was confirmed by EDS analyses that the particles consisted of about 25% Al, 64% Cu, and 11% O (in wt%) after 1 hour at open circuit. Some of the aluminum detected by EDS was probably due to electron interaction with underlying areas which were not subject to corrosion. The presence of either metallic copper or cuprous oxide on the electrode surface could not be confirmed by XRD due to the small concentration present. Since the OCP of AA2014-T6 was much more negative than the oxidation potential of copper, it was likely that any cuprous oxide which may have been detected by EDS was formed in the air before analyses. Electrochemical measurements indicated that the stability of the OCP was maintained despite dealloying and enrichment of the electrode surface with copper. At open circuit, AA2014-T6 was polarized to the pitting potential so such enrichment cannot further ennoble the corrosion potential, but probably increased the corrosion current, which was under cathodic control, due to the high cathodic efficiency of copper and the large surface area of the dealloyed structure.

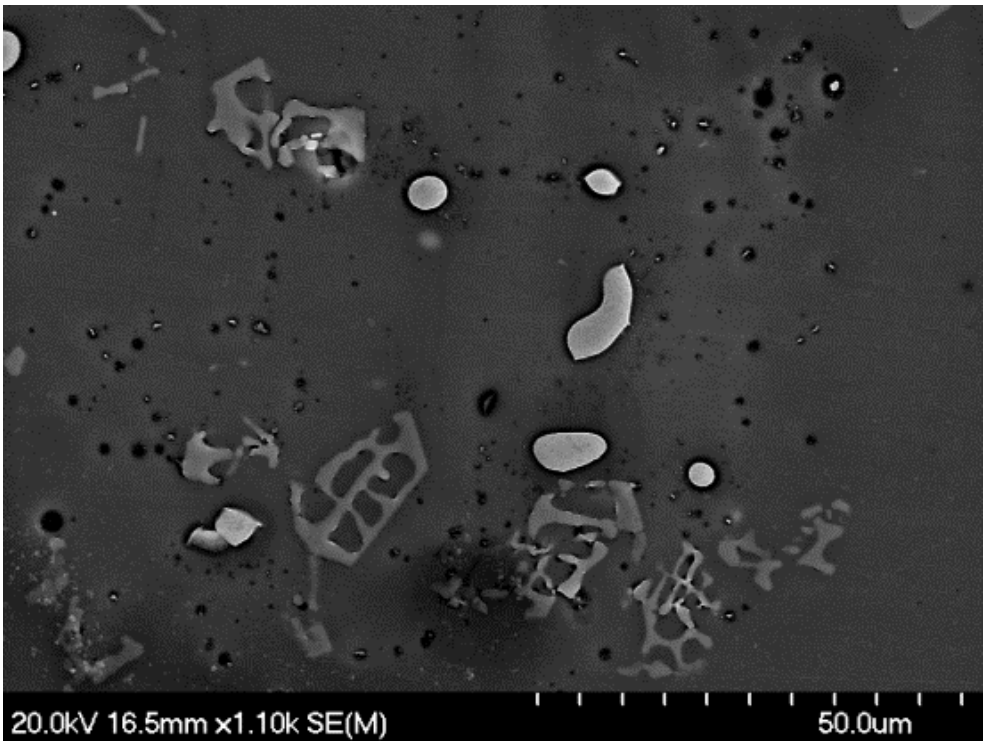

Figure 7.13 – SEM micrograph of AA2014-T6 after 1 hour at OCP.

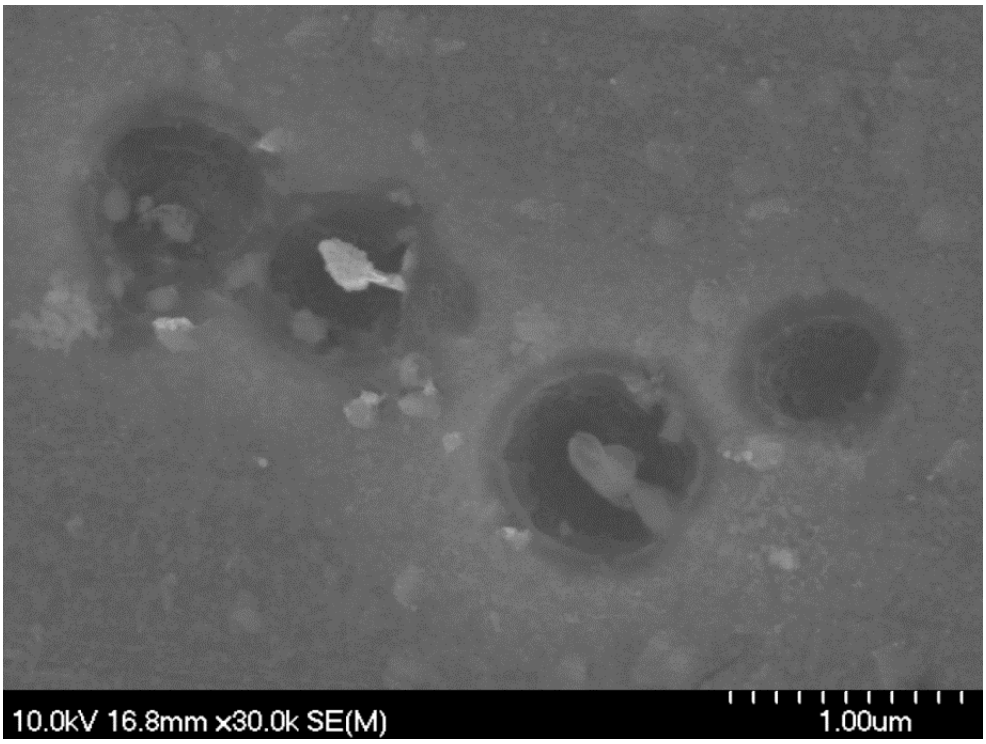

Figure 7.14 – SEM micrograph of pits formed in the matrix of AA2014-T6 after 1 hour at OCP.

The attack around α-AlFeMnSi was also believed to be due to a cathodic trenching mechanism outlined by [149,152], where chemical dissolution of the surrounding matrix is a consequence of the hydroxide ions generated by cathodic reactions occurring on the intermetallic. The high iron-content of α-AlFeMnSi probably enhanced its efficiency as a cathode and stability against local alkalization. The only compositional change after corrosion was a selective dealloying of aluminum, which has also been observed by [161]. In the present work the EDS analyses showed that the aluminum content decreased to about 54wt% after 1 hour at open circuit from 61wt% before corrosion. The sporadic nature of the trenching around α-AlFeMnSi, Figure 7.13, may imply that its role as a cathode was affected by the presence of other intermetallics in the vicinity.

7.4 CONCLUSIONS

After a short incubation period, the OCP of Alumix 123-T1 deviated and stabilized to highly negative values (*ca.* $-1.0V_{SCE}$). This was postulated to be due to a reaction leading to a reduction in cathode area or depassivation induced by propagating crevice corrosion within residual porosity. The sizing operation in Alumix 123-T2 effectively reduced surface porosity through plastic deformation and sealed a portion of the residual porosity with sizing fluid to an extent that crevice corrosion did not initiate in the material.

At open circuit conditions the corrosion of Alumix 123-T1 was partially under anodic control and proceeded with hydrogen evolution, while the corrosion of Alumix 123-T2 and AA2014-T6 were predominantly under cathodic control and proceeded with oxygen reduction. The corrosion rate of Alumix 123-T1 was two times greater than

Alumix 123-T2 and four times greater than AA2014-T6. The disparity was partially due to the high surface area of the P/M materials which could not be accounted for.

In the P/M materials pitting was not associated with copper- or iron-rich intermetallics. This was attributed to the unique refractory layer formed as a result of the sintering process. In AA2014-T6 pitting was associated with θ-$CuAl_2$, α-AlFeMnSi ($(CuFeMn)_3Si_2Al_{15}$), and other small unidentifiable intermetallic particles. The attack involving θ-$CuAl_2$ was attributed to the anodic trenching mechanism whereas the attack involving α-AlFeMnSi was attributed to the cathodic trenching mechanism.

7.5 ACKNOWLEDGEMENTS

The authors gratefully acknowledge the National Sciences and Engineering Research Council of Canada (NSERC) and AUTO21 Network of Centers of Excellence for providing financial support during this work. The authors would also like to thank the Minerals Engineering Centre (MEC) at Dalhousie University for chemical and particle size analyses, the Institute for Research in Materials (IRM) at Dalhousie University for use of the SEM/EDS system, ECKA Granules for supply of the P/M pre-mix, and GKN Sinter Metals for sintering the P/M material.

CHAPTER 8 CORROSION BEHAVIOUR OF ALUMIX 123 P/M ALLOY AND AA2014-T6. PART II: POTENTIOSTATIC POLARIZATION

W.D. Judge[1], D.P. Bishop[1], and G.J. Kipouros[2,*]

[1]Materials Engineering, Process Engineering and Applied Science, Dalhousie University, 1360 Barrington Street, Room F201, Halifax, Nova Scotia, Canada, B3H 4R2

[2]Chemical Engineering, College of Engineering, University of Saskatchewan, 57 Campus Drive, Saskatoon, Saskatchewan, Canada, S7N 5A9

(*Corresponding author: georges.kipouros@usask.ca)

Status: To be submitted to *Journal of the Electrochemical Society*

The following experimental procedures, results, and discussions were completed by W.D. Judge with reviewer and editorial roles played by D.P. Bishop and G.J. Kipouros.

ABSTRACT

The corrosion behaviour of the commercial aluminum powder metallurgy (P/M) alloy 'Alumix 123' and a compositionally similar wrought alloy, AA2014-T6, has been studied in naturally aerated 3.5wt% NaCl by potentiostatic polarization at a variety of characteristic potentials and the subsequent corrosion morphology characterized by scanning electron microscopy (SEM) and energy dispersive X-ray spectroscopy (EDS). In the P/M materials, which were studied in the 'as-sintered' condition (T1 temper) or after a standard sizing operation (T2 temper), cathodic hydrogen evolution and oxygen reduction was associated with film breakdown in the matrix and on copper- and iron-rich intermetallics. Below the pitting potential, the majority of anodic current passed on Alumix 123-T1 was generated from creviced areas within residual porosity which eventually repassivated when the concentration of anodic reaction products exceeded the solubility limit. Above the pitting potential, the majority of attack in the P/M materials was intergranular in nature. SEM observations of AA2014-T6 suggested that cathodic deposition of copper occurs on copper- and iron-rich intermetallics and that cathodic trenching around iron-rich intermetallics may have liberated copper from the matrix in a non-Faradaic process. Above the pitting potential, extensive attack of AA2014-T6 occurred via crystallographic pitting and intergranular corrosion.

Keywords: aluminum alloy; corrosion; electrochemistry; powder metallurgy; crevice corrosion; intermetallics; Alumix 123; AA2014

8.1 INTRODUCTION

The 'press-and-sinter' aluminum powder metallurgy (P/M) alloys were first commercialized in the 1960s by Alcoa [15] and have since remained in large scale production for a variety of applications, the most prominent being in the automotive industry, consumer durables, and business machinery [1]. Despite the proven commercial successes, there remains hesitation to specify P/M aluminum in new designs and most P/M aluminum is used in non-critical applications which require only low-grade properties [1]. This is in part due to the limited information on the performance of P/M aluminum alloys in some environments involving, for example, conditions of dynamic stress, high temperature, or corrosive media [1]. Recently, our laboratory has undertaken extensive investigations on the corrosion behaviour of commercial P/M aluminum alloys which provide thermodynamic and kinetic data that can be used to predict material performance [4,224].

We have previously investigated the corrosion behaviour of the commercial P/M aluminum alloy 'Alumix 123' and a compositionally similar wrought alloy, AA2014-T6, by open circuit potential (OCP), cathodic polarization, and cyclic potentiodynamic polarization experiments in naturally aerated 3.5wt% NaCl [224]. The P/M alloy was studied in either the 'as-sintered' condition or after a standard sizing operation, which are generally denoted by the T1 and T2 temper, respectively. Sizing is a cold forming process used industrially to improve dimensional tolerances after sintering. The OCP of Alumix 123-T1 was initially found to be transient but eventually stabilized at more negative values which was attributed to the initiation and propagation of crevice corrosion within residual porosity. The sizing operation effectively reduced and sealed a fraction of surface porosity such that crevice corrosion did not initiate in Alumix 123-T2. Cathodic and

cyclic potentiodynamic polarization then showed the OCP of Alumix 123-T1 was stabilized at potentials near the onset of hydrogen evolution where corrosion was partially under anodic control and proceeded via cathodic hydrogen evolution, while the OCP of Alumix 123-T2 and AA2014-T6 was stabilized at the pitting potential where corrosion was predominantly under cathodic control and proceeded via cathodic oxygen reduction. Through these observations, in conjunction with microstructural analyses, the electrochemical characteristics of some microstructural features, particularly residual porosity, and their role in the corrosion process was hypothesized.

In the present work, we continue our investigations on the corrosion behaviour of Alumix 123-(T1, T2) and AA2014-T6 by potentiostatic polarization in naturally aerated 3.5wt% NaCl and characterize the subsequent corrosion morphology. The characteristic potentials were generated from previous OCP and potentiodynamic plots. The microstructural analyses aim to further investigate the electrochemistry of some microstructural features and their role in the overall corrosion process.

8.2 EXPERIMENTAL

8.2.1 Materials and Materials Preparation

Alumix 123 pre-mix was obtained from ECKA Granules Germany GmbH (Fürth, Bavaria, Germany); its chemical and particle size analyses, and detailed P/M processing, processing response, and preparation are presented elsewhere [224]. Green compacts 15mm in diameter were made by uniaxially compacting 2.5g of pre-mix at 300MPa, yielding a green density of 2.623±0.004gcm^{-3} (94.5±0.2% theoretical), and were sintered amongst industrial production at GKN Sinter Metals (Conover, North Carolina, U.S.A.) yielding a sintered density of 2.561±0.008gcm^{-3} (92.2±0.3% theoretical). After sintering,

a portion of the compacts were sized at 310MPa, which corresponded to a 5% reduction in height, using sizing fluid provided by GKN Sinter Metals. The P/M material was tested in the 'as-sintered' or 'as-sized' conditions which are denoted by the T1 and T2 temper, respectively.

AA2014-T6 extruded rod was obtained from Kaiser Aluminum (Jackson, Tennessee, U.S.A.); its chemical analysis and detailed preparation were presented elsewhere [224]. Specimens were extracted so that during electrochemical testing the transverse plane was in contact with the electrolyte. Immediately prior to testing, AA2014-T6 specimens were abraded on wet SiC paper, polished with oil-based diamond suspensions (to 1μm), degreased ultrasonically in acetone, thoroughly rinsed with deionized water, and dried using a hand drier.

8.2.2 Electrochemical Testing

All electrochemical tests were conducted at ambient temperature in naturally aerated 3.5wt% NaCl electrolyte which was prepared immediately prior to testing using analytical-grade NaCl (>99.0% assay) and ultrapure 'Type 1' deionized water (>18MΩ·cm). The electrochemical instrumentation, whose detailed description is given elsewhere [224], consisted of a standard three electrode bulb cell connected to a Princeton Applied Research (PAR) Model 273A EG&G Potentiostat/Galvanostat. The electrochemical cell contained a working electrode which exposed a nominal area of 1cm^2 of the test specimen, two high-purity fully dense graphite counter electrodes, and a saturated calomel reference electrode (SCE) brought in close proximity to the working electrode via a Luggin capillary.

Prior to potentiostatic polarization, the OCP of the working electrode was monitored versus time for a period of 2 hours for Alumix 123-(T1, T2) and 1 hour for AA2014-T6. During potentiostatic polarization, the potential of the working electrode was held constant at either $-1.50V_{SCE}$, $-1.10V_{SCE}$, $-0.75V_{SCE}$, $-0.70V_{SCE}$, or $-0.50V_{SCE}$ and current transients were recorded at a rate of one point per second. Potentiostatic polarization at $-1.10V_{SCE}$, $-0.75V_{SCE}$, and $-0.70V_{SCE}$ was maintained for 6 hours, while polarization at $-1.50V_{SCE}$ and $-0.50V_{SCE}$ was maintained for 3 hours. The corrosion convention for current polarity was used where net cathodic current was indicated by negative current and net anodic current was indicated by positive current. Immediately after testing, specimens were thoroughly washed with deionized water and dried using a hand drier.

8.2.3 Materials Characterization

Micrographs were captured using a Hitachi Model S-4700 cold field emission scanning electron microscope (SEM) containing an integrated unit for energy dispersive X-ray spectroscopy (EDS). The SEM was operated with a 10kV accelerating voltage for imaging and a 20kV accelerating voltage for EDS analyses. Prior to analyses, Alumix 123-T2 specimens were treated in a Soxhlet apparatus for 8 hours with petroleum ether to remove all traces of sizing fluid. To analyse cross sections, some specimens were mounted by vacuum impregnation with a self-curing epoxy resin, sectioned, polished, and carbon coated using a high vacuum evaporator platform.

8.3 RESULTS AND DISCUSSION

8.3.1 Electrochemistry

Current transients during the potentiostatic polarization of the three electrodes, Alumix 123-(T1, T2) and AA2014-T6, at $-1.50V_{SCE}$ are presented in Figure 8.1. The relatively large current densities observed may be expected from the cathodic polarization diagrams that showed the efficiency of hydrogen evolution was increased in this domain [224], which was related to the hydration of the oxide layer and resembled the passive-active transition encountered near the passivation potential of a metal [110,125,127].

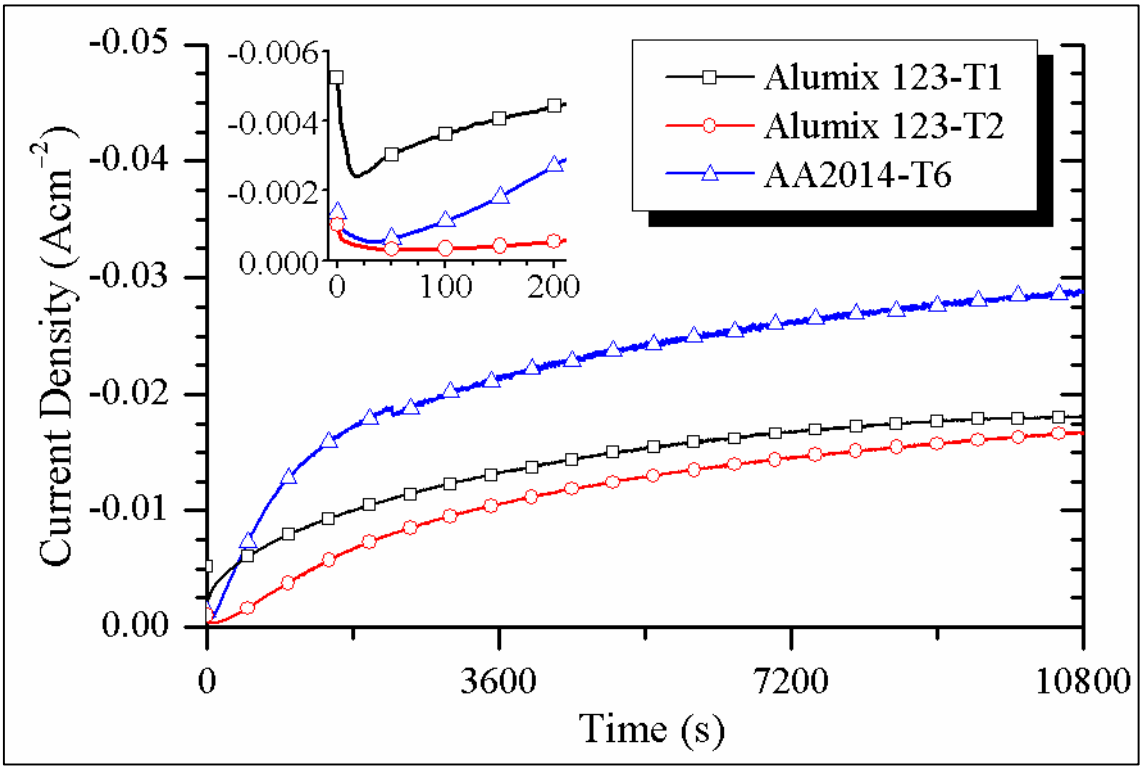

Figure 8.1 – Current transients during potentiostatic polarization at $-1.50V_{SCE}$.

In solution, the passive layer on aluminum has a duplex structure consisting of a porous partially hydrated outer layer comprised of aluminum hydroxides and an inner

barrier layer comprised of mostly amorphous alumina [113], which upon polarization to sufficiently negative potentials becomes totally hydrated and ionically conductive, allowing hydrogen evolution to take place directly on aluminum metal [125,127]. Complete hydration did not occur immediately however, as shortly after polarization the current passed on all three electrodes went through a minimum, Figure 8.1, which was caused by the generation of an anodic current related to barrier film formation prior to film hydration [119,124]. Eventually, the current passed on all three electrodes increased as the hydrated portion of the duplex film penetrated towards the metal and a stable oxide layer could no longer be maintained [125,127]. Under these conditions, intense alkalization led to the chemical dissolution of aluminum [125,127] which may be responsible for gradual changes in current after film hydration, as the surface area was increased from the alkaline etching or the film composition and conductivity was changed as alloying elements which do not oxidize were accumulated within the film.

When comparing the three electrodes, the current passed on AA2014-T6 appeared to increase faster and was maintained at a higher magnitude than the P/M materials which suggested that the total hydration of the passive film on AA2014-T6 occurs at a more noble potential than the P/M materials. These observations could be related to the surface state and composition of the P/M materials which, as a result of the sintering process, were found to possess a thicker refractory layer enriched with magnesium [224]. The concentration of magnesium on the surface of the P/M materials was believed to be in the oxidized state, and its presence could have affected the formation, growth, and ionic conductivity of the hydrated layer due to the stability of magnesium in alkaline conditions.

The refractory layer on the P/M materials may also be expected to exhibit lower electronic conductivity due to its increased thickness compared to the wrought material. This was somewhat alluded to by observations of the corrosion morphology at open circuit conditions [224] where localized attack in the P/M materials was not associated with copper- or iron-rich intermetallics which suggested the thick refractory layer retained integrity over these intermetallics which are not readily accessible for cathodic processes. Some characteristics of the refractory layer were revealed by the current transients at $-1.10V_{SCE}$, Figure 8.2, which corresponded to the potential domain where a stable oxide film was maintained and cathodic hydrogen evolution was the predominant cathodic process [102-108].

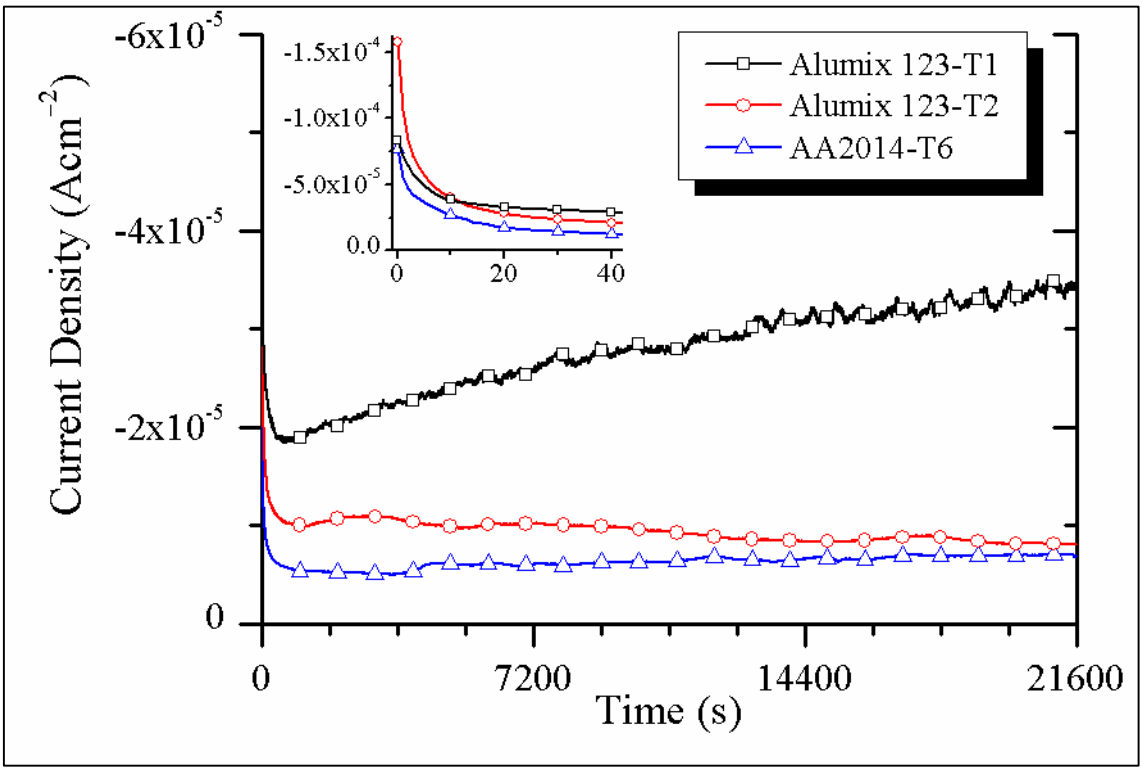

Figure 8.2 – Current transients during potentiostatic polarization at $-1.10V_{SCE}$.

The current passed on all three electrodes during potentiostatic polarization at –1.10V_{SCE} was comparable in magnitude, despite the significantly larger surface area of the P/M materials, particularly Alumix 123-T1. It is hypothesized that on a true per surface area basis AA2014-T6 can support more cathodic hydrogen evolution than the P/M materials, and that this was due to the greater accessibility of copper- and iron-rich intermetallics in AA2014-T6 to support such processes.

The net current passed on Alumix 123-T1 during potentiostatic polarization at –1.10V_{SCE} increased gradually with time which suggested that the cathodic component of the net current was increasing with time or the anodic component of the net current was decreasing with time. The former would imply the surface area available for cathodic hydrogen evolution or the efficiency of cathodic hydrogen evolution was increasing with time and could mean the refractory layer was gradually succumbing to breakdown in some areas. The possibility that the anodic current was decreasing may be equally significant due to the close relation of –1.10V_{SCE} to the OCP of Alumix 123-T1 [224], and in fact it can be seen in the current transients at –0.75V_{SCE}, Figure 8.3, that the anodic current of Alumix 123-T1 displayed a decaying transient which could be responsible for the behaviour in Figure 8.2.

The current transient for Alumix 123-T1 in Figure 8.3 corresponded to a region in the potentiodynamic polarization diagram where the current passed on Alumix 123-T1 was largely independent of applied potential [224] – this behaviour was characteristic of an electrode in the passive state and the current transient in Figure 8.3 would then be associated with the growth of a passive film. However, the growth of a passive film was not assumed for Alumix 123-T1 because of the presence of residual porosity which may be a site for propagating crevice corrosion, generating most of the anodic current. In the

case of crevice corrosion, the decaying transient in Figure 8.3 could be related to the repassivation of some creviced areas as the solubility product of the hydroxide in some areas was exceeded from the accumulation of anodic reaction products.

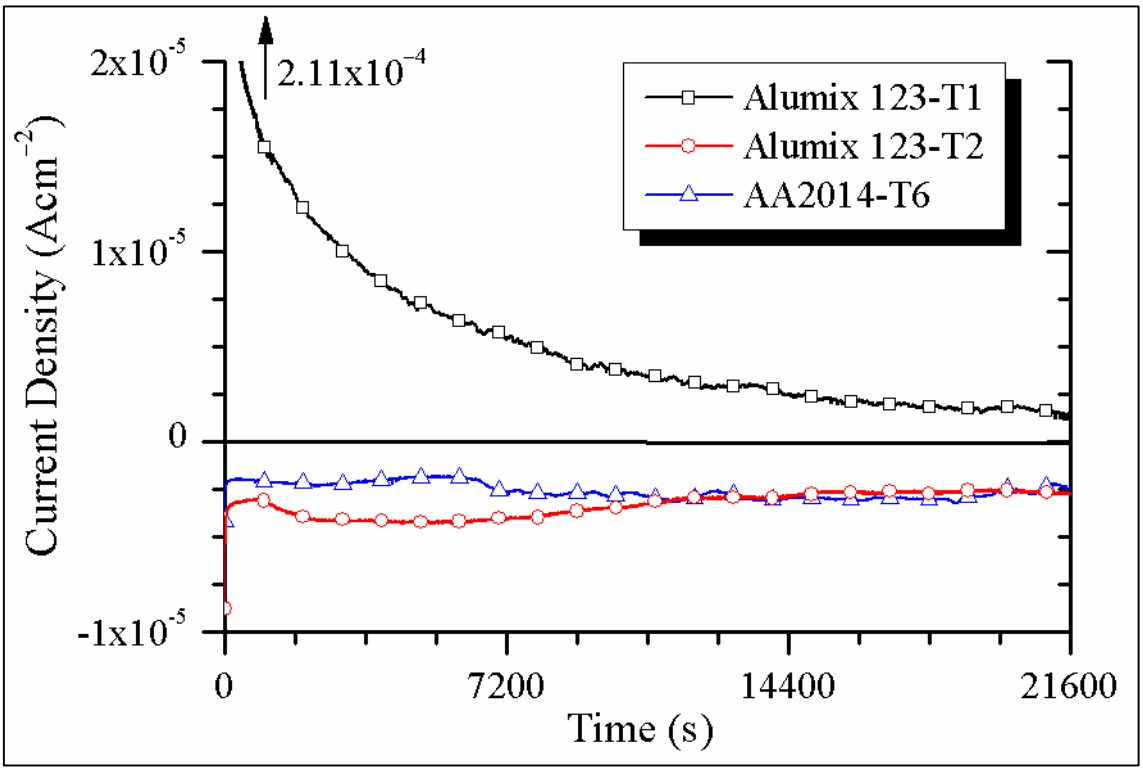

Figure 8.3 – Current transients during potentiostatic polarization at $-0.75V_{SCE}$.

The current transients for Alumix 123-T2 and AA2014-T6 at $-0.75V_{SCE}$, Figure 8.3, corresponded to a potential region which was marginally more negative than the OCP and cathodic oxygen reduction was the predominant cathodic process [102-108]. Both Alumix 123-T2 and AA2014-T6 displayed fairly steady current densities which were of comparable magnitude. In potentiodynamic polarization diagrams [224] the limiting diffusion current for oxygen reduction on Alumix 123-T2 was significantly larger than AA2014-T6, however in potentiostatic current transients the two current densities became

comparable soon after polarization, Figure 8.3. This behaviour was particularly interesting for Alumix 123-T2 considering the OCP stabilized at the pitting potential where the corrosion was under cathodic control [224] and a reduction in cathodic current would correspond to a reduction in the corrosion rate.

Above the pitting potential considerable active dissolution of Alumix 123-(T1, T2) and AA2014-T6 is possible, as shown by the current transients for $-0.70V_{SCE}$, Figure 8.4. Initially, the current passed on Alumix 123-T1 went through a pronounced minimum which can be interpreted as the growth of a barrier film prior to the adsorption of chlorine on the oxide layer [111,147]. On all three electrodes, there was an incubation period before the current became substantial. This rise in current could be related to the adsorption of chloride on the oxide surface which affects the electric field in the double layer in a manner that accelerates the transport of aluminum ions into solution [111,142].

The current passed on the P/M materials during potentiostatic polarization at $-0.70V_{SCE}$ increased rapidly to pronounced maxima which were only maintained momentarily before the current then decreased to a point where it then remained largely static for the duration of the polarization, Figure 8.4. The observation of the current peak in Alumix 123-T2, whose sizing operation reduced total surface porosity through plastic deformation and sealed residual porosity with sizing fluid, indicated that residual porosity did not play a major role in determining the current transients of the P/M materials in Figure 8.4. It is possible that the current peak for the P/M materials was related to the unique refractory layer formed as a result of the sintering process that was found to be enriched with magnesium [224]. The refractory layer on the P/M materials appeared to lose stability rapidly which would indicate that these materials were more affected by the adsorption of chlorine than the wrought material.

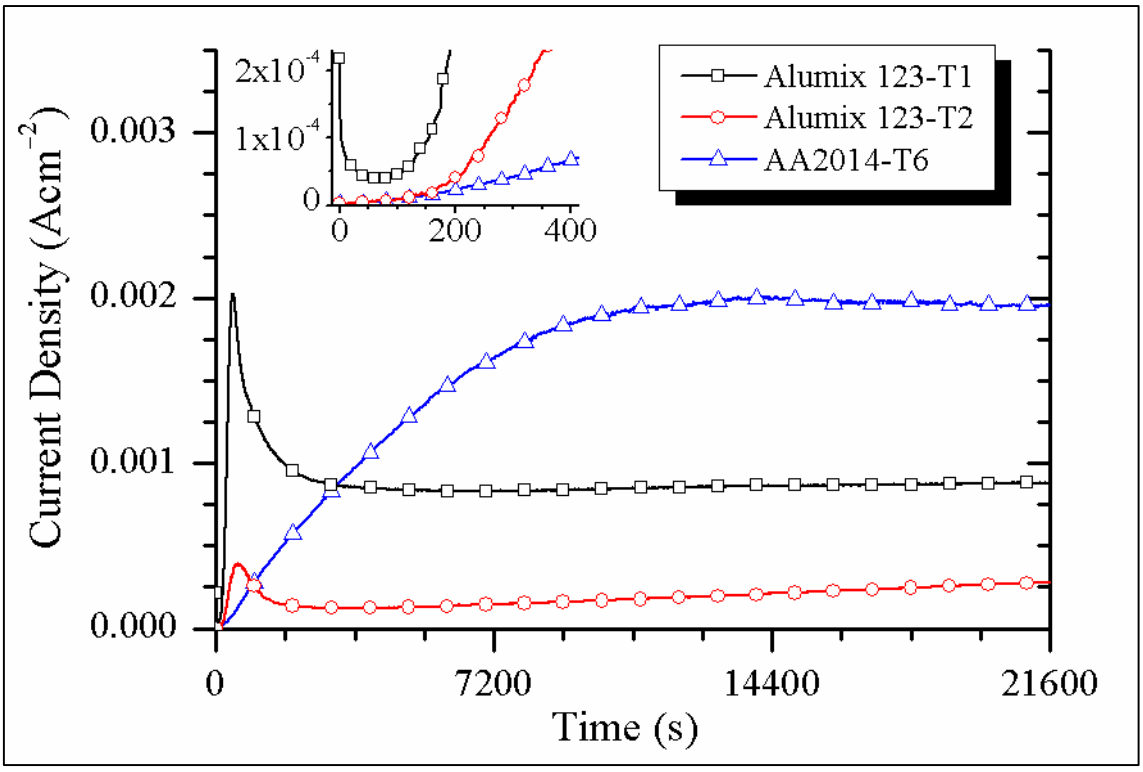

Figure 8.4 – Current transients during potentiostatic polarization at –0.70V_{SCE}.

The current passed on AA2014-T6 during potentiostatic polarization at –0.70V_{SCE} gradually increased to a maximum where it remained constant for the duration of polarization, Figure 8.4. The gradual increase in current was due to an increase in the total number of pits or the growth of existing pits, and a limiting current density per pit may result from ohmic control at the pit entrance or mass transfer control within them [111,141]. The attainment of a steady state maximum current density indicated that the current density at individual pits was decreasing and/or that some pits were eventually repassivating [111].

The current transients for polarization at –0.50V_{SCE}, Figure 8.5, corresponded to a potential region where breakdown occured rapidly and the steady state dissolution of aluminum was limited by convective diffusion. At this potential, vigorous gas evolution

and grain fallout was apparent on all three electrode materials. The evolving gas was probably hydrogen produced from the reaction of subvalent aluminum ions with water at the oxide/solution interface, usually referred to as the 'negative difference effect' (NDE) [108,111]. The NDE occurs at smaller anodic overpotentials, but is more apparent at –0.50V_{SCE} because the flux of subvalent aluminum ions to the oxide/solution interface is increased in proportion to anodic polarization. This hydrogen evolution during anodic polarization prevents the formation of a salt film on aluminum even at high rates of dissolution [130].

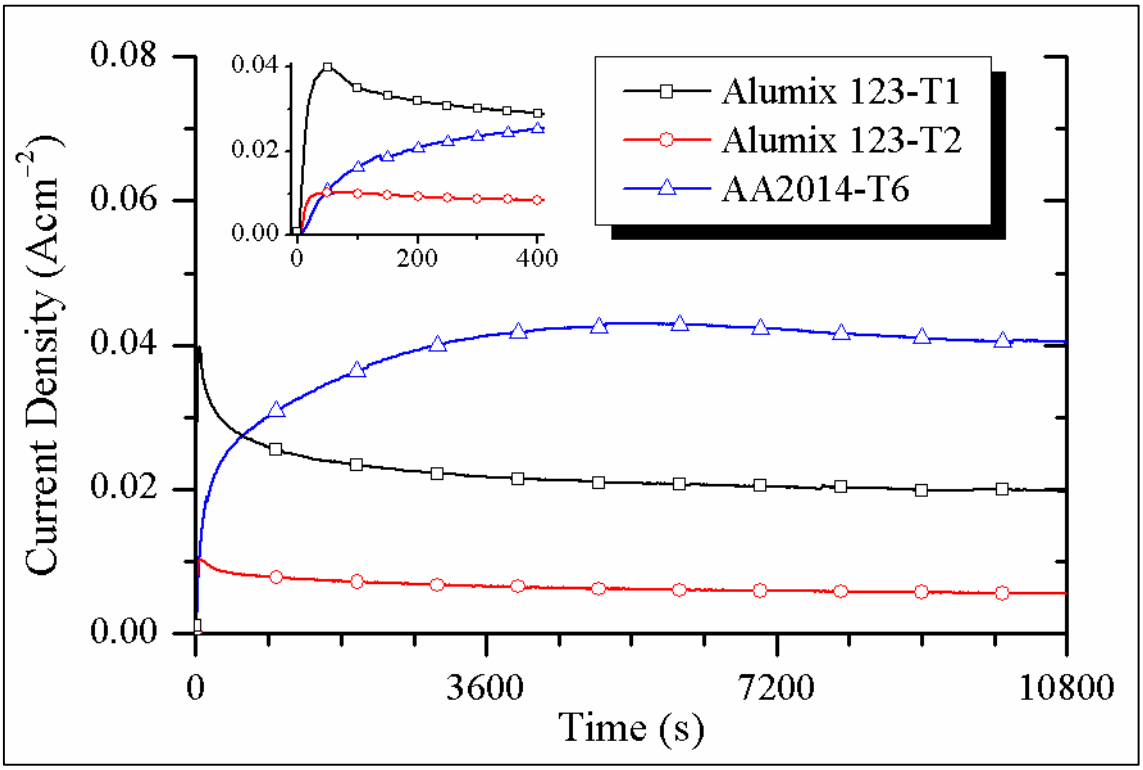

Figure 8.5 – Current transients during potentiostatic polarization at –0.50V_{SCE}.

8.3.2 Microstructure after Potentiostatic Polarization

8.3.2.1 Alumix 123-(T1, T2)

Prior examinations of the microstructure of Alumix 123-(T1, T2) showed a unique refractory layer is formed on the surface of the compacts as a result of the sintering process, which by EDS analyses was found to consist of oxygen (*ca.* 8wt%), carbon (*ca.* 6wt%), and magnesium (*ca.* 2wt%) [224]. Lubricant residues which redeposited during the sintering process were identified by SEM and EDS analyses in discrete areas on the surface of Alumix 123-(T1, T2) [224]. SEM, EDS, and XRD analyses identified two major intermetallic phases in Alumix 123-(T1, T2) [224] which were distributed predominantly along grain boundaries: one an aluminum-based intermetallic rich in copper (*ca.* 40wt%) and containing minor amounts of magnesium (*ca.* 2wt%) and silicon (*ca.* 1wt%); and the other an aluminum-based intermetallic rich in iron (*ca.* 30wt%) but also containing copper (*ca.* 14wt%) and silicon (*ca.* 7wt%). After 2 hours corrosion at open circuit conditions, microstructural analyses of Alumix-(T1, T2) showed that localized corrosion did not initiate at copper- or iron-rich intermetallics which was attributed to the high integrity of the refractory layer over these intermetallics [224].

During potentiostatic polarization at $-1.50V_{SCE}$ the refractory layer on Alumix 123-(T1, T2) could not be maintained and the intense alkalization etched the electrode face. SEM and EDS analyses showed some copper- and iron-rich remnants of intermetallics remained embedded in the surface film after polarization at $-1.50V_{SCE}$, which demonstrated the stability of these intermetallics in highly alkaline conditions. The surface film was found by EDS analyses to be enriched with copper, magnesium, and silicon, which suggested that the copper- and iron-rich phases are subject to dealloying of magnesium and silicon in alkaline conditions. Copper originating from the matrix was

probably accumulated in the surface film since it did not oxidize as the rest of the matrix is dissolved.

SEM and EDS analyses of the cross section of Alumix 123-T1 after potentiostatic polarization at $-1.50V_{SCE}$ revealed that a similar film was formed within residual porosity near the electrode face, which suggested that film hydration and hydrogen evolution occured within residual porosity, but may not be as substantial as on the electrode face as less copper was detected in the film within residual porosity. This is supported by electrochemical measurements which showed that the current passed on Alumix 123-T1 was only slightly larger in Alumix 123-T2 indicating its electrochemically active area was only marginally greater than in Alumix 123-T2, despite its much higher surface area.

Microstructural analyses of Alumix 123-(T1, T2) after potentiostatic polarization at $-1.10V_{SCE}$ showed areas of darker contrast distributed throughout the microstructure which were found by EDS analyses to be enriched with oxygen (*ca.* 20wt%). It is not clear if these areas were original sites where lubricant residue was redeposited during sintering because EDS analyses showed carbon was not concentrated in these areas. Upon close examination of these areas cracks in the refractory layer were observed, Figure 8.6, which may be evidence of hydrogen evolution [137]. This suggested that film breakdown allowed for hydrogen evolution to occur on the matrix as well as copper- and iron-rich intermetallics. In some areas film breakdown was associated with a colloidal corrosion product, Figure 8.6, which may have formed as a result of the cathodic processes occurring in these areas. The observation of film breakdown on Alumix 123-T1 thereby suggested that part of the increase in current passed during potentiostatic polarization at $-1.10V_{SCE}$ was due to an increase in the area available for cathodic hydrogen evolution as the refractory layer succumbed to breakdown.

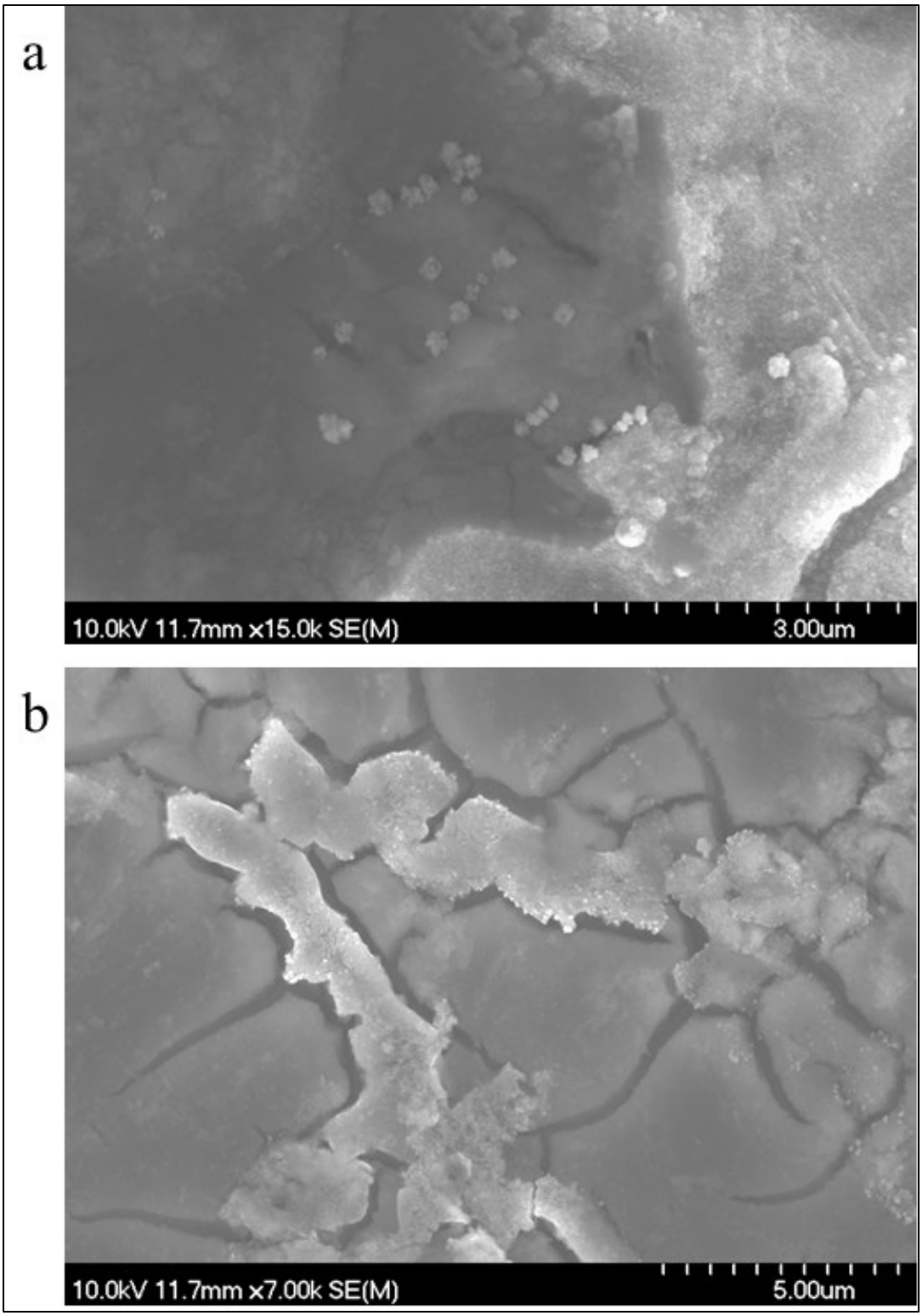

Figure 8.6 – SEM micrograph of Alumix 123-T1 after potentiostatic polarization at –1.10V_{SCE} showing areas of film breakdown: (a) in the matrix; (b) over a copper-rich intermetallic.

Microstructural analyses of Alumix 123-T2 after potentiostatic polarization at –0.75V_{SCE}, Figure 8.7, has shown film breakdown also occurs in the domain of cathodic oxygen reduction. The hemispherical pit shape, Figure 8.7, is characteristic of cathodic pitting [124] and suggested that oxygen reduction was capable of occurring on the matrix.

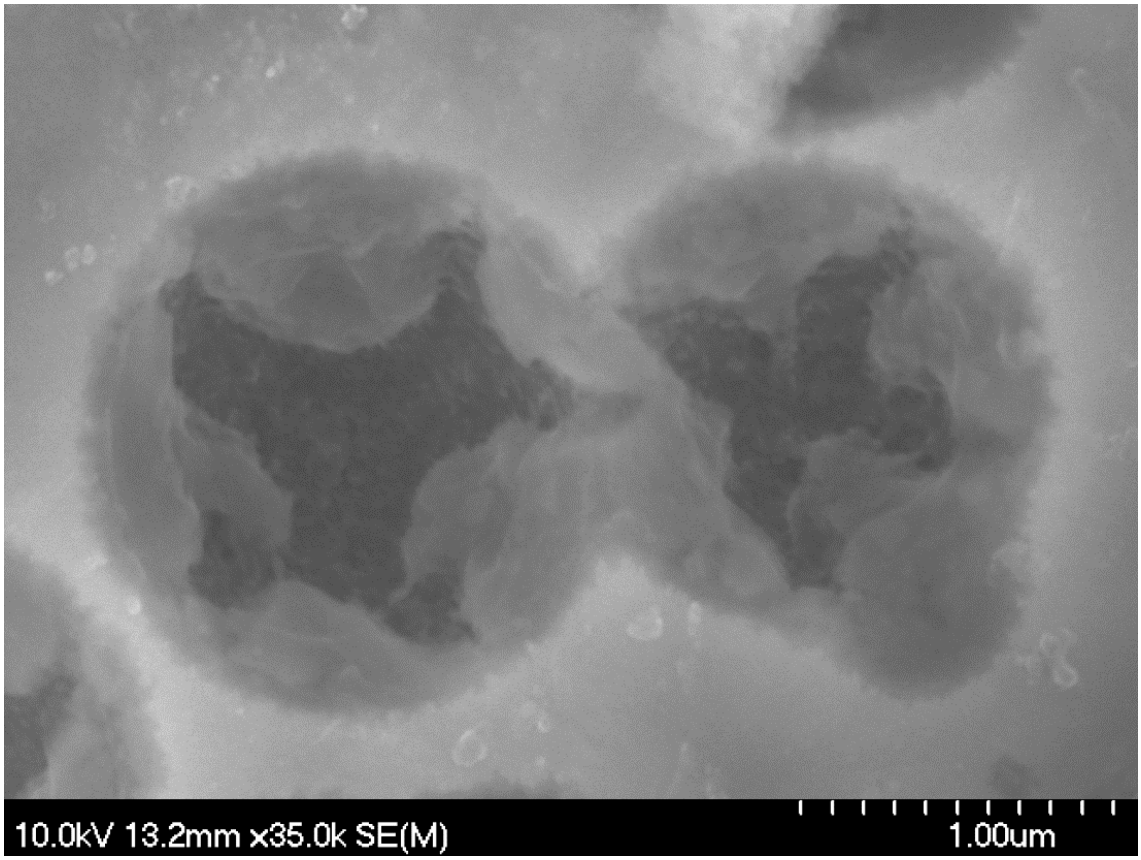

Figure 8.7 – SEM micrograph of Alumix 123-T2 after potentiostatic polarization at –0.75V_{SCE} showing two hemispherical cathodic pits.

Potentiostatic polarization of Alumix 123-T1 at $-0.75V_{SCE}$ yielded a net anodic current which is hypothesized to be generated from creviced areas within residual porosity. The structure of residual porosity in Alumix 123-T1 after potentiostatic polarization at $-0.75V_{SCE}$ is shown in Figure 8.8 and Figure 8.9. There was a large nodular corrosion product around some porosity, Figure 8.8. This feature appeared as though it originated from within the porosity, and in some instances it had evolved to a point that reduced the area of the pore entrance. The cross section of Alumix 123-T1, Figure 8.9, shows that there were significant amounts of corrosion product accumulated within some porosity. These observations are consistent with the crevice corrosion model where the anodic current at open circuit conditions is primarily generated from creviced areas within residual porosity. Electrochemical measurements indicated that as the anodic reaction proceeded the current generated gradually decayed which could be the result of some creviced areas repassivating as the solubility product of aluminum hydroxide was exceeded leading to precipitation within creviced areas, Figure 8.9, and flocculation in areas immediately surrounding them, Figure 8.8.

The intermetallics on the electrode face of Alumix 123-T1 may have also played a role in the corrosion process at $-0.75V_{SCE}$, as shown in Figure 8.10. In some areas there was an acicular corrosion product, Figure 8.10. EDS analyses suggested it was formed preferentially over copper-rich intermetallics. EDS analyses of the areas of lighter contrast in Figure 8.10 yielded an approximate composition of 5wt% Cu, 2wt% Si, and 1wt% Mg, which was a similar level of copper detected in the matrix. It is not immediately clear if these were intermetallics that existed prior to corrosion but could not be detected previously or were a direct consequence of corrosion.

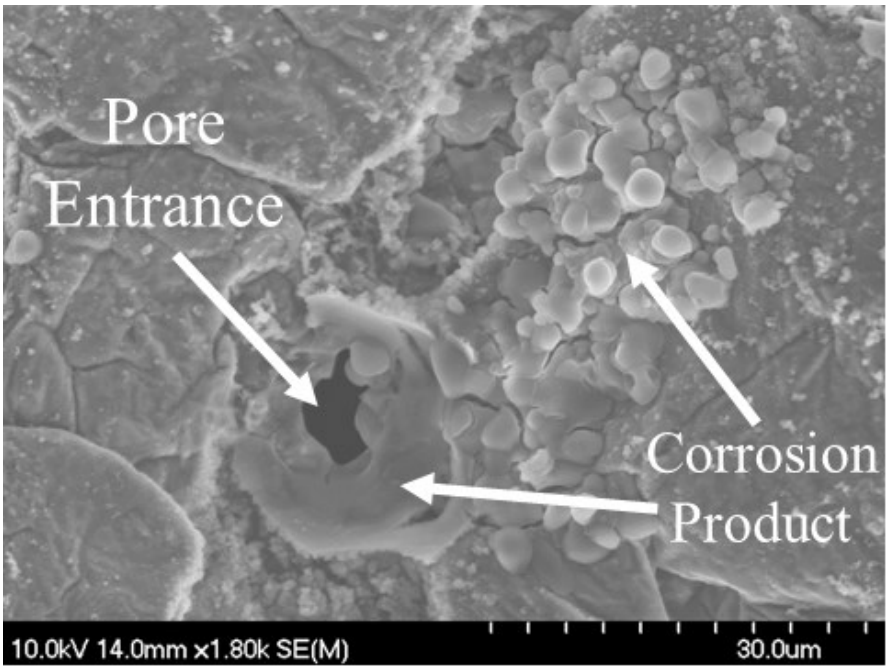

Figure 8.8 – SEM micrograph of Alumix 123-T1 after potentiostatic polarization at –0.75V_{SCE} showing the deposition of corrosion product near residual porosity.

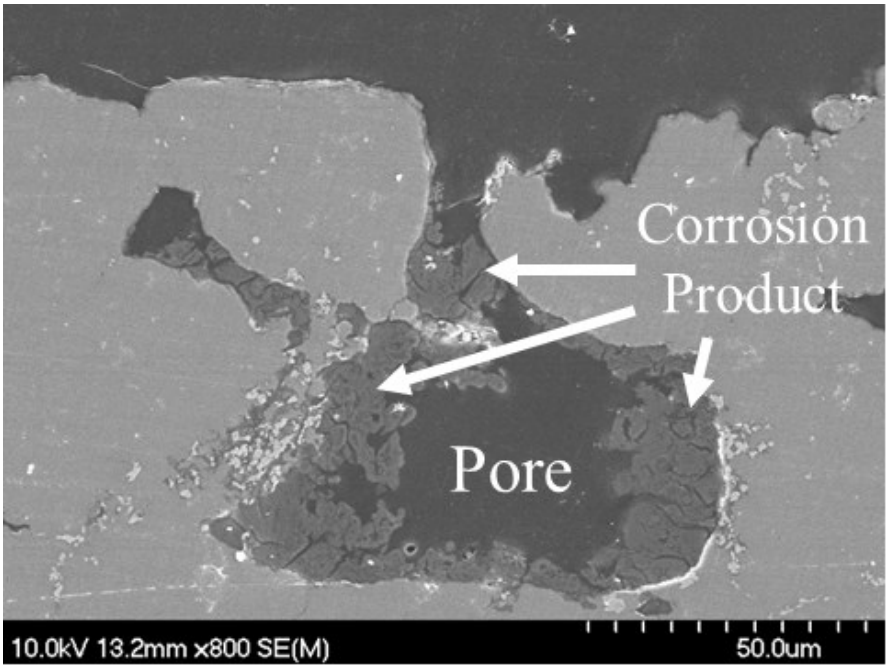

Figure 8.9 – SEM micrograph of the cross section of Alumix 123-T1 after potentiostatic polarization at –0.75V_{SCE} showing corrosion product accumulated in residual porosity.

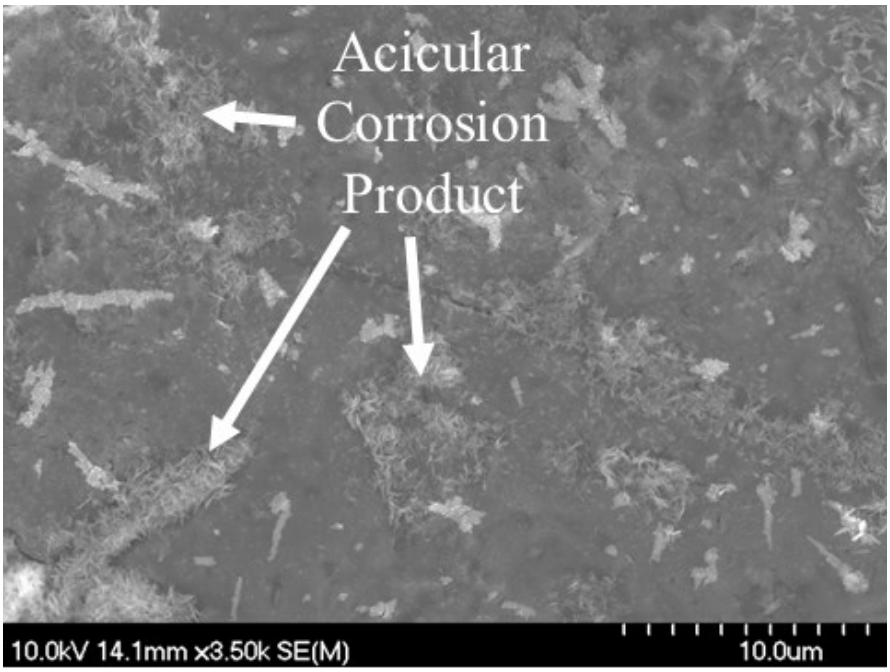

Figure 8.10 – SEM micrograph of Alumix 123-T1 after potentiostatic polarization at –0.75V_{SCE} showing an acicular corrosion product in some areas.

Above the pitting potential, the oxide layer loses stability and active dissolution of Alumix 123-(T1, T2) was expected. This was evident by the significant amount of nodular corrosion product generated on the electrode face of Alumix 123-T1 after polarization at –0.70V_{SCE}, Figure 8.11. The morphology of the nodular corrosion product and its composition by EDS analyses were consistent with Bayerite [113]. Although –0.70V_{SCE} is noble to the pitting potential of Alumix 123-(T1, T2) [224], there was no obvious pitting in matrix grains and the distribution of corrosion product on the electrode face was more characteristic of uniform corrosion. However, in the cross section of Alumix 123-(T1, T2) intergranular corrosion was very prevalent, Figure 8.12, in some areas having penetrated over 200µm inward from the electrode face. Since most intermetallics were located along grain boundaries, they probably contributed to the extensive amount of intergranular corrosion observed. The current peak during

potentiostatic polarization of Alumix 123-(T1, T2) at $-0.70V_{SCE}$ was hypothesized to be related to the refractory layer on the P/M parts but it was difficult to discern whether this was truly the case from microstructural analyses.

After potentiostatic polarization at $-0.50V_{SCE}$ the majority of corrosion in Alumix 123-(T1, T2) remained intergranular in nature, Figure 8.13. However, crystallographic pitting of grain interiors was also observed. The attack from polarization at $-0.50V_{SCE}$ resembled exfoliation corrosion and penetrated to a depth exceeding 500μm from the electrode face. The grains may have been detached from the electrode by the generation of a voluminous corrosion product at grain boundaries or by mechanical agitation from intense hydrogen evolution.

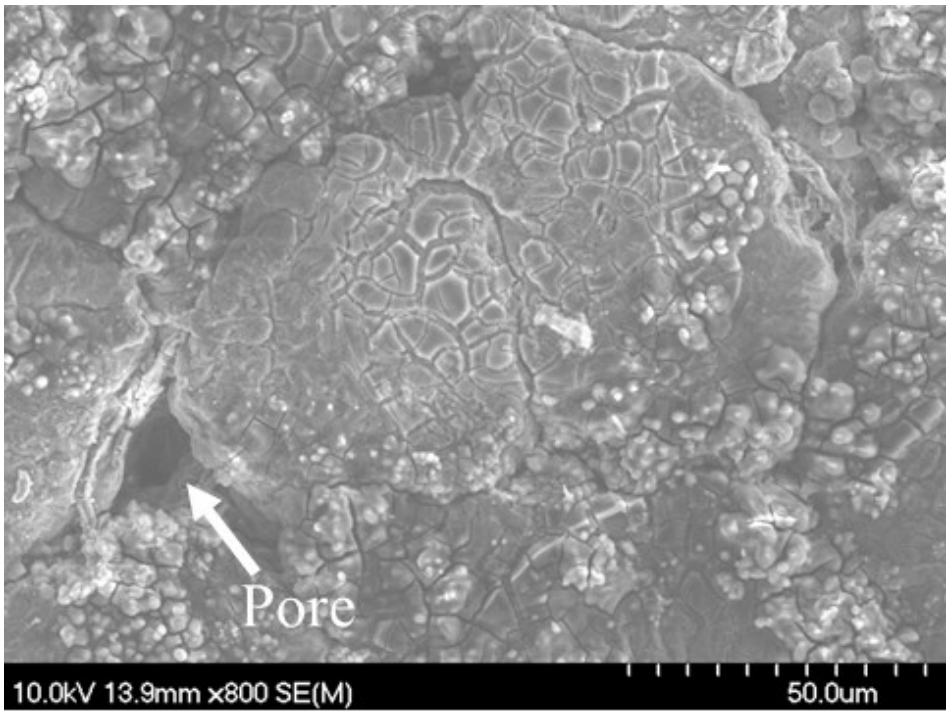

Figure 8.11 – SEM micrograph of Alumix 123-T1 after potentiostatic polarization at $-0.70V_{SCE}$ showing a uniform distribution of corrosion product.

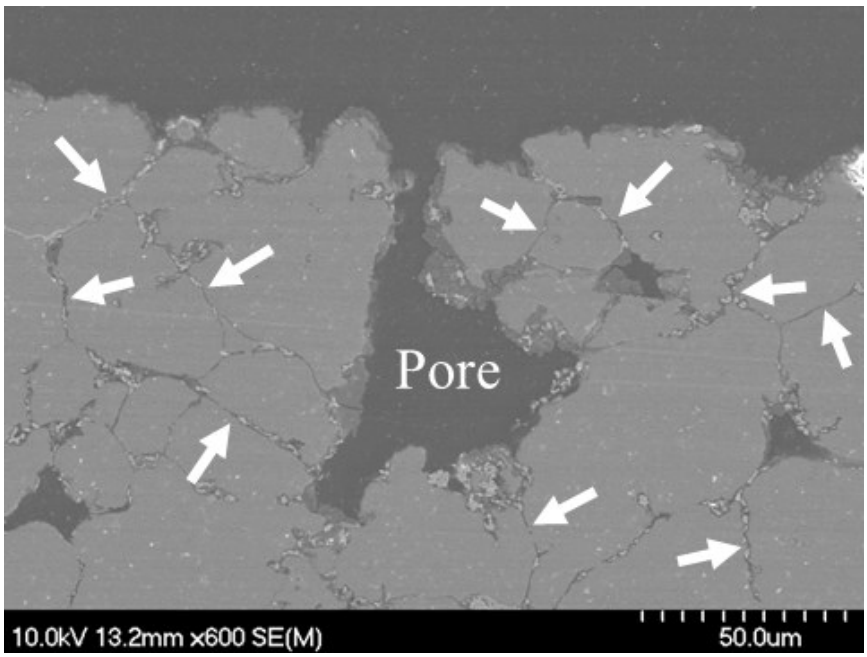

Figure 8.12 – SEM micrograph of the cross section of Alumix 123-T1 after potentiostatic polarization at $-0.70V_{SCE}$ showing intergranular corrosion (indicated by arrows).

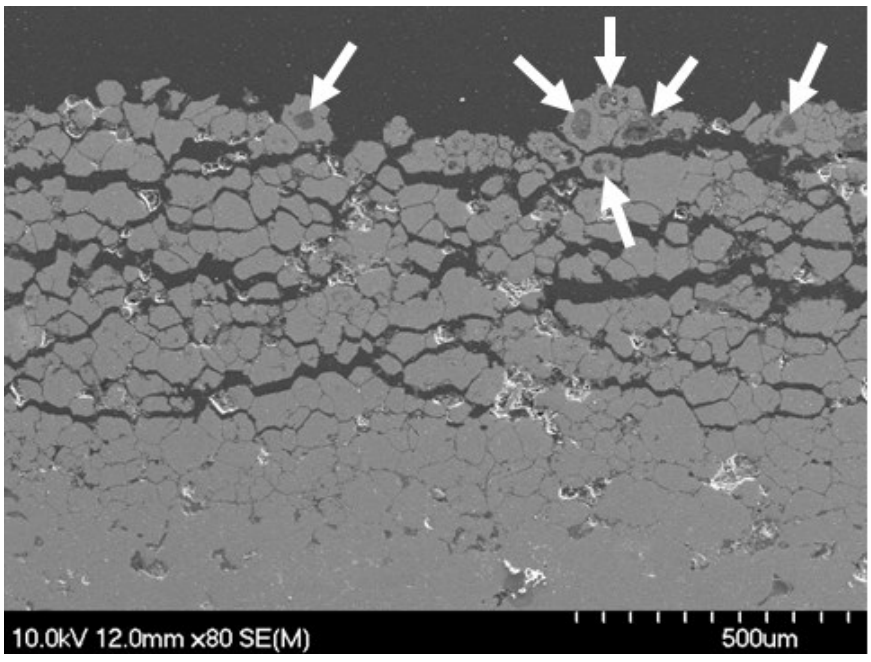

Figure 8.13 – SEM micrograph of the cross section of Alumix 123-T1 after potentiostatic polarization at $-0.50V_{SCE}$ showing sporadic crystallographic pitting (indicated by arrows) and extensive intergranular corrosion.

8.3.2.2 AA2014-T6

In a companion manuscript [224], θ-$CuAl_2$ and α-AlFeMnSi ($(CuFeMn)_3Si_2Al_{15}$) intermetallics were identified in the microstructure of AA2014-T6 by SEM, EDS, and XRD analyses. Smaller intermetallic particles which were distributed throughout the matrix could not be identified but were hypothesized to be Q-phase ($Cu_2Mg_8Si_6Al_5$) precipitates or small θ' and θ-$CuAl_2$ precipitates along grain boundaries. Part of the role of intermetallics in the corrosion of AA2014-T6 was revealed by SEM and EDS observations of the localized corrosion associated with these intermetallics at open circuit conditions [224]. Both θ-$CuAl_2$ and α-AlFeMnSi were believed to have behaved as high efficiency cathodes in the corrosion of AA2014-T6 [224].

SEM and EDS analyses of AA2014-T6 after potentiostatic polarization at $-1.50V_{SCE}$ are consistent with these hypotheses. A significant amount of the electrode face was etched away by the intense alkalization at $-1.50V_{SCE}$. However, a copper-rich dealloyed structure of θ-$CuAl_2$ and an iron-rich dealloyed structure of α-AlFeMnSi remained embedded in the surface film, thereby demonstrating the stability of these intermetallics under intense alkalization. The cross section of the electrode showed the surface film to be approximately 25μm thick and EDS analyses showed enrichment with copper, manganese, magnesium, silicon, and zinc as compared to the underlying matrix. It appeared that under these highly alkaline conditions manganese and silicon were dealloyed from α-AlFeMnSi while iron was not, undoubtedly due to the stability of iron in alkaline conditions. The concentration of copper, magnesium, and zinc in the film probably originated from the matrix as it was etched away from the intense alkalization.

The efficiency of the intermetallics for hydrogen evolution, under conditions where the oxide layer remained stable, can be construed from the microstructural observations after potentiostatic polarization at $-1.10V_{SCE}$, Figure 8.14. The matrix in the immediate vicinity of most intermetallic particles appeared to have been removed, Figure 8.14, yet this was expected to have occurred during the 1 hour stabilization at open circuit conditions prior to potentiostatic polarization [224]. There was cracking in the matrix surrounding some intermetallic particles, Figure 8.14, that can be considered to be evidence of hydrogen evolution [137]. Most cracking was observed surrounding θ-$CuAl_2$, which may indicate that the majority of cathodic current for hydrogen evolution was supported by θ-$CuAl_2$.

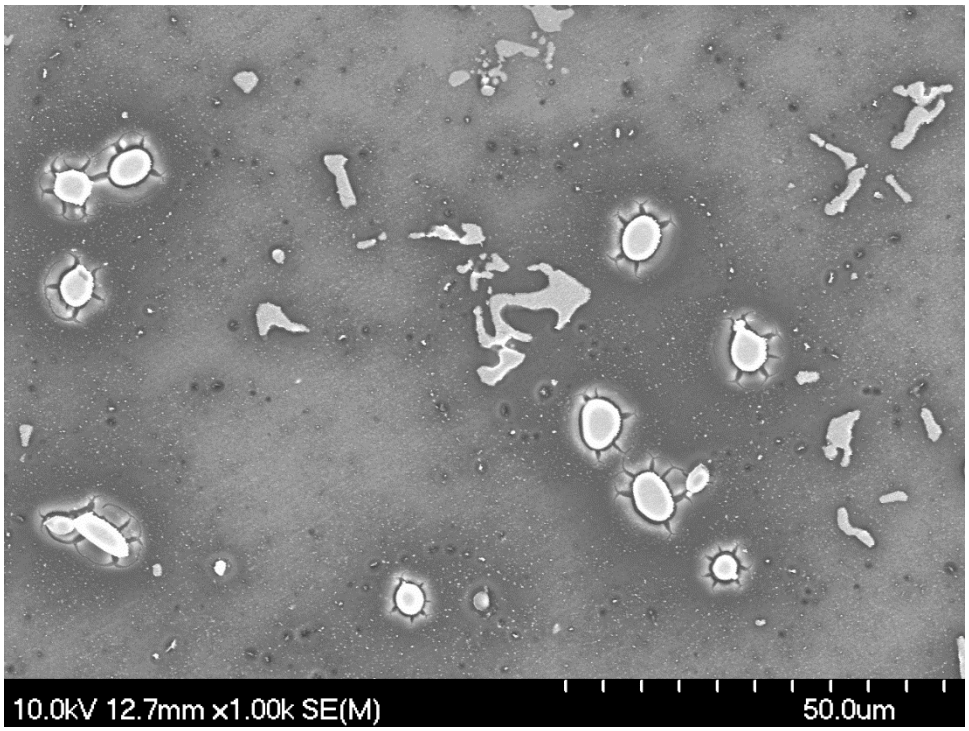

Figure 8.14 – SEM micrograph of AA2014-T6 after potentiostatic polarization at $-1.10V_{SCE}$ showing cracking in the matrix surrounding θ-$CuAl_2$, possibly a result of hydrogen evolution.

In addition, there appeared to be a fine nano-scale deposit on θ-$CuAl_2$ and α-AlFeMnSi after potentiostatic polarization at $-1.10V_{SCE}$, Figure 8.15, that preferentially nucleated along polishing lines. The scale of the deposit was too small to be accurately analysed by EDS, however, copper- and iron-rich intermetallics are known to be cathodic sites for the redeposition of copper ions which have been liberated during corrosion [155,160,163,177]. The mechanism of copper redistribution during corrosion of the 2*xxx* series aluminum alloys has been studied extensively [123,159,166], yet the role of θ-$CuAl_2$ in the liberation of copper remains controversial. In Ref. [166] a mechanism was proposed for the redistribution of copper from S-phase ($CuMgAl_2$) and θ-$CuAl_2$, where the intermetallics were selectively dealloyed of active elements leaving copper-rich remains which coarsened to a crystalline nanoporous structure and were subject to the non-Faradaic liberation of copper clusters by mechanical means (*e.g.* convection of the electrolyte, hydrogen evolution). Once the copper clusters were electrically isolated from the electrode, they attained their own OCP and were able to oxidize [166]. However, it is unclear whether this mechanism is significant in alloys which do not contain the S-phase intermetallic [123], such as AA2014. In the work of Ref. [123], during *in situ* atomic emission spectroelectrochemistry (AESEC) analysis of corroding AA2214, copper clusters were not detected in the electrolyte. Another potential source of copper may be the small intermetallics distributed throughout the matrix and along grain boundaries, as the attack around these intermetallics was frequently so extensive that the particle became dislodged or electrically isolated from the matrix, which allowed for the oxidation of copper.

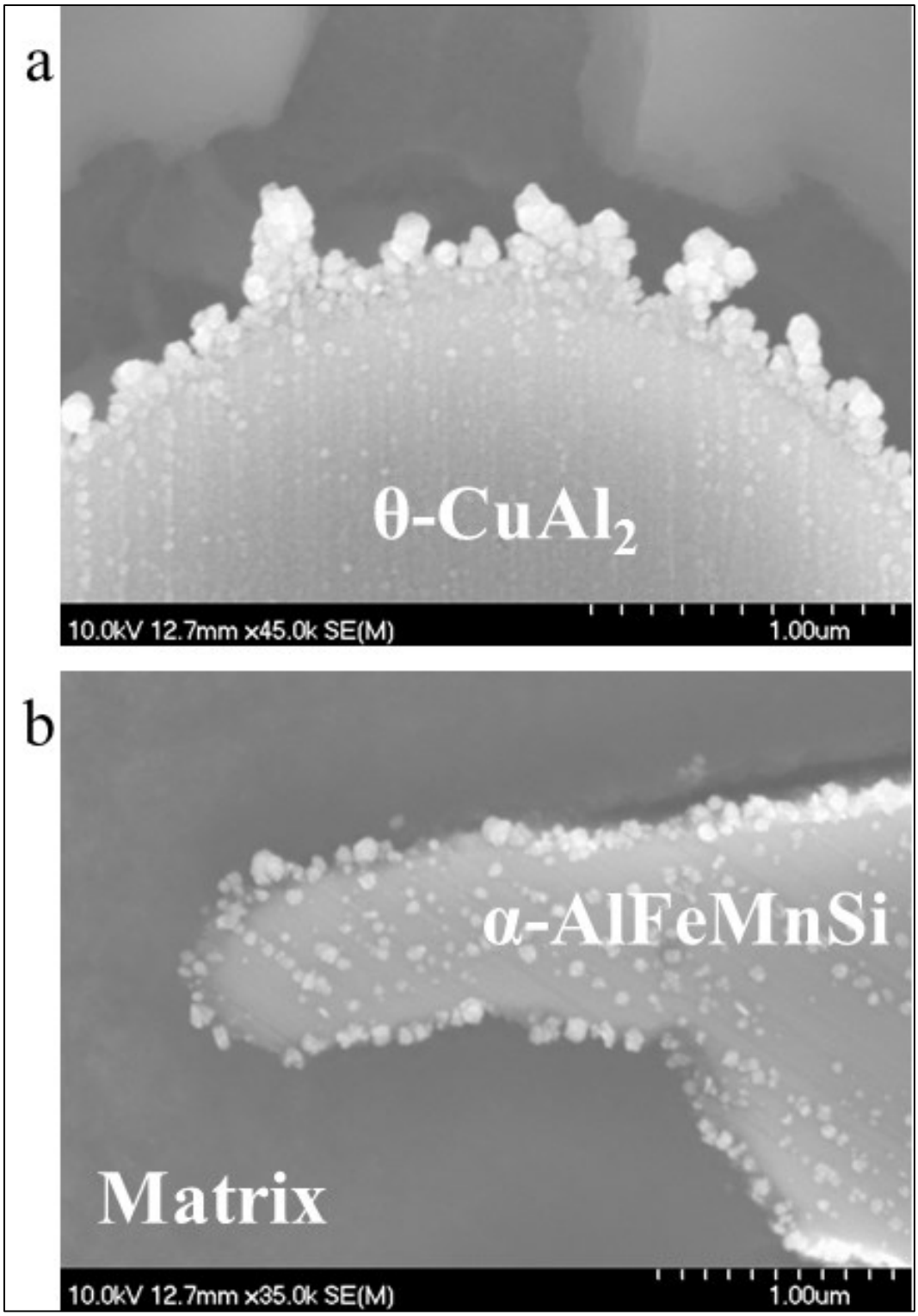

Figure 8.15 – SEM micrographs of AA2014-T6 after potentiostatic polarization at –1.10V_{SCE} showing: (a) θ-$CuAl_2$ and (b) α-AlFeMnSi. The fine, nodular deposit on the intermetallics is postulated to be rich in copper.

The α-AlFeMnSi intermetallic may have also played a role in the redistribution of copper during the corrosion of AA2014-T6, as suggested by microstructural analyses after potentiostatic polarization at $-0.75V_{SCE}$, Figure 8.16. Around the periphery of α-AlFeMnSi there appeared areas of lighter contrast which were too small for accurate analyses by EDS but were postulated to be rich in copper given their bright atomic contrast. If these deposits were rich in copper, their location around the periphery of α-AlFeMnSi suggested that copper may have been liberated from the matrix during cathodic trenching, oxidized, and then redeposited on the α-AlFeMnSi cathodes in the immediate vicinity. As the aluminum matrix was dissolved chemically, any copper present in solid solution should not oxidize, so long as it remains electrically connected to the bulk electrode. However, due to the small amount of copper in the matrix (*ca.* 4.5wt%) it cannot be selectively dealloyed of aluminum in the same way as copper-rich intermetallics. Therefore, copper, or copper-rich fragments, may simply pass into the electrolyte without oxidizing, and the liberation of copper in this manner may be considered non-Faradaic in nature. Once electrically isolated from the bulk electrode, the fragments attain their own OCP, which allows copper to oxidize. The close proximity of $-0.75V_{SCE}$ to the OCP of AA2014-T6 [224] suggested that the deposition of copper may play a role in the cathodic process at open circuit conditions.

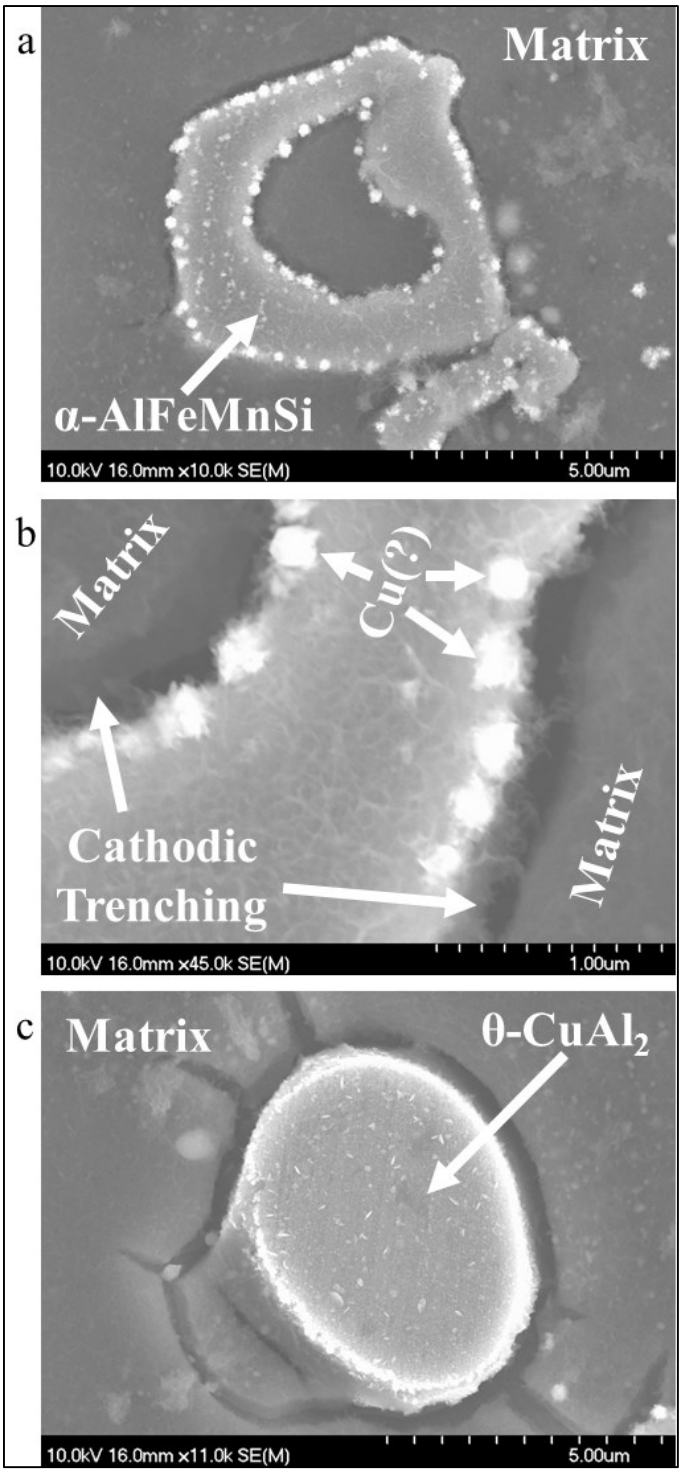

Figure 8.16 – SEM micrographs of AA2014-T6 after potentiostatic polarization at –0.75V_{SCE} showing: (a, b) α-AlFeMnSi and (c) θ-$CuAl_2$. It is postulated that cathodic trenching around α-AlFeMnSi liberated copper from the matrix in a non-Faradaic process.

Deposition on θ-$CuAl_2$ was less apparent after potentiostatic polarization at –0.75V_{SCE}, Figure 8.16, and there was only minor cracking in the matrix surrounding θ-$CuAl_2$, probably due to the lower amount of hydrogen evolution occurring at this potential. The dealloyed structure of θ-$CuAl_2$ was especially apparent in Figure 8.16 and in some areas platelets were observed on the surface of the dealloyed structure. The platelets may have formed from occluded electrolyte remaining in the highly porous structure even after thorough washing, from which a salt is precipitated during drying.

The microstructure of AA2014-T6 after potentiostatic polarization at –0.70V_{SCE}, Figure 8.17, shows that above the pitting potential the matrix is subject to dissolution via crystallographic pitting and intergranular corrosion was able to propagate deep within the electrode, in some areas observed to extend to depths over 200μm from the electrode face. The fact that existing pits appeared to have growth to a substantial size, Figure 8.17, suggested that at least part of the increasing anodic current during potentiostatic polarization at –0.70V_{SCE} was due to the growth of this feature.

As may be expected, the amount of matrix dissolution increased from potentiostatic polarization at –0.50V_{SCE}, Figure 8.18. At this noble potential, intergranular corrosion was much less apparent and crystallographic pitting initiated on virtually the entire electrode face with the depth of attack having extended to approximately 500μm below the surface. Pitting appeared to undercut some grains which may eventually detach from continued pitting or from mechanical agitation during intense hydrogen evolution.

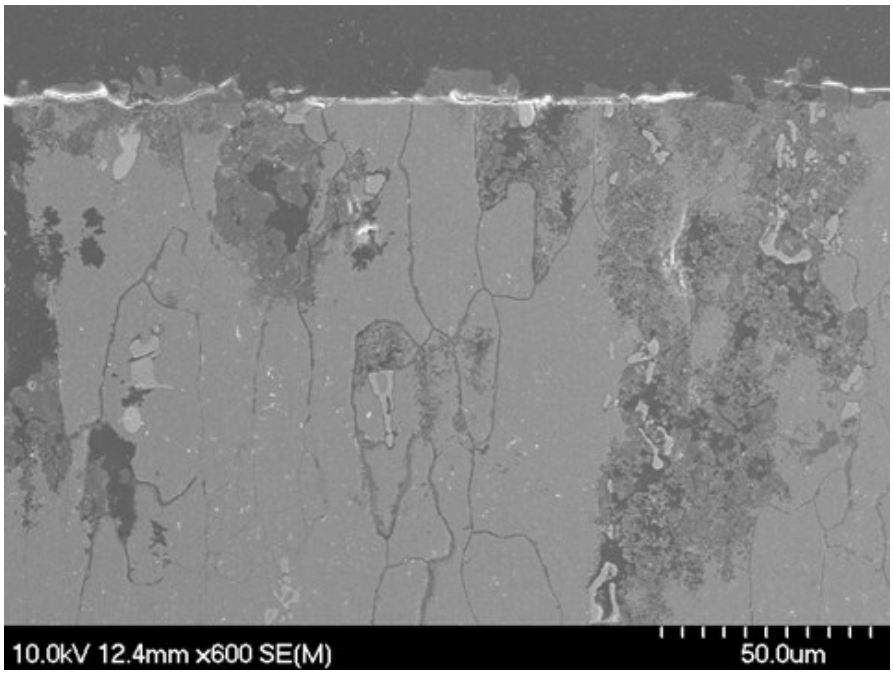

Figure 8.17 – SEM micrograph of the cross section of AA2014-T6 after potentiostatic polarization at –0.70V_{SCE} showing crystallographic pitting and intergranular corrosion.

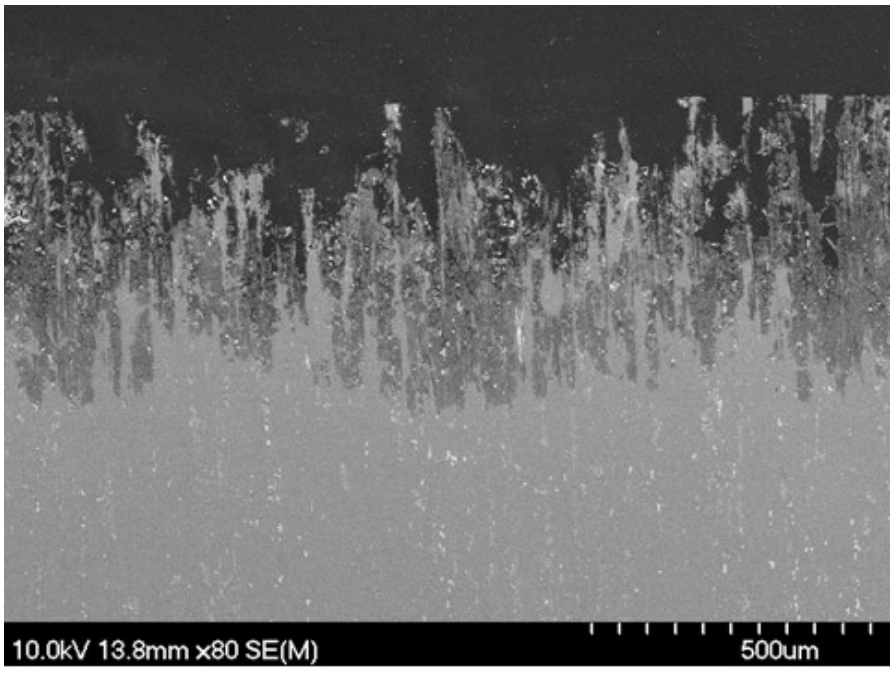

Figure 8.18 – SEM micrograph of the cross section of AA2014-T6 after potentiostatic polarization at –0.50V_{SCE} showing extensive crystallographic pitting.

8.4 CONCLUSIONS

In Alumix 123-(T1, T2), cathodic hydrogen evolution and oxygen reduction were associated with film breakdown occurring on the matrix as well as copper- and iron-rich intermetallics. Under highly alkaline conditions these intermetallics were selectively dealloyed of active elements leaving copper- and iron-rich remains.

At potentials more negative than the pitting potential, the majority of anodic current passed on Alumix 123-T1 was generated from creviced areas within residual porosity. The creviced areas eventually repassivated when the concentration of anodic reaction products exceeded the solubility limit and precipitation occurred.

At potentials noble to the pitting potential, Alumix 123-(T1, T2) display unusual current transients and the vast majority of attack was intergranular in nature. Crystallographic pitting was scarcely observed even at highly anodic potentials. The high tendency for intergranular corrosion could be related to the preferential location of intermetallics in these areas.

In AA2014-T6, cathodic hydrogen evolution and oxygen reduction primarily occurred on θ-$CuAl_2$ and α-AlFeMnSi intermetallics. Under highly alkaline conditions these intermetallics were selectively dealloyed of active elements leaving copper- and iron-rich remains.

SEM observations of AA2014-T6 suggest that cathodic deposition of copper occurred on θ-$CuAl_2$ and α-AlFeMnSi particles and that cathodic trenching around α-AlFeMnSi particles may have liberated copper from the matrix in a non-Faradaic process. At potentials noble to the pitting potential, extensive attack of AA2014-T6 by crystallographic pitting and intergranular corrosion was observed.

8.5 ACKNOWLEDGEMENTS

The authors gratefully acknowledge the National Sciences and Engineering Research Council of Canada (NSERC) and AUTO21 Network of Centers of Excellence for providing financial support during this work. The authors would also like to thank the Institute for Research in Materials (IRM) at Dalhousie University for use of the SEM/EDS system, ECKA Granules for supply of the P/M pre-mix, and GKN Sinter Metals for sintering the P/M material.

CHAPTER 9 EFFECT OF COMPACTION PRESSURE ON CORROSION BEHAVIOUR OF ALUMIX 123

Intuitively, compaction pressure would be expected to have an effect on corrosion behaviour due to its influence on sintered density, surface area, and the size/shape of residual pores. Sintered density is of concern as it has a direct influence on the calculation of corrosion rate. Likewise, surface area presumably affects the kinetics of corrosion by changing the magnitude of the electrochemically active area and, due to roughness factors, may also affect the characteristics of the static diffusion layer.

The influence of pore morphology is expected to be particularly acute as it can influence corrosion response through several means. For instance, the electrochemically active area may also be affected by wettability which, in occluded areas, could depend partially on pore morphology. In another scenario pore morphology may also influence certain aspects of the initiation and propagation of crevice corrosion, wherein a galvanic macro-couple is formed between the creviced area within pores and the external electrode surface. Crevice corrosion typically initiates via a differential aeration mechanism whose incubation time could be affected by the volume of electrolyte in the crevice (*i.e.* pore size) and the capacity for oxygen transport within it (*i.e.* pore shape). Once crevice corrosion is propagating, pore size and shape should then have a direct influence on the ratio of cathodic to anodic area (*i.e.* the ratio of creviced to exterior area) which may in turn affect electrode kinetics and potential. Finally, pore morphology should also have an influence on the transport of corrosion products and reactants which control the composition of the crevice electrolyte so as to effect on electrode kinetics and potential.

In the present work, experimental results on the effect of compaction pressure on corrosion behaviour of laboratory sintered Alumix 123-T1 were only partially successful; selected results are shown in Figure 9.1 through Figure 9.5. Quantitative relationships were clearly observed for kinetic properties, Figure 9.3, however some thermodynamic properties, namely the open circuit potential (OCP) and corrosion potential (E_{corr}), were complicated by especially poor reproducibility. Since the value of these thermodynamic parameters were hypothesized to be related to the propagation of crevice corrosion in residual porosity, it is possible that their poor reproducibility was due to inconsistent sintered density at the electrode face between individual specimens, which may have been affected by temperature heterogeneity during sintering in the laboratory furnace or the polishing procedure of the specimens prior to electrochemical testing. Polishing may have led to smearing over some porosity and inadvertently polishing to inconsistent depths may have exposed slightly different sintered densities at the electrode face between different specimens (*cf.* Figure 6.3). There is, however, some qualitative behaviour that can be discerned about the effect of compaction pressure on the OCP and corrosion potential, as illustrated in Figure 9.1 and Figure 9.2.

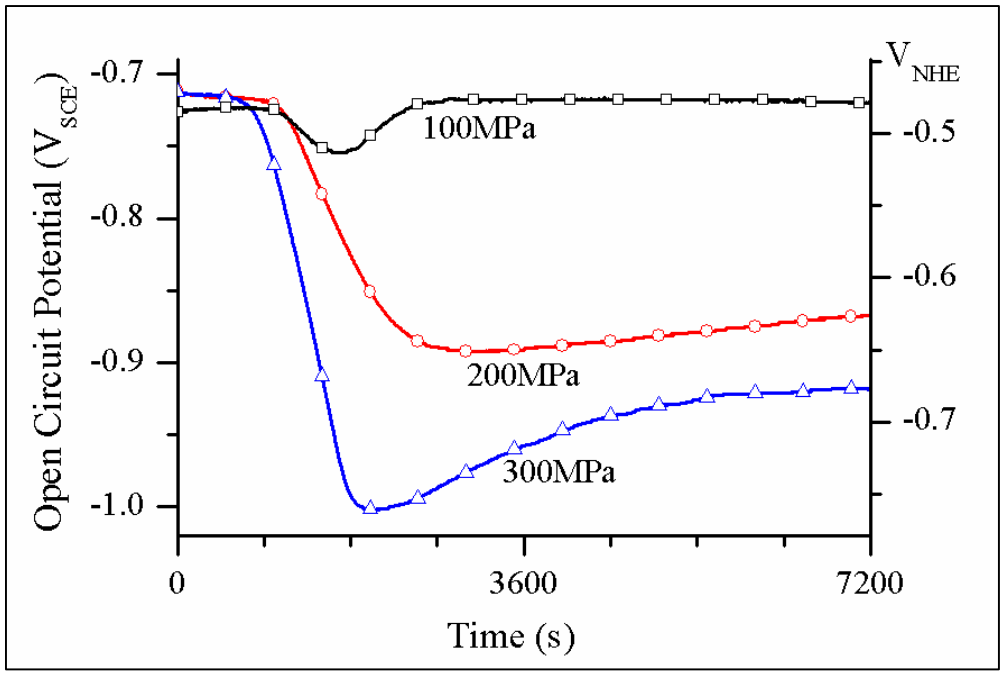

Figure 9.1 – Effect of compaction pressure on the evolution of the OCP of laboratory sintered Alumix 123-T1.

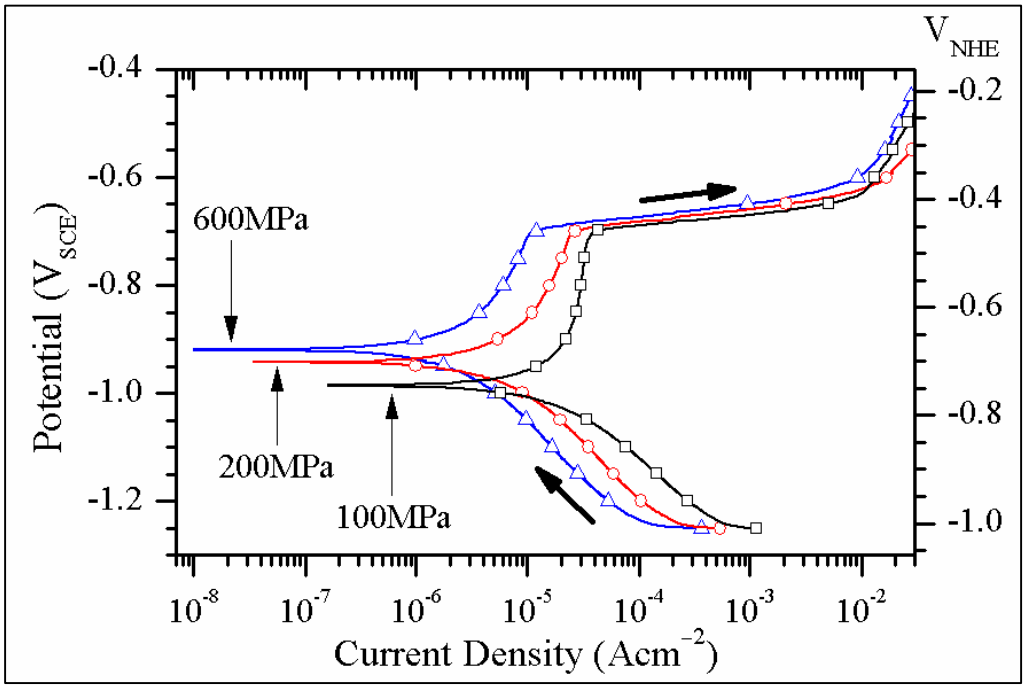

Figure 9.2 – Effect of compaction pressure on potentiodynamic polarization curves of laboratory sintered Alumix 123-T1. The reverse scans have been excluded from the figure for clarity.

Typically, thermodynamic parameters are intrinsic material properties which should not be affected by compaction pressure. However, in the case of Alumix 123-T1 its corrosion behaviour is characterized by the galvanic macro-couple formed between the creviced areas within pores and the external electrode surface, meaning that electrochemical behaviour essentially depends upon the morphology of the electrode. The magnitude of the shift in the open circuit potential in the more negative direction increases with compaction pressure up to 300MPa, Figure 9.1. It is hypothesized that the magnitude of the shift is controlled by pore size and shape which affects the ratio of cathodic to anodic area and the composition of the electrolyte in the crevice. For the samples compacted at 100MPa, the shift of the open circuit potential in the more negative direction was always followed by a shift of similar magnitude in the positive direction, Figure 9.1. This suggested a repassivation process was occurring and the reestablishment of equilibrium to more a more positive electrode potential was transient in nature; perhaps relating to the ionic mobility or diffusivity of corrosion products and reactants to and from crevices.

During the course of cyclic polarization, the application of cathodic potentials resulted in the reestablishment of the corrosion potential to values more negative than the open circuit potential, Figure 9.2. This was especially pronounced for the samples compacted at 100MPa, Figure 9.1 and Figure 9.2. The direction of the shift to more negative values was counter to what would be expected during the storage of charge at the double layer. Alternatively, a change in the composition of the crevice electrolyte as a result of the generation of cathodic current and hydroxide ions may alter the corrosion potential.

Despite the poor reproducibility of the OCP and corrosion potential, there was still a clear trend of the corrosion current (i_{corr}) and passive current (i_{pass}) with compaction pressure, Figure 9.3. Both parameters decreased steadily as compaction pressure increased to 400MPa, at which point steady state was attained, Figure 9.3. The corrosion rate, which takes in to account sintered density, displayed a similar trend to the other kinetic parameters, Figure 9.5. Such behaviour may be expected solely based off surface area considerations, however this is contrary to studies on P/M stainless steels which found corrosion resistance reached a minimum at 87-90% theoretical density – an area termed the 'crevice sensitive region' [209]. The results here were also contrary to other work from this laboratory on Alumix 321-T1 P/M alloy [4] which found that above 100MPa, corrosion rate increased with increasing compaction pressure. However, Alumix 321 has a low copper content of 0.25wt% and sinters to 96-98% theoretical density [4]. Hence, its corrosion behaviour may not be comparable to Alumix 123 which only sinters to 83-91% theoretical density and is a copper-rich formulation (~4.5wt%).

The corrosion current and corrosion rate of laboratory sintered Alumix 123-T1 samples compacted at 300MPa was about one half of that for industrially sintered Alumix 123-T1 samples (Chapter 7, Table 7.2) which were also compacted at 300MPa and exhibited a similar bulk density. The industrially sintered Alumix 123-T1 samples probably possessed a much lower sintered density and higher surface area at the electrode face because they were not polished prior to electrochemical testing (*cf.* Figure 6.3).

The pitting potential (E_{pit}) and repassivation potential (E_{repass}), Figure 9.4, were for the most part not affected by compaction pressure. The pitting potential is related to the stability of the oxide layer in the electrolyte and is therefore not expected to vary with compaction pressure. The repassivation potential was also seemingly independent of

compaction pressure with the exception of samples pressed at the lowest pressure considered, 100MPa. The repassivation potential of these samples is hypothesized to be the result of their low density and high surface area which means the true anodic current density passed was probably significantly less than other compaction pressures. The repassivation potential is sensitive to the amount of anodic current passed, which may explain the more noble value for the samples compacted at 100MPa. It is for this same reason that it is sometimes debated whether the repassivation potential is or is not a true material property since its measurement is to a large degree dependent upon experimental parameters.

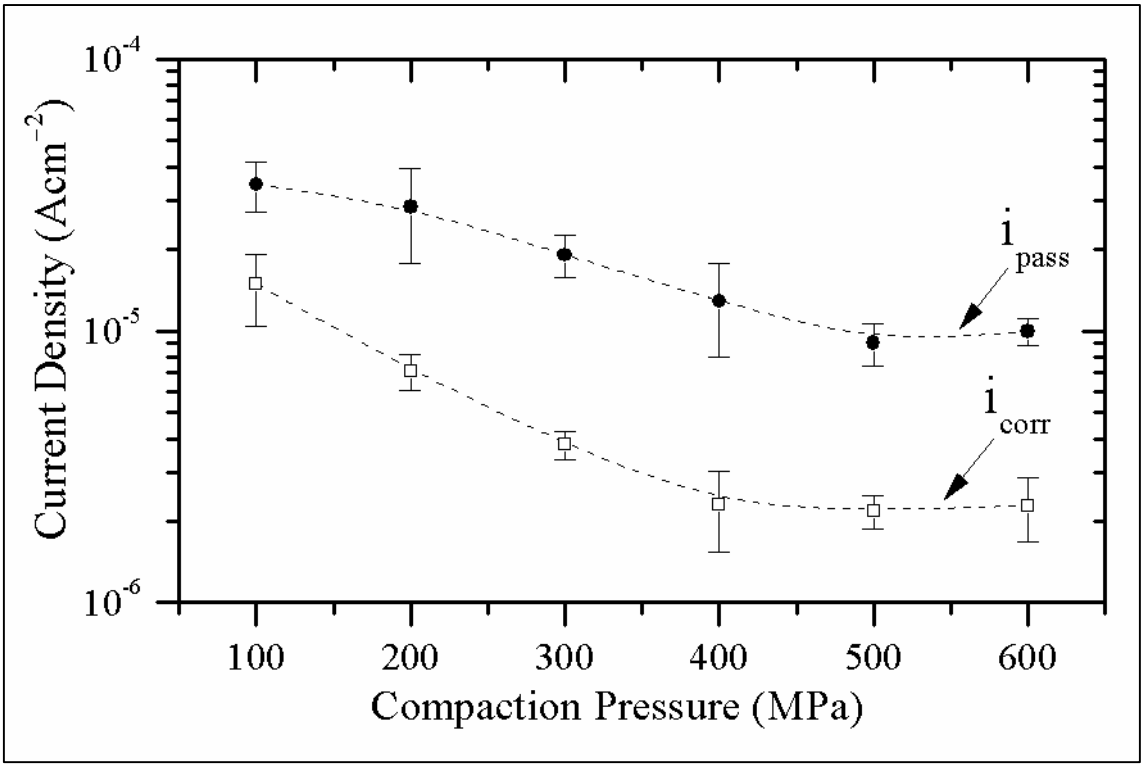

Figure 9.3 – Effect of compaction pressure on corrosion current (i_{corr}) and passive current (i_{pass}) of laboratory sintered Alumix 123-T1.

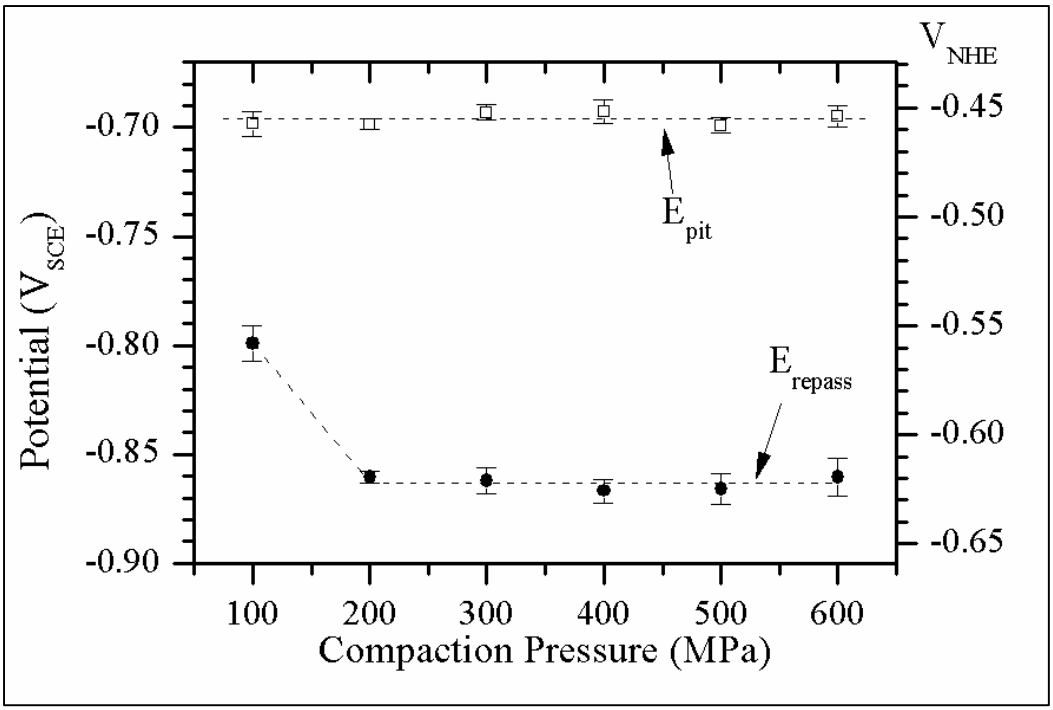

Figure 9.4 – Effect of compaction pressure on pitting potential (E_{pit}) and repassivation potential (E_{repass}) of laboratory sintered Alumix 123-T1.

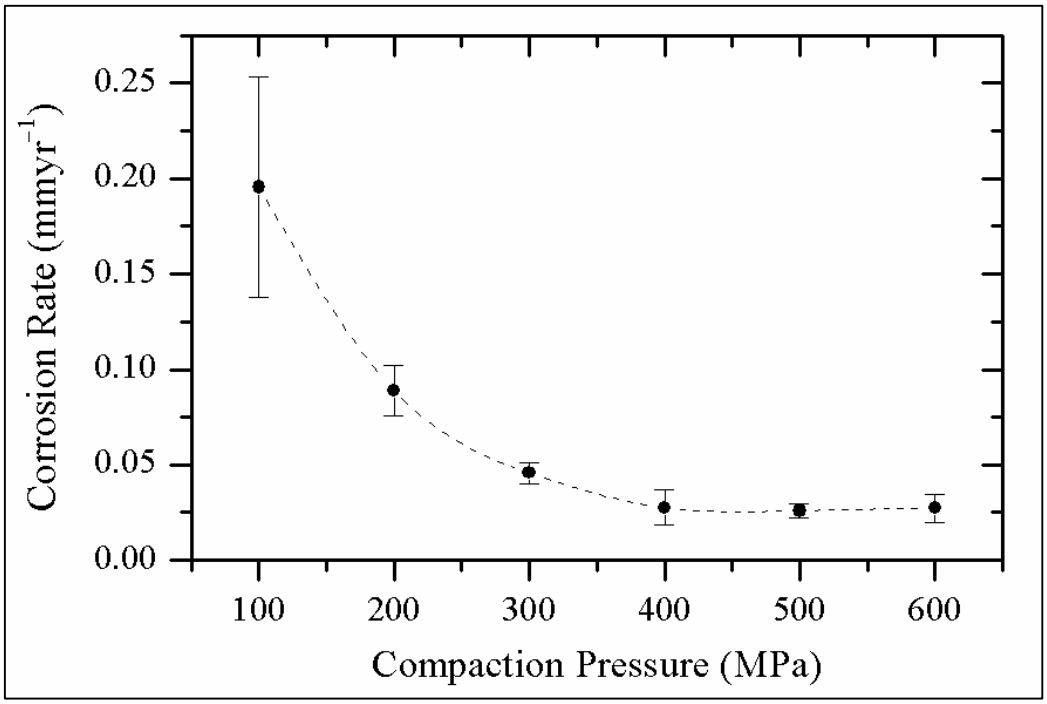

Figure 9.5 – Effect of compaction pressure on corrosion rate of laboratory sintered Alumix 123-T1.

CHAPTER 10 CONCLUSIONS

During sintering, Alumix 123 compacts swelled which limited the sintered density to about 92% theoretical density. As a result of sintering, SEM and EDS analyses showed compacts possessed a thick refractory layer containing carbon, oxygen, and magnesium, and areas of redeposited lubricant residues.

The microstructure of Alumix 123-T1 was characterized by a large amount of irregularly shaped porosity and polyhedral aluminum grains with intermetallics primarily situated along grain boundaries. Two predominant intermetallics were identified by SEM and EDS; both were aluminum-based, but one was rich in copper and one was rich in iron.

The OCP of Alumix 123-T1 deviated to more negative values after a short incubation period and stabilized at potentials near the onset of hydrogen evolution (*ca.* $-1.0V_{SCE}$), where corrosion was partially under anodic control and proceeded via cathodic hydrogen evolution. This is postulated to be due to a reduction in cathode area or depassivation induced by propagating crevice corrosion within residual porosity.

The OCP of Alumix 123-T2 stabilized at the pitting potential where corrosion was predominantly under cathodic control and proceeded via cathodic oxygen reduction. The sizing operation of Alumix 123-T2 reduced the amount of residual porosity through plastic deformation and sealed surface porosity with sizing fluid so that crevice corrosion did not initiate.

At open circuit conditions, pitting in Alumix 123-(T1, T2) was not associated with copper- or iron-rich intermetallics, which was postulated to be due to the refractory layer formed as a result of the sintering process retaining integrity over these intermetallics.

The corrosion rate of Alumix 123-T1 was two times greater than Alumix 123-T2 and four times greater than AA2014-T6. Part of this disparity may be attributed to differences in surface area.

During cathodic potentiostatic polarization of Alumix 123-(T1, T2), cathodic hydrogen evolution and oxygen reduction occurred on the matrix as well as on copper- and iron-rich intermetallics, and was associated with film breakdown in these areas. Local alkalinity generated from cathodic processes can selectively de-alloy intermetallics in Alumix 123-(T1, T2) of active elements leaving copper- and iron-rich remains.

During anodic potentiostatic polarization of Alumix 123-T1 at potentials more negative than the pitting potential, the majority of anodic current passed was generated from creviced areas within residual porosity which eventually repassivated as the concentration of anodic reaction products exceeded the solubility limit and precipitation occurred.

During anodic potentiostatic polarization of Alumix 123-(T1, T2) at potentials noble to the pitting potential, unconventional current transients were observed and the majority of attack was intergranular in nature. Crystallographic pitting was scarcely observed, even at highly anodic potentials. The high tendency for intergranular corrosion was probably related to the location of intermetallics in these areas.

Compaction pressure affected the corrosion behaviour of Alumix 123-T1 – when increased from 100MPa through 400MPa a steady decrease in corrosion rate was observed. However, the pitting potential and repassivation potential of Alumix 123-T1 were essentially independent of compaction pressure.

In the microstructure of AA2014-T6 the θ-$CuAl_2$ and α-AlFeMnSi ($(CuFeMn)_3Si_2Al_{15}$) intermetallics were identified by SEM, EDS, and XRD analyses. Small micron and sub-micron intermetallics were also distributed throughout the matrix of AA2014-T6 which could not be identified.

The OCP of AA2014-T6 stabilized at the pitting potential, where corrosion was predominantly under cathodic control, and proceeded via cathodic oxygen reduction. At open circuit conditions, pitting in AA2014-T6 was associated with θ-$CuAl_2$, α-AlFeMnSi, and other small intermetallic particles. The attack involving θ-$CuAl_2$ was attributed to the anodic trenching mechanism and the attack involving α-AlFeMnSi was attributed to the cathodic trenching mechanism.

During cathodic potentiostatic polarization of AA2014-T6, cathodic hydrogen evolution and oxygen reduction occurred predominantly on θ-$CuAl_2$, α-AlFeMnSi, and other small intermetallics. Local alkalinity generated from cathodic processes can selectively de-alloy intermetallics in AA2014-T6 of active elements leaving copper- and iron-rich remains.

After cathodic potentiostatic polarization of AA2014-T6, SEM observations suggested that cathodic deposition of copper can occur on θ-$CuAl_2$ and α-AlFeMnSi particles, and that cathodic trenching around α-AlFeMnSi particles may have liberated copper from the matrix in a non-Faradaic process.

During anodic potentiostatic polarization of AA2014-T6, the current passed gradually increased until a steady state was reached and there was extensive attack by crystallographic pitting and intergranular corrosion.

10.1 FUTURE WORK

The corrosion behaviour of aluminum P/M alloys is much less understood and characterized than that of the wrought and cast aluminum alloys. In the present work, the understanding of corrosion mechanisms in aluminum P/M alloys has been expanded, but has also raised further questions which warrant continued investigations. The following list is a suggestion of areas of work which, in the author's opinion, should eventually be addressed and would serve to advance the understanding of corrosion mechanisms in aluminum P/M alloys:

1. The surface state of aluminum P/M alloys should be characterized prior to corrosion testing; ideally the real surface area and real sintered density at the electrode face would be quantified.
2. The refractory layer of 'as-sintered' aluminum P/M alloys should be better characterized, particularly its composition, structure, and thickness, and its response to differing electrolyte conditions, including bulk pH and chloride ion concentration, should be quantified.
3. The corrosion behaviour of aluminum P/M alloys should be studied in deaerated electrolyte to mitigate difficulties encountered from the initiation and propagation of crevice corrosion in residual porosity.
4. Aspects of the initiation and propagation of crevice corrosion in residual porosity should be further studied in an attempt to identify mechanisms behind the shift in electrode potential and whether depassivation occurs in some creviced areas.

5. The behaviour of aluminum P/M alloys under conditions of stress corrosion and corrosion fatigue should be examined considering their high susceptibility to intergranular corrosion.
6. The effect of heat treatment on the corrosion behaviour of aluminum P/M alloys, including response to stress corrosion and corrosion fatigue, should be studied. Heat treatment may change the distribution of intermetallics and reduce the tendency for intergranular corrosion.
7. The role of aluminum nitride (AlN), which is largely responsible for the enhanced densification during sintering under nitrogen atmospheres, in the corrosion behaviour of aluminum P/M alloys should be determined.

One last general recommendation regards the standardization of aluminum P/M alloys. The existing system defining P/M aluminum standards is much less rigorous than for cast or wrought aluminum, and furthermore the P/M process introduces numerous variables which may need to be addressed, including characteristics of powder and powder production methods (*e.g.* particle size, alloying method), powder compaction (*e.g.* compaction pressure, type of lubricant), sintering (*e.g.* time, temperature, heating rate, atmosphere), cooling (*e.g.* cooling rate, atmosphere), and secondary processing (*e.g.* sizing, heat treatment). In order to reconcile results between different investigations, it is recommended to thoroughly characterize aluminum P/M material prior to corrosion testing in an attempt to discern whether any differences in corrosion behaviour may be ascribed to a different alloy structure as a result of differences in the powder pre-mix or processing conditions.

REFERENCES

[1] M. Qian and G.B. Schaffer. "Sintering of Aluminium and its Alloys" in *Sintering of Advanced Materials.* Woodhead Publishing Limited, Cambridge (2010): 291-323.

[2] J.D. Draper, M.K. Gala and C.B. Thompson. "Al P/M Parts Fabrication." *Modern Developments in Powder Metallurgy* **10**: 305-323, (1977).

[3] E.M. Daver, W.J. Ullrich and K.B. Patel. "Aluminum P/M Parts - Materials, Production and Properties." *Key Engineering Materials* **29-31**: 401-428, (1989).

[4] A.M. Ibrahim. *Processing of Alumix 321 PM Alloy and its Corrosion Behaviour in 3.5 wt% Saline Solution.* Ph.D. Thesis. Dalhousie University, (2013)

[5] J.H. Dudas and K.J. Brondyke. "Aluminum P/M Parts - Their Properties and Performance." *Society of Automotive Engineers* Report No. 700141. (1970).

[6] J.H. Dudas. "Aluminum Powder-Metal Alloys Offer Unique Property Mix." *SAE Journal* **78**(6): 40-42, (1970).

[7] R.E. Roesel. "Aluminum Powder Metallurgy–Production, Properties and Potential." *Powder Metallurgy International* **5**(2): 89-93, (1973).

[8] The Aluminum Association. "International Alloy Designations and Chemical Composition Limits for Wrought Aluminum and Aluminum Alloys." (2009).

[9] J.G. Kaufman. *Introduction to Aluminum Alloys and Tempers.* ASM International, Materials Park, O.H. (2000): 16-20,24,31,57-59,65-73.

[10] J.T. Stanley. "History of Wrought-Aluminum-Alloy Development" in *Aluminum Alloys: Contemporary Research and Applications.* Academic Press, Boston, M.A. (1989): 3-31.

[11] L.F. Mondolfo. *Aluminum Alloys: Structure and Properties.* Butterworths, London (1976).

[12] *Alloying: Understanding the Basics.* J.R. Davis (Ed.). ASM International, Materials Park, O.H. (2001): 360,371,379.

[13] G.J. Hildeman and M.J. Koczak. "Powder-Metallurgy Aluminum Alloys" in *Aluminum Alloys–Contemporary Research and Applications.* Academic Press, Boston (1989): 323-364.

[14] J.H. Dudas and W.A. Dean. "The Production of Precision Aluminum P/M Parts." *Progress in Powder Metallurgy* **25**: 101-130, (1969).

[15] J.H. Dudas and W.A. Dean. "The Production of Precision Aluminum P/M Parts." *International Journal of Powder Metallurgy* **5**(2): 21-36, (1969).

[16] Anonymous. "New P/M Advances Focus on Aluminum." *Materials Engineering* **70**(1): 59,73, (1969).

[17] Anonymous. "Progress in Aluminum Powder Metallurgy." *Precision Metal* **27**(6): 41-44,77, (1969).

[18] R. Khol. "At Last... Parts from Aluminum Powder." *Machine Design* **41**(16): 110-114, (1969).

[19] B.D. Wakefield. "Aluminum PM Parts: A Good Start." *Iron Age* **205**(12): 60-61, (1970).

[20] Anonymous. "Application Outlook for Aluminum P/M Parts." *Metal Progress* **99**(4): 60-64,66, (1971).

[21] K.H. Miska. "Aluminum P/M Parts are Strong, Economical and they Save Weight." *Materials Engineering* **81**(4): 32-36, (1975).

[22] J.D. Generous. "The Quiet Success of Aluminum P/M." *Metal Progress* **116**(6): 52-54, (1979).

[23] Anonymous. "Aluminium Powders in Powder Metallurgy." *Metal Powder Report* **35**(5): 187-191, (1980).

[24] Anonymous. "Aluminum Powder Parts Pay Off in Business Machines." *Modern Metals* **36**(10): 76,78,80, (1980).

[25] J.D. Generous. "Aluminum P/M Applications in Business Machines." *Modern Developments in Powder Metallurgy* **13**: 501-510, (1981).

[26] J.D. Generous and W.C. Montgomery. "Aluminum P/M – Properties and Applications" in *Powder Metallurgy: Applications, Advantages and Limitations.* American Society for Metals, Metals Park, Ohio (1983): 211-234.

[27] J.E. Foss and D. DeFranco. "The Northstar Cam Bearing Caps: A New Application for Aluminum P/M." *Society of Automotive Engineers* Report No. 940429. (1994).

[28] L.F. Pease III and W.G. West. *Fundamentals of Powder Metallurgy.* Metal Powder Industries Federation, Princeton, New Jersey (2002): 340.

[29] K.J. Brondyke and T.F. McCormick. "Melting, Remelting, Degassing, Fluxing and Handling" in *Aluminum: Vol. III Fabrication and Finishing.* American Society for Metals, Metals Park (1967): 1-42.

[30] D.A. Granger. "Ingot Casting in the Aluminum Industry" in *Aluminum Alloys– Contemporary Research and Applications.* Academic Press, Inc., San Diego (1989): 109-135.

[31] S.J. Paterson and T. Sheppard. "Structural Changes Occuring during Thermal Treatments during Extrusion of Al-Cu-Mg-Mn-Si (AA2014) Alloy." *Metals Technology* **9**(1): 389-398, (1982).

[32] L. Bäckerud, E. Król and J. Tamminen. *Solidification Characteristics of Aluminium Alloys. Volume 1: Wrought Alloys.* Tangen Trykk A/S, Norway (1986).

[33] R.E. Sanders Jr. "Technology Innovation in Aluminum Products." *Journal of Metals* **53**(2): 21-25, (2001).

[34] T. Sheppard. "On the Relationship between Extrusion Conditions, Mechanical Properties, and Surface Acceptibility in some Hard Aluminum Alloys" in *Proceedings of the Seventh International Aluminum Extrusion Technology Seminar: Shaping the Future. May 16-19 2000, Chicago.* (2000): 307-322.

[35] ASTM International. "ASTM B918. Standard Practice for Heat Treatment of Wrought Aluminum Alloys." (2009).

[36] H.C. Neubing and J. Gradl. "Quality Aspects during the Manufacturing and Testing of Aluminium-Premixes" in *P/M in to the 1990's: International Conference on Powder Metallurgy, Wembley Conference Centre, London, UK, 2-6 July 1990.* The Institute of Metals, (1990): 252-257.

[37] J.D. Edwards. "Comminuted Forms of Aluminum" in *Powder Metallurgy.* J. Wulff (Ed.). American Society for Metals, (1942): 124-131.

[38] L.W. Kempf. "Properties of Compressed and Heated Aluminum Alloy Powder Mixtures" in *Powder Metallurgy.* J. Wulff (Ed.). American Society for Metals, Cleveland (1942): 314-316.

[39] G.D. Cremer and J.J. Cordiano. "Recent Developments in the Formation of Aluminum and Aluminum Alloys by Powder Metallurgy." *Transactions of the American Institute of Mining and Metallurgical Engineers* **52**: 152-165, (1943).

[40] R.L. Bickerdike. "Aluminium Components" in *Symposium on Powder Metallurgy.* Iron & Steel Institute, (1947): 185-191.

[41] J.B. Haertlein and J.F. Sachse. "Review of Aluminum Powder Metallurgy." *Proceedings of the Metal Powder Association*: 83-94, (1953).

[42] E.M. Daver. "Process and Material Considerations for Aluminum Powder Metallurgy" *Society of Manufacturing Engineers* Report No. EM71-276. (1971).

[43] C.G. Goetzel. *Treatise on Powder Metallurgy. Volume I: Technology of Metal Powders and their Products.* Interscience Publishers, Inc., New York (1949): 36,37,39,70,195,196,217,225-229,682-685.

[44] S. Özbilen, A. Ünal and T. Sheppard. "Influence of Oxygen on Morphology and Oxide Content of Gas Atomized Aluminium Powders" in *Physical Chemistry of Metal Powders.* The Minerals, Metals & Materials Society, Warrendale, P.A. (1989): 489-505.

[45] J.S. Thompson. "A Study of Process Variables in the Production of Aluminium Powder by Atomization." *Journal of the Institute of Metals* **74**: 101-132, (1948).

[46] A.V. Ramana Rao. "Preparation of Aluminium Powder by Atomisation." *Transactions of the Powder Metallurgy Association of India* **3**: 20-25, (1976).

[47] B. Williams. "Aluminium Powder Production at ALPOCO." *Metal Powder Report* **41**(1): 43-44, (1985).

[48] A.P. Savitskii, O.B. Afanas'ev, V.G. Gopienko, L.S. Martsunova, G.N. Romanov and T.L. Zayats. "Effect of Aluminum Particle Size on the Volume Changes Experienced by Compacts from a Mixture of Aluminum and Copper Powders during Liquid-Phase Sintering." *Soviet Powder Metallurgy and Metal Ceramics* **25**(9): 721-725, (1986).

[49] D.P. Bishop, B. Hofmann and K.R. Couchman. "Properties and Attributes of Commercially Available AC2014-Type Aluminum P/M Alloys" in *Proceedings of the 2000 International Conference on Powder Metallurgy & Particulate Materials.* (2000): 1-14.

[50] I. Amato, S. Corso and E. Sgambetterra. "Sintering Procedures for Aluminium P/M Parts and Metallographic Examination during the Process." *Powder Metallurgy* **19**(3): 171-176, (1976).

[51] J.H. Dudas, R.H. Stevens and B.K. Gildersleeve. "Metallography and Structure Interpretation of Aluminum P/M Parts." *International Journal of Powder Metallurgy & Powder Technology* **10**(4): 285-293, (1974).

[52] T. Watanabe and K. Yamada. "Effects of Copper-Adding Methods on the Strength of Sintered Aluminum-Copper Alloys." *Report of the Castings Research Laboratory, Waseda University* (19): 21-29, (1968).

[53] T. Watanabe and K. Yamada. "Effects of Methods of Adding Copper on the Strength of Sintered Aluminum Copper Alloys." *International Journal of Powder Metallurgy* **4**(3): 37-47, (1968).

[54] S. Storchheim. "Aluminum Powder Metallurgy Finally made Commercially Practical." *Progress in Powder Metallurgy* **18**: 124-130, (1962).

[55] W. Kehl, M. Bugajska and H.F. Fischmeister. "Internal Or Die Wall Lubrication for Compaction of Al Powders?" *Powder Metallurgy* **26**(4): 221-227, (1983).

[56] R.N. Lumley and G.B. Schaffer. "The Effect of Additive Particle Size on the Mechanical Properties of Sintered Aluminium-Copper Alloys." *Scripta Materialia* **39**(8): 1089-1094, (1998).

[57] F.J. Esper and G. Leuze. "The Influence of the Powder Particle Size on the Properties of Aluminum P/M Parts." *Powder Metallurgy International* **3**(3): 123-126, (1971).

[58] W. Kehl and H.F. Fischmeister. "Liquid-Phase Sintering of Al-Cu Compacts." *Powder Metallurgy* **23**(3): 113-119, (1980).

[59] E. Mehl. "Production of Metal Powders: Electrolytic Deposition from Aqueous Solution." *Metal Treatment* **17**(62): 118-122,124,126,128, (1950).

[60] F. Wills and E.J. Clugston. "Production of Electrolytic Copper Powder." *Journal of the Electrochemical Society* **106**(4): 362-366, (1959).

[61] C.G. Goetzel. *Treatise on Powder Metallurgy. Volume III: Classified and Annotated Bibliography.* Interscience Publishers, Inc., New York, N.Y. (1952): 470-475.

[62] W.W. Moss Jr. "Magnesium Powder Fabrication." *Light Metal Age* **2**(1, 2): 10-13,17-19,24,30,38, (1944).

[63] D.J. Brown. "Powder Metallurgy of Magnesium" in *Symposium on Powder Metallurgy, Pre Print, Group III.* Iron & Steel Institute, (1954): 100-104.

[64] Anonymous. "Aluminium Powder." *Metal Industry* **66**(2): 22, (1945).

[65] J.A. Gann. "Metallic Powder and Method of Making." U.S. Patent 1,871,450. (1932).

[66] F. Farzin Nia and B.L. Davies. "Production of Al-Cu and Al-Cu-Si Alloys by PM Methods." *Powder Metallurgy* **25**(4): 209-215, (1982).

[67] B.L. Davies and F. Farzin Nia. "Precipitation Hardening of P/M Aluminum-Copper Alloys." *International Journal of Powder Metallurgy & Powder Technology* **19**(3): 197-209, (1983).

[68] C.G. Goetzel. *Treatise on Powder Metallurgy. Volume II: Applied and Physical Powder Metallurgy.* Interscience Publishers, Inc., New York (1950): 489-500,598,722-727.

[69] A.Y. Kem. "Effect of the Compacting Conditions on the Structure and Properties of Powdered Aluminum Alloys Containing Copper and Magnesium." *Soviet Powder Metallurgy and Metal Ceramics* **31**(8): 675-679, (1992).

[70] H.G. Taylor. "The Influence of Tooling Methods on the Density Distribution in Complex Metal-Powder Parts." *Powder Metallurgy* **3**(6): 87-124, (1960).

[71] L.S. Martsunova, A.P. Savitskii, ÉN. Ushakova and B.I. Matveev. "Sintering of Aluminum with Copper Additions." *Soviet Powder Metallurgy and Metal Ceramics* **12**(12): 956-959, (1973).

[72] P.E. Matthews. "Effects of Processing Variables on the Properties of Sintered Aluminum Compacts." *International Journal of Powder Metallurgy* **4**(4): 39-46, (1968).

[73] D.P. Bishop, R.L. McNally Jr. and T.E. Geiman. "Metallurgical Considerations in the Manufacturer and Development of Aluminum P/M Camshaft Bearing Caps" in *Proceedings of the 2nd International Conference on Powder Metallurgy Aluminum & Light Alloys for Automotive Applications.* W.F. Jandeska and R.A. Chernenkoff (Eds.). Metal Powder Industries Federation, (2000): 177-185.

[74] A.P. Savitskii and G.N. Romanov. "Effect of Porosity on the Volume Changes Experienced by Al-Cu Compacts during Liquid-Phase Sintering." *Soviet Powder Metallurgy and Metal Ceramics* **26**(7): 532-536, (1987).

[75] J.H. Dudas and C.B. Thompson. "Improved Sintering Procedures for Aluminum P/M Parts." *Modern Developments in Powder Metallurgy* **5**: 19-36, (1971).

[76] Anonymous. "Sintering Practices for Aluminum Powdered Metal Parts Affect Properties." *Industrial Heating* **37**(9): 1654-1656, (1970).

[77] W.C. Dimon. "Sintering Furnaces: A New Breed Coming." *Precision Metal* **28**(4): 54-57, (1970).

[78] T. Watanabe and M. Kanazawa. "Observations on the Melt-Off Pores of Sintered Aluminum-5%Copper Alloy Compacts made from Mixed Powder by the use of Scanning Electron Microscope." *Report of the Castings Research Laboratory, Waseda University* **24**: 13-16, (1973).

[79] T. Watanabe and M. Kanazawa. "Observations on the Melt-Off Pores of Sintered Al-5%Cu Alloy Compacts by the use of Scanning Electron Microscope." *Journal of the Japan Society of Powder and Powder Metallurgy* **20**(3): 87-88, (1973).

[80] A.P. Savitskii. *Sintering of Systems with Interacting Components.* Trans Tech Publications, (2009): 175-210.

[81] A.P. Savitskii, G.N. Romanov, L.S. Martsunova and V.V. Zhdanov. "Nature of the Growth of Al-Cu Powder Compacts during Liquid-Phase Sintering." *Soviet Powder Metallurgy and Metal Ceramics* **27**(5): 348-351, (1988).

[82] A.P. Savitskii and G.N. Romanov. "Structure Formation during the Sintering of Aluminum-Copper Alloys." *Soviet Powder Metallurgy and Metal Ceramics* **25**(3): 184-187, (1986).

[83] A.P. Savitskii and G.N. Romanov. "Prevention of Compact Swelling during Liquid Phase Sintering of the Al-Cu System." *Science of Sintering* **22**(2): 73-77, (1990).

[84] A.P. Savitskii, G.N. Romanov and L.S. Martsunova. "Deformation of Aluminum-Copper Powder Solids during Liquid-Phase Sintering." *Soviet Powder Metallurgy and Metal Ceramics* **24**(8): 617-621, (1985).

[85] V.A. Brodov, S.V. Belov, A.V. Zhil'tsov, Y.V. Levinskii and G.V. Malakhov. "Formation of the Structure in Sintering and the Strength Properties of Al-Cu P/M Alloys." *Soviet Powder Metallurgy and Metal Ceramics* **29**(10): 808-812, (1990).

[86] H. Mitani and H. Nagai. "On the Sintering Process of Al-Cu Binary Mixed Powder Compacts." *Journal of the Japan Society of Powder and Powder Metallurgy* **20**(6): 178-183, (1973).

[87] A.P. Savitskii and L.S. Martsunova. "Effect of Solid-State Solubility on the Volume Changes Experienced by Aluminum during Liquid-Phase Sintering." *Soviet Powder Metallurgy and Metal Ceramics* **16**(5): 333-337, (1977).

[88] R.N. Lumley and G.B. Schaffer. "The Effect of Solubility and Particle Size on Liquid Phase Sintering." *Scripta Materialia* **35**(5): 589-595, (1996).

[89] S. Storchheim. "Aluminum Powder Metallurgy Now Feasible." *Precision Metal* **26**(6): 67-68,73, (1968).

[90] A. Kimura, M. Shibata, K. Kondoh, Y. Takeda, M. Katayama, T. Kanie and H. Takada. "Reduction Mechanism of Surface Oxide in Aluminum Alloy Powders Containing Magnesium Studied by X-Ray Photoelectron Spectroscopy using Synchrotron Radiation." *Applied Physics Letters* **70**(26): 3615-3617, (1997).

[91] G.B. Schaffer, J.-. Yao, S.J. Bonner, E. Crossin, S.J. Pas and A.J. Hill. "The Effect of Tin and Nitrogen on Liquid Phase Sintering of Al-Cu-Mg-Si Alloys." *Acta Materialia* **56**: 2615-2624, (2008).

[92] V.A. Brodov, A.V. Zhil'tsov, N.M. Ionova and I.P. Melashenko. "Effect of Alloying Method on Sintering and Physico-Mechanical Properties of Al-4.4%Cu-0.5%Mg Powder Alloy." *Soviet Powder Metallurgy and Metal Ceramics* **27**(10): 790-794, (1988).

[93] A.B. Al'tman, V.A. Brodov, A.V. Zhil'tsov and I.P. Melashenko. "Effect of Sintering Conditions on the Structure and Mechanical Properties of P/M Aluminum Base Alloys." *Soviet Powder Metallurgy and Metal Ceramics* **26**(9): 713-717, (1987).

[94] G.S. Upadhyaya and P. Thareja. "Activated Sintering of Aluminium-Copper Alloys with Boron Addition." *Transactions of the Powder Metallurgy Association of India* **2**: 22-26, (1975).

[95] T.B. Sercombe and G.B. Schaffer. "The Effect of Trace Elements on the Sintering of Al-Cu Alloys." *Acta Materialia* **47**(2): 689-697, (1999).

[96] A.P. Savitskii, G.N. Romanov and V.G. Gopienko. "Influence of Solubility in the Solid Phase on Volume Changes in Liquid-Phase Sintering of Aluminum-Base Powder Metallurgy Specimens." *Soviet Powder Metallurgy and Metal Ceramics* **27**(7): 568-571, (1988).

[97] G.B. Schaffer and B.J. Hall. "The Influence of the Atmosphere on the Sintering of Aluminum." *Metallurgical and Materials Transactions A* **33**(10): 3279-3284, (2002).

[98] P.E. Matthews. "The Mechanical Properties of Brass and Developmental Nonferrous P/M Materials." *International Journal of Powder Metallurgy* **5**(4): 59-69, (1969).

[99] P.E. Matthews. "The Mechanical Properties of Brass and Developmental Non-Ferrous P/M Materials." *Progress in Powder Metallurgy* **25**: 15-27, (1969).

[100] P.E. Matthews. "Mechanical Properties of Brass and Developmental Non-Ferrous Powder Compacts." *American Society of Tool and Manufacturing Engineers* Report No. EM69-558. (1969).

[101] K.E. Buchovecky and M.R. Rearick. "Aluminum P/M Forgings." *Metal Progress* **101**(2): 74-78, (1972).

[102] N.D. Tomashoff. "Corrosion of Metals with Oxygen Depolarization [I.]." *Light Metals* **10**(119): 637-645, (1947).

[103] N.D. Tomashoff. "Corrosion of Metals with Oxygen Depolarization [II.]." *Light Metals* **11**(120): 8-14, (1948).

[104] N.D. Tomashoff. "Corrosion of Metals with Oxygen Depolarization [III.]." *Light Metals* **11**(121): 104-112, (1948).

[105] N.D. Tomashoff. "Corrosion of Metals with Oxygen Depolarization [IV.]." *Light Metals* **11**(122): 155-160, (1948).

[106] N.D. Tomashoff. "Corrosion of Metals with Oxygen Depolarization [V.]." *Light Metals* **11**(126): 388-396, (1948).

[107] N.D. Tomashoff. "Corrosion of Metals with Oxygen Depolarization [VI.]." *Light Metals* **11**(128): 503-509, (1948).

[108] N.D. Tomashov. *Theory of Corrosion and Protection of Metals.* Translated by B.H. Tytell, I. Geld and H.S. Preiser. The Macmillan Company, New York, N.Y. (1967).

[109] M.J. Pryor and D.S. Keir. "The Nature of Aluminum as a Cathode." *Journal of the Electrochemical Society* **102**(10): 605-607, (1955).

[110] G.A. DiBari and H.J. Read. "Electrochemical Behavior of High Purity Aluminum in Chloride Containing Solutions." *Corrosion* **27**(11): 483-493, (1971).

[111] A. Despić and V.P. Parkhutik. "Electrochemistry of Aluminum in Aqueous Solutions and Physics of its Anodic Oxide" in *Modern Aspects of Electrochemistry No. 20.* Plenum Press, New York, N.Y. (1989): 401-503.

[112] K.F. Lorking. "Initiation and Inhibition of Corrosion of Aluminium in Aqueous Solutions." *Journal of the Australian Institute of Metals* **7**(2): 136-140, (1962).

[113] H.P. Godard. "Aluminum" in *The Corrosion of Light Metals.* John Wiley & Sons, Inc., New York, N.Y. (1967): 1-218.

[114] A.I. Krasil'shchikov. "Electrochemical Ionization of Oxygen." *Protection of Metals* **1**(6): 547-557, (1965).

[115] B. Bianchi, F. Mazza and T. Mussini. "Electrochemical Processes of Oxygen and Hydrogen Peroxide in Metal Corrosion and Protection" in *2nd International Congress on Metallic Corrosion; New York, N.Y., March 11-15, 1963.* National Association of Corrosion Engineers, (1966): 893-904.

[116] R. Grauer and E. Wiedmer. "Investigations into the Behaviour of Aluminium Under Cathodic Polarization." *Werkstoffe und Korrosion* **24**(2): 128-130, (1973).

[117] Y.N. Mikhailovskii, V.A. San'ko and V.M. Popova. "Dissolution of Aluminum and Alloy D-16 during Polarization by External Current in Media with Different Degrees of Aeration." *Protection of Metals* **12**(6): 564-568, (1976).

[118] E.P.G.T. van de Ven and H. Koelmans. "The Cathodic Corrosion of Aluminum." *Journal of the Electrochemical Society* **123**(1): 143-144, (1976).

[119] K. Nis¸ancioĞlu and H. Holtan. "Cathodic Polarization of Aluminium in Acetate-Buffered Chloride Media." *Electrochimica Acta* **24**(12): 1229-1235, (1979).

[120] K. Nis¸ancioĞlu and H. Holtan. "Corrosion of Aluminum in Aqueous Chloride Media" in *7th Scandinavian Corrosion Congress.* (1975): 418-433.

[121] I.L. Rozenfel'd, V.P. Persiantseva and V.E. Zorina. "Anodic Solution of Aluminum in Neutral Media." *Protection of Metals* **15**(1): 69-72, (1979).

[122] E.M. Khairy and M.K. Hussein. "The Static Electrode Potential Behavior of Aluminum and the Anodic Behavior of the Pure Metal and its Alloys in Chloride Media." *Corrosion* **13**(12): 27-32, (1957).

[123] K. Ogle, M. Serdechnova, M. Mokaddem and P. Volovitch. "The Cathodic Dissolution of Al, Al_2Cu, and Al Alloys." *Electrochimica Acta* **56**(4): 1711-1718, (2011).

[124] K. Nisancioglu and H. Holtan. "Cathodic Polarization of Commercially Pure Aluminium." *Corrosion Science* **19**(8): 537-552, (1979).

[125] J. Radošević, M. Kliškić, P. Dabić, R. Stevanović and A. Despić. "Processes on Aluminium on the Negative Side of the Open-Circuit Potential." *Journal of Electroanalytical Chemistry and Interfacial Electrochemistry* **277**(1/2): 105-119, (1990).

[126] K.G. Cowan and J.A. Harrison. "Automation of Electrode Kinetics−V. the Dissolution of Al in Cl^- and F^- Containing Aqueous Solutions." *Electrochimica Acta* **25**(9): 1153-1163, (1980).

[127] A.R. Despić, D.M. Dražić, J. Balakšina, L. Gajić-Krstajić and R.M. Stevanović. "Investigation of Oxidation Potentials of Substances Accumulated during Cathodic Polarization of Aluminium." *Electrochimica Acta* **35**(11/12): 1747-1755, (1990).

[128] K. Minakawa, M. Izu, E. Sato and Y. Itoi. "Anodic Polarization Behavior of High Purity Aluminum in Sodium Chloride Aqueous Solution Adjusted to various pH's." *Journal of Japan Institute of Light Metals* **34**(3): 182-189, (1984).

[129] D.M. Dražić and A.R. Despić. "Electrochemistry of Aluminium in Aqueous Solutions." *Documenta Chemica Yugoslavica* **48**(Supplement): S5-S36, (1983).

[130] T.R. Beck. "Salt Film Formation during Corrosion of Aluminum." *Electrochimica Acta* **29**(4): 485-491, (1984).

[131] V.F. Lazarev, L.S. Sukhanova and A.I. Levin. "Mechanism of the Anodic Dissolution of Aluminum." *Soviet Electrochemistry* **11**(5): 784, (1975).

[132] E. Deltombe and M. Pourbaix. "The Electrochemical Behavior of Aluminum: Potential pH Diagram of the System Al-H_2O at 25 C." *Corrosion* **14**(11): 16-20, (1958).

[133] D.M. Dražić, S.K. Zečević, R.T. Atanasoski and A.R. Despić. "The Effect of Anions on the Electrochemical Behaviour of Aluminium." *Electrochimica Acta* **28**(5): 751-755, (1983).

[134] W. Lynes. "The Oxygen Concentration Cell as a Factor in the Localized Corrosion of Metals." *Journal of the Electrochemical Society* **103**(8): 467-474, (1956).

[135] K. Nis¸ancioĞlu and H. Holtan. "Correlation of the Open-Circuit and Electrochemical Measurements for the Pitting Corrosion of Aluminium in Chloride Media." *Werkstoffe und Korrosion* **30**(2): 105-113, (1979).

[136] K. Sugimoto, Y. Sawada and S. Morioka. "Effects of Matrix Purity and Environment Factors on the Anodic Pitting Dissolution Behaviours of Aluminium." *Journal of the Japan Institute of Metals* **32**(9): 842-848, (1968).

[137] T. Suter and R.C. Alkire. "Microelectrochemical Studies of Pit Initiation at Inclusions in Al 2024-T3." *Journal of the Electrochemical Society* **148**(1): B36-B42, (2001).

[138] I.G. Murgulescu, O. Radovici and S. Ciolac. "Potentio-Kinetic Studies on some Aluminum Binary Alloys" in *2nd International Congress on Metallic Corrosion; New York, N.Y., March 11-15, 1963*. National Association of Corrosion Engineers, (1966): 942-952.

[139] P.L. Bonora, G.P. Ponzano and V. Lorenzelli. "Contribution to the Study of Localised Corrosion of Aluminium and its Alloys II. Influence of the Environment." *British Corrosion Journal* **9**(2): 112-115, (1974).

[140] A.R. Despić, D.M. Dražić, S.K. Zečević and R.T. Atanasoski. "Abnormal Polarization Change in Anodic Dissolution of Aluminium at High Current Densities." *Electrochimica Acta* **26**(1): 173-177, (1981).

[141] B.N. Stirrup and N.A. Hampson. "Pit Propagation in Aluminium Under Anodic Polarization in Aqueous Chloride Electrolyte." *Journal of Applied Electrochemistry* **7**(1): 91-92, (1977).

[142] E. McCafferty. "Sequence of Steps in the Pitting of Aluminum by Chloride Ions." *Corrosion Science* **45**(7): 1421-1438, (2003).

[143] W. Beck, F.G. Keihn and R.G. Gold. "Corrosion of Aluminum in Potassium Chloride Solutions. I. Effects of Concentrations of KCl and Dissolved Oxygen." *Journal of the Electrochemical Society* **101**(8): 393-399, (1954).

[144] N. Birbilis and R.G. Buchheit. "Electrochemical Characteristics of Intermetallic Phases in Aluminum Alloys: An Experimental Survey and Discussion." *Journal of the Electrochemical Society* **152**(4): B140-B151, (2005).

[145] K. Sugimoto, Y. Sawada and S. Morioka. "Anodic Polarization Behaviour of Pure Aluminum and SAP (Sintered Aluminum Powder) in Halide Solutions." *Journal of the Japan Institute of Metals* **30**(10): 971-977, (1966).

[146] K. Tohma and K. Yamada. "Change of Corrosion Potentials of Aluminum and Aluminum Alloys with Pit Growth." *Journal of Japan Institute of Light Metals* **30**(2): 85-91, (1980).

[147] R.M. Stevanovic, A.R. Despić and D.M. Dražić. "Activation of Aluminium in Chloride Containing Solutions." *Electrochimica Acta* **33**(3): 397-404, (1988).

[148] G.O. Ilevbare, O. Schneider, R.G. Kelly and J.R. Scully. "*In Situ* Confocal Laser Scanning Microscopy of AA 2024-T3 Corrosion Metrology. I. Localized Corrosion of Particles." *Journal of the Electrochemical Society* **151**(8): B453-B464, (2004).

[149] O. Schneider, G.O. Ilevbare, J.R. Scully and R.G. Kelly. "*In Situ* Confocal Laser Scanning Microscopy of AA 2024-T3 Corrosion Metrology. II. Trench Formation Around Particles." *Journal of the Electrochemical Society* **151**(8): B465-B472, (2004).

[150] J.R. Scully, T.O. Knight, R.G. Buchheit and D.E. Peebles. "Electrochemical Characteristics of the Al_2Cu, Al_3Ta and Al_3Zr Intermetallic Phases and their Relevancy to the Localized Corrosion of Al Alloys." *Corrosion Science* **35**(1-4): 185-195, (1993).

[151] N. Birbilis and R.G. Buchheit. "Investigation and Discussion of Characteristics for Intermetallic Phases Common to Aluminum Alloys as a Function of Solution pH." *Journal of the Electrochemical Society* **155**(3): C117-C126, (2008).

[152] R.P. Wei, C.M. Liao and M. Gao. "A Transmission Electron Microscopy Study of Constituent-Particle-Induced Corrosion in 7075-T6 and 2024-T3 Aluminum Alloys." *Metallurgical and Materials Transactions A* **29**(4): 1153-1160, (1998).

[153] P. Leblanc and G.S. Frankel. "A Study of Corrosion and Pitting Initiation of AA2024-T3 using Atomic Force Microscopy." *Journal of the Electrochemical Society* **149**(6): B239-B247, (2002).

[154] J.F. Li, Z. Ziqiao, J. Na and T. Chengyu. "Localized Corrosion Mechanism of 2×××-Series Al Alloy Containing S(Al_2CuMg) and Θ′(Al_2Cu) Precipitates in 4.0% NaCl Solution at pH 6.1." *Materials Chemistry and Physics* **91**(2): 325-329, (2005).

[155] M. Bethencourt, F.J. Botana, M.J. Cano, M. Marcos, J.M. Sánchez-Amaya and L. Gonzalez-Rovira. "Behaviour of the Alloy AA2017 in Aqueous Solutions of NaCl. Part I: Corrosion Mechanisms." *Corrosion Science* **51**(3): 518-524, (2009).

[156] R.G. Buchheit, L.P. Montes, M.A. Martinez, J. Michael and P.F. Hlava. "The Electrochemical Characteristics of Bulk-Synthesized Al_2CuMg." *Journal of the Electrochemical Society* **146**(12): 4424-4428, (1999).

[157] S.J. Ketcham. "Polarization and Stress-Corrosion Studies of an Al-Cu-Mg Alloy." *Corrosion Science* **7**(6): 305-314, (1967).

[158] T. Aburada, J.M. Fitz-Gerald and J.R. Scully. "Pitting and Dealloying of Solute-Rich Al-Cu-Mg-Based Amorphous Alloys: Effect of Alloying with Minor Concentrations of Nickel." *Journal of the Electrochemical Society* **158**(9): C253-C265, (2011).

[159] M.B. Vukmirovic, N. Dimitrov and K. Sieradzki. "Dealloying and Corrosion of Al Alloy 2024-T3." *Journal of the Electrochemical Society* **149**(9): B428-B439, (2002).

[160] B. Mazurkiewicz and A. Piotrowski. "The Electrochemical Behaviour of the Al_2Cu Intermetallic Compound." *Corrosion Science* **23**(7): 697-707, (1983).

[161] K. Nis¸ancioĞlu. "Electrochemical Behavior of Aluminum-Base Intermetallics Containing Iron." *Journal of the Electrochemical Society* **137**(1): 69-77, (1990).

[162] F. Keller and J.D. Edwards. "Composition and Properties of the Natural Oxide Film on Aluminum." *Metal Progress* **54**(2): 195-200, (1948).

[163] A.C. Fraker and A.W. Ruff Jr. "Observations of Hot Saline Water Corrosion of Aluminum Alloys." *Corrosion* **27**(4): 151-156, (1971).

[164] S.W. Smith Jr. and R.W. Latanision. "The Redistribution of Cathodic Activity on an Aluminum Surface in Seawater upon the Introduction of Copper Ions" in *Corrosion 81*. (1981): 1-15.

[165] N. Dimitrov, J.A. Mann and K. Sieradzki. "Copper Redistribution during Corrosion of Aluminum Alloys." *Journal of the Electrochemical Society* **146**(1): 98-102, (1999).

[166] R.G. Buchheit, M.A. Martinez and L.P. Montes. "Evidence for Cu Ion Formation by Dissolution and Dealloying the Al_2CuMg Intermetallic Compound in Rotating Ring-Disk Collection Experiments." *Journal of the Electrochemical Society* **147**(1): 119-124, (2000).

[167] M. Whitaker. "A Review of Information on the Effect of Impurities on the Corrosion Resistance of Aluminium. Part I: General Considerations." *Metal Industry* **80**(10): 183-186, (1952).

[168] M. Whitaker. "A Review of Information on the Effect of Impurities on the Corrosion Resistance of Aluminium. Part II: Aluminium." *Metal Progress* **80**(11): 207-212, (1952).

[169] W.O. Kroenig. "Corrosion of Cast Aluminium Alloys." *Transactions of the Central Aero-Hydrodynamical Institute* **91**: 1-32, (1931).

[170] W.O. Kroenig. "The Corrosion of Duralumin as Affected by its Chemical Composition." *Transactions of the Central Aero-Hydrodynamical Institute* **72**: 1-99, (1931).

[171] D.C.G. Lees. "Effect of Alloying Elements on Corrosion Resistance of Casting Alloys: A Summary of Recent Investigations." *Light Metals* **14**(162): 494-502, (1951).

[172] A.M. Zossi, A.M. Torres, S.M. de De Micheli and H. Biloni. "Effect of Solidification Microstructure on Corrosion Behavior of the Chill Zone in Aluminum Binary Alloys." *Metallurgical Transactions A* **7**(10): 1489-1496, (1976).

[173] V.S. Agarwala and Y.V.V.R.S. Murty. "Selective Corrosion Behavior of Al-4.5 Cu Alloy in Sodium Chloride Solution" in *Corrosion 75.* (1975): 1-12.

[174] I.L. Muller and J.R. Galvele. "Pitting Potential of High Purity Binary Aluminium Alloys. I. Al-Cu Alloys. Pitting and Intergranular Corrosion." *Corrosion Science* **17**(3): 179-193, (1977).

[175] K. Sugimoto, Y. Sawada and S. Morioka. "Effects of Alloying Elements on the Pitting Corrosion of Aluminum." *Transactions of the Japan Institute of Metals* **13**(5): 345-351, (1972).

[176] N.D. Tomashov. "Behaviour of a Separate Local Cathode Under Conditions of Oxygen Depolarization." *Comptes Rendus (Doklady) de l'Académie des Sciences de l'URSS* **27**(9): 983-986, (1940).

[177] H.M. Obispo, L.E. Murr, R.M. Arrowood and E.A. Trillo. "Copper Deposition during the Corrosion of Aluminum Alloy 2024 in Sodium Chloride Solutions." *Journal of Materials Science* **35**(14): 3479-3495, (2000).

[178] M. Whitaker. "A Review of Information on the Effect of Impurities on the Corrosion Resistance of Aluminium. Part III: Wrought Aluminium-Copper-Magnesium Alloys (Al-Cu-Mg)." *Metal Industry* **80**(12): 227-230, (1952).

[179] M. Whitaker. "A Review of Information on the Effect of Impurities on the Corrosion Resistance of Aluminium. Part VIII: Cast Aluminum-Copper-Silicon and Aluminium-Magnesium Alloys." *Metal Industry* **80**(17): 331-332, (1952).

[180] L. Priester. *Métaux: Corrosion-Industries* **44**(527/528): 259-260, (1969).

[181] L. Priester. "Influence of Impurities in Aluminium on its Behaviour in Cathodic Polarization." *Metals Abstracts* **3**: 35 0161, (1970).

[182] K. Nis¸ancioĞlu, K.Y. Davanger, O. Strandmyr and H. Holtan. "Cathodic Behavior of Impure Aluminum in Aqueous Media." *Journal of the Electrochemical Society* **128**(7): 1523-1526, (1981).

[183] T. Morinaga and H. Nagasawa. "Effect of various Elements on the Properties of Duralumin. (the 4th Report.)." *Journal of the Japan Institute of Metals* **6**(1): 45-56, (1942).

[184] W. Bungardt and H. Grober. *Metall* (13/14): 217-220, (1948).

[185] W. Bungardt and H. Grober. "On the Influence of Zinc on some of the Properties of Commercial Aluminium-Copper-Magnesium Wrought Alloys." *Metallurgical Abstracts* **16**: 538, (1949).

[186] K. Tohma, N. Takahashi and Y. Takeuchi. "Compound Effects of Additional Zn, Cu and Mn on Electrochemical Properties and Corrosion Resistance of Aluminum." *Journal of Japan Institute of Light Metals* **33**(9): 518-526, (1983).

[187] K. Tohma, N. Takahashi and Y. Takeuchi. "Compound Effects of Additional Zn, Cu and Mn on the Electrochemical Properties and Corrosion Resistance of Aluminium." *Aluminium* **61**(4): 277-279, (1985).

[188] M.V. Bhat and K.I. Vasu. "Stress Corrosion Characteristics of Al-5%Zn and Al-5%Cu Alloys; Effect of Ti Addition." *Journal of the Electrochemical Society of India* **30**(3): 258, (1981).

[189] M.V. Bhat and K.I. Vasu. "Effect of Titanium Addition on the Activation Parameters of Stress Corrosion Cracking in Al-5%Cu and Al-5%Zn Alloys." *Journal of the Electrochemical Society of India* **31**(3): 65-71, (1982).

[190] M.V. Bhat and K.I. Vasu. "Relevance of Microstructure to Stress Corrosion Cracking in Al-5%Zn and Al-5%Cu Alloys Containing Titanium." *Praktische Metallographie* **20**(3): 130-137, (1983).

[191] M.V. Bhat and K.I. Vasu. "Electrochemical Aspects of Stress Corrosion Cracking in Al-5%Zn and Al-5%Cu Alloys Containing Added Ti." *Journal of the Electrochemical Society of India* **32**(3): 245-251, (1983).

[192] M.V. Bhat and K.I. Vasu. "Strain Rate Sensitivity of Stress Corrosion Cracking in Al-5%Cu and Al-5%Zn Alloys Containing Titanium." *Transactions of the Indian Institute of Metals* **36**(2): 101-105, (1983).

[193] T.Z. Kattamis. "Solidification Microstructure of Aluminium Alloys and its Effects on Mechanical and Corrosion Behaviours" in *Seventh International Light Metals Congress, Leoben/Vienna, 22-26 June 1981.* Aluminium-Verlag GmbH, (1981): 100-102.

[194] J.R. Davis. *Corrosion of Aluminum and Aluminum Alloys.* ASM International, Materials Park, O.H. (1999): 36-38,63,64,67-69,74,102-105,108-111.

[195] R.B. Mears, R.H. Brown and E.H. Dix Jr. "A Generalized Theory of Stress Corrosion of Alloys" in *Special Technical Publication 64: Symposium on Stress-Corrosion Cracking of Metals.* American Society for Testing Materials, Philadelphia, P.A. (1945): 323-344.

[196] A. Garner and D. Tromans. "Direct Observation of Intergranular Corrosion in Al-4wt% Cu Alloy." *Corrosion* **35**(2): 55-60, (1979).

[197] P. Doig and J.W. Edington. "Use of Microelectrodes in the Study of Stress Corrosion in Aged Al-7.2wt% Mg and Al-4.4wt% Cu Alloys." *British Corrosion Journal* **9**(2): 88-90, (1974).

[198] M. Tanaka, G. Girard, R. Davis, A. Peuto and N. Bignell. "Recommended Table for the Density of Water between 0 °C and 40 °C Based on Recent Experimental Reports." *Metrologia* **38**(4): 301-309, (2001).

[199] M.L. Delgado, E.M. Ruiz-Navas, E. Gordo and J.M. Torralba. "Enhancement of Liquid Phase Sintering through Al-Si Additions to Al-Cu Systems." *Journal of Materials Processing Technology* **162-163**: 280-285, (2005).

[200] J.M. Martin and F. Castro. "Sintering Response & Microstructural Evolution of an Al-Cu-Mg-Si Premix." *International Journal of Powder Metallurgy* **43**(6): 59-69, (2007).

[201] L. Meluch. *Warm Compaction of Aluminium Alloy Alumix 123.* Ph.D. Thesis. University of Birmingham, (2009).

[202] *Aluminum: Properties and Physical Metallurgy.* J.E. Hatch (Ed.). ASM International, Materials Park, O.H. (1984): 70.

[203] D. Munson. "A Clarification of the Phases Occurring in Aluminium-Rich Aluminium-Iron-Silicon Alloys, with Particular Reference to the Ternary Phase α-AlFeSi." *Journal of the Institute of Metals* **95**(7): 217-219, (1967).

[204] J.M. Martin and F. Castro. "Liquid Phase Sintering of P/M Aluminium Alloys: Effect of Processing Conditions." *Journal of Materials Processing Technology* **143-144**: 814-821, (2003).

[205] S. Huo, B. Heath and D. Ryan. "Applications of Powder Metallurgy Aluminums for Automotive Valve-Trains." *SAE International Journal of Materials Manufacturing* **1**(1): 511-515, (2009).

[206] J.M. Capus. *Metal Powders: A Global Survey of Production, Applications and Markets 2001–2010.* Elsevier, (2005): 127.

[207] L. Fedrizzi, J. Crousier, P.-L. Bonora and J.-P. Crousier. "Corrosion Mechanisms of an AISI Type 316L Sintered Stainless Steel in Sodium Chloride Solution." *Werkstoffe und Korrosion* **42**(8): 403-409, (1991).

[208] M.C. Baran and B.A. Shaw. "Understanding Corrosion Modes of P/M Ferritic Stainless Steels Encountered in Automotive Applications" in *Corrosion 98.* (1998): 1-15.

[209] E. Klar and P.K. Samal. *Powder Metallurgy Stainless Steels: Processing, Microstructures, and Properties.* ASM International, Materials Park, O.H. (2007).

[210] I.L. Rosenfeld and I.K. Marshakov. "Mechanism of Crevice Corrosion." *Corrosion* **20**(4): 115t-125t, (1964).

[211] A.I. Golubev, I.B. Ulanovskii and Y.M. Korovin. "Corrosion of Aluminum and Titanium in Fissures" in *Corrosion of Metals and Alloys (Korroziya Metallov i Splavov) Collection No. 2.* Israel Program for Scientific Translation, Jerusalem (1967): 298-304.

[212] F.P. IJsseling. "Electrochemical Methods in Crevice Corrosion Testing." *British Corrosion Journal* **15**(2): 51-69, (1980).

[213] D.W. Siitari and R.C. Alkire. "Initiation of Crevice Corrosion. I. Experimental Investigations on Aluminum and Iron." *Journal of the Electrochemical Society* **129**(3): 481-487, (1982).

[214] O.V. Kurov. "Chloride Solution pH in Cracks during the Corrosion of Metals." *Protection of Metals* **18**(4): 517-518, (1982).

[215] R. Ambat and E.S. Dwarakasa. "The Influence of pH on the Corrosion of Medium Strength Aerospace Alloys 8090, 2091 and 2014." *Corrosion Science* **33**(5): 681-690, (1992).

[216] R. Ambat and E.S. Dwarakasa. "Studies on the Influence of Chloride Ion and pH on the Electrochemical Behaviour of Aluminium Alloys 8090 and 2014." *Journal of Applied Electrochemistry* **24**(9): 911-916, (1994).

[217] K.G. Watkins, Z. Liu, M. McMahon, R. Vilar and M.G.S. Ferreira. "Influence of the Overlapped Area on the Corrosion Behaviour of Laser Treated Aluminium Alloys." *Materials Science and Engineering A* **252**(2): 292-300, (1998).

[218] D.P. Bishop, J.R. Cahoon, M.C. Chaturvedi, G.J. Kipouros and W.F. Caley. "On Enhancing the Mechanical Properties of Aluminum P/M Alloys." *Materials Science and Engineering A* **290**(1-2): 16-24, (2000).

[219] P.H. Chong, Z. Liu, P. Skeldon and G.E. Thompson. "Large Area Laser Surface Treatment of Aluminium Alloys for Pitting Corrosion Protection." *Applied Surface Science* **208**: 399-404, (2003).

[220] Z. Liu, P.H. Chong, A.N. Butt, P. Skeldon and G.E. Thompson. "Corrosion Mechanism of Laser-Melted AA 2014 and AA 2024 Alloys." *Applied Surface Science* **247**(1): 294-299, (2005).

[221] Z. Liu, P.H. Chong, P. Skeldon, P.A. Hilton, J.T. Spencer and B. Quayle. "Fundamental Understanding of the Corrosion Performance of Laser-Melted Metallic Alloys." *Surface & Coatings Technology* **200**(18): 5514-5525, (2006).

[222] X.L. Zhang, Z.H. Jiang, Z.P. Yao, Y. Song and Z.D. Wu. "Effects of Scan Rate on the Potentiodynamic Polarization Curve obtained to Determine the Tafel Slopes and Corrosion Current Density." *Corrosion Science* **51**(3): 581-587, (2009).

[223] A.I. Golubev. *Zhurnal Fizicheskoi Khimii* **22**: 591-601, (1948).

[224] W.D. Judge, D.P. Bishop and G.J. Kipouros. "Corrosion Behaviour of Alumix 123 P/M Alloy and AA2014-T6. Part I: OCP and Potentiodynamic Polarization." Unpublished manuscript, (2015).

APPENDIX A FULL RESULTS OF CHEMICAL ANALYSES

Table A.1 – Full results of chemical analysis of AA2014.

Element	Analysed (ppm)
Ag	<5
Al (Difference)	923075
As	<10
Ba	<5
Be	0.1
Bi	321
Ca	60
Cd	<5
Ce	<5
Co	<10
Cr	651
Cu	47339
Fe	3635
Ga	124
Ge	<10
In	<50
K	<100
La	<5
Li	<10
Mg	4896
Mn	11458

Element	Analysed (ppm)
Mo	<10
Na	108
Nb	<50
Ni	287
P	<100
Pb	134
S	<50
Sb	<50
Se	<50
Si	5602
Sn	<50
Sr	<5
Ta	<50
Te	<50
Ti	209
Tl	<50
V	109
W	<50
Zn	1958
Zr	36

Table A.2 – Full results of chemical analysis of Alumix 123.

Element	Analysed (ppm)
Ag	<2
Al	917097
As	<50
Ba	10.5
Be	0.1
Bi	<50
Ca	314
Cd	<5
Ce	<10
Co	<5
Cr	11
Cu	45685
Fe	1116
Ga	86
Ge	<100
In	<100
K	<50
La	<5
Li	<10
Mg	5211
Mn	28

Element	Analysed (ppm)
Mo	<10
Na	152
Nb	<50
Ni	78
P	277
Pb	104
S	158
Sb	<50
Se	<50
Si	7955
Sn	173
Sr	1.0
Ta	<25
Te	<50
Ti	49
Tl	<50
V	95
W	<100
Zn	454
Zr	5

APPENDIX B FULL RESULTS OF PARTICLE SIZE ANALYSIS

Table B.1 – Full results of particle size analysis of Alumix 123.

Size (μm)	Volume Density (%)	Cumulative Volume (%)
1.13	0	0
1.28	0.07	0.07
1.45	0.09	0.16
1.65	0.09	0.25
1.88	0.11	0.36
2.13	0.10	0.46
2.42	0.12	0.58
2.75	0.14	0.72
3.12	0.15	0.87
3.55	0.18	1.05
4.03	0.20	1.25
4.58	0.23	1.48
5.21	0.27	1.75
5.92	0.31	2.06
6.72	0.37	2.43
7.64	0.43	2.86
8.68	0.52	3.38
9.86	0.62	4.00
11.2	0.71	4.71
12.7	0.79	5.50
14.5	0.85	6.35
16.4	0.86	7.21
18.7	0.83	8.04
21.2	0.75	8.79
24.1	0.66	9.45
27.4	0.60	10.05
31.1	0.65	10.70
35.3	0.89	11.59
40.1	1.36	12.95
45.6	2.12	15.07
51.8	3.17	18.24
58.9	4.41	22.65
66.9	5.73	28.38
76.0	6.98	35.36
86.4	7.96	43.32
98.1	8.57	51.89
111	8.70	60.59
127	8.34	68.93
144	7.57	76.50
163	6.51	83.01
186	5.30	88.31
211	4.06	92.37
240	2.95	95.32
272	2.00	97.32
310	1.29	98.61
352	0.75	99.36
400	0.40	99.76
454	0.18	99.94
516	0.06	100
586	0	100

APPENDIX C LABORATORY SINTER PROFILES

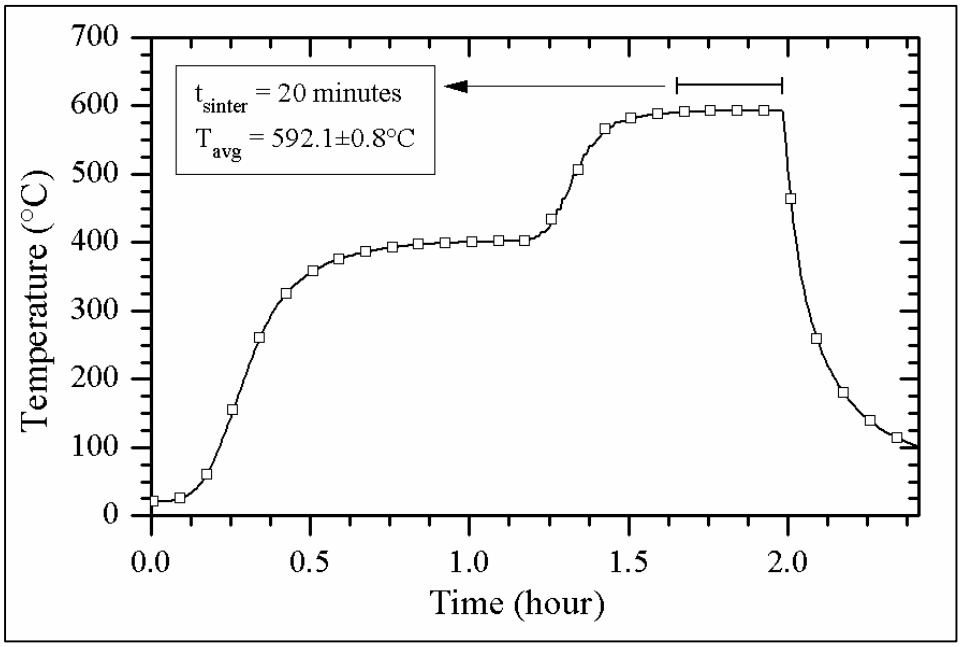

Figure C.1 – Laboratory sinter profile for Alumix 123 samples compacted at 100, 200, and 300MPa which were subsequently corrosion tested.

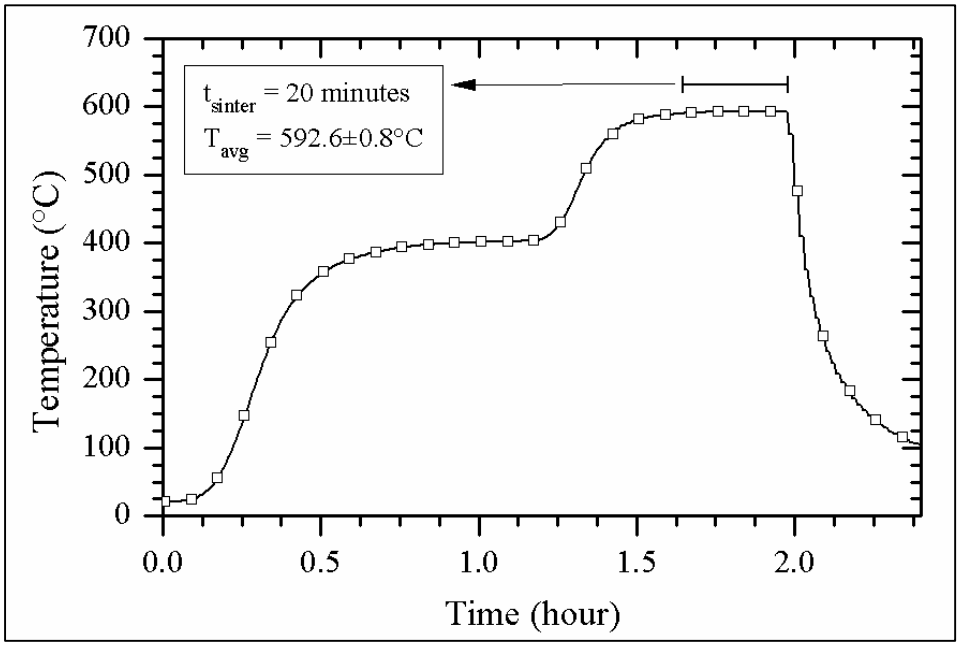

Figure C.2 – Laboratory sinter profile for Alumix 123 samples compacted at 400, 500, and 600MPa which were subsequently corrosion tested.

APPENDIX D FULL RESULTS OF DENSITY, DIMENSION, AND MASS CHANGE

Table D.1 – Green density of Alumix 123.

Compaction Pressure (MPa)	Green Density[a]		*No.* of determinations
	gcm^{-3}	% theoretical[b]	
100	2.335±0.010	84.1±0.4	4
200	2.551±0.008	91.9±0.3	4
300	2.623±0.004	94.5±0.2	27
400	2.654±0.007	95.6±0.3	4
500	2.662±0.008	95.9±0.3	4
600	2.673±0.005	96.3±0.2	4

[a]Values are given as mean ± standard deviation

[b]Theoretical density calculated as $2.777 gcm^{-3}$

Table D.2 – Density of laboratory sintered Alumix 123.

Compaction Pressure (MPa)	Sintered Density[a]		*No.* of determinations
	gcm^{-3}	% theoretical[b]	
100	2.303±0.012	82.9±0.4	2
200	2.448±0.031	88.2±1.1	2
300	2.522±0.030	90.8±1.1	5
400	2.526±0.045	91.0±1.6	2
500	2.537±0.033	91.4±1.2	2
600	2.533±0.035	91.2±1.3	2

[a]Values are given as mean ± standard deviation

[b]Theoretical density calculated as $2.777 gcm^{-3}$

Table D.3 – Dimension and mass change of laboratory sintered Alumix 123.

Compaction Pressure (MPa)	% Change After Sintering[a]			*No.* of determinations
	Diameter	Thickness	Mass	
100	–0.63±0.09	0.80±0.19	–1.41±0.16	4
200	–0.02±0.08	1.78±0.33	–1.51±0.10	4
300	0.07±0.11	2.28±0.07	–1.42±0.16	4
400	0.23±0.13	2.54±0.35	–1.31±0.14	4
500	0.28±0.06	2.64±0.36	–1.52±0.09	4
600	0.25±0.06	2.77±0.12	–1.52±0.08	4

[a]Values are given as mean ± standard deviation

Table D.4 – Density of industrially sintered Alumix 123.

Compaction Pressure (MPa)	Sintered Density[a]		*No.* of determinations
	gcm^{-3}	% theoretical[b]	
300	2.561±0.008	92.2±0.3	17

[a]Values are given as mean ± standard deviation

[b]Theoretical density calculated as 2.777gcm^{-3}

Table D.5 – Dimension and mass change of industrially sintered Alumix 123.

Compaction Pressure (MPa)	% Change After Sintering[a]			*No.* of determinations
	Diameter	Thickness	Mass	
300	–0.23±0.09	2.41±0.40	–1.55±0.08	34

[a]Values are given as mean ± standard deviation

Table D.6 – Effect of sizing pressure on reduction in height of industrially sintered Alumix 123.

Sizing Pressure (MPa)	Reduction in Height[a] (%)	*No.* of determinations
100	0.6±0.2	2
200	1.7±0.1	3
300	4.2±0.2	2
310	5.3±0.5	8
390	10.0±0.6	2
400	10.4±0.2	2
460	15.3±0.5	2
500	18.2±0.6	2
600	24.8±0.4	2

[a]Values are given as mean ± standard deviation

APPENDIX E FULL RESULTS OF EFFECT OF COMPACTION PRESSURE ON CORROSION BEHAVIOUR OF ALUMIX 123

Table E.1 – Effect of compaction pressure on electrochemical parameters of laboratory sintered Alumix 123-T1.

Compaction Pressure (MPa)	Electrochemical Parameter[a]				*No.* of experiments
	Corrosion Current (μAcm^{-2})	Passive Current (μAcm^{-2})	Pitting Potential (mV_{SCE})	Repassivation Potential (mV_{SCE})	
100	14.81±4.38	34.57±7.23	–699±4	–799±8	5
200	7.14±1.07	28.63±10.90	–693±3	–860±3	6
300	3.80±0.45	19.05±3.37	–693±6	–862±6	5
400	2.29±0.76	12.87±4.81	–699±3	–867±5	6
500	2.17±0.31	9.02±1.58	–695±5	–866±7	6
600	2.28±0.61	9.98±1.14	–699±4	–861±9	6

[a]Values are given as mean ± standard deviation

Table E.2 – Effect of compaction pressure on corrosion rate of laboratory sintered Alumix 123-T1.

Compaction Pressure (MPa)	Corrosion Rate[a,b,c] ($mmyr^{-1}$)
100	0.1954±0.0578
200	0.0887±0.0133
300	0.0458±0.0055
400	0.0276±0.0092
500	0.0260±0.0037
600	0.0273±0.0074

[a]Calculated using sintered density

[b]Values are given as mean ± standard deviation

[c]The propagated error from sintered density and corrosion current measurements is given